UNIVERSITÉ DE GRENOBLE

THÈSE

Pour obtenir le grade de

DOCTEUR DE L'UNIVERSITÉ DE GRENOBLE

Spécialité : **Mécanique et Matériaux**
Arrêté ministériel : 7 août 2006

Présentée par

Qi ZHANG

Thèse dirigée par **Amen Agbossou**
codirigée par **Daniel Guyomar et Zhihua FENG**

préparée au sein du **LOCIE**
dans **l'École Doctorale SISEO**

Récupération de micro-énergie renouvelable par couplage multiphysique des matériaux : applications aux bâtiments

Thèse soutenue publiquement le **14 avril 2011**
devant le jury composé de :

M. Orphée CUGAT
Dir. Rech. G2Elab - ENSE3, Grenoble, (Président)
M. Jean-François ROUCHON
Pr. INP de Toulouse (Rapporteur)
M. Christophe GOUPIL
Pr. CRISMAT UMS-CNRT, ENSI Caen, (Rapporteur)
M. Guillaume FOISSAC
Ing., EDF R&D, Moret sur Loing, (Membre)
M. Adrien BADEL
MCF, Université de Savoie, SYMME, Annecy, (Membre)
M. Amen AGBOSSOU
Pr. Université de Savoie, LOCIE, Chambéry, (Dir. Thèse, Membre)
M. Daniel GUYOMAR
Pr. INSA - LGEF, Lyon, (Co-dir., Membre)
M. Zhihua FENG
Pr. University of Science and Technology of China, (Co-dir., Membre)

Table of contents

Acknowledgement

This thesis is a summary of my major scientific research in France between 2009 and 2011. It is supported by “Region Rhone-Alpes” through the project “PIVOTER”. I gratefully acknowledge in advance the directors of the “Region Rhone-Alpes” for their confidence. Besides, I would like to acknowledge in advance the two reviewers of this thesis Professor Jean-François Rouchon and Professor Christophe Goupil for their valuable suggestions on the improvement of my work in the PhD. Great acknowledgement also to the three examiners of my defense Orphée Cugat, Guillaume Foissac and Adrien Badel for their participation and patience.

At the end of this PhD study which is also the start of another new journey in my life, I would like to express my deepest and heartfelt thanks to all these people below who helped me to progress in academics and to grown up personally.

Thanks to my advisor Professor Amen Agbossou who helps me to distinguish scientific problem and engineer problem. He is encouraging, enlightened, full of imagination and able to make a research interesting. His patience and zealousness in his job give me a completely fresh comprehension of scientific research. He is kind to the people and his smile is always impressed.

Thanks to my co-advisor Professor Zhihua Feng who opens the door of the magic world to me. His deep insight in physics and excellent capability of expression is admirable. He is diligent in work, religious in research, creative in design and persistence in pursuit of science. He is strict and thoughtful with student. His selfless attitude to the life as a researcher always moves me on when meeting with great challenges.

Thanks to my co-advisor Professor Daniel Guyomar who provides me with the opportunity to study with Professor Amen Agbossou. His confidence makes me brave in improving my scientific career and in fulfilling my personal best.

Thanks to the colleagues in this research Gael Sebald, Mathieu Cosnier, Anne-Cecile Grillet and Thierry Goldin. They helped a lot in this study.

Thanks to all the members in LOCIE, Université de Savoie with special gratitude for Professor Lingai Luo (Director of LOCIE). They are always friendly and passional. Special thanks to the Chinese team! - Yilin Fan, Xiaofeng Guo, Hua Zhang, Xiangdi Huang, Hui Liu, Bin Cao, Yu Bai, Tong Zhang, Limin Wang. They make my life in France full of laugh and joy.

Thanks to my parents and all my relatives for their constant love and confidence in me. Finally, thanks to my wife Wenxiang Han. She is a good partner in my life and research. She has been always loving, supportive and understanding.

Abstract

The aim of this study is to investigate ambient energy harvesting with coupling effect of piezoelectric, pyroelectric and thermoelectric materials.

Three basic problems lie in an energy harvesting process with these coupling effects: (i) design and optimize a structure which is able to accumulate the micro-power from the energy source and transform it into the favorable loading on the active material, (ii) improve the energy conversion efficiency according to the suitable choice of material properties and (iii) develop an energy harvesting circuit which is able to improve the energy conversion efficiency.

The developed approach was experimental and numerical studies at first in laboratory conditions for deep understanding of energy harvesting process and then in outside conditions for verifying actual performance of the realized devices.

On the thermoelectric coupling effect, a new method of harvesting solar and ambient energy is presented. The method is based on thermoelectric and both sensitive and latent heat effects for energy harvesting day and night. A maximum power generation of $1Wm^{-2}$ is achieved with thermoelectric material (Bi_2Te_3).

On the pyroelectric effect, the inherent fluctuation with time of the natural wind speed was used. A maximum time variation of temperature of 16°C/minute was achieved which corresponds to an average power of $0.6mWm^{-2.}$

On the piezoelectric effect, a mechanical structure which is enlightened from harmonica was developed and dynamic fluid-structure problems were addressed. The developed prototype begins to work for wind speed around $2ms^{-1}$ and a maximum power generation of $8.9mWm^{-2}$ was achieved.

Ultimately, a typical building application (automatic control of water cooling photovoltaic panel) with the harvested solar thermal energy is introduced. The proposed application highlights an example of using harvested micro-energy to improve macro-energy production (around 10%).

Keywords: ambient energy harvesting, thermoelectric, pyroelectric, piezoelectric, phase change material.

Résumé

L'objet de l'étude menée vise la récupération de micro-énergie renouvelable au moyen des matériaux piézoélectriques, pyroélectriques et thermoélectriques.

Cette étude porte sur l'optimisation de trois aspects de la récupération de micro-énergie : (i) le couplage entre le générateur et l'environnement, (ii) l'efficacité de conversion d'énergie par le choix adéquat de matériaux et (iii) l'extraction de l'énergie électrique.

Des études expérimentales et théoriques ont été menées en premier lieu dans des conditions de laboratoire pour une meilleure compréhension des phénomènes de récupération de micro-énergie, puis dans des conditions réelles pour vérifier les performances effectives des dispositifs réalisés.

Concernant l'effet thermoélectrique, une nouvelle méthode de récupération de micro-énergie ambiante est présentée. Cette méthode utilise les générateurs thermoélectriques et les effets de chaleur sensible et chaleur sensible des matériaux à changement de phase pour produire des micro-énergies aussi bien de jour que de nuit. Une puissance maximale de $1Wm^{-2}$ avec un matériau thermoélectrique (Bi_2Te_3) a été obtenue.

Concernant l'effet pyroélectrique, les variations de vitesses du vent au cours du temps sont exploitées. Une variation temporelle maximale de la température de 16°C/mn est disponible avec l'air ambiant et le rayonnement solaire. La puissance moyenne alors récupérée est de $0.6mWm^{-2}$.

Concernant l'effet piézo-électrique, une structure mécanique de type harmonica a été développée ainsi qu'une estimation des efforts d'interaction fluide-structure. Le prototype développé fonctionne à partir des vitesses du vent de $2ms^{-1}$ et génère une production d'énergie électrique de $8.9mWm^{-2}$.

A titre d'illustration, une application typique a été présentée (refroidissement de panneau photovoltaïque). Elle a montré une augmentation de la production d'électricité autour de 10%. L'application met en évidence l'utilisation des micro-énergies renouvelables au service de la production de macro-énergie.

Mots clés : récupération de micro-énergie renouvelable, effets thermoélectrique, pyroélectrique, piézo-électrique, matériaux à changement de phase.

List of Latin Symbols

A	Equivalent surface area of a piezo element as a disk structure (m^2)
A_e	Surface area of the capacitor of a electrostatic power generator (m^2)
A_{PYEG}	Surface area of the PYEG (mm^2)
A_{TEG}	Sectional (or surface) area of the TEG (m^2)
$a(u)$	Average width along the sides of a cantilever (m)
A_{wind}	Sectional area of the inlet of the cavity (m^2)
B	Strength of the magnetic field (T)
B_i	Biot number
b	The size of the aperture when a cantilever is stopped (mm)
C	Structural damping factor of a cantilever (Nsm^{-1})
C_0	Clamped capacitance of the piezo element (nF)
C_c	Flow contraction coefficient for flow through a sharp edged slit = 0.61
c_E	Volume specific heat of the PYEG ($Jm^{-3}°C^{-1}$)
C^E	Matrix of elastic stiffness constant in short circuit condition (Pa)
C_E	Thermal capacitance of the electrode in the TEG ($JKg^{-1}°C^{-1}$)
C_e	Capacitance of a electrostatic power generator (mF)
C^D	Matrix of elastic stiffness constant in open circuit condition (Pa)
C_D	Drag coefficient
C_{gmax}	Concentrating ratio of the solar collector
c_L	Capacitance of the energy storage capacitor (nF)
c_{PYEG}	Electrical capacitance of PYEG (nF)
C_P	Thermal capacitance of the ceramic plate in the TEG ($JKg^{-1}°C^{-1}$)
C_{PCM}	Thermal capacitance of the PCM ($JKg^{-1}°C^{-1}$)
C_{PYEG}	Thermal capacitance of PYEG ($JKg^{-1}°C^{-1}$)
C_s	Thermal capacitance of the heat sink ($JKg^{-1}°C^{-1}$)
C_{TEG}	Thermal capacitance of TEG ($JKg^{-1}°C^{-1}$)
C_{TEG_X}	Specific heat of sub-sections in the TEG ($JKg^{-1}°C^{-1}$)
D	Electric displacement of the PIEG (Cm^{-2})
d	Matrix of piezoelectric strain constant (CN^{-1})
dQ_p	Generated charges from the PYEG (C)
D_s	Saturated surface charge density of the piezo element (Cm^{-2})
d^t	Transpose of d (CN^{-1})
dT	Average temperature difference on the TEG during the day (°C)
$dT(t)$	Temperature variation with time (°C)
E	Electric field (Vm^{-1})
$E(t)$	Total harvested energy as a function of time (J)
e	Matrix of piezoelectric stress constant (Cm^{-2})
E_{break}	Maximum field applied on the piezo element (V/m)
E_{dp}	Depoling electric field of the piezo element (V/m)
EI	Flexural rigidity of the cantilever ($Pa*m^4$)
E_{Normal}	Harvested energy normalized
E_M	Maximum Electric field (V/m)

$\boldsymbol{e^t}$	Transpose of $\boldsymbol{e}$ (Cm^{-2})
$\boldsymbol{F}$	Equivalent force loading on the cantilever (N)
$\boldsymbol{F_{max}}$	Maximum equivalent force applied on the cantilever (N)
$\boldsymbol{F_p}$	Restoring force of the piezo element (N)
$\boldsymbol{F_{sta}}$	Steady static force yield on the cantilever (N)
$\boldsymbol{F(t)}$	Total active force on the cantilever (N)
$\boldsymbol{F(t)_{max}}$	Amplitude of the total active force on the cantilever (N)
$\boldsymbol{f(t, x)}$	Local active force on the cantilever (N)
$\boldsymbol{f(u)}$	Total exit area of the aperture of the cavity (mm^2)
$\boldsymbol{G}$	Gravitational constant = 9.81 (ms^{-2})
$\boldsymbol{g}$	Matrix of piezoelectric voltage constant (VmN^{-1})
$\boldsymbol{G_{sc}}$	Solar constant = 1367 (Wm^{-2})
$\boldsymbol{g^t}$	Transpose of $\boldsymbol{g}$ (VmN^{-1})
$\boldsymbol{H}$	Equivalent heat flux applied to the TEG in FEM simulation (Wm^{-2})
$\boldsymbol{h}$	Matrix of piezoelectric charge constant (Vm^{-1})
$\boldsymbol{h_c}$	Convection coefficient ($Wm^{-2}°C^{-1}$)
$\boldsymbol{h_{in}}$	Input heat flux from hot reservoir to the TEG (Wm^{-2})
$\boldsymbol{h^t}$	Transpose of $\boldsymbol{h}$ (Vm^{-1})
$\boldsymbol{H_{TEG}}$	Thickness of the TEG (mm)
$\boldsymbol{H_{TEG\_X}}$	Thickness of sub-sections in the TEG (mm)
$\boldsymbol{I}$	Output current of the active material (A)
$\boldsymbol{I_P}$	Pyroelectric current (µA)
$\boldsymbol{k}$	Eccentricity correction factor
$\boldsymbol{K_f}$	Thermal conductivity of air = 0.0263 ($Wm^{-1}K^{-1}$)
$\boldsymbol{K_{PE}}$	Equivalent stiffness of the piezoelement in short circuit (Nm^{-1})
$\boldsymbol{K_{PYEG}}$	Thermal conductivity of the PYEG ($Wm^{-1}°C^{-1}$)
$\boldsymbol{K_S}$	Equivalent stiffness of the cantilever (Nm^{-1})
$\boldsymbol{k_t}$	Factor characterize shape of the cavity
$\boldsymbol{K_{TEG}}$	Thermal conductivity of the TEG ($Wm^{-1}°C^{-1}$)
$\boldsymbol{K_{TEG\_X}}$	Thermal conductivity of sub-sections in the TEG ($Wm^{-1}°C^{-1}$)
$\boldsymbol{k_{xx}}$	Electromechanical coupling factor ($\boldsymbol{xx}$ = 33, 31, p or 15)
$\boldsymbol{L}$	Thickness of the bulk pillar piezoelement (mm)
$\boldsymbol{l}$	Length of the coil (m)
$\boldsymbol{L_0}$	Length of the cantilever (m)
$\boldsymbol{L_{Bi}}$	Characteristic length when estimate Biot number (m)
$\boldsymbol{L_c}$	Characteristic length of the objective when estimate convection (m)
$\boldsymbol{L_{TEG\_X}}$	Length of sub-sections in the TEG (mm)
$\boldsymbol{M}$	Rigid mass of a cantilever (g)
$\boldsymbol{M_p}$	Mass of proof at the tip of a cantilever (g)
$\boldsymbol{N}$	Number of turns in the coil
$\boldsymbol{n}$	Number of the day of the year starting from the first of January
$\boldsymbol{Nu}$	Nusselt number
$\boldsymbol{p}$	Pyroelectric coefficient without temperature dependence ($\mu Cm^{-2}°C^{-1}$)
$\boldsymbol{p(T)}$	Pyroelectric coefficient with temperature dependence ($\mu Cm^{-2}°C^{-1}$)

$p(t)$	Dynamic pressure on the cantilever from the fluid flow (Pa)
P_{max}	Maximum electrical power achieved by the active material (mW)
P_{PIEG}	Generated electrical power in the PIEG (mW)
P_{solar}	Instantaneous extraterrestrial solar radiation on a horizontal surface (W)
P_{TEG}	Generated power from the TEG (W)
P_{wind}	Input power of the wind (W)
p_{wind}	Power density of the wind (Wm^{-2})
Q_e	Charge in a electrostatic power generator (C)
Q_{emi}	Heat radiation from the surface of the TEG to the environment (W)
Q_h	Heat taken from the hot reservoir of a PYEG (Jm^{-3})
Q_H	Heat absorbed from the hot side of the TEG (W)
Q_C	Heat released to the cold side of the TEG (W)
Q_M	Quality factor of the piezoelement
Q_I	Quality factor of the LC oscillator in an SSHI circuit
Q_{in}	Heat flow absorbed by the energy harvesting device (W)
$Q_i(t)$	Projection of the imposed force on the mode i
Q_J	Heat flow generated by Joule effect (W)
Q_{pyo}	Heat flow converted to electricity with pyroelectric effect (mW)
Q_{rad}	Intensity of solar radiation (Wm^{-2})
Q_P	Heat flow converted by Peltier effect (mW)
R	Resistor connected to the rectified voltage (Ω)
Ra	Rayleigh number
r_{ext}	Resistance of the external resistor (Ω)
R_{cov}	Thermal resistance induced by convection ($°CW^{-1}$)
r_L	Resistance of the external resistor (Ω)
R_{opt}	Optimal external resistance of the generator (Ω)
r_{PYEG}	Electrical resistance of PYEG (GΩ)
R_{PCM}	Thermal resistance from the TEG to the PCM ($°CW^{-1}$)
R_s	Thermal resistance of the heat sink
r_{TEG}	Internal electrical resistance of TEG (Ω)
R_{TEG}	Thermal resistance of TEG ($°CW^{-1}$)
R_{TEG_L}	Thermal resistance of leg in the TEG ($°CW^{-1}$)
R_{TEG_S}	Thermal resistance of solder layer in the TEG ($°CW^{-1}$)
S	Strain
S_0	Sectional area of the cantilever (mm^2)
S^E	Matrix of elastic compliance constant in short circuit condition (m^2N^{-1})
S^D	Matrix of elastic compliance constant in open circuit condition (m^2N^{-1})
S_m	Maximum strain in the piezo element
T	Stress (Pa)
T_0	Period of the vibration of the cantilever (s)
T_1, T_2	Temperature on the two surfaces of the TEG (K)
$T(t)_1$, $T(t)_2$	Measured temperature in the PYEG (°C)
t_1	The time when cantilever reaches maximum displacement (s)
T_a	Ambient temperature (°C)

T_c	Temperature on the cold face of the TEG (°C)
t_e	Thickness of the capacitor of a electrostatic power generator (mm)
T_f	Film temperature (°C)
T_h	Temperature on the hot face of the TEG (°C)
T_{in}	Uniform initial temperature in the TEG (°C)
T_m	Maximum stress in the piezo element (Pa)
T_{avg}	Average temperature in the TEG (K)
T_{PCM}	Temperature in the PCM (°C)
t_{PYEG}	Thickness of the PYEG (mm)
T_{TEG}	Calculated temperature on the irradiated surface of the TEG (°C)
t_{TEG}	Thickness of the TEG (m)
T_x	Average temperature in the internal part of the TEG (x=1~7) (°C)
u	Equivalent displacement of the cantilever considered as rigid mass (m)
U_0	A constant input volumetric flow rate (m^3s^{-1})
U_{ab}	Generated voltage on the PYEG (V)
U_{cd}	Voltage on the energy storage capacitor (V)
u_{max}	Maximum displacement of the cantilever (m)
$U(t)$	Volumetric air flow rate through the aperture (m^3s^{-1})
$u(t)$	Displacement at the tip of the cantilever (m)
V	Output voltage of the active material (V)
$V_1(t)$	Time function of $V(t, x)$
$V_2(x)$	Space function of $V(t, x)$
$V_2(0)$	Reference speed near the clamped end of the cantilever (m/s)
V_c	Volume of the cavity (m^3)
V_{CC}	Rectified voltage after the bridge circuit when it becomes stable (V)
V_{coi}	Induced voltage on a coil (V)
V_d	Forward voltage of diode (V)
V_{DC}	Rectified voltage after the bridge circuit (V)
V_e	Voltage in a electrostatic power generator (V)
V_L	Voltage generated on the external electrical load (V)
V_{open}	Maximum open circuit voltage across the coil (V)
V_{out}	Voltage on the main output of the LTC3108 converter (V)
V_{store}	Voltage on the energy storage port of the LTC3108 converter (V)
V_{PCM}	Volume of PCM (m^3)
V_{p-p}	Peak to peak voltage (V)
$V(t, x)$	Normal component of the wind velocity adjacent to the cantilever
V_w	Speed of the wind (ms^{-1})
W	Width of the cantilever (mm)
W_{TEG_X}	Width of sub-sections in the TEG (mm)
x	Distance from a local point to the clamped end of the cantilever (m)
x_0	"roughness length" (m)
X_e	Distance the coil moves through the magnetic field (m)
Z	Figure of merit of the thermoelectric device (K^{-1})
ZT	Dimensionless figure of merit of the thermoelectric device

List of Greek Symbols

α	Heat absorption rate on the energy harvesting device
α_0	Force factor of piezo element in the equivalent model (Cm^{-1})
α_d	Thermal diffusivity of air = $2.24e^{-5}$ (m^2s^{-1})
α_s	Seebeck coefficient ($V°C^{-1}$)
β	Volumetric thermal expansion coefficient = 1/298 (K^{-1})
β^S	Matrix of permittivity constant with prohibited deformation (Fm^{-1})
β^T	Matrix of permittivity constant with free deformation (Fm^{-1})
Γ	Entropy (JK^{-1})
ΔE	Latent heat per unit volume of the paraffin wax (J)
ΔT	Temperature difference across the TEG (°C)
Δt	Time of half a day (s)
ΔT_{max}	Maximum temperature difference across the TEG (°C)
δ	Declination which causes an annual variation of solar radiation
ε	Emissivity of the energy harvesting device on the surface
ε_e	Permittivity of the dielectric in a electrostatic power generator (Fm^{-1})
ε^S	Matrix of dielectric constant with prohibited deformation (Fm^{-1})
ε^T	Matrix of dielectric constant with free deformation (Fm^{-1})
$\varepsilon^{\theta}_{33}$	Dielectric constant of the PYEG (Fm^{-1})
η	Total energy conversion efficiency of a power generator
$\eta_c(t)$	Carnot efficiency which is associated with time
η_m	Energy conversion efficiency of the active material
η_E	Energy conversion efficiency based on experimental test
η_{max}	Maximum energy conversion efficiency
θ	Temperature (°C)
θ_h	Temperature in the hot reservoir(°C)
θ_c	Temperature in the cold reservoir(°C)
ν	Kinematic viscosity of air = $1.59e^{-5}$ (m^2s^{-1})
v_s	The speed of sound (m/s)
v_{wind}	Velocity of the wind (m/s)
$v(x,t)$	Transient displacement of each point in the cantilever (m)
ρ_{air}	Density of the air (Kgm^{-3})
ρ_b	Density of the cantilever beam ($Kg\ m^{-3}$)
ρ_{TEG_e}	Electrical resistivity of the TEG (Ωm)
ρ_{TEG_X}	Density of sub-sections in the TEG ($Kg\ m^{-3}$)
ρ_{PYEG}	Density of the PYEG(Kgm^{-3})
σ	Stefan–Boltzmann constant = $5.67e^{-8}$ ($Wm^{-2}K^{-4}$)
Φ	Magnetic flux through the coil (Wb)
φ	Latitude of a location on earth (°)
ω	Angular frequency of the vibrated cantilever
ω_s	Sunset hour angle

Récupération de micro-énergie renouvelable par couplage multiphysique des matériaux : applications aux bâtiments

Résumé étendu de 20 pages en français

Résumé étendu de 20 pages en français

Titre de la thèse en français : Récupération de micro-énergie renouvelable par couplage multiphysique des matériaux : applications aux bâtiments
Titre de la thèse en anglais : "Ambient energy harvesting based on coupling effects in materials: applications in buildings"

Introduction

Le développement ces dernières années de l'électronique de faible puissance (en particulier les Ultra-low-Power devices), et le besoin grandissant en autonomie d'énergie des systèmes électroniques ont conduit à un regain des travaux de recherches sur la récupération de micro-énergie renouvelable. Parmi les défis scientifiques et techniques d'importances, on peut noter le remplacement des piles par un système de récupération d'énergie renouvelable de faible puissance. On peut également noter dans le bâtiment le besoin de l'utilisation des énergies renouvelables de faible puissance pour le confort thermique et l'économie d'énergie de chauffage, de climatisation ou de production de macro-énergie.
L'étude menée dans cette thèse vise la récupération de micro-énergie renouvelable au moyen des couplages multiphysiques des matériaux piézoélectriques, pyroélectriques et thermoélectriques. Cette étude porte sur l'optimisation de trois aspects de la récupération de micro-énergie:

1. le couplage entre le générateur et l'environnement,
2. l'efficacité de conversion d'énergie par le choix adéquat de matériaux et
3. l'extraction de l'énergie électrique.

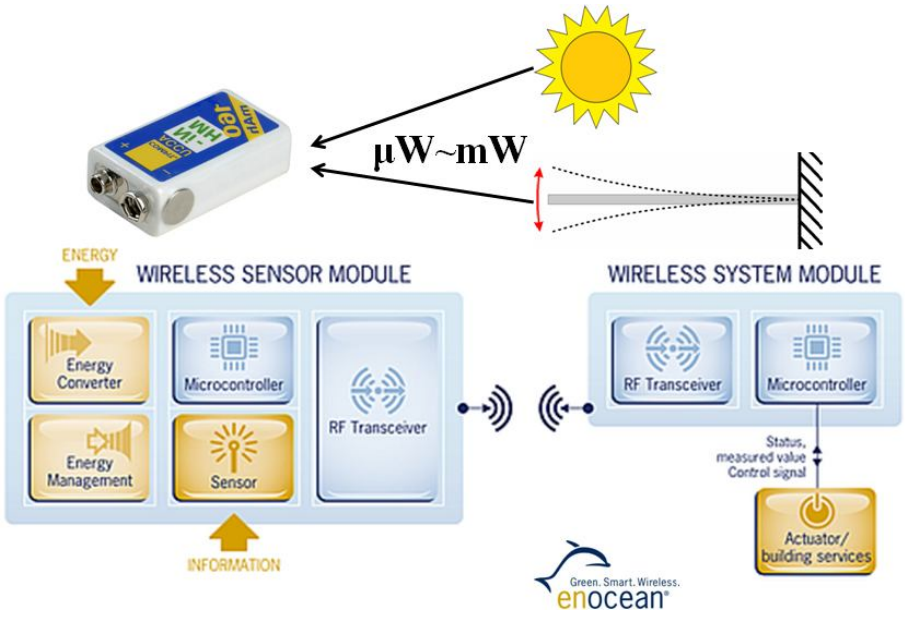

Figure (a1) : Contexte et situation de l'étude.

Les travaux ont porté sur des études expérimentales et théoriques développées dans un premier temps en conditions de laboratoire pour une meilleure compréhension des phénomènes de récupération de micro-énergie, puis dans un second temps en conditions réelles pour vérifier les performances effectives des dispositifs réalisés.
Dans ce résumé étendu en français, nous exposons les principaux développements après un bref panorama de l'état de l'art sur les trois couplages multiphysiques étudiés.

Résumé de synthèse bibliographique

Les trois effets de couplage analysés pour la récupération de micro-énergie renouvelable concernent l'effet thermoélectrique, l'effet pyroélectrique~~s~~ et l'effet piézoélectrique~~s~~. Les équations issues des théories linéaires régissant les grandeurs physiques caractéristiques de ces effets sont ci-dessous :

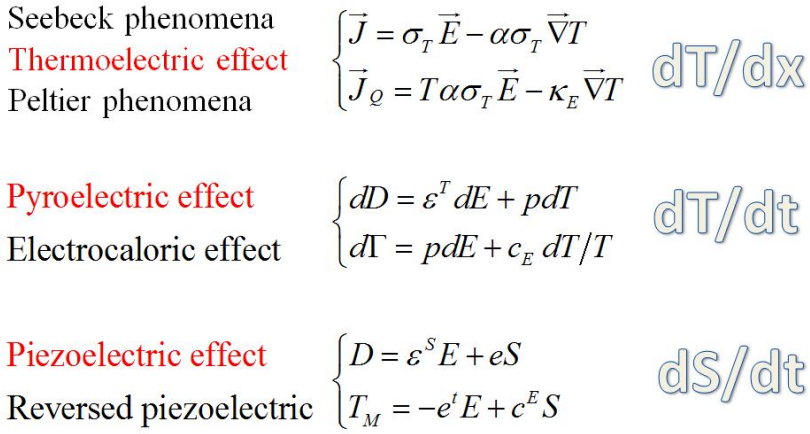

Figure (a2) : Rappel des lois de couplage multiphysique des matériaux étudiés

L'effet thermoélectrique provient de la diffusion thermique des porteurs de charge. L'effet pyroélectrique exprime la polarisation rémanente qui dépend de la température et provoque une variation de la densité de charges électriques de surface. L'effet piézo-électrique décrit la relation entre la déformation et la modification de la polarisation rémanente dans le matériau.

Etat de l'art sur l'effet thermoélectrique et la récupération d'énergie :

Le transfert d'énergie dans un thermoélectrique (TEG) comprend deux parties. La première partie est caractérisée par le transfert d'énergie entre la source thermique et le matériau actif (transfert qui dépend dans l'étude menée du coefficient de Carnot $\eta_c(t)$). La seconde partie du transfert d'énergie intègre l'élément thermoélectrique entier et conduit à définir un rendement global $\eta=\eta_c(t)*\eta_m$. Ainsi, pour un thermoélectrique (TEG) donné, le défi dans l'étude menée est d'améliorer le rendement global en œuvrant particulièrement sur le rendement de Carnot qui dépend du temps du fait de la variation de température de la source d'énergie.

Etat de l'art sur l'effet pyroélectrique et la récupération d'énergie :

Tout comme les thermoélectriques, le transfert d'énergie dans un élément pyroélectrique (PYEG) comprend également deux étapes, mais ces deux étapes sont complètement différentes de celles des thermoélectriques (Figure (a3)). Le grand défi concernant les éléments pyroélectriques (PYEG) est de développer une méthode capable de générer des variations temporelles de températures significatives sur l'élément actif à partir d'une source de température ambiante qui varie peu instantanément.

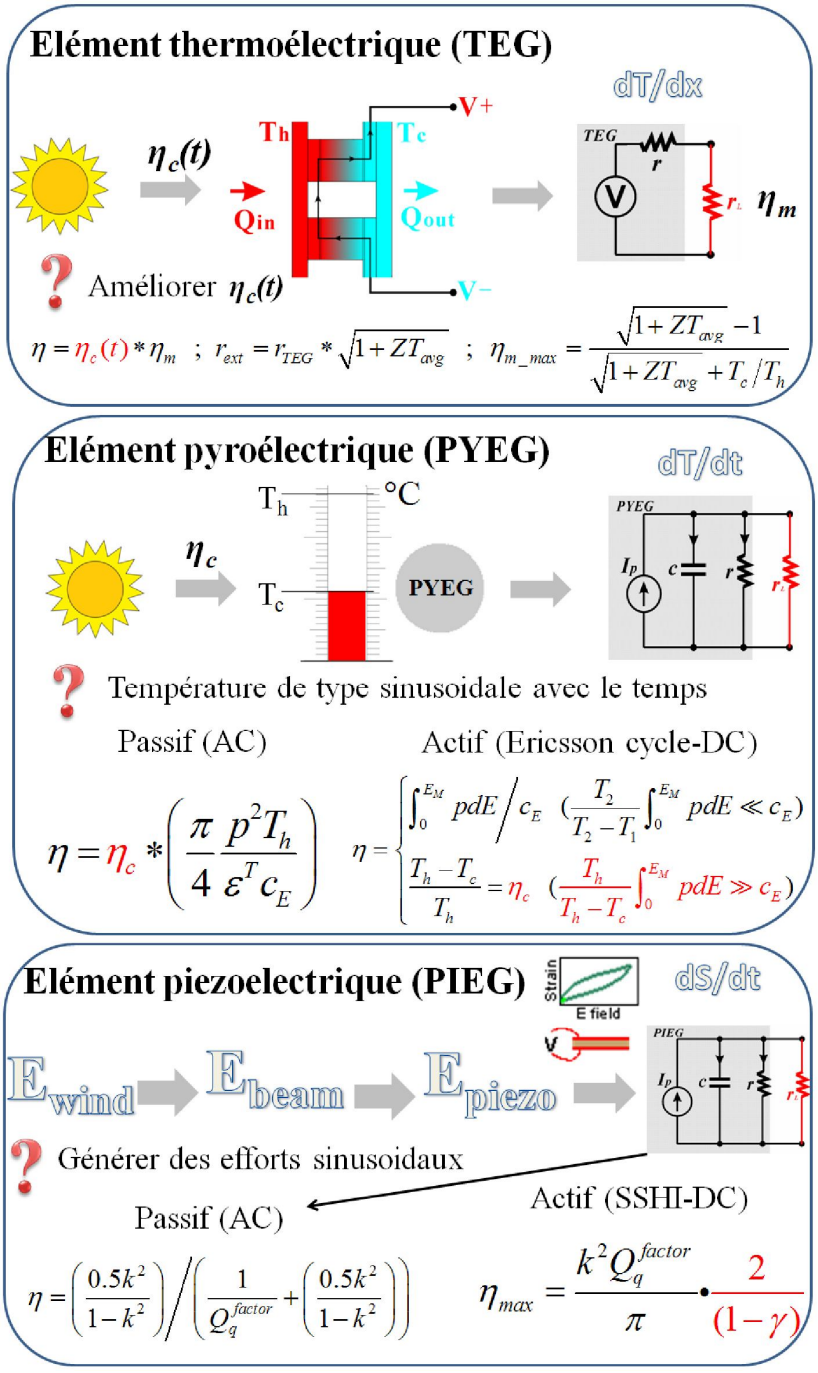

Figure (a3) : Schémas illustratifs des objectifs de l'étude menée

Etat de l'art sur l'effet piézoélectrique et la récupération d'énergie :

Quant aux matériaux piezoélectriques (PIEG), le rendement dépend de l'application visée. Dans l'étude menée, le problème scientifique majeur est celui du transfert d'énergie du vent (de faible vitesse < 5m/s) à une structure mécanique qui doit transmettre l'énergie mécanique au matériau actif piézoélectrique. Un des problèmes abordés dans l'étude piézoélectrique a porté sur la manière de produire une sollicitation mécanique sinusoïdale à partir d'un flux d'air laminaire ambiant de vitesse faible.
En quelques mots, les travaux menés se sont focalisés sur l'étude de :

1. la variation de température dans l'espace (gradient de température) pour une source de température qui dépend du temps,
2. la variation rapide de température en fonction du temps (vitesse de température) pour une source de température peu fluctuante instantanément,
3. la variation temporelle de déformation d'une poutre avec un flux d'air continue de faible vitesse.

La finalité de ces analyses est la récupération de micro-énergie renouvelable avec des matériaux thermoélectriques, des matériaux pyroélectriques et des matériaux piézoélectriques. Le point commun de ces trois analyses reste l'amélioration du rendement des dispositifs développés.

III / Principaux résultats

III-1/ Effet thermoélectrique et production de micro-énergie renouvelable

III-1.1/ Etudes expérimentales sur les thermoélectriques

Une méthode originale de récupération de micro-énergie ambiante et solaire est présentée. Cette méthode utilise les générateurs thermoélectriques et les effets de chaleur sensible et chaleur latente des matériaux à changement de phase pour produire des micro-énergies. La figure ci-dessous résume le principe de fonctionnement du dispositif développé. Elle compare également le système proposé au système usuel de récupération d'énergie solaire par effet thermoélectrique. On note que le rayonnement solaire qui arrive sur le thermoélectrique (TEG) du système usuel se décompose en deux parties : une partie transmise au matériau thermoélectrique (TEG) et une autre partie dissipée dans l'environnement par échange de chaleur entre la surface ensoleillée et l'environnement.
Les deux principaux inconvénients du dispositif usuel sont : (i) le fonctionnement possible uniquement de jour (avec le rayonnement solaire) et (ii) la réduction des performances lorsque la température du côté froid (Tc) est peu stable ou qu'elle augmente.

Système usuel de récupération d'énergie solaire avec les thermoélectriques (TEG)

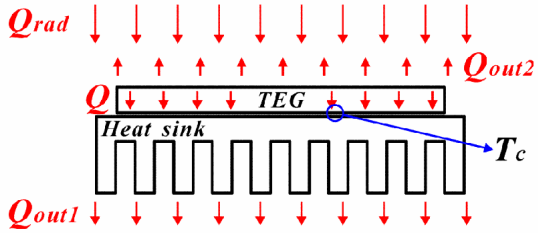

- Faible flux de chaleur Q avec l'augmentation de T_c
- Faible durée de récupération d'énergie

Nouveau système de récupération d'énergie solaire développé avec les TEG

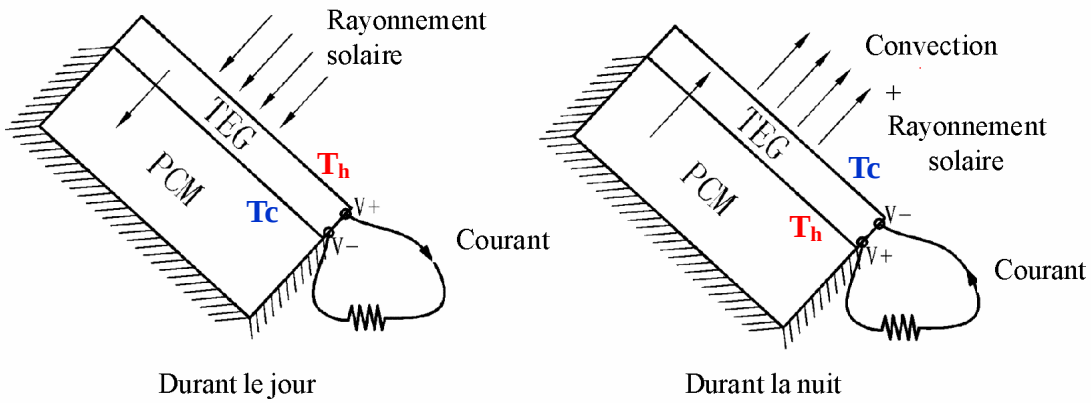

Figure (a4) : Principe de fonctionnement du nouveau dispositif développé (TEG + PCM)

Le nouveau système proposé vise à palier à ces inconvénients en utilisant des matériaux à changement de phase (PCM).
Comme illustré sur la figure (a4), un matériau à changement de phase (PCM) est alors placé du côté non ensoleillé du thermoélectrique (TEG). Ce matériau est ensuite placé dans un isolant comme indiqué sur la figure. Dans la journée, le matériau à changement de phase (PCM) permet de maintenir stable le plus longtemps possible la température du côté froid et de stocker de la chaleur qui sera restituée au thermoélectrique lorsque le rayonnement solaire disparaitra (c-à-d la nuit). La production d'électricité par effet thermoélectrique reste possible du fait de l'augmentation du rayonnement solaire durant la journée. Ainsi, par rapport au dispositif usuel de récupération d'énergie solaire, le nouveau système proposé permet de produire des micro-énergies sans interruption, aussi bien de jour que de nuit.
Un tel dispositif est un système qui permet de créer un gradient de température sur un thermoélectrique alors que la source de température est dépendante du temps.
Pour vérifier le concept de base du dispositif développé, un prototype a été fabriqué.
Un thermoélectrique (TEG (Bi_2Te_3)) est relié sur une face à un radiateur dont le rôle est d'augmenter les échanges de flux sur la surface froide. Ce système représente le dispositif usuel. Le radiateur du système usuel est à l'air libre et soumis à la convection naturelle.
Pour réaliser le dispositif développé, le radiateur du dispositif usuel est plongé dans un

bain de matériau à changement de phase noyé dans une boîte en polystyrène afin de limiter les fuites d'énergie thermique sur les côtés. Un couvercle en verre est ensuite placé au-dessus du thermoélectrique (face ensoleillée) de sorte à contrôler l'échange de chaleur (augmenter le flux de chaleur et réduire le phénomène de convection). Le facteur de merite ZT mesurée du thermoélectrique utilisé est de 0,21 ce qui correspond à un rendement maximum Carnot de 5%.

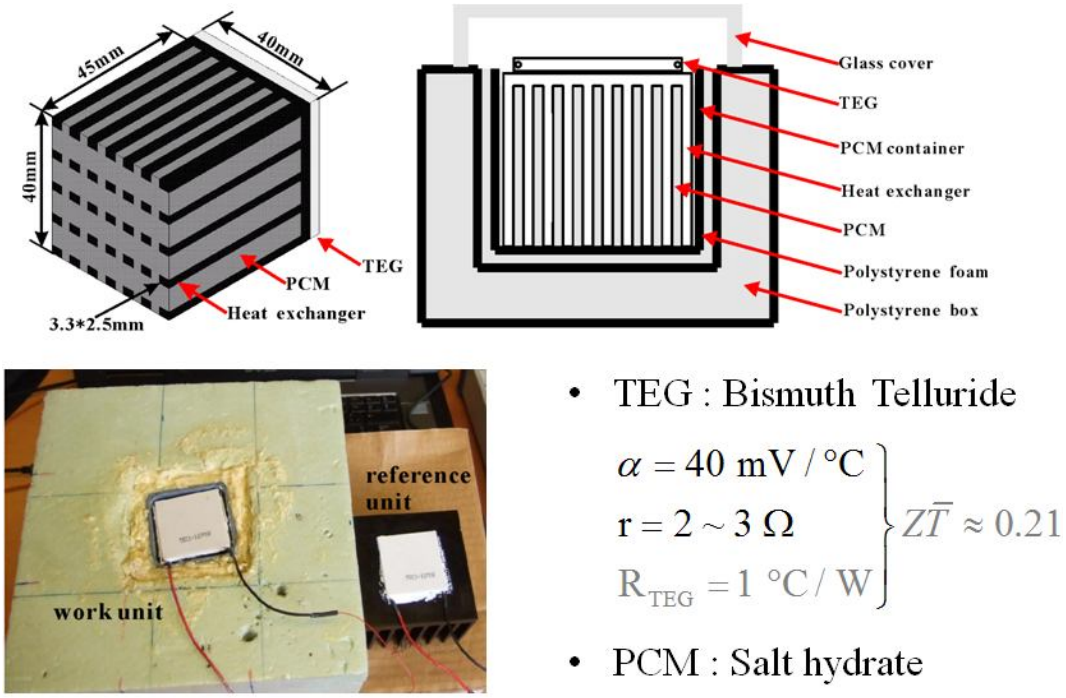

Figure (a5) : Prototype du système développé (TEG + PCM)

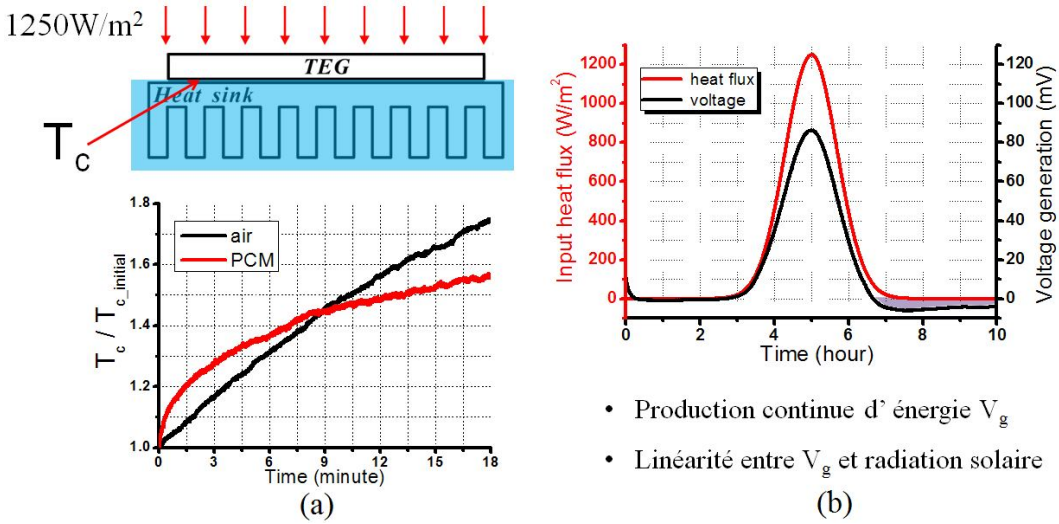

Figure (a6) : Exemples typiques de résultats en laboratoire : (a) Evolution pendant 18 mn de la température T_c sur la face froide du thermoélectrique (TEG), (b) Evolution de l'énergie récupérée sur une durée de 10 heures en laboratoire.

Afin de vérifier la stabilité de la température préconisée pour le dispositif proposé, un flux de chaleur constant est appliqué sur une face du thermoélectrique des deux systèmes (système usuel et nouveau dispositif). Sur la face froide du thermoélectrique du système usuel, le radiateur est laissé à l'air libre (convection naturelle en laboratoire) alors que pour le dispositif développé, il est placé dans le matériau à changement de phase isolé dans une boite polystyrène.
La figure (a6)-a montre le profil de températures enregistrées sur la face froide du thermoélectrique (Tc : courbe noire pour le système usuel et courbe rouge pour le dispositif développé). On note bien que la température T_c avec le matériau à changement de phase (PCM) devient plus stable pour de longs temps. Cela indique une meilleure performance possible sur une journée entière avec le nouveau système.

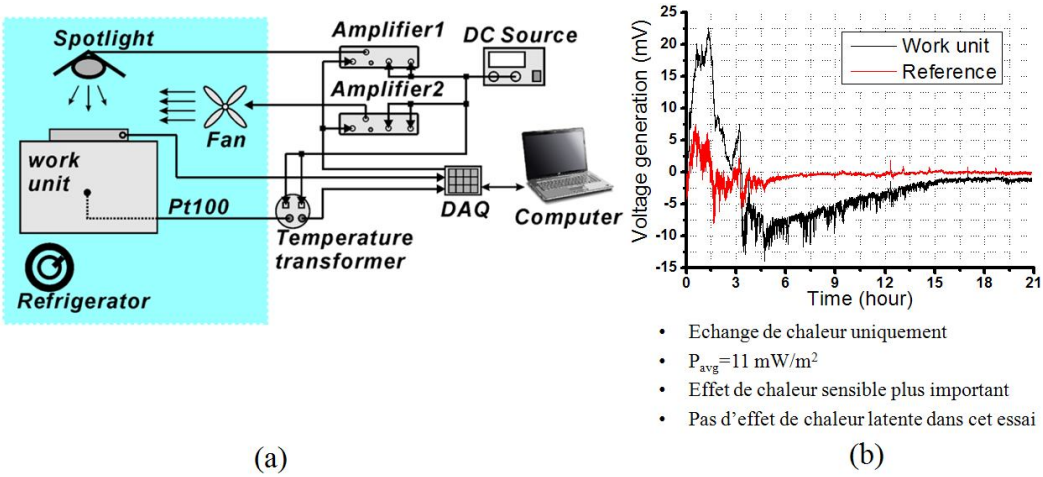

Figure (a7) : (a) Dispositif d'essai en laboratoire, (b) Energie récupérée à l'extérieur avec le dispositif laboratoire (un seul thermoélectrique)

Pour explorer les possibilités du dispositif développé et valider des modèles qui sont développés, il a été mené des essais en laboratoire avec contrôle de quelques grandeurs d'entrée. La figure (a7)-a présente le dispositif d'essai.
Dans ce dispositif, le rayonnement solaire, la convection forcée, et la température ambiante sont simulés respectivement par une lampe pilotée par ordinateur, un ventilateur et un caisson réfrigérant.
Avec un flux de chaleur d'entrée représenté par la courbe rouge, figure (a6)-b qui simule le rayonnement solaire, on note (courbe en noir) que la génération de tension du thermoélectrique (TEG) est non-nul pendant la nuit. Cela confirme la seconde idée de base du dispositif proposé (à savoir produire des micro-énergies la nuit ou en absence de rayonnement solaire).
On note également, figure (a6)-b que, de jour, la tension générée est quasiment proportionnelle au rayonnement solaire. Par contre, de nuit, la production d'énergie reste faible du fait des faibles effets de convection en laboratoire (figure (a6)-b). Une convection renforcée devrait permet d'accroître significativement la production d'énergie la nuit. La quantité d'énergie récupérable la nuit dépend donc essentiellement

de la quantité de chaleur stocker dans le matériau à changement de phase (PCM) et des phénomènes de convection et de rayonnement la nuit.
En complément à l'étude en laboratoire, le dispositif de base avec un seul thermoélectrique a été testé en condition réelle (à l'extérieur) pendant des journées typiques d'hivers.
Un exemple de résultats obtenus en condition réelle avec un seul thermoélectrique est présenté sur la figure (a7)-b. La tension enregistrée est représentée par la courbe noire avec le dispositif développé et celle du système usuel est tracée avec la couleur rouge. Il est à constater que la tension récupérée avec le système proposé est 4 fois plus élevée que celle avec le système usuel (système de référence). Dans les conditions de test hivernal (faible ensoleillement) la production d'énergie de l'unité de base (un seul thermoélectrique) atteint 11 mW/m^2. L'énergie récupérée pendant la nuit reste cependant faible.
La faible valeur de l'énergie récupérée pendant la nuit (figure (a7)) peut s'expliquer par la diminution linéaire de la tension récupérée. Cela témoigne d'une utilisation de la chaleur sensible du matériau à changement de phase (PCM) au lieu de l'utilisation de sa chaleur latente. En effet, durant ces essais où l'ensoleillement était faible, le matériau à changement de phase est resté en dessous de sa température de changement de phase. Il n'y a donc pas eu de stockage de chaleur latente.

Pour explorer les potentialités du concept validé par analyse en laboratoire, nous avons fabriqué, dans un second temps, un nouveau dispositif de récupération d'énergie couplé à un autre matériau à changement de phase (paraffine Wax).
Ce nouveau dispositif, représenté en figure (a8)-a, est composé de 12 pièces de thermoélectriques connectées en série. Pour une meilleure absorption des radiations solaires dans le thermoélectrique, la surface chauffée par le rayonnement solaire a été peinte en noir. La nouvelle unité de travail a été testée à l'extérieur pendant 60 heures en continu. Le rayonnement solaire et la température ambiante sont représentés (figure (a8)-b) par les courbes rouges. Les courbes en noire représentent la tension aux bornes de la résistance de charge du thermoélectrique (TEG) et la température à l'intérieur du matériau à changement de phase (PCM).
Ces résultats montrent clairement l'effet visible de la chaleur latente, qui se traduit par le changement de pentes des courbes vers 25 heures et 49 heures. Ces changements de pentes traduisent l'effet de changement de phase dans le matériau à changement de phase du côté de la source froide des thermoélectriques.
On note (Figure (a6)-b et Figure (a7)-b), qu'avec l'effet de la chaleur latente, la génération de tension devient plus stable au cours de la nuit. La puissance maximale mesurée atteint 1 W/m^2 ce qui correspond à un rendement de Carnot supérieure à 2%. Cette performance peut être améliorée avec l'augmentation des propriétés de la chaleur latente et de température de fusion du matériau à changement de phase.

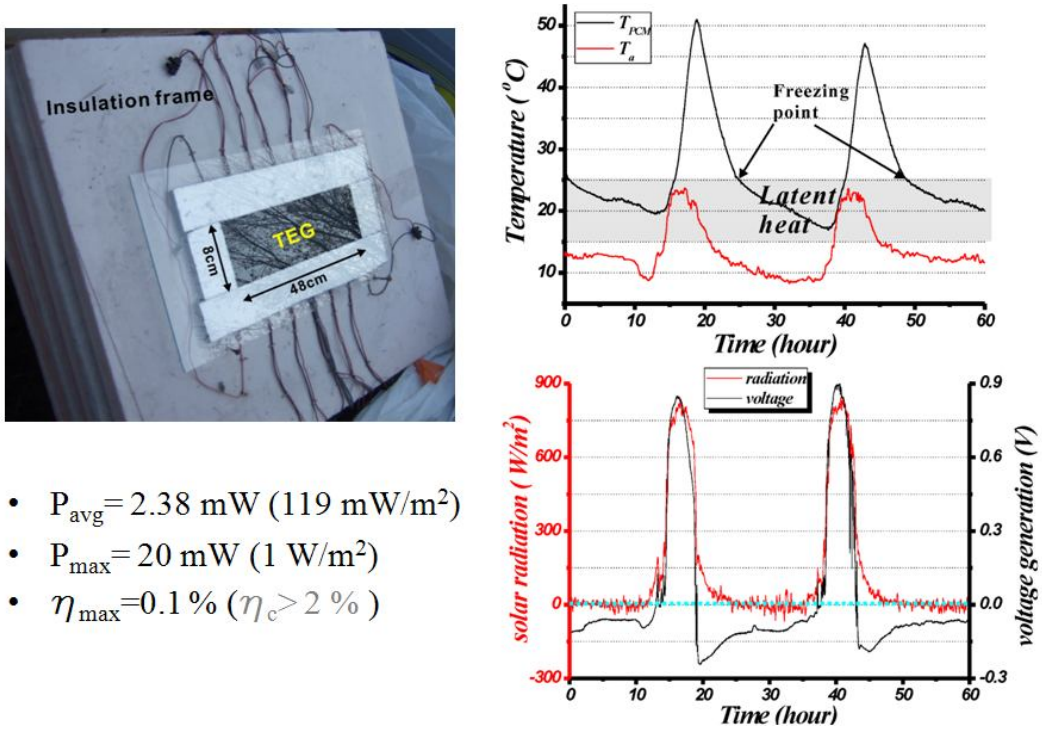

- P_{avg}= 2.38 mW (119 mW/m²)
- P_{max}= 20 mW (1 W/m²)
- η_{max}=0.1 % (η_c> 2 %)

Figure (a8) : Second prototype pour des essais à l'extérieur en conditions réelles : 12 thermoélectriques peints en noir avec de la paraffine wax (a) Dispositif d'essai (b) Exemple de résultats d'essai sur 60 heures.

III-1.1/ Modélisation du dispositif thermoélectrique développé

En dehors de l'étude expérimentale, nous avons développé un modèle numérique (MEF) pour analyser le comportement du dispositif développé et pour fournir des outils de dimensionnement d'un tel système.

Les deux développements numériques principaux ont portés sur :

1. l'analyse par la méthode des éléments finis (MEF° qui a été mise en œuvre avec l'outil numérique (ANSYS). Pour estimer de façon précise la performance transitoire de dispositif, il a été implémenté dans ANSYS, une boucle spécifique de calculs permettant à chaque pas fin de calculs, de déterminer les températures exactes aux bornes des thermoélectriques (Figure (a9)-a). Avec la connaissance à chaque instant des températures aux bornes du thermoélectrique, on calcule à nouveau pour le pas suivant, le flux de chaleur d'entrée à appliquer sur le thermoélectrique et celui dissipé par convection et rayonnement.
2. l'analyse avec un modèle simplifié (Figure (a10). Dans ce modèle, le matériau à changement de phase (PCM) et le radiateur sont considérés respectivement comme une capacité thermique variable et une résistance thermique fixe. Le thermoélectrique (TEG) est représenté par deux capacités et une résistance. L'effet de couplage est pris en compte par un flux thermique de type Peltier produisant de la chaleur par effet Joule. Les conditions limites sont de conditions thermiques prenant en compte les effets de rayonnement et de convection sur le côté recevant le rayonnement solaire.

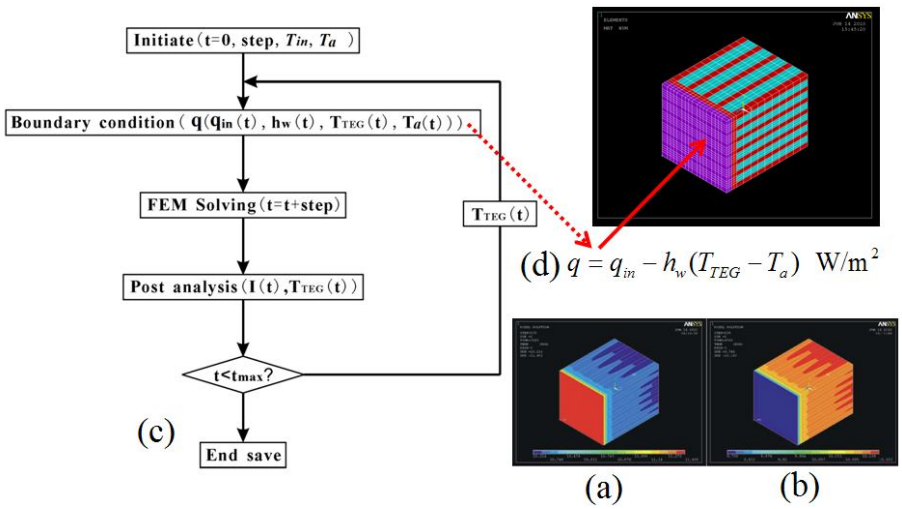

Figure (a9) : Modèle éléments finis et exemple de distribution de la température dans un élément de base (1TEG+MCP) (a) durant le jour (b) pendant la nuit, (c) et (d) organigramme de l'analyse transitoire

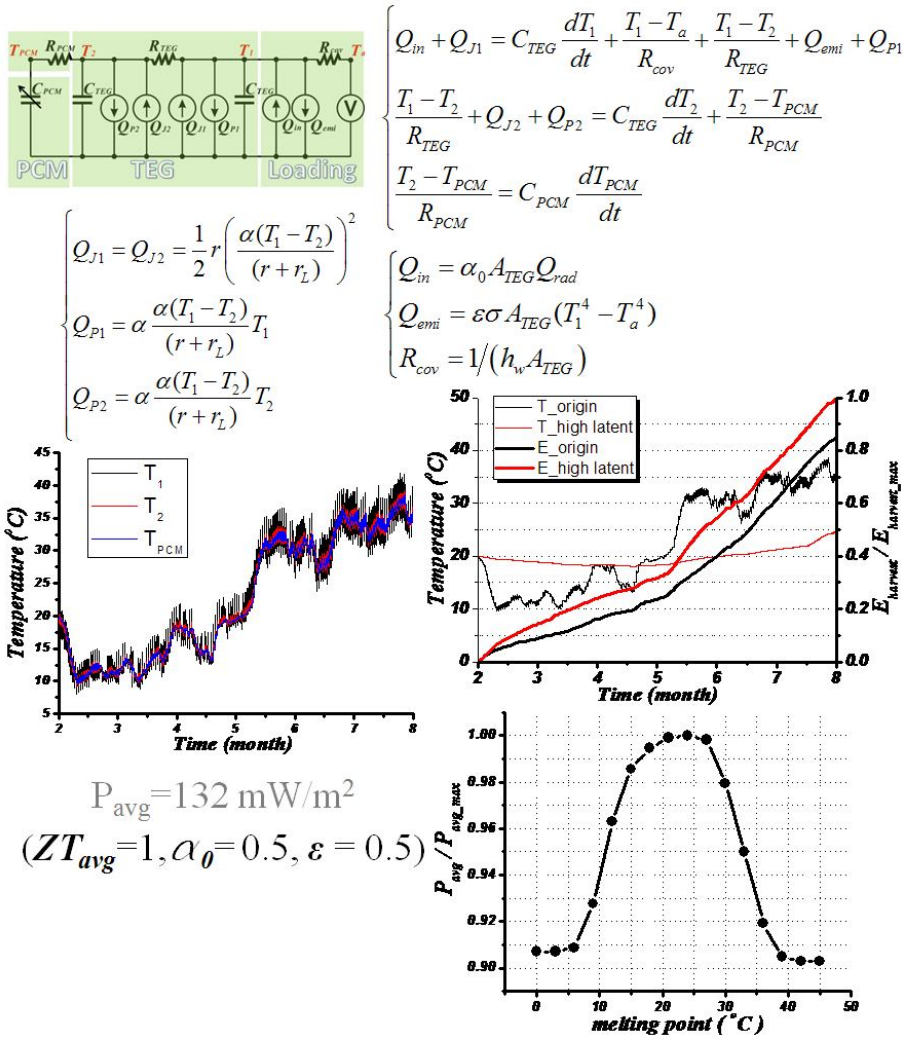

Figure (a10) : Modèle simplifié et résultats de simulation sur 6 mois

Avec des données météorologiques sur deux jours, la simulation (FEM) montre une production d'énergie de 83 mW/m2.
Le modèle numérique par éléments finis (FEM) développé s'est avéré bien précis mais très coûteux en temps de calculs. D'où le développement du modèle simplifié.
Les figures (a9)-a et b montrent des exemples de résultats obtenus avec le modèle éléments finis développé. La figure (a10)-b montre les résultats de simulation du modèle simplifié, avec des données de calculs issues de mesures effectuées sur site du Bourget du Lac pendant 6 mois.
Sur la période de 6 mois, avec le modèle simplifié dans lequel on fixe un taux d'absorption ZT = 1, et une émissivité de 0,5 on obtient une production d'énergie de 132 mW/m^2. Les résultats de ces simulations montrent clairement l'augmentation des performances due aux effets de chaleur latente (performances 10 fois plus élevées) et de la température de fusion du matériau à changement de phase (augmentation de 15% en fonction du type de MCP). Cette analyse révèle qu'avec le dispositif proposé, il existe des caractéristiques et des conditions idéales de MCP pour une récupération optimale d'énergie renouvelable.

III-2/ Effet pyroélectrique et production de micro-énergie renouvelable

Concernant l'effet pyroélectrique, l'étude s'est focalisée sur les variations de température avec le temps sous l'effet du rayonnement solaire et du vent.

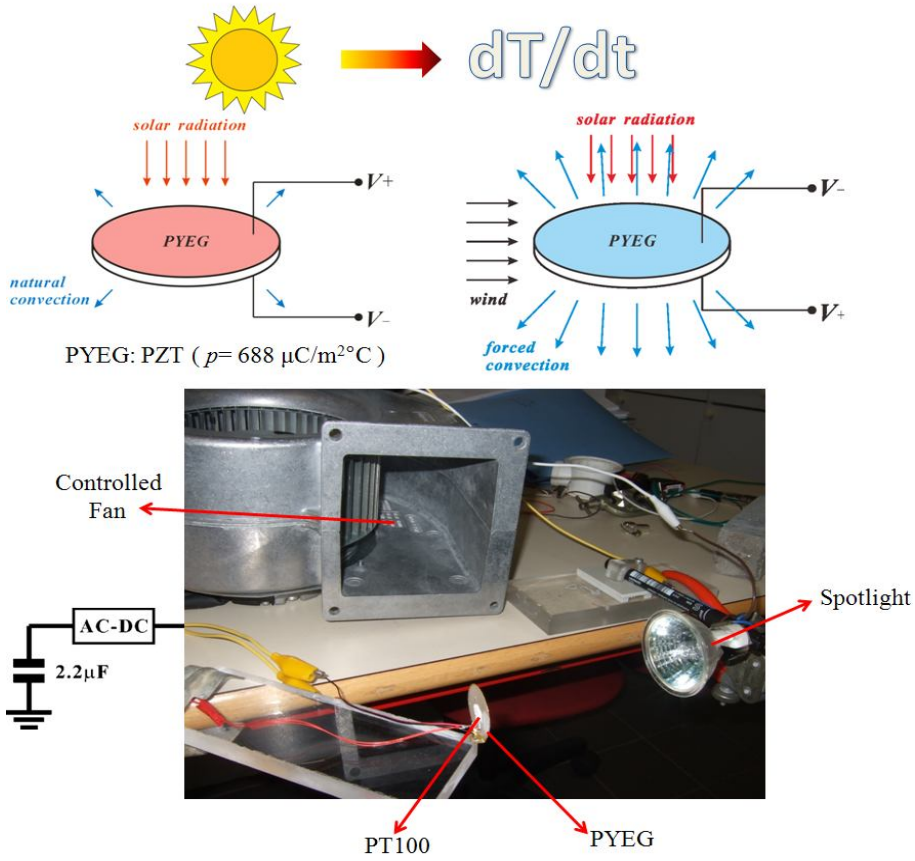

Figure (a11) : (a) Principe de récupération de l'énergie solaire par effet pyroélectrique (b) Dispositif expérimental de laboratoire

L’idée nouvelle explorée a consisté à combiner le rayonnement solaire et les fluctuations du vent pour créer la sollicitation thermique variable indispensable pour la récupération d’énergie par effet pyroéléctrique. Le dispositif développé est représenté en figure (a11).
En absence de vent et sous un rayonnement solaire, la température du matériau pyroélectrique augmente jusqu’à une valeur relativement élevée correspondant à un point d'équilibre thermique. Ce point d’équilibre est celui de fort ensoleillement et faible convection naturelle. Lorsqu’un vent frais est envoyé sur ce matériau pyroélectrique, sa température tend à diminuer jusqu'à un nouvel état d’équilibre thermique correspondant à celui d’une vitesse de vent donné. La variation de température du matériau pyroélectrique résultante de la combinaison de l’effet du rayonnement solaire et de la fluctuation de la vitesse du vent constitue le principe de récupération de micro-énergie développé avec les matériaux pyroélectriques.
Cette idée a été explorée avec un volet expérimental et un volet modélisation numérique. Les résultats montrent qu’une variation temporelle maximale de la température de 16°C/mn est disponible dans l’ambiant. Avec une telle variation, la puissance moyenne d’énergie récupérée est de 0.6mWm^{-2}.
La figure (a12) illustre le modèle de simulation numérique développé pour le générateur pyroélectrique.

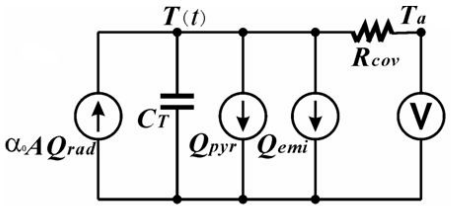

$$I_p(t+step) = p\frac{T(t)-T(t-step)}{step}$$

$$\begin{cases} Q_{emi} = \varepsilon A_{PYEG}\sigma\left(T(t)^4 - T_a^4\right) \\ Q_{pyr} = I_p(t)\times U_{ab}(t) \\ R_{cov} = \dfrac{1}{h_w \times 2A_{PYEG}} \\ C_T = \rho C_{pt} V_{PYEG} \end{cases}$$

$$\alpha_0 Q_{rad} A_{PYEG} = C_T\frac{dT(t)}{dt} + \frac{T(t)-T_a}{R_{cov}} + Q_{emi} + Q_{pyr}$$

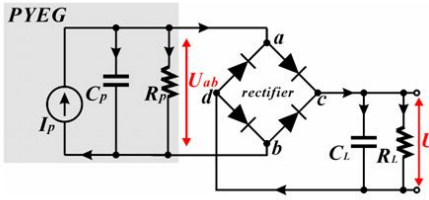

$$\begin{cases} I_p(t) = C_p\dfrac{dU_{ab}(t)}{dt} + \dfrac{U_{ab}(t)}{R_p} + C_L\dfrac{dU_{cd}(t)}{dt} + \dfrac{U_{cd}(t)}{R_L} \\ |U_{ab}| = |U_{cd}| + 2V_d \qquad (|U_{ab}| > |U_{cd}| + 2V_d) \end{cases}$$

$$\begin{cases} I_p(t) = C_p\dfrac{dU_{ab}(t)}{dt} + \dfrac{U_{ab}(t)}{R_p} \\ C_L\dfrac{dU_{cd}(t)}{dt} = \dfrac{U_{cd}(t)}{R_L} \end{cases} \qquad (|U_{ab}| \le |U_{cd}| + 2V_d)$$

Figure (a12) : Modèle numérique de simulation de la récupération d’énergie par effet pyroélectrique.

La figure (a13) résume les principales conclusions de la simulation numérique du générateur pyroélectrique développé.
Les influences du rayonnement solaire et de la vitesse du vent sont estimées avec le modèle numérique. Les résultats (figure (a13)) montrent que l'amplitude des tensions de l’énergie récupérée par effet pyroélectrique est proportionnelle au rayonnement solaire absorbé par le matériau. Ils montrent également que la capacité de

refroidissement due au vent reste importante, même pour de faibles vitesses de vent, dès lors que le rayonnement solaire est élevé.

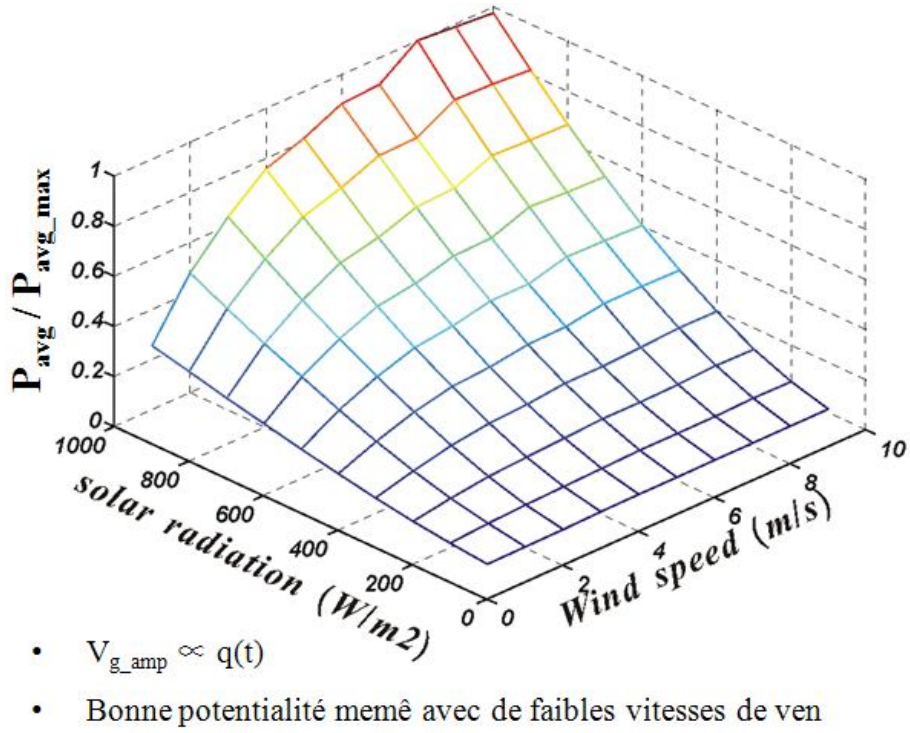

Figure (a13) : Evolution de l'énergie récupérée par effet pyroélectrique en fonction du rayonnement solaire et de la vitesse du vent.

III-3/ Effet piezoélectrique et production de micro-énergie renouvelable

Concernant l'effet piézo-électrique, une structure mécanique de type « harmonica » a été développée ainsi qu'une estimation des efforts d'interaction fluide-structure.

La structure étudiée utilise les travaux similaires disponibles dans la littérature (Figure (a14)). Un flux d'air est envoyé dans un caisson obstrué en sa partie inférieure par une poutre cantilever de dimension plus faible que l'excavation de sortie d'air. Sous l'effet d'un écoulement continu d'air, il en résulte, par le jeu de surpression et dépression, une pression dynamique sur la poutre cantilever. Cette pression dynamique met en mouvement de vibration une poutre cantilever sur laquelle est collée une plaque piézoélectrique de récupération de l'énergie de vibration. La plaque piézoélectrique, collée dans la zone de forte déformation de la poutre, fonctionne en mode d_{31} (traction/compression).

Les mesures ont donné des valeurs de pression dynamique qui évoluaient à la même fréquence de vibration que la poutre. Il a également été montré expérimentalement une forte sensibilité des performances de récupération d'énergie avec d'une part la taille de l'excavation autour de la poutre et d'autre part les « promoteurs » de surpression que l'on peut introduire dans le caisson.

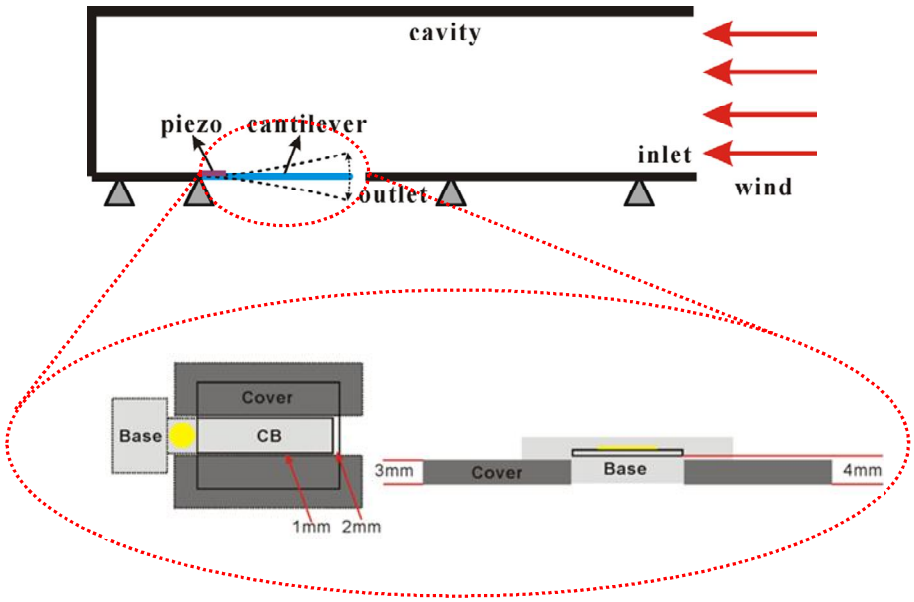

Figure (a14) : Dispositif type « harmonica » pour la récupération d'énergie par effet piézoélectrique ; Poutre cantilever avec patch piézoélectrique (d_{31}) collé.

Comme le montre la Figure (a15), le dispositif étudié en laboratoire présente une valeur limite minimale de vitesse du vent (2 m/s) en dessous de laquelle il est difficile de récupérer de l'énergie. Avec une charge optimisée de 90 kΩ, la puissance maximale récupérée en essais de laboratoire est de 0.2mW avec une vitesse du vent à 4.7 m /s. Le rendement maximum est de 0.03% avec une vitesse du vent à 3 m/s. Le prototype développé génère une production d'énergie électrique de 8.9mWm^{-2} en conditions d'analyse laboratoire.

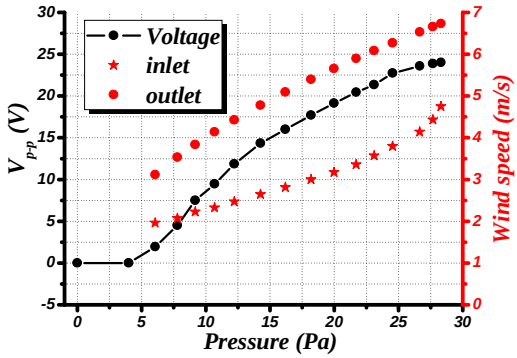

- Absence de vibrations pour de très faibles vitesses < 1.5 m/s
- Bon couplage "vent-structure" pour de faibles vitesses
- Augmentation de la vitesse du vent au niveau de l

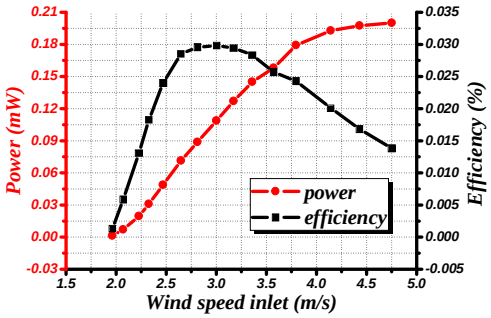

- P_{max}=8.9 mW/m^2 (4.7m/s)
- η_{max}= 0.03% (3m/s)

Figure (a15) : Effet piézoélectrique et récupération de micro-énergie ; dispositif caisson « harmonica » testé en condition de laboratoire.

En condition réelle (à l'extérieur) par un jour de vent moyen (voire vent fort), le test effectué avec le même dispositif (que celui utilisé en laboratoire) donne une pression dynamique représentée par la courbe noire de la Figure (a16). Les pressions maximales peuvent atteindre 150 Pa. La variation de tension récupérée dans un condensateur de 1500 micro Farad est représentée avec la courbe rouge. On note qu'en condition réelle, on peut obtenir une tension de 3V en moins de 2 heures. Ce qui est suffisant pour alimenter ou piloter un dispositif sans fil dans une application bâtiment.

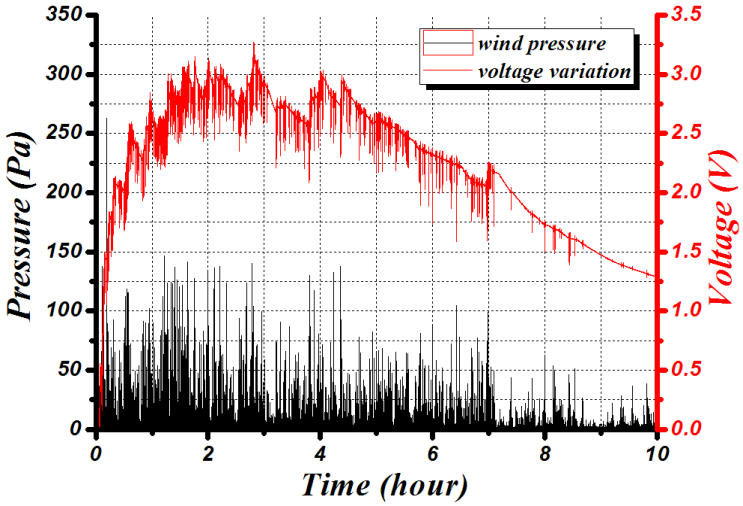

Figure (a16) : Effet piézoélectrique et récupération de micro-énergie ; dispositif caisson « harmonica » testé en condition extérieure par une journée moyennement ventée à Aix-les-Bain le Revard.

III-4/ Exemple d'application de l'utilisation des micro-énergies récupérées

A titre d'illustration, une application typique a été présentée (refroidissement de panneau photovoltaïque).

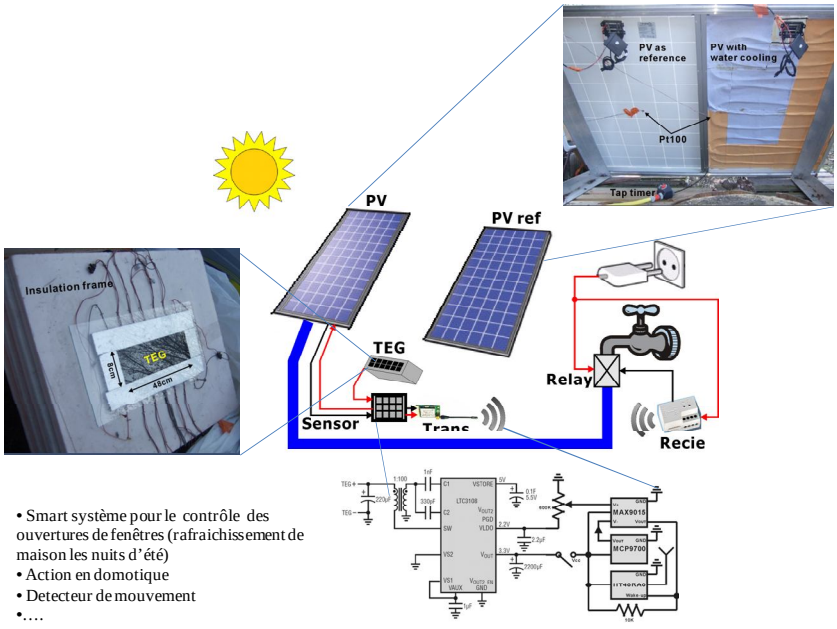

Figure (a17) : Exemple d'application d'utilisation des micro-énergies récupérées.

L'application développée consiste à réaliser un « smart système » dans lequel s'intègre le dispositif de récupération d'énergie œuvrant comme un capteur et émetteur de signal sans fil vers un récepteur d'action de refroidissement du panneau.
Le « smart système » réalisé est schématisé sur la figure (a17). L'idée explorée dans l'application réalisée est d'augmenter le rendement des panneaux photovoltaïques en assurant un meilleur refroidissement au moment les plus chauds de la journée (car il est établi que le rendement des panneaux photovoltaïques diminue avec l'élévation de leur température). Le principe de refroidissement des PV développé consiste à sécher un tissu humide collé à l'arrière du panneau. Pour sécher, le tissu humidifié va pomper l'énergie nécessaire dans son environnement immédiat qui est le panneau. Par conséquent, le phénomène de séchage va induire une diminution de la température du panneau. L'humidification régulière du tissu (pendant un temps fixé) conduit à une régulation de la température du panneau. Le signal d'ouverture de la vanne d'eau pour l'humidification du tissu à l'arrière de panneau à refroidir est envoyé dès lors que le rayonnement solaire est suffisamment élevé pour charger le condensateur du dispositif (TEG+PCM). Lorsque la charge du condensateur atteint une valeur seuil, il y a déclenchement d'un signal vers un récepteur sans fils qui commande l'électrovanne d'ouverture d'eau.

L'application, réalisée en mode semi-automatique en automne 2010 à Aix-les-Bains, a montré une augmentation de la production d'électricité autour de 10%. Cette application montre une utilisation possible des micro-énergies renouvelables au service de la production de macro-énergie.

IV / Conclusion générale et perspective

En conclusion générale, cette étude a porté sur le développement des méthodes de récupération d'énergie renouvelable disponible dans l'environnement ambiant du bâtiment en utilisant trois couplages typiques de matériaux. L'enjeu essentiel a porté sur comment optimiser le transfert des énergies vers le matériau actif et comment améliorer le rendement des dispositifs proposés alors que la source de sollicitation est variable et de faibles amplitudes.
- Concernant l'effet thermoélectrique, il a été montré que les matériaux à changement de phase (PCM) couplés aux thermoélectriques peuvent permettre la transformation d'une variation temporelle de température en un gradient de température favorable à la récupération de micro énergie par effet thermoélectrique.
L'originalité du dispositif proposé est qu'il permet, sur une période d'un jour, de valoriser deux fois l'énergie solaire par le stockage et déstockage d'énergie emmagasiné dans le matériau à changement de phase.
L'énergie récupérée de jour est proportionnelle au rayonnement solaire absorbé par le thermoélectrique. Celle de nuit dépend essentiellement de la quantité de chaleur absorbée par le matériau à changement de phase (PCM), mais aussi des phénomènes de convection et de rayonnement qui limitent la durée de la récupération d'énergie la nuit. La puissance maximale atteinte en condition réelle, à l'extérieur est $1W/m^2$ qui

correspond à un rendement de Carnot supérieur à 2%.

- *Concernant l'effet pyroélectrique,* il a été montré que les fluctuations du vent ambiant couplées au rayonnement solaire peuvent générer des variations temporelles de température suffisamment importantes pour produire des micro-énergies récupérables par effet pyroélectrique. L'amplitude des tensions récupérables est proportionnelle au rayonnement solaire absorbé. Le rendement de Carnot estimé à 13,3% est prometteur pour cette approche.

- *Concernant l'effet piézoélectrique,* il a été souligné l'importance du caisson type « harmonica ». Le caisson développé permet le transfert de l'énergie du vent en énergie de vibrations de poutre sur laquelle est collé un patch piézoélectrique travaillant en mode d_{31}. Le rendement total de l'étude menée est de 0.03%. Cette performance comparée à d'autres études similaires de la littérature est 10 fois meilleures que certains résultats, mais 10 fois plus faible que les résultats d'une étude de cette année. L'analyse expérimentale actuelle a permis d'identifier les marges de progression qui portent (i) sur les dispositifs à mettre à l'intérieur du caisson actuel pour accroitre la pression dynamique (les promoteurs de pression dans le caisson) et (ii) sur les dimensions de la poutre ainsi que celle de l'excavation dans le caisson.

Pour comparer les performances des différents prototypes examinés dans cette thèse, le tableau ci-dessous donne les éléments de comparaison.

	TEG	**PYEG**	**PIEG**
Rendement total	0.1 %	$6e^{-5}$ %	0.03 %
Rendement de Carnot	>2 %	5 %	----
Puissance (W/m^2)	1	$6e^{-4}$	$9e^{-3}$
η_{max} *rendement maximum attendu*	*0.5 %*	*1 %*	*10 %*
	ZT=1 (resistive)	*100p (AC)*	*SSHI (DC)*

Les perspectives intéressantes pour une telle étude peuvent être :

1. l'étude des effets électrocaloriques des matériaux pyroélectriques
2. la modélisation d'interaction fluide-structure du dispositif caisson harmonica
3. l'extension de la technique d'amplification SSHI au dispositif pyroélectrique développé
4. l'étude de la récupération de micro-énergie par torsion de tube polarisé comme schématisé sur la figure ci-dessous.

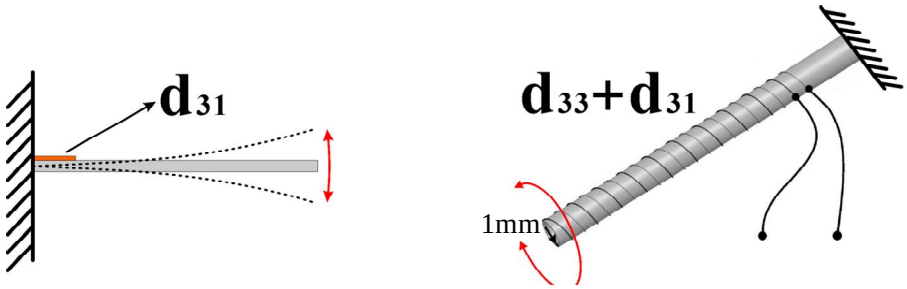

Le dispositif de torsion peut conduire à un meilleur rendement du fait des coefficients de couplage plus favorable. De plus, les tubes en torsion semblent, à priori, compatibles avec les contraintes de réalisation de dispositifs compacts de récupération d'énergie.

“Ambient energy harvesting based on coupling effects in materials: applications in buildings”

« Récupération de micro-énergie renouvelable par couplage multiphysique des matériaux : applications aux bâtiments »

1. General introduction

The development of ultra-low power electronics especially those function as wireless sensors engenders a large quantities of demand in micro-power source. The ordinary battery cell is no longer suitable in those smart applications due to the consensus of the people on the sustainable science and technology. Consequently, those techniques which provide with substitutions to ordinary batteries become more and more popular in the scientific researches and they are recognized as energy harvesting (or energy scavenging).

There are many physical effects which are able to convert thermal, mechanical or RF energy into micro-electric power including thermoelectric, pyroelectric, piezoelectric, electrostatic, electromagnetic, etc. Among all these effects which can be utilized in energy harvesting technique, the coupling effects in active materials (including piezoelectric, thermoelectric and pyroelectric) are dominant in current researches [ANT 2007][COO 2008][RIF 2003][DEN 2009][HUD 2008]. They are interdisciplinary techniques with material science which have higher potential of development.

There are three basic problems lie in an energy harvesting process with coupling effect.

1. The first one is to design and optimize a structure which is able to accumulate the micro-power from the energy source and transform it into the favorable loading on the active material.
2. The second one is to improve the energy conversion efficiency according to the suitable choice of material properties.
3. The third one is to develop a right energy harvesting circuit which is able to improve the energy conversion efficiency through coupling process and electric power storage or consumption.

The second problem belongs to the researches in material science which is not the focus of the energy harvesting technique. However, it provides with the basic limitations for the maximum energy conversion efficiency. The idea of improve the energy conversion efficiency through circuit is valid with the direct piezoelectric [GUY 2005] and pyroelectric effect [GUY 2009] since these two effects are reversible and the applied electrical energy is stored in another form of potential energy. The thermoelectric effect which is described by Peltier, Seebeck and Thomson phenomena is invalid with such mechanism since the Joule heat generation in the thermoelectric device is not reversible. The power generation of an energy harvesting device depends on the condition of the electrical load. In the case of resistive load, there is a matched value for a piezoelectric generator (PIEG), a pyroelectric generator (PYEG) and a thermoelectric generator (TEG). In the case of a capacitive load, the problem in the PIEG (or PYEG) is different

from that in the TEG. The PIEG (or PYEG) with high internal impedance is able to provide with high alternating voltage and low current, it is able to charge a capacitor with simply an AC-DC transformer. On the contrary, the thermoelectric generator with low internal impedance provides with low direct voltage and relative high current. A DC-DC transformer is necessary in order to charge a capacitor until an applicable voltage sometimes.

It can be recognized that the first problem is always inevitable and essential with any kinds of energy harvesting system. The thermoelectric generator needs a constant large temperature difference in space while the pyroelectric generator needs a quick and large variation of temperature. The piezoelectric generator needs a force loading with the similar characteristics of temperature loading for pyroelectric generator. Therefore, a great challenge is to transform all the potential energies into these favorable loadings for the coupling effect.

When the ultra-low power electronics are located in a building the energy sources become clear. The solar radiation, wind flow, ambient temperature variation, etc are potential candidate to be harvested. The question is how much energy (or power) can we extract from these ambient energy sources with those coupling effects introduced above? What are the advantages and disadvantages of them as an independent micro-power source? How can we use the harvested micro-energy in the buildings?

This study will answer these three questions step by step. Therefore, in the next section, a brief summary is given on those energy harvesting techniques based on thermoelectric, pyroelectric, piezoelectric, electrostatic and electromagnetic effect. Special attention is paid to the ability of thermal energy storage with the phase change material which will be proved valuable in the thermoelectric energy harvesting process.

The section 3 illustrates the characteristics of the ambient energy sources especially as solar radiation. Different methods of utilizing ambient energy sources with the coupling effect are addressed.

Our major contribution in harvesting solar energy and wind (or airflow) power through thermoelectric, pyroelectric and piezoelectric effect is expanded from section 4 to section 6. Both experimental study and modeling method are utilized in our analysis.

In order to emphasize the feasibility of our prototype thermoelectric energy harvesting system in building applications, a typical case study is dwelled in section 7.

This study is ended in section 8 with comparison between the potential ability of these three kinds of power generator. It is described with the measured average power. Perspectives and future work on this study are stated at last.

2. Energy harvesting and thermal energy storage with some well known effect

2.1 Thermoelectric coupling effect and energy harvesting

2.1.1 Thermoelectric effect

The thermoelectric effect indicates that the thermal diffusion of the charge carriers in the thermoelectric material can generate electricity while an applied flow of charge carriers can influence the thermal balance in material.
When a temperature difference is achieved on the thermoelectric material, the charge carriers on the hot side possess larger kinetic energy. They diffuse to the cold side and accumulate at that place. They diffusion causes difference in the quantity of charge carriers between the hot and cold side. Consequently an internal electrical field is achieved. The generated internal field will decrease the diffusion of the rest charge carriers. When the electrical potential reaches thermal potential, the diffusion of charge carriers will stop.
When an electrical current passes through the thermoelectric material, the charge carriers move in a fixed direction. It takes away the kinetic energy of the vibrated molecule on one side and releases them to another side. This causes temperature difference between the two sides in the material.

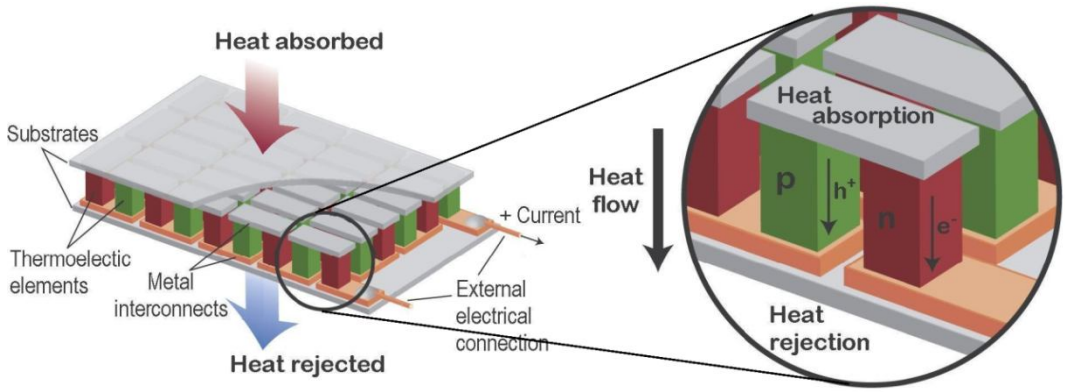

Figure 2. 1: Schematic of a thermoelectric generator [SNY 2008]

A typical structure of a thermoelectric device is shown in Figure 2. 1. There are many thermoelectric couples in this device. They are placed in parallel thermally. From the electrical point of view, the p type and the n type semiconductors work as a group and all the groups are connected in series. This structure can help to increase the total voltage output when it works as generator. Besides, it helps to match the input

impedance of the current source when it aims to generate temperature difference. The basic equation which describes the performance of a thermoelectric generator are:

$$\begin{cases} V = \alpha_s (T_h - T_c) = \alpha_s \Delta T \\ Q_H = \alpha_s T_h I \\ Q_C = \alpha_s T_c I \end{cases} \quad (2.\ 1)$$

Where $\boldsymbol{V}$ is the generated voltage from the thermoelectric device when applied with temperature difference, $\boldsymbol{\alpha_s}$ is the total Seebeck coefficient which describes the capability of the coupling effect, $\boldsymbol{T_h}$ and $\boldsymbol{T_c}$ are the temperature on the hot side and cold side of the thermoelectric element. $\boldsymbol{Q_H}$ is heat absorbed from the hot side of the TEG while $\boldsymbol{Q_C}$ is heat released to the cold side. $\boldsymbol{I}$ is the generated electrical current when collected with an external resistor. The detailed analysis to the thermoelectric effect is addressed in [Gou 2009] and [SNY 2003] where the thermoelectric potential and compatibility are defined to understand the coupling process from micro point of view.

Generally, a TEG is considered as a voltage source in series with its internal resistance $\boldsymbol{r_{TEG}}$. When it is connected with an external load $\boldsymbol{r_{ext}}$, the generated power $\boldsymbol{P_{TEG}}$ useful can be calculated:

$$P_{TEG} = \left(\frac{V}{r_{TEG} + r_{ext}} \right)^2 r_{ext} = I^2 r_{ext} \quad (2.\ 2)$$

Then the total energy conversion efficiency of a TEG $\boldsymbol{\eta}$ can be expressed by:

$$\eta = \frac{P_{TEG}}{Q_h} = \frac{I^2 r_{ext}}{\alpha_s T_h I - 0.5 I^2 r_{TEG} + \Delta T / R_{TEG}} \quad (2.\ 3)$$

Where $\boldsymbol{R_{TEG}}$ is the thermal resistance of the TEG. Given $\boldsymbol{r = r_{ext} / r_{TEG}}$, the total efficiency can be expressed in another way:

$$\begin{cases} \eta = \dfrac{T_h - T_c}{T_h} * \dfrac{r}{(1+r) - \dfrac{T_h - T_c}{2T_h} + \dfrac{(1+r)^2}{ZT_h}} = \eta_c(t) * \eta_m \\ Z = \dfrac{R_{TEG} \alpha_s^2}{r_{TEG}} \end{cases} \quad (2.\ 4)$$

Where Z is the figure of merit for the TEG. The expression of total energy conversion efficiency of a TEG in (2.4) indicates that it is the product of the Carnot efficiency $\eta_c(t)$ and the material efficiency η_m. The material efficiency depends on the external load r_{ext} with a given temperature difference. It can be deduced that when $r = (1+ZT_{avg})^{1/2}$ ($T_{avg} = (T_c + T_h)/2$) the maximum efficiency η_{max} is achieved as:

$$\eta_{\max} = \eta_c(t) * \frac{\sqrt{1+ZT_{avg}} - 1}{\sqrt{1+ZT_{avg}} + T_c/T_h} \qquad (2.5)$$

It is found that the maximum total efficiency is determined by Z, T_h and T_c while the dimensionless figure of merit ZT_{avg} is dominant in the maximum material efficiency. The material efficiency with different ZT_{avg} and r is shown in Figure 2. 2.

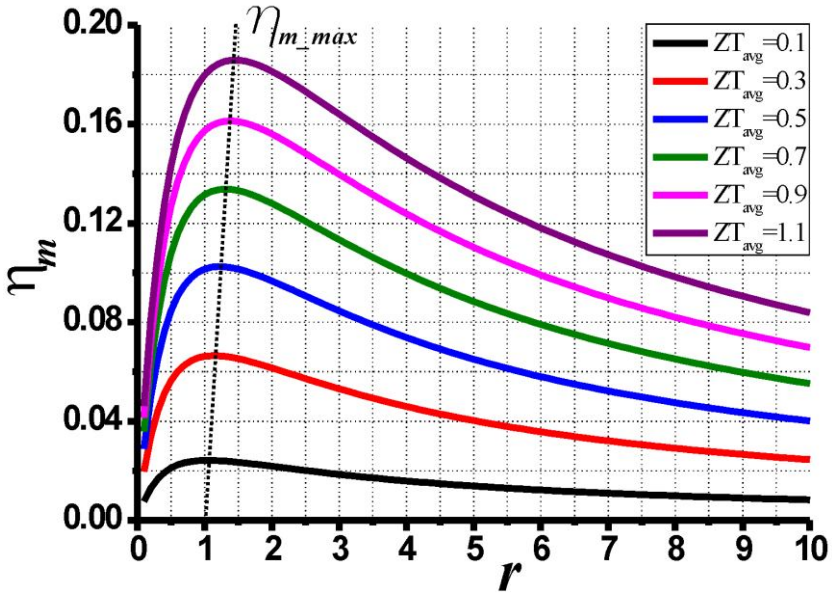

Figure 2. 2: Material efficiency with different r and ZT_{avg}

It is found that the variation of η_m with r is significant when the ZT_{avg} is large. It is noteworthy that the optimized value of external resistor for power generation is a little higher than the internal resistor of the TEG, as highlighted with the dashed line in this figure. This characteristic is achieved when the incoming heat flow of the TEG is given. Nowadays, by manipulating the nanostructure of the materials, the reported ZT_{avg} has reached 5.8 [NI 2009]. In actual situation, the Seebeck coefficient, electrical resistivity and thermal conductivity of the thermoelectric material are all associated with temperature [YAM 2008]. Consequently ZT_{avg} associates with the temperature. The material with ZT_{avg}=1 is currently available and it possess maximum material energy conversion efficiency around 17%.

2.1.2 Review of literature

Thermoelectric material is a promising candidate for power generation, being highly reliable, free of moving parts and environmentally friendly. Much scientific research has been devoted to the application of this material for energy. Categorized by species of heat source, varieties of temperature difference are available for this energy conversion process. We present here a brief review of recent progress of thermoelectric application with fossil fuel, waste heat and living being.

Due to the energy conversion efficiency of a thermoelectric device which is closely associated with the applied temperature difference, it is favorable with power generation with high temperature difference. A self-powered residential heating system operating entirely on fuel combustion is developed [QIU 2008]. The structure and performance of this system are shown in Figure 2. 3.

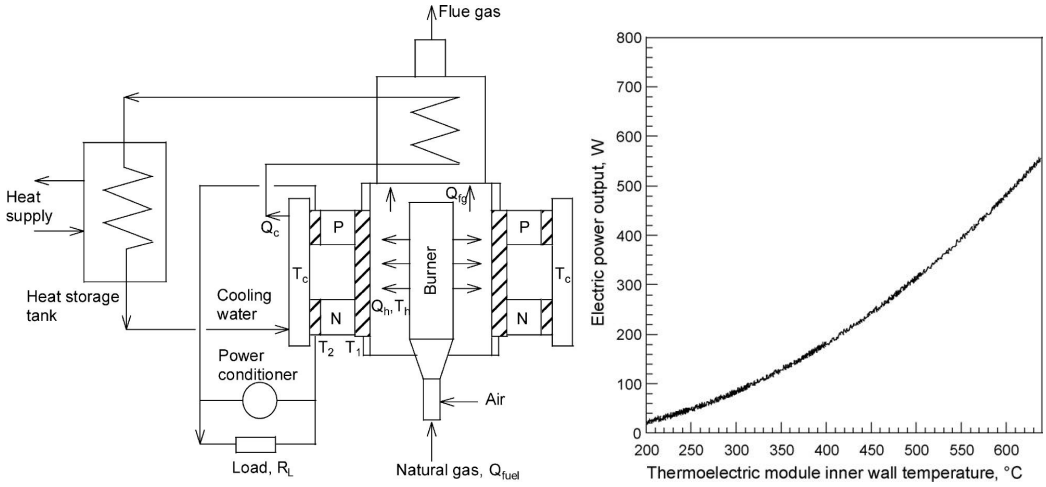

Figure 2. 3: TEG with stove [QIU 2008]

The thermoelectric module in this system is a radial type that fits in well with the burner of the stove. The thermoelectric elements in the module are made from PbSnTe doped to have either p- or n-type semiconductor properties. The module has 325 couples with each couple consisting of a p-type element and an n-type element. It is found that such a TEG can provide a power generation capacity of 550W at a temperature difference of 552°C. A similar system [JIA 2011] is introduced after but with much smaller dimension. Both of these two systems can work with an energy conversion efficiency as high as 1% since a large temperature difference is achieved by the combustion of fuel and water cooling. When the thermal loading on the cold face of the thermoelectric device changes into natural convection as reported in [NUW 2005], the maximum steady-state temperature difference achieved is 150°C which leads to a much lower efficiency. The difference between the water cooling method and the convection cooling method of a stove based thermoelectric power generator is addressed in [CHA 2010].

The power generation with thermoelectric device in stove consumes fossil fuel and it can achieve high efficiency. However, it is far from the scope of this study which aims to analyze the power generation when the intensity of the heat source is much lower. Such as those thermoelectric device works with waste heat. A typical application is to harvest energy from exhaust pipe of a motorcycle [SCH 2008]. The experimental prototype and performance of such a system is shown in Figure 2. 4.

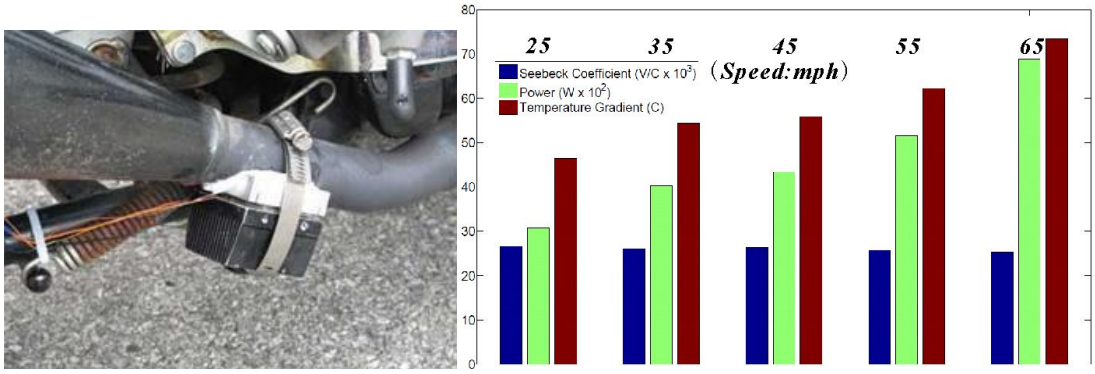

Figure 2. 4: Waste heat recovery from exhaust pipe [SCH 2008]

The thermoelectric module used in this study is Melcor HT3-12-30. It is 1.18 inch wide by 1.34 inch long and 0.126 inch tall, consisting of 127 Bismuth Telluride thermocouples soldered together with 271°C SnSb solder and enclosed in Alumina ceramic plates. With different driving speed of the motorcycle (from 25 to 65 mph), the generated temperature difference on the thermoelectric devices varied from 47°C to 73°C). It produced an average of 0.4694W from an average temperature difference of 48.73°C. A similar study is presented by [HSU 2010]. Their focus is on the optimization of the heat sink. A mathematic model of thermoelectric module with applications on waste heat recovery from automobile engine is introduced by [HSI 2010]. The maximum power density produced from their prototype thermoelectric module is 51.13mWcm^{-2} at 290°C temperature difference. The model also shows that TE module presents better performance on the exhaust pipe than on the radiator.

Another typical study of harvesting waste heat in liquid is reported [NIU 2009]. The focus of this study is to examine experimentally the influences of the hot and cold fluid inlet temperatures, flow rates and the load resistance, on the power output and conversion efficiency. The experimental prototype is shown in Figure 2. 5. The thermoelectric material adopted in their study is Bi_2Te_3. Their experiments are conducted for a range of operating conditions as: the hot fluid inlet temperature between 50°C and 150°C, the cold fluid inlet temperature between 20°C and 30°C, and the ranges of both cold and hot fluid flow rate between 0.2m^{2}h^{-1} and 0.6m^{2}h^{-1}.

When the hot and cold fluid inlet temperature are respectively 150°C and 30°C, the system produce a maximum power output of 146.5W which correspond to a conversion efficiency of 4.44%. A numerical model of such an energy harvesting system [YU 2007] is presented by them two years ago which predict the actual performance well.

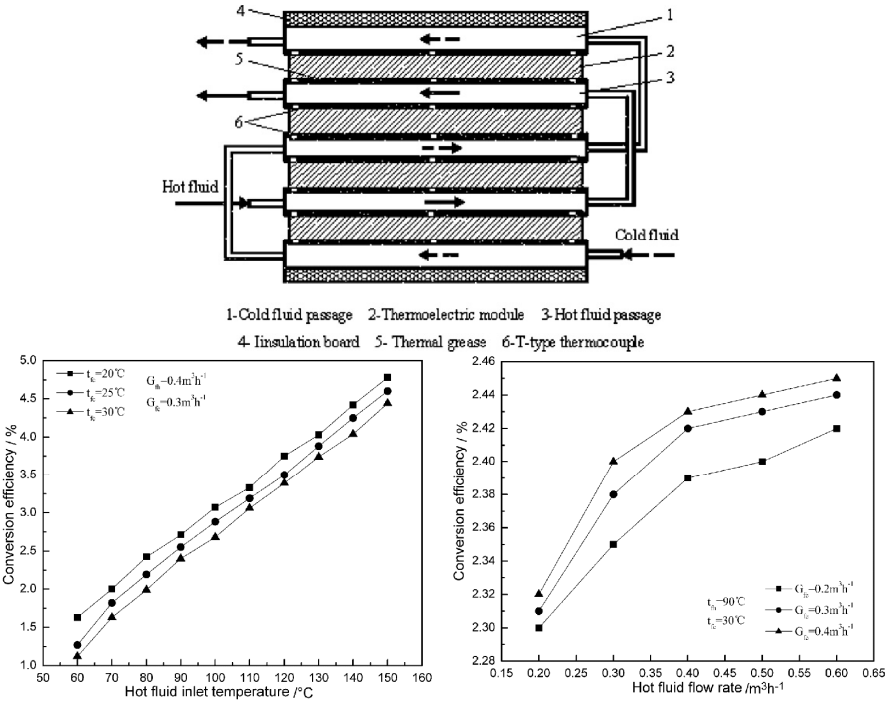

Figure 2. 5: Waste heat recovery from double hydro-pipe [NIU 2009]

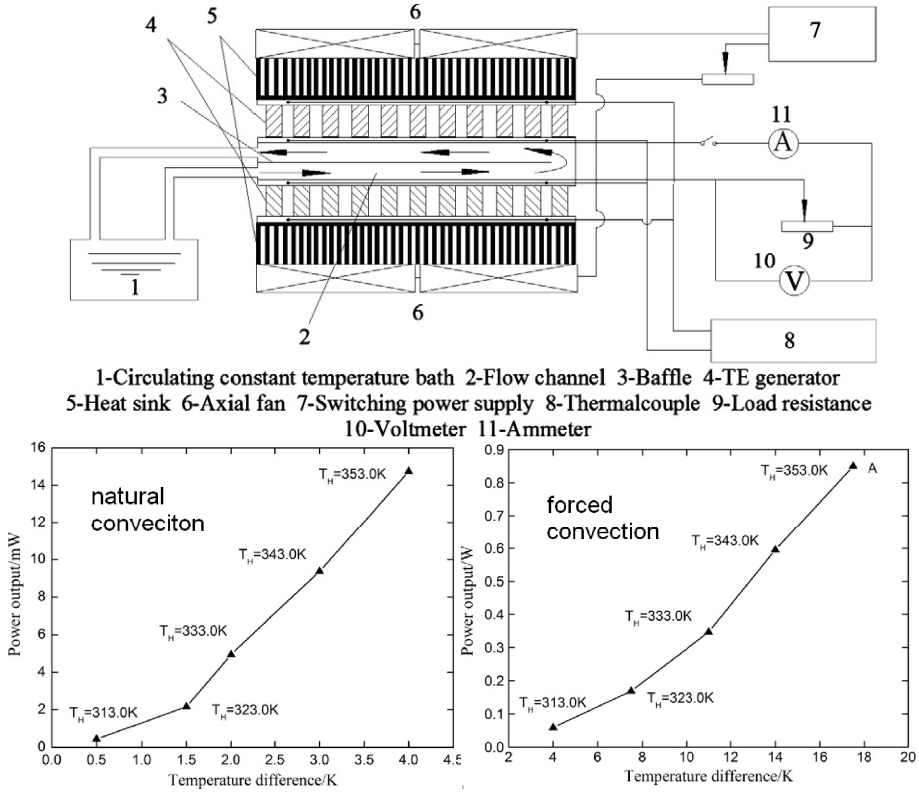

Figure 2. 6: Waste heat recovery from water pipe and convection [GOU 2010]

Another waste heat recovery system [GOU 2010] with fluid as the heat source is introduced in Figure 2. 6. Instead of another hydro-pipe, a heat sink is used as the cold

reservoir in this system. Water is used as the energy transferring mass and the maximum temperature of the heat source is 90°C. It is more close to an ordinary situation.

With the similar thermoelectric device, the performance of this system is distinct with the foregoing prototype [NIU 2009]. When the temperature of the heat source is 90°C, the temperature difference achieved is 17.5°C with forced convection and only 4°C with natural convection. It indicates that the thermal boundary condition is essential with the performance of a waste heat recovery system which utilize thermoelectric device.

The thermoelectric energy harvesting system with waste heat is still large in dimension. Another attractive research on thermoelectric energy harvesting with much smaller dimension aims to utilize the heat from the body of living being.

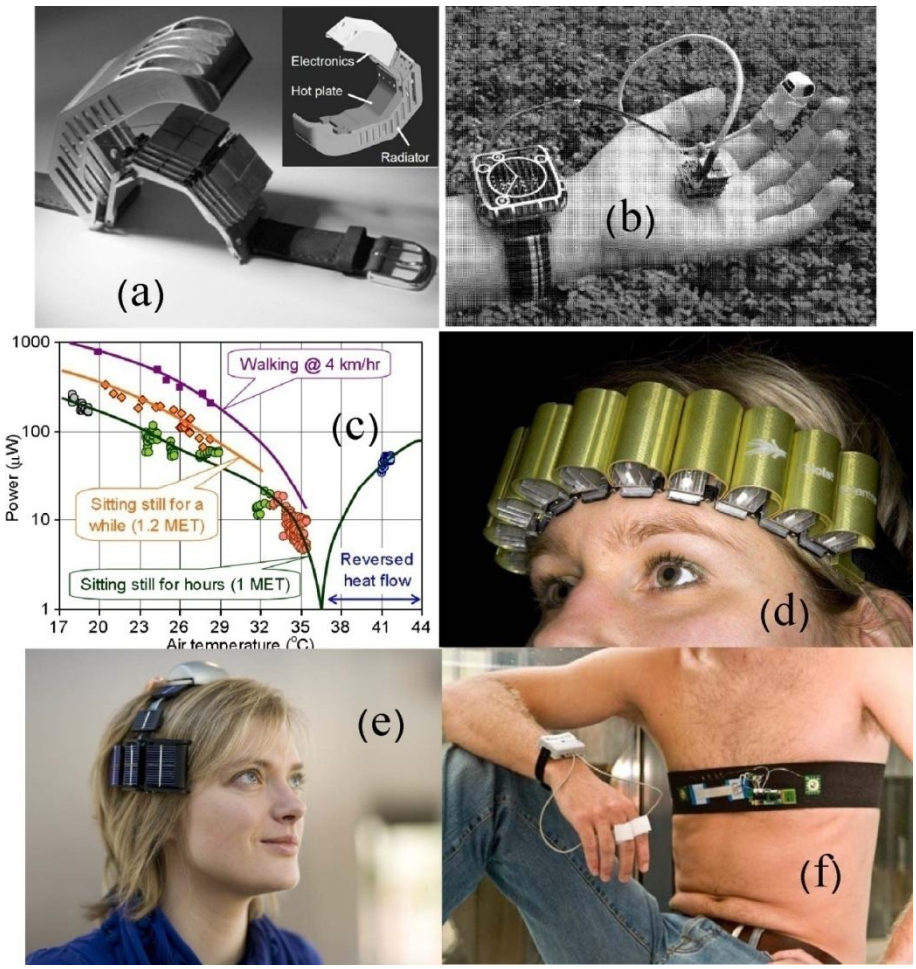

Figure 2. 7: Varieties of wearable TEG prototype system: (a) [GYS 2005] (b)(c) [TOR 2006] (d) [PEN 2008] (e) [TOR 2008] (f) [PEN 2009]

According to [STA 2006], the warmness of a human body (and also an animal body) can be used as steady energy source, and the amount of energy released by the metabolism (traditionally measured in Met; 1 Met = 58.15 W/m² of body surface)

mainly depends on the amount of muscular activity. A normal adult has a surface area in average of 1.7 m², so that such a person in thermal comfort with an activity level of 1 Met will have a heat loss of about 100 W. The metabolism can range from 0.8 Met (46 W/m²) while sleeping up to about 9.5Met (550W/m²) during sports activities as running with 15 km/h. A Met rate commonly used is 1.2 (70 W/m²), corresponding to normal work when sitting in an office, which leads to a person's power dissipation of about 119 W, burning about 10.3 MJ a day.

The first body powered TEG [GYS 2005] reported in literature is 6 years ago. According to [LEO 2007], this wearable TEG serves as power supply for wireless sensor nodes on a wrist. It had been fabricated in 2004 as shown in Figure 2. 7(a). With ambient temperature at 22 °C, it produced a power of 100μW. In 2006, a wireless pulse oximeter has been designed, fabricated and tested on people, Figure 2. 7(b). The power generation the thermoelectric device in such a system is shown in Figure 2. 7(c). The idea of wrist watch progressed in 2007 as reported in [LEO2 2007]. The human++ project keeps on progress in the topic of wearable thermoelectric power generation [PEN 2008][TOR 2008][PEN 2009].

Mateu et al. [MAT 2007] proposed to harvest energy between a human hand and the ambient environment. With a Peltier element PKE 128 A 1030, the gradient between the hand and the heat sink in ambient temperature can provide a maximum output current of 18mA and output voltage between 150mV and 250mV. The corresponding maximum output power is approximately 3mW. Similar research includes also [LOS 2010]. It distinguishes the problem of optimization in power generation and efficiency when the energy source is weak.

A medical healthcare system [HOA 2009] which is based on thermoelectric device is introduced most recently. Based on their experimental test results, the accumulated energy is around 1.369 mJ which is able to power the loads comprising of sensor, RF transmitter and its associated electronic circuits. The sensed information is transmitted in 5 digital words of 12-bit data across a transmission period of 120 msec. The receiver platform displays the patient identification number and sounds out an alarm buzzer for aid if a fall event is detected. Another medical care application of thermoelectric device is reported by [LAY 2009] which aims to extract warmth from body tissue to supply a hearing aid.

Unlike the wearable thermoelectric application, the thermoelectric device is also proposed to be planted under the skin of a human body [YAN 2007] to drive a medical device. It is found that a stabilized temperature difference of 1.3°C is achieved with a thermoelectric module TEC1-00706T125 planted in the muscle tissue of a rabbit. The corresponding voltage generation is 5mV. The temperature difference can increase to 5.5°C when an ice water is put on the skin of the rabbit.

The most amazing work is introduced by [GHA 2008] which design, fabricate and test an implantable micro-scale thermoelectric power scavenging device that utilizes the body temperature of beetles as an energy source, as shown in Figure 2. 8. The brief study shows that the maximum body-ambient temperature difference was about 11 °C, measured on the back of the beetle close to the wings base.

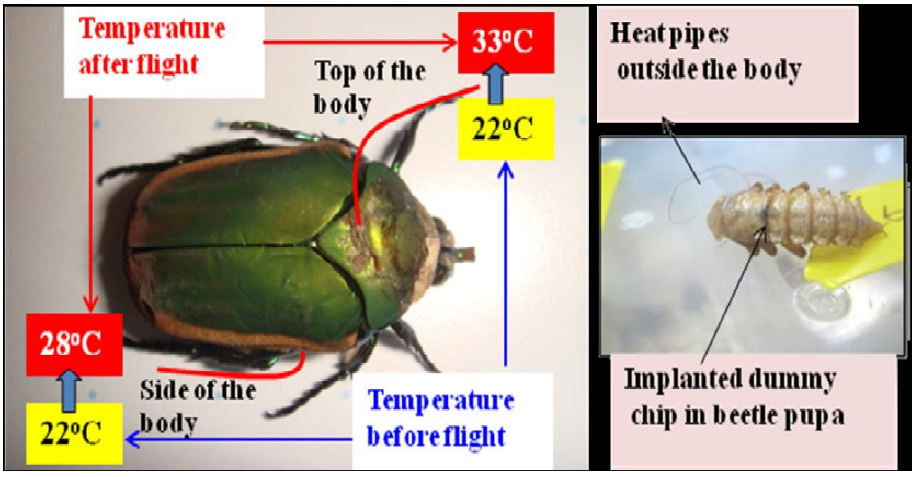

Figure 2. 8: Experiments on beetles (a) Temperature distribution over beetle's body before and after flight (b) Implanted dummy chip inside beetle's pupa [GHA 2008]

The foregoing review in power generation and energy harvesting with thermoelectric device shows clearly the popularity of this effect in scientific research. However, it is not the only direction of progress in thermoelectric effect. More effort is devoted to the structure design [WEB 2006][YAD 2008][WHA 2008] and fabrication technique [SUD 2005][WAN 2009][CAR 2010] of TEG. Besides, the power management circuit of a TEG [KIM 2008][YU 2009][CAR2 2010] is also an important topic in the realm of thermoelectric.

The scope of this study which focuses on those applications in buildings is in the range of harvesting waste heat. The intensity of energy source is neither as strong as the fossil fuel nor as weak as body heat. There is also no strict requirement in the dimensions of the energy harvesting system in this study. A more similar research on the scope of building applications will be addressed in section 3.

2.2 Pyroelectric coupling effect and energy harvesting

2.2.1 Pyroelectric effect

The pyroelectric effect indicates that the remanent polarization in pyroelectric material is associated with temperature. A variation of the temperature in material causes generation of free charges on the surface, perpendicular to the direction of polarization. The generated charges yield a voltage across the material before they are released by an external circuit or internal resistance. A typical process of generation of pyroelectric current is shown in Figure 2. 9.

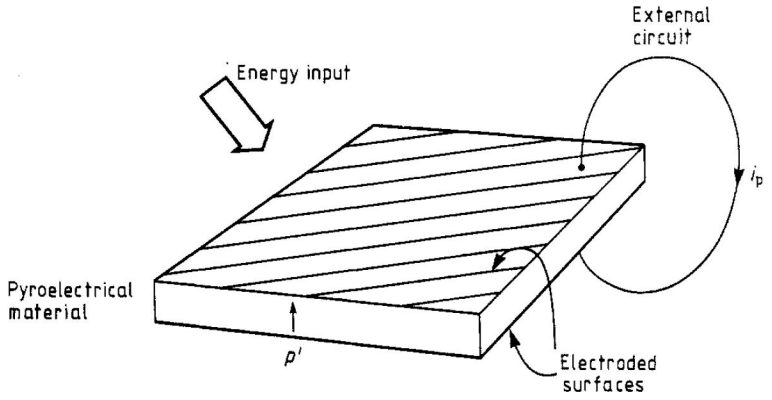

Figure 2. 9: Electroded pyroelectric element showing flow of pyroelectric current due to change in temperature [WHA 1978]

The relationship between the generated charges $\boldsymbol{dQ_p}$ and the temperature variation $\boldsymbol{dT(t)}$ is shown below:

$$dQ_p = p(T)A_{PYEG}dT(t) \quad \text{or} \quad I_p = p(T)A_{PYEG}\frac{dT(t)}{dt} \qquad (2.\ 6)$$

Where $\boldsymbol{A_{PYEG}}$ is the surface area of the pyroelectric device which is covered by an electrode, $\boldsymbol{p(T)}$ is the pyroelectric coefficient which is associated with temperature. Without taking the temperature dependence of $\boldsymbol{p(T)}$ into account, it shows clearly that a large and quick temperature variation is a favorable condition for generating large quantities of electric charge, which potentially generates high power.

2.2.2 Review of literature

The pyroelectric device is advantageous in smart and intelligent systems. It is widely researched in relation to sensors and power generators. Research on pyroelectric sensors dates back to the 1930s, when [TA 1938] demonstrated the possibility of detecting infrared radiation with pyroelectric crystals. Much research followed over the rest of the century, and progress was made on modeling [CHI 1984], developing materials [WHA 1978], improving electrical interface [MUN 1991] and in other areas. Nowadays, commercial pyroelectric sensors are already popular for industrial and everyday applications. The research on pyroelectric power generation began with its energy conversion efficiency which is still a great challenge up to now. Fatuzzo et al. [FAT 1966] revealed that the theoretical maximum efficiency with direct resistive loading at room temperature is below 1%. A typical solar generator can only reach 0.025%, as calculated by Vanderziel [VAN 1974]. The efficiency was improved when Olsen [OLS 1982] proposed using the Ericsson cycle in the pyroelectric energy harvest. It also introduced a regenerative method which enables the Pyroelectric Generator (PYEG) to approach Carnot efficiency.

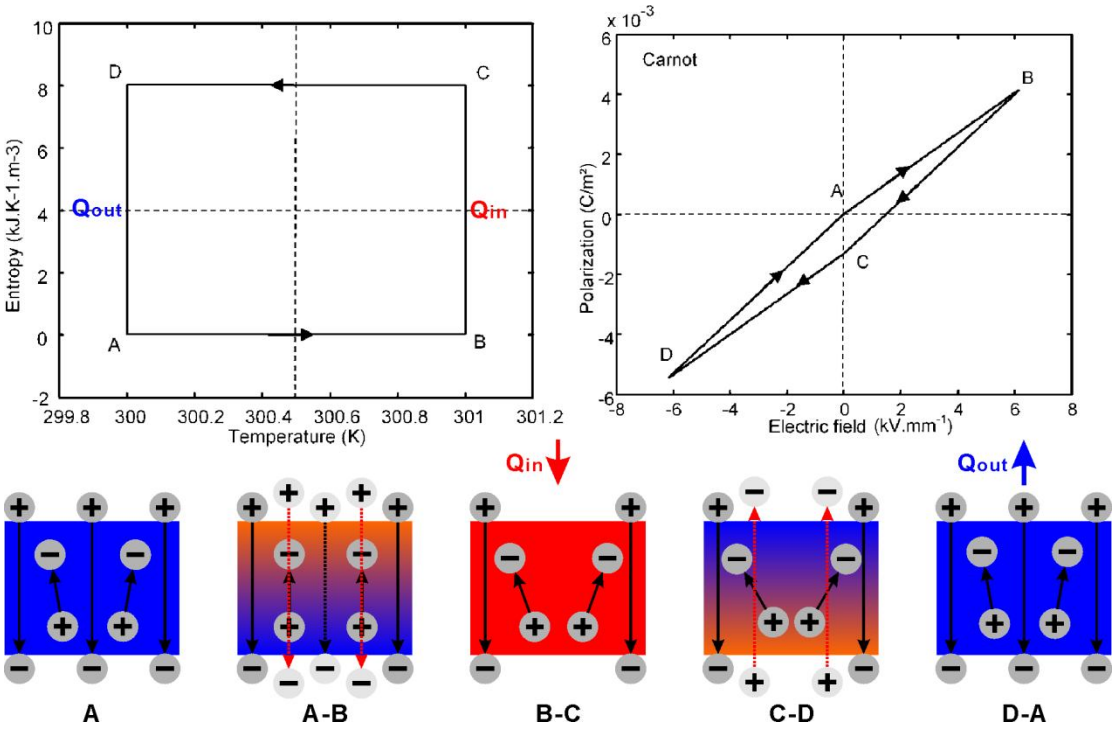

Figure 2. 10: Pyroelectric energy conversion process by Carnot cycle [SEB 2008]

Different from the thermoelectric generator whose energy conversion efficiency is determined with the Carnot efficiency and material efficiency, the pyroelectric energy conversion efficiency have two expressions. When a resistive load is connected, the total energy conversion efficiency is expressed by [SEB 2008]:

$$\begin{cases} \eta = \eta_c(t) * \left(\dfrac{\pi}{4} \dfrac{p^2 \theta_h}{\varepsilon_{33}^{\theta} c_E} \right) \\ \varepsilon_{33}^{\theta} = \dfrac{dD}{dE}\Big|_{\theta} \, , p = \dfrac{dD}{d\theta} = \dfrac{d\Gamma}{dE} \, , c_E = \dfrac{dU}{d\theta}\Big|_E \end{cases} \quad (2.\ 7)$$

Where $\boldsymbol{\theta_h}$ is the temperature in the hot reservoir, $\boldsymbol{\varepsilon^{\theta}_{33}}$ is the dielectric constant of the PYEG, $\boldsymbol{c_E}$ is the volume specific heat. The pyroelectric coefficient $\boldsymbol{p}$ is considered as a constant here.

When an active strategy is utilized the total efficiency can approach Carnot efficiency [SEB 2008], as shown in Figure 2. 10. The Carnot cycle is defined as two adiabatic (AB and CD) and two isothermal (BC and DA) steps. In the coupling process of pyroelectric effect (or electrocaloric effect), there are also four steps correspond to the thermal process:

(A-B, electrocaloric process such as the isentropic compression in a heat engine): An electric field with the direction reverse to that of the internal dipole is applied to the pyroelectric material. With the electrocaloric effect, the temperature in the material increases. The electric energy converts to thermal energy during this process and no energy is harvested at this time. At the end of this step, a relatively high electric field remains on the pyroelectric material which is favorable for the power generation from the induced free charge.

(B-C, pyroelectric process such as the reversible isothermal expansion in a heat engine): The pyroelectric material is connected to an external load and the charge begins to release. The thermal energy converts to the electric energy and it is harvested during this process. At the end of this step, the electric field across the pyroelectric material decrease to zero and the remanent polarization is in accordance with this high temperature.

(C-D, electrocaloric process such as the isentropic expansion in a heat engine): An electric field with the same direction of the internal dipole is applied to the pyroelectric material. With the electrocaloric effect, the temperature in the material decreases. The thermal energy converts to electric energy during this process however there is no thermal energy which is harvested at this time. At the end of this step, another relatively high electric field remains on the pyroelectric material again.

(D-A, pyroelectric process such as the reversible isothermal compression in a heat engine): The intensity of applied electric field decreases. The electric energy converts to the thermal energy during this process. At the end of this step, the electric field across the pyroelectric material decrease to zero and the remanent polarization goes back to zero supposing the temperature can return to its initial value.

The energy harvesting process only occurred in the step B-C. However, a great advantage lies in this strategy. When the incoming heat begins to drive the dipole, the remanent polarization has been enhanced already. The pyroelectric material needs to absorb more heat to disturb the original direction of the polar and to achieve a steady

remanent dipole in this step. In micro point of view, the vibration of dipole is restricted to its original direction by the external electric field tightly. It needs to be hit by more times from the external molecule and to receive more momentum in other directions before it changes the original direction of vibration.
In order to estimate the efficiency of this energy harvesting process, the governing equations of a pyroelectric material is established [SEB 2008]:

$$\begin{cases} dD = \varepsilon_{33}^{\theta} dE + p d\theta \\ d\Gamma = p dE + c_E \dfrac{d\theta}{\theta} \end{cases} \tag{2. 8}$$

where ***D***, ***E***, ***θ***, and ***Γ*** are electric displacement, electric field, temperature, and entropy, respectively. Then the variation of temperature and electric field in the step A-B is expressed as:

$$\frac{d\theta}{\theta} + \frac{p}{c_E} dE = 0 \quad \text{or} \quad \ln(\frac{\theta_h}{\theta_c}) + \frac{p}{c_E} E_M = 0 \tag{2. 9}$$

Where $\boldsymbol{E_M}$ is the maximum amplitude of the applied electric field. The subscript ***h*** and ***c*** stand for high and low temperature representatively.
In the isothermal decrease of the electric field (path B-C):

$$d\Gamma = p dE = \frac{dQ}{\theta} \quad \text{or} \quad Q_h = -pE_M\theta_h \tag{2. 10}$$

where $\boldsymbol{Q_h}$ is the heat taken from the hot reservoir. The electric energy obtained in step CD equals to that consumed in step AB while the electric energy consumed in step DA is only determined by $\boldsymbol{\theta_c}$. It is recognized that the energy conversion of this process is in accordance with Carnot efficiency $\boldsymbol{\eta_c(t)}$:

$$\eta_c(t) = \frac{(-pE_M\theta_h) - (-pE_M\theta_c)}{Q_h} = 1 - \frac{\theta_c}{\theta_h} \tag{2. 11}$$

The pyroelectric energy harvesting based on Carnot cycle is impractical since one should know first the temperature variation before starting the cycle. Moreover, it is hardly realistic to force the electric field at a given value without paying a lot of wasted energy [SEB 2008].

The more realistic cycle for pyroelectric energy harvesting is Ericsson cycle and a lot of work is progressed in this approach [SEB2 2008][KHO 2009][GUY 2008]. They

consist of two constant electric field paths and two isothermal paths as shown in Figure 2. 11.

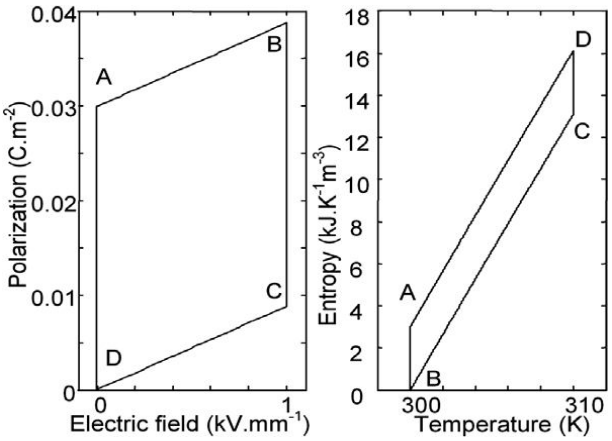

Figure 2. 11: Pyroelectric energy conversion process by Ericsson cycle [SEB2 2008]

When the temperature is low, an external field is applied quickly in order to maintain the current polarization. When the temperature is high, the external field is released quickly in order to let the polarization go back. The total efficiency is described:

$$\eta = \eta_c(t)\frac{\int_0^{E_M} p\theta_h dE}{c_E(\theta_2-\theta_1)+\int_0^{E_M} p\theta_h dE} \qquad (2.\ 12)$$

Thanks to the electrocaloric effect which provides possibility of large material efficiency. The estimated total efficiency with different pyroelectric material at this time is shown in Table 2. 1:

Table 2. 1: Estimated energy harvesting ability for several ferroelectric ceramics showing outstanding electrocaloric ability. [SEB2 2008]

Material	η/η_{Carnot} ***(%)***	***Reference***
$0.95PbSc_{0.5}Ta_{0.5}O_3$–$0.05PbSc_{0.5}Sb_{0.5}O_3$	14	[SHE 1992]
$0.85Pb(Mg_{1/3}Nb_{2/3})O3$–$0.15PbTiO_3$	15	[LIU 2004]
$0.90Pb(Mg_{1/3}Nb_{2/3})O3$–$0.15PbTiO_3$	5	[SEB2 2008]
PLZT	6	[BIR 1986]
0.90Pb(Mg1/3Nb2/3)O3–0.15PbTiO3 thin film	34	[MIS 2006]
(111)0.75Pb(Mg1/3Nb2/3)O3–0.25PbTiO3 single crystal	11	[SEB 2006]
0.75Pb(Mg1/3Nb2/3)O3–0.25PbTiO3 ceramic	10	[SEB 2006]
PZST75/20/5	21	[TUT 1981]
$PbZr_{0.95}Ti_{0.05}O_3$ ***thin film***	54	[MIS2 2006]

The maximum efficiency is expected to reach 50% of the Carnot efficiency. The Olsen cycle of pyroelectric energy harvesting is addressed by simulation [VAN 2008] and is optimized [NAV 2010] most recently. Apart from the optimized strategy of work cycle in energy harvesting, the progress of pyroelectric power generation also developed in other aspect.

New pyroelectric materials were developed [BUC 1999][KOU 2007][NAV2 2010] especially for energy harvesting. Development in pyroelectric material within nano scale [MOR 2010] found that the pyroelectric coefficient strongly increases with the nanowire radius decrease and diverges at critical radius corresponding to the size-driven transition into paraelectric phase. Some in lab prototype systems comes out most recently.

The experimental study on pyroelectric energy harvesting with SSHI technique which is originally designed for electromechanical conversion is implemented in INSA de Lyon [GUY 2009]. The experimental results show that the SSHI technique increases the converted energy by a factor which is about 2.5 times of the standard interface. The efficiency reaches 0.05% of Carnot cycle. In this study, the produced electrical power for temperature amplitude 7K is more than 0.3mW for an energy harvesting device composed of 8 g of active material.

Fang et al.[FAN 2010] proposed to harvest nanoscale thermal radiation with their specially designed system as shown in Figure 2. 12. This prototype system using 60/40 porous poly (vinylidene fluoride–trifluoroethylene) achieved a 0.2% efficiency and a 0.84 $mWcm^{-2}$ electrical power output for the cold and hot sources at 273 K and 388 K.

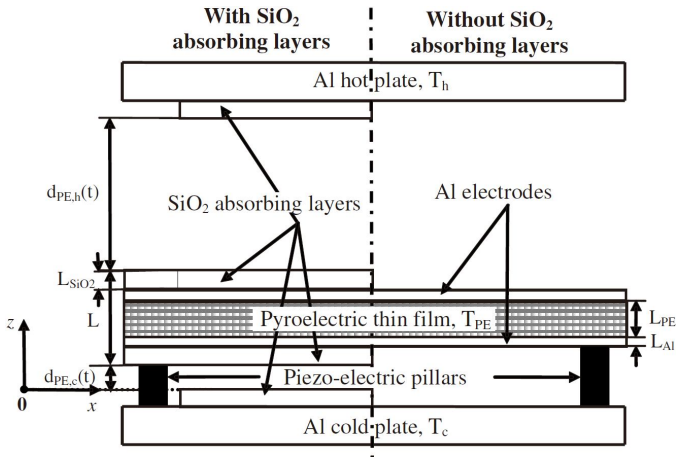

Figure 2. 12: PYEG prototype with oscillatory plate [FAN 2010]

The study on using PZT and PVDF as the pyroelectric material for power generation is addressed in [CUA 2010] and [XIE 2010]. In the study of [CUA 2010], the generated currents and charges were respectively in the order of 10^{-7} A and 10^{-5} C for temperature fluctuations from 300K to 360K in a time period of the order of 100s, it agrees with their theoretical model. In the study of [XIE 2010], a maximum power density of 0.36μWcm^{-2} is calculated with PMN-PT and that for thin-film lead

scandium tantalate is over 125μWcm^{-2}. Therefore, this study concludes that the power density in an actual situation is highly dependent upon the surface area and pyroelectric coefficient of the material.

Moreover, the study in this thesis would like to inspect the inherent relationship between the pyroelectric power generation and the characteristics of the energy source. It will be addressed in section 5.

2.3 Piezoelectric coupling effect and energy harvesting

2.3.1 Piezoelectric effect

The piezoelectric effect is understood as the linear electromechanical interaction between the mechanical and the electrical state in crystalline materials with no inversion symmetry. If there is no hysteresis, the piezoelectric effect is a reversible process. The piezoelectric materials exhibit the direct piezoelectric effect (the internal generation of electrical charge resulting from an applied mechanical force). They also exhibit the reverse piezoelectric effect (the internal generation of a mechanical force resulting from an applied electrical field. The direct and reverse piezoelectric effects are illustrated in Figure 2. 13.

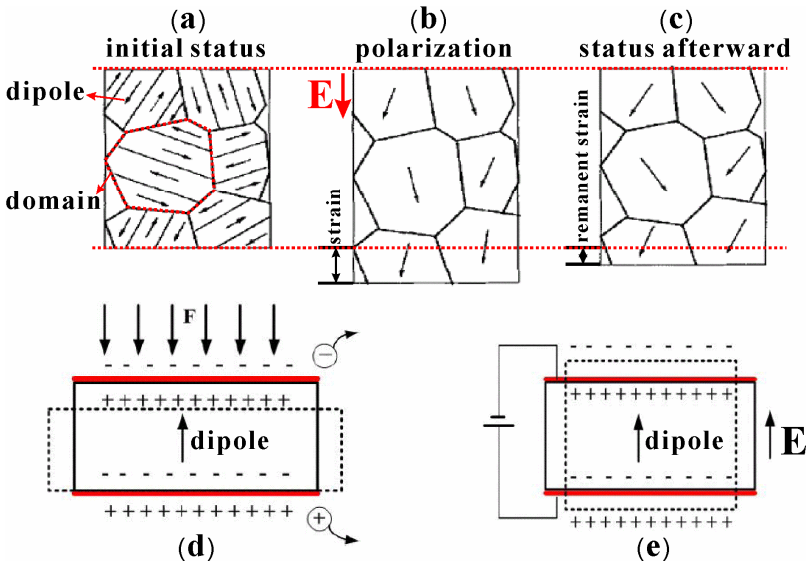

Figure 2. 13: Illustration of piezoelectric effect

In a polycrystal, there are many domains within the material that have a different polar axis of dipole, as shown in subfigure (a). In order to produce the piezoelectric effect, the polycrystal is heated under the application of a strong electric field. The heat allows the molecules to move more freely and the electric field forces all of the dipoles in the crystal to line up and face in nearly the same direction, as shown in subfigure (b). A strain is generated also in the crystal at this time. Then the crystal is cooled down and the external electric field is moved away. The dipoles internal can't return to its initial status and a remanent polarization is formed, as shown in subfigure (c). The crystal is activated now! When an external force compresses the crystal along the direction of dipole, the dipole is shorten and it changes to be more neutral electrically inside the crystal. In order to keep the entire structure neutral electrically, some part of the bound charges on the surface of the crystal becomes free and is able to escape, as shown in

subfigure (d). Since the original bound charges have a distribution as the polarization, a voltage corresponds to the electric field of polarization is generated. This is the principle of direct piezoelectric effect which is adopted for Piezoelectric Generator (PIEG) or piezoelectric sensors. The reverse piezoelectric effect is illustrated in subfigure (e) and it is easier to understand. When an external electric field as the same as the polarization is applied to the crystal, the dipole internal tend to face the same direction again. This turning movement will expand the crystal in the direction of polarization as if another process of polarization begins. The reverse piezoelectric effect is utilized in piezoelectric actuator [BUD 2004].

In order to describe the relationship between the stress, strain, electric field and electric displacement in the piezoelectric material, a solid model of a piezoelectric element with predefined coordinate system, as shown in Figure 2. 14, is proposed. The direction of the polarization or that of the polarity of a single crystal is along axis 3 while the surface 12 is perpendicular to axis 3.

The stress and strain are tensors of first order in the 3D coordinate system while the electric field and electric displacement are vectors. The parameters of each component are: $\boldsymbol{T}=\boldsymbol{T}_{ij}$(stress), $\boldsymbol{S}=\boldsymbol{S}_{ij}$(strain), $\boldsymbol{E}=\boldsymbol{E}_{i}$(electric field), $\boldsymbol{D}=\boldsymbol{D}_{i}$(electric displacement). According to the linear theory of piezoelectric effect, the piezoelectric material is considered ideal elastic material. The damping loss is neglected in mechanical movement, electrical effect and coupling effects. It is also considered as thermal insulation with environment. There are four types of governing equations for piezoelectric effect which correspond to four types of boundary condition [IEEE 1987].

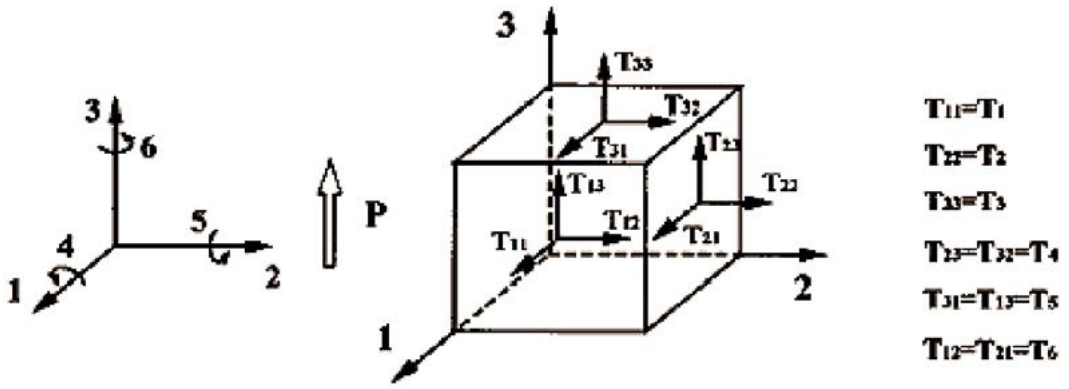

Figure 2. 14: Definition of piezoelectric crystal

When the deformation is free and short circuit, the strain-charge form is:

$$\begin{cases} D = \varepsilon^{T} E + dT \\ S = d^{t} E + s^{E} T \end{cases} \quad (2.\ 13)$$

When the deformation is prohibited and short circuit, the stress-charge form is:

$$\begin{cases} D = \varepsilon^S E + eS \\ T = -e^t E + c^E S \end{cases} \tag{2. 14}$$

When the deformation is free and open circuit, the strain-field form is:

$$\begin{cases} E = \beta^T D - gT \\ S = g^t D + s^D T \end{cases} \tag{2. 15}$$

When the deformation is prohibited and open circuit, the stress-field form is:

$$\begin{cases} E = \beta^S D - hS \\ T = -h^t D - c^D S \end{cases} \tag{2. 16}$$

Where ***d***, ***e***, ***g*** and ***h*** are respectively the matrix of strain, stress, voltage and charge constant. $\boldsymbol{d}^t$, $\boldsymbol{e}^t$, $\boldsymbol{g}^t$ and $\boldsymbol{h}^t$ are respectively the transpose of ***d***, ***e***, ***g*** and ***h***. $\boldsymbol{S}^E$ and $\boldsymbol{S}^D$ are the matrix of elastic compliance constant in short and open circuit condition, $\boldsymbol{C}^E$ and $\boldsymbol{C}^D$ are the matrix of elastic stiffness constant in short and open circuit condition, $\boldsymbol{\varepsilon}^S$ and $\boldsymbol{\varepsilon}^T$ are the matrix of dielectric constant when the deformation is prohibited and free, $\boldsymbol{\beta}^S$ and $\boldsymbol{\beta}^T$ are the matrix of permittivity constant when the deformation is prohibited and free.
According to the symmetrical characteristics of a tensor and the coordinate system in Figure 2. 14, the expanded strain-charge form of governing equations 2.11 is:

$$\begin{cases} \begin{bmatrix} S_1 \\ S_2 \\ S_3 \\ S_4 \\ S_5 \\ S_6 \end{bmatrix} = \begin{bmatrix} s_{11}^E & s_{12}^E & s_{13}^E & 0 & 0 & 0 \\ s_{12}^E & s_{11}^E & s_{13}^E & 0 & 0 & 0 \\ s_{13}^E & s_{13}^E & s_{33}^E & 0 & 0 & 0 \\ 0 & 0 & 0 & s_{44}^E & 0 & 0 \\ 0 & 0 & 0 & 0 & s_{44}^E & 0 \\ 0 & 0 & 0 & 0 & 0 & s_{66}^E \end{bmatrix} \begin{bmatrix} T_1 \\ T_2 \\ T_3 \\ T_4 \\ T_5 \\ T_6 \end{bmatrix} + \begin{bmatrix} 0 & 0 & d_{31} \\ 0 & 0 & d_{31} \\ 0 & 0 & d_{33} \\ 0 & d_{15} & 0 \\ d_{15} & 0 & 0 \\ 0 & 0 & 0 \end{bmatrix} \begin{bmatrix} E_1 \\ E_2 \\ E_3 \end{bmatrix} \\ \begin{bmatrix} D_1 \\ D_2 \\ D_3 \end{bmatrix} = \begin{bmatrix} 0 & 0 & 0 & 0 & d_{15} & 0 \\ 0 & 0 & 0 & d_{15} & 0 & 0 \\ d_{31} & d_{31} & d_{33} & 0 & 0 & 0 \end{bmatrix} \begin{bmatrix} T_1 \\ T_2 \\ T_3 \\ T_4 \\ T_5 \\ T_6 \end{bmatrix} + \begin{bmatrix} \varepsilon_{11}^T & 0 & 0 \\ 0 & \varepsilon_{11}^T & 0 \\ 0 & 0 & \varepsilon_{33}^T \end{bmatrix} \begin{bmatrix} E_1 \\ E_2 \\ E_3 \end{bmatrix} \end{cases} \tag{2. 17}$$

2.3.2 Review of literature

The energy harvesting based on piezoelectric effect has been widely researched for a long time [KHA 2010]. So far, a comprehensive literature review on this topic is challenging. The most recent review on piezoelectric energy harvesting [ANT 2007][COO 2008] provide with brief introduction on the current state of art in materials, structures of the piezoelectric transducers, coupling structures between the transducer and those varieties of energy sources, electric conditioning circuit between transducer and energy storage device and optimized strategies for energy harvesting.

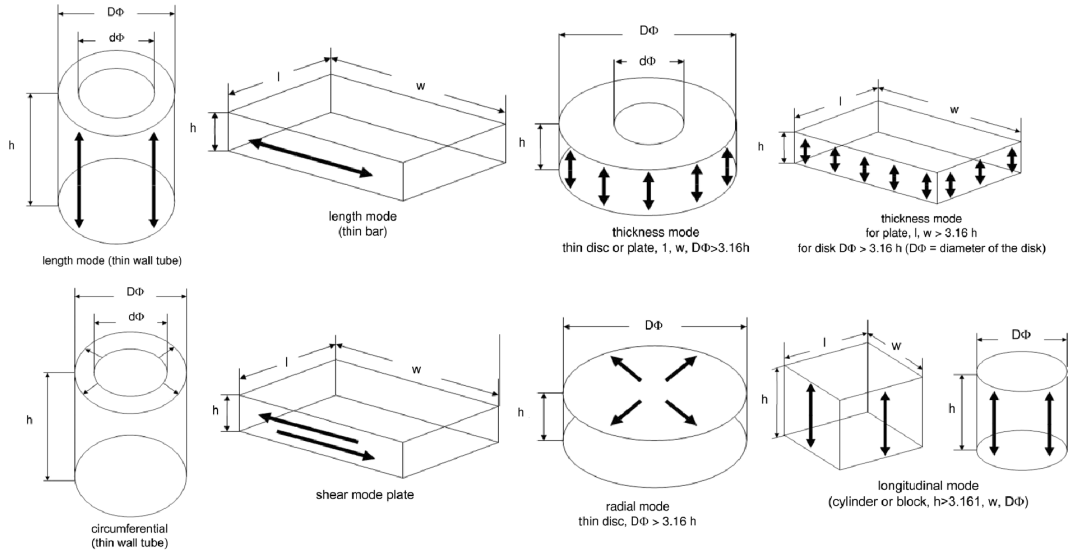

Figure 2. 15: Common modes of vibration in piezoelectric element [WEB 1999]

The piezoelectric material and structure which is utilized for energy harvesting include monolithic PZT [LEE 2005], PVDF film coated with PEDOT/PSS electrodes [LEE 2004], piezofiber composite [CHU 2003], MFC composite [SOD 2004], …… The energy conversion efficiency of those piezoelectric materials is determined with the electromechanical coupling factor (k_{33}, k_{31}, k_p, or k_{15}). Subscripts denote the relative directions of electrical and mechanical quantities and the kind of motion involved. They can be associated with vibration modes of certain simple transducer shapes. Some well known vibration modes with certain shapes of the transducer are summarized by [WEB 1999] as shown in Figure 2. 15. k_{33} is appropriate for a long thin bar, electroded on the ends, and polarized along the length, and vibrating in a simple length expansion and contraction. k_{31} relates to a long thin bar, electroded on a pair of long faces, polarized in thickness, and vibrating in simple length expansion and contraction. k_p signifies the coupling of electrical and mechanical energy in a thin round disc, polarized in thickness and vibrating in radial expansion and contraction. k_{15} describes the energy conversion in a thickness shear vibration. When the piezoelectric material work at quasi-static status the k_{33} is expressed as [IEEE 1987]:

$$k_{33} = \sqrt{\frac{\text{electrical energy stored}}{\text{mechanical energy applied}}} = \sqrt{\frac{d_{33}^2}{s_{33}^E \varepsilon_{33}^T}} \qquad (2.\ 18)$$

There are also many modes of vibration and mechanical coupling structure of the piezoelectric element which can be utilized for energy harvesting. They are shown in Figure 2. 16. Examples of the coupling structures are: unimorphs, bimorphs, multilayered stacks, rainbows, s-morphs, moonie and cymbal.

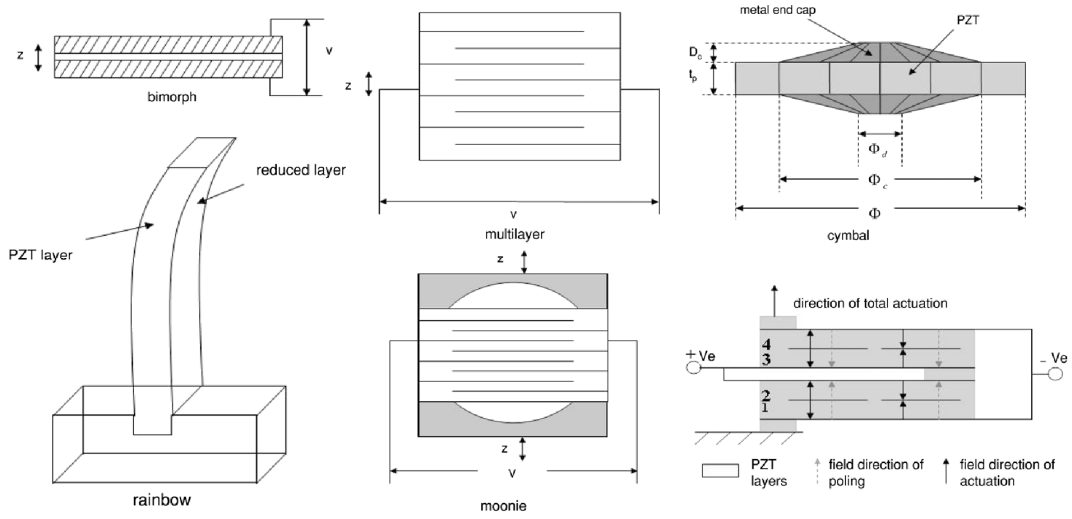

Figure 2. 16: Common modes of mechanical coupling structure of piezoelectric element [WEB 1999]

According to the scope of this study, a more detailed introduction is given to an energy harvesting system which uses bulk piezoelectric ceramic material and driven by a vibrating cantilever (bimorph or unimorph), as shown in Figure 2. 17. Those important problems in such an energy harvesting system will be addressed further.

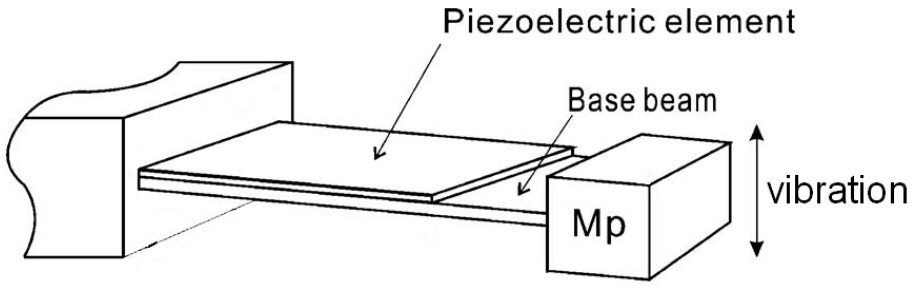

Figure 2. 17: PIEG based on vibrating cantilever

There are three basic parts in such a cantilever. The base beam is always made from metal and it works as a support and converts mechanical load to the active material. The piezoelectric element is bonded to the base beam and a unimorph structure is formed. A

proof mass M_P is attached to the free tip of the base beam, adjusting the resonant frequency of the system. The piezoelectric element works mainly at d_{31} mode in this structure. It is always placed adjacent to the clamped end of the base beam where the strain is higher. There are lots of questions for such an energy harvesting system:

1. What is the power generation of such a system with given input mechanical loading and external electric load?
2. What is the limitation for the maximum power generation with a typical piezoelectric element?
3. How can we optimize the structure of the cantilever based piezoelectric energy harvesting system?
4. How can we improve the power generation when the input mechanical load is changing?

The first question can be answered by the modeling of the electromechanical structure of the system as shown in Figure 2. 18 [LEF 2005]. A simplified model is proposed to describe the behavior of the system at resonant status such as a cantilever at its first bending model. It is based on a (mass + spring + damper + piezoelement) system with one degree of freedom as shown below.

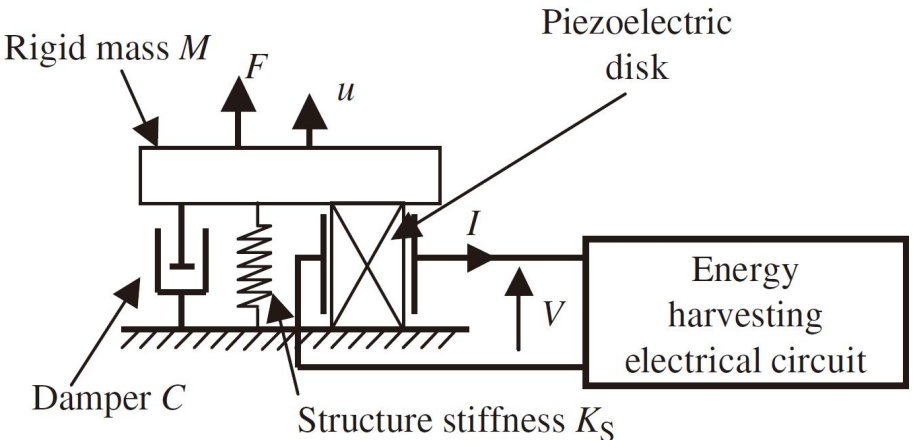

Figure 2. 18: Single-mode model of a PIEG based on a cantilever [LEF 2005]

In this model, the cantilever is considered as a rigid mass M. A spring with stiffness K_S is connected with the mass and it represents the total stiffness of the cantilever + piezoelement structure. A damper C is also connected which taking account the total structure damping from the mechanical system. The piezoelement is represented by a bulk pillar with thickness L and sectional area of A. When excited an external force F is applied to the mass, meanwhile the internal force include three parts. F_P is yield from the piezoelement while the spring and damper provide with elastic and viscous force respectively. The generated displacement of the mass is denoted by u. I and V are the current and voltage generation in the piezoelement when connected with a typical energy harvesting circuit. Based on the previous basic expression of piezoelectric effect

(2.14), the governing equation of the piezoelement is:

$$\begin{cases} F_P = K_{PE}u + \alpha_0 V \\ I = \alpha_0 \dot{u} - C_0 \dot{V} \end{cases}$$
$$K_{PE} = \frac{c_{33}^E A}{L}, C_0 = \frac{\varepsilon_{33}^S A}{L}, \alpha_0 = \frac{e_{33} A}{L} \quad (2.19)$$

$\boldsymbol{K_{PE}}$ is the stiffness of the piezoelement with constant electric field while $\boldsymbol{C_0}$ is its capacitance with constant strain. $\boldsymbol{\alpha_0}$ is a force factor which is based on the piezoelectric constant.
The dynamic response of the cantilever is governed by the second law of Newton:

$$M\ddot{u} = F - F_p - K_S u - C\dot{u} = F - (K_{PE} + K_S)u - \alpha_0 V - C\dot{u} \quad (2.20)$$

The energy conservation in the system is taking account by the integration of the equation (2.20) product velocity with time:

$$\int F\dot{u}dt = \frac{1}{2}M\dot{u}^2 + \frac{1}{2}(K_{PE} + K_S)u^2 + \int C\dot{u}^2 dt + \int \alpha_0 V\dot{u}^2 dt$$
$$\int \alpha_0 V\dot{u}^2 dt = \frac{1}{2}C_0 V^2 + \int VIdt \quad (2.21)$$

It is noteworthy that the energy balance takes account six parts – the work done the external force, the kinetic energy of the structure, the elastic potential energy stored in the structure, the thermal energy yield by the damping, the electrical potential energy stored in the piezoelement and the electrical energy delivered to the external energy harvesting circuit.

There are also two methods to harvest electrical energy with PIEG. They are resistive and capacitive loads. When a resistive load is connected with the PIEG, the energy conversion efficiency of the active material is analyzed by [RIC 2004]:

$$\eta_m = \left(\frac{0.5k_{xx}^2}{1-k_{xx}^2}\right) \Big/ \left(\frac{1}{Q_M} + \left(\frac{0.5k_{xx}^2}{1-k_{xx}^2}\right)\right) \quad (2.22)$$

Where $\boldsymbol{k_{xx}}$ is the typical electromechanical coefficient and $\boldsymbol{Q_M}$ is the quality factor of the piezoelement.

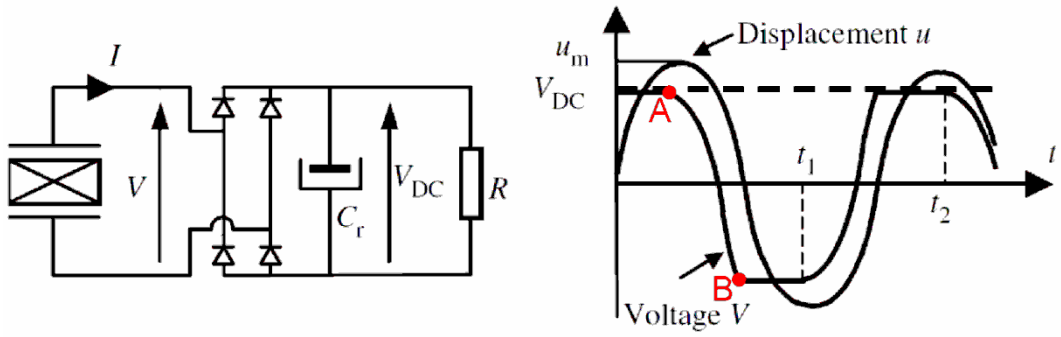

Figure 2. 19: Standard energy harvesting circuit and voltage generation [LEF 2005]

When a capacitive load is used to store the harvested energy, the standard circuit is shown in Figure 2. 19. Suppose the cantilever is driven at resonance by the external force ***F***. The bridge circuit is ideal and the rectified voltage V_{DC} is assumed to be constant. When the voltage generation ***V*** is lower than V_{DC}, the piezoelectric element is in open circuit status. When ***V*** reaches V_{DC}, the bridge is open and ***V*** is maintained to V_{DC}. The bridge will be closed when the voltage generation from the piezoelement begins to decrease at the maximum deformation of the cantilever. A typical profile of voltage in the piezoelement and the displacement of the rigid mass are shown on the right side of Figure 2. 19.

When the V_{DC} becomes stable, it can be recognized that all the generated charges from the piezoelectric element will be released by the resistor ***R***. According to the conservation of charge, the voltage and power generation can be deduced:

$$\left|\int_{t_1}^{t_1+\frac{T_0}{2}} Idt\right| = \frac{V_{DC}}{R}\frac{T_0}{2}$$

$$V_{DC} = \frac{2\alpha_0 R}{2C_0 R\omega + \pi}\omega u_{\max} \ , \ P = \frac{V_{DC}^2}{R} = \frac{4\alpha_0^2 R}{(2C_0 R + \pi)^2}\omega^2 u_{\max}^2 \qquad (2.\ 23)$$

$$R_{opt} = \frac{\pi}{2\omega C_0} \ , \ P_{\max} = \frac{\alpha_0^2 \omega}{2\pi C_0}u_{\max}^2 \ , \ \omega = \frac{2\pi}{T_0}$$

Where T_0 is the period of the vibration and ω is the angular frequency. t_1 is the time when ***u*** reaches its extreme values. u_{max} is the maximum displacement of the cantilever and P_{max} is the maximum electrical power achieved by the piezo element. R_{opt} is the optimal resistance of the external load. It is noteworthy that this power is achieved with weak electrometrical coupling. When the converted electric power is too high and its influence to the mechanical vibration can't be neglected, then the maximum amplitude of the cantilever needs to be modified as below with the energy equation in (2.21):

$$u_{\max} = \frac{F_{\max}}{C\omega + (2R\omega\alpha_0^2 / (RC_0\omega + (\pi/2))^2)} \qquad (2.\ 24)$$

Where the F_{max} is the maximum equivalent force applied on the cantilever. The formula (2.20)(2.21)(2.23) give an estimation of the power generation with piezoelectric energy harvesting system based on cantilever.

The second question is addressed in [LIU 2007]. It revealed that the maximum energy which can be harvested from a piezoelectric element in a typical work cycle is limited by its maximum strain S_m and stress T_m, maximum field E_{break} and surface charge density D_s (saturation), or depoling due to an electric field E_{dp} applied in the opposite direction of poling. According to the relationship of E_{dp} (E_{break}), T_m and S_m, there are several kinds of optimized work cycle for a given piezoelectric element. When the positive and negative maximum strain in the piezoelectric element is reachable and the piezoelectric element is relatively stiff, so it cannot get the maximum strain with the maximum stress while the field tries with all its effort to block the element's deformation. The proposed work cycle is illustrated in Figure 2. 20.

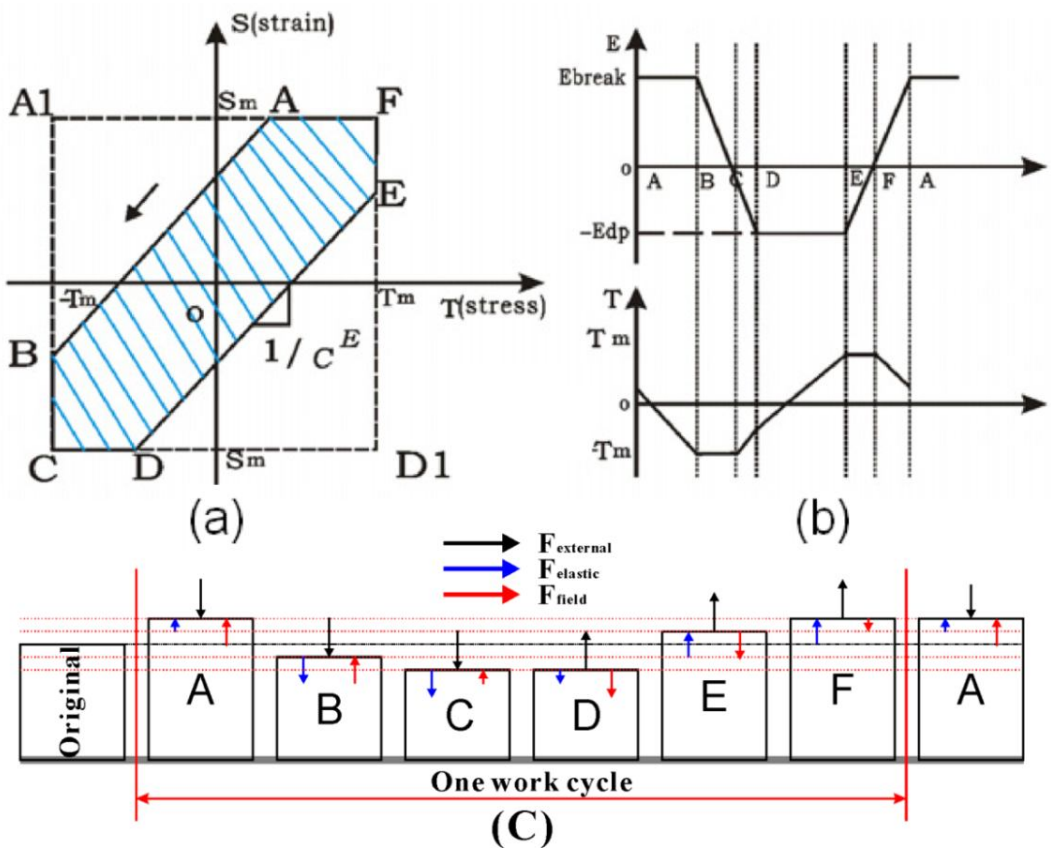

Figure 2. 20: Work cycle of piezoelectric element with maximum power generation. (a) stress-strain relationship (b) wave form of electric field and stress (c) sketch map [LIU 2007]

The piezoelectric element is set into state A at first where it reaches the maximum positive deformation. There are six steps in this work cycle. (AB): The positive electric field keeps constant and the external force compresses the piezoelectric element. The internal stress decreases from a positive value to the negative extremum $-\boldsymbol{T_m}$. (BC): The electric field begins to decrease until the strain reaches negative extremum $-\boldsymbol{S_m}$. (CD): The electric field reverses and the stress increases. (DE): The negative electric field keeps constant and the external force stretches the piezoelectric element. The internal stress increase from a negative value to the positive extremum $\boldsymbol{T_m}$. (EF): The electric field begins to increase until the strain reaches positive extremum $\boldsymbol{S_m}$. (FA): The electric field reverses and the stress decreases. There are two objectives for the applied electric field in this strategy. The first one is to generate a shift between the external force and elastic force, decreasing the exchange between elastic potential energy and external energy. The second one is to maximize the deformation of the piezoelectric element which increases the displacement of the external force. It is noteworthy that this analysis is based on a quasi-static deformation of the piezoelectric material. It is only effective when the frequency of the vibration of cantilever is far from the resonant frequency of the piezoelectric element [LIU 2007].

The third question mentions about the structure coupling between the support of the cantilever and the piezoelectric material. Researches in this problem aim to use the minimum volume of active material to generate the maximum power with arbitrary input mechanical loading. The modeling of the structure coupling in the bimorph is addressed in [WAN 1999] and [ROU 2005] gave a brief review on the structure optimization. One of the shortcomings for the common cantilever structure is that the strain distribution is not uniform over the length direction. The strain concentrates at the supporting end and that at the free tip is zero. Therefore, Goldschmidtboeing et al. [GOL 2008] proposed to triangular shaped cantilever instead of common rectangular shaped. Zhao et al. [ZHA 2010] designed a uniform-strain cantilever with varied thickness along the length direction. Xu et al. [XU 2010] proposed a right-angle cantilever which inherently achieves a uniform strain distribution on the piezoelectric element, as shown in Figure 2. 21. The piezoelectric element is placed at the original base where it is perpendicular to the vibrating cantilever. It can generate a useful power twice that of a traditional cantilever under the same strain limitation.

Question four relates to the tuning of the cantilever and broadband energy harvesting. It is essential for an energy harvesting system in an actual situation. Zhu et al. [ZHU 2010] provides with a review on the current technologies as shown in Table 2. 2.

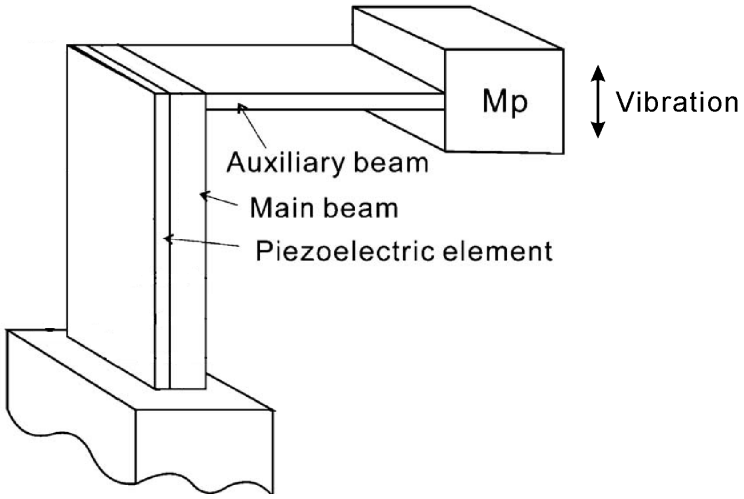

Figure 2. 21: A typical cantilever with improved strain distribution [XU 2010]

Table 2. 2: Strategies of harvesting broadband vibration [ZHU 2010]

Strategies	Advantages	Disadvantages
Mechanical tuning	• High efficiency	• Extra system and energy are required • Responds to only one frequency at a time • Slow response to a change in a vibration frequency
• Change dimension	• Does not affect damping	• Difficult to implement • Not suitable for tuning *in situ*[a]
• Change centre of gravity	• Does not affect damping	• Not suitable for tuning *in situ*
• Change spring stiffness continuously	• Suitable for *in situ* tuning	• Consumes energy when generators work at resonance
• Apply axial load (change spring stiffness intermittently)	• Easy to implement • Suitable for *in situ* tuning • No energy is required when generators work at resonance • Damping is not affected when the tensile load is applied	• Increased damping when the compressive load is applied
Electrical tuning	• Easy to implement • No energy is required when generators work at resonance • Suitable for *in situ* tuning	• Low tuning efficiency
Widen bandwidth	• No tuning mechanism required • Respond to different frequencies at the same time • Immediate response to a change in vibration frequency	• Complexity in design
• Generator array	• Damping is not affected	• Complexity in design • Low volume efficiency
• Use mechanical stopper	• Easy to implement	• Fatigue problem • Decrease in the maximum output power
• Coupled oscillators	• Easy to implement	• Decrease in the maximum output power
• Nonlinear generators	• Better performance at excitation frequencies higher than resonant frequency	• Complexity in design • Hysteresis
• Bi-stable structure	• Better performance at excitation frequencies much lower than resonant frequency	• Complexity in design

[a] Tuning while the generator is mounted on the vibration source and working.

2.3.3 Enhanced energy conversion efficiency with SSHI technique

The foregoing review on literature indicates that the key to improve the piezoelectric power generation lies in the optimization of work cycle. Professor Guyomar et al. [GUY 2005] had put forward a technique named SSHI (synchronized switching harvesting with an inductor) which uses nonlinear processing to improve the energy conversion efficiency of the piezoelectric material. It is derived from SSD (synchronized switch damping) [RIC 2000], which is previously developed to address the problem of vibration damping on mechanical structures. The proposed energy harvesting circuit is shown in Figure 2. 22.

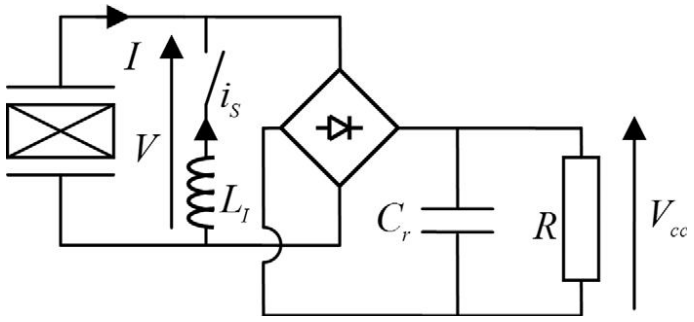

Figure 2. 22: Energy harvesting circuit with SSHI technique [GUY 2005]

According to the standard energy harvesting circuit in Figure 2. 19, when the cantilever reaches the maximum displacement and start to change the direction of the vibration, as the point A in Figure 2. 19, the generated voltage on the piezoelectric element begins to decrease. The free charges on the piezoelectric element can't go into the energy storage device until the absolute value of the generated voltage is greater than that in the storage device next time, as the point B in Figure 2. 19. It can be recognized that some part of the generated electrical potential energy before point A converts to the kinetic energy of the structure between A and B. If the DC voltage in the energy storage device is high, the loss of electrical potential energy between A and B can be significant. In order to solve this problem, it is suggested to reverse the polarity of the voltage in the piezoelectric element at point A and let the charges in the piezoelectric element keeps on accumulating and the absolute value of the voltage increasing. To reverse the voltage in the piezoelectric element, it is suggested to use an inductor connected in parallel with the piezoelectric element, creating a LC oscillator. Then the voltage in the piezoelectric element (capacitor) will reverse in half period of the LC oscillator and the inductor is disconnected at that time. Generally, the period of an electrical oscillator can be higher than that of a mechanical vibrator. Therefore this strategy can be realized.

According to the foregoing analysis, the waveform achieved in the piezoelectric element is shown in Figure 2. 23 (a).The inductor and capacitor (piezoelement) in the LC oscillator are not ideal in actual situation. There is leakage and high frequency radiation in the switching process. Therefore, the absolute value of the inverse voltage

at the maximum displacement of the cantilever is decreased. The loss can be described by the quality factor of the LC oscillator $\boldsymbol{Q_I}$. It can be defined for the inversion oscillating network in Figure 2. 23 (a).

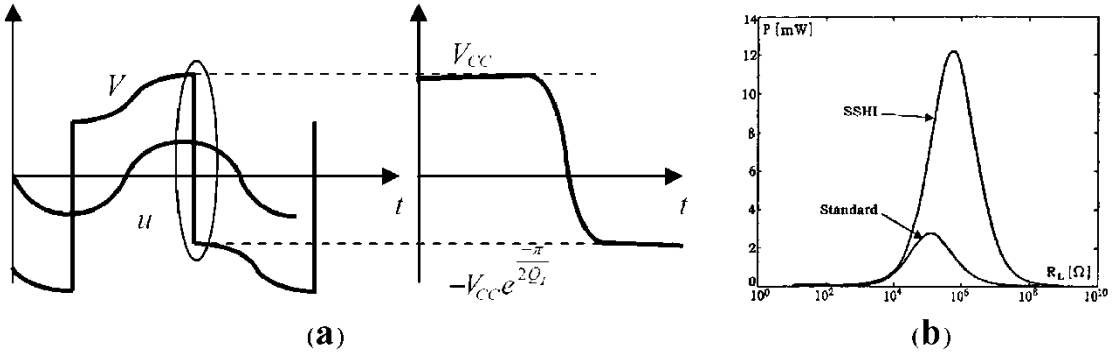

Figure 2. 23: SSHI technique: (a) voltage generation refers to the displacement of the cantilever [GUY 2005] (b) power generation compared with standard circuit [LIU 2008]

It can be recognized that the rectified voltage $\boldsymbol{V_{cc}}$ will reach a constant value when the input mechanical loading is stable. This constant value can be deduced by considering the charge transfer during half period of the vibration. The charges released to the resistor R in half period $0.5\boldsymbol{T_0}$ include these generated from the piezoelectric element and those transferred from the inductor at the beginning of this time.

$$\left|\int_{t_1}^{t_1+\frac{T_0}{2}} Idt\right| + C_0 V_{cc}(1+e^{\frac{-\pi}{2Q_I}}) = \frac{V_{cc}}{R}\frac{T_0}{2} \tag{2. 25}$$

Therefore, the constant regulated voltage and power generation is achieved below:

$$V_{cc} = \frac{2\alpha_0 R}{C_0 R(1-e^{\frac{-\pi}{2Q_I}})\omega + \pi}\omega u_{\max}$$
$$P = \frac{V_{cc}^2}{R} = \frac{4\alpha_0^2 R}{\left(C_0 R(1-e^{\frac{-\pi}{2Q_I}})\omega + \pi\right)^2}\omega^2 u_{\max}^2 \tag{2. 26}$$

According to the energy conservation during the same semi-period above, the displacement amplitude $\boldsymbol{u_{max}}$ is achieved:

$$\int_{t_1}^{t_1+\frac{T_0}{2}} F\dot{u}dt = C\int_{t_1}^{t_1+\frac{T_0}{2}} \dot{u}^2 dt + \frac{1}{2}C_0 V_{cc}^2(1-e^{\frac{-\pi}{Q_I}}) + \frac{V_{cc}^2}{R}\frac{T_0}{2}$$

$$u_{max} = F_{\max}\Bigg/\left(C\omega + \frac{4R\omega\alpha_0^2}{\pi}\frac{(RC_0(1-e^{\frac{-\pi}{Q_I}})\omega + 2\pi)}{(RC_0(1-e^{\frac{-\pi}{2Q_I}})\omega + \pi)^2}\right) \qquad (2.\ 27)$$

For structure with a weak electromechanical coupling, the expression of the generated power (2.25) can be simplified as:

$$P = \frac{V_{cc}^2}{R} = \frac{4\alpha_0^2 R}{\left(C_0 R(1-e^{\frac{-\pi}{2Q_I}})\omega + \pi\right)^2}\frac{F_{\max}^2}{C^2}$$

$$R_{opt} = \frac{\pi}{C_0\omega(1-e^{\frac{-\pi}{2Q_I}})}\ ,\ P_{\max} = \frac{\alpha_0^2}{\pi C_0\omega(1-e^{\frac{-\pi}{2Q_I}})}\frac{F_{\max}^2}{C^2} \qquad (2.\ 28)$$

For a structure driven out of its resonance or for a structure in which the displacement is forced, the power reaches a maximum for the same optimal load $\boldsymbol{R_{opt}}$.
Combined expression (2.20)(2.21)(2.25), when the quality factor is given at 2.6 which is correspond to a preliminary experimental setup [GUY 2005], the power generation of SSHI technique and standard circuit with different resistor $\boldsymbol{R}$ is shown in Figure 2. 23(b). The output power with SSHI technique is more than 4 times higher in this case.

2.4 Electromagnetic and electrostatic effects for energy harvesting

2.4.1 Electromagetic energy harvesting

Electromagnetic power conversion results from the relative motion of an electrical conductor in a magnetic field. Typically the conductor is wound in a coil to make an inductor. The relative motion between the coil and magnetic field causes a current to flow in the coil. The induced voltage Vcoi on the coil is determined by Faraday's Law:

$$V_{coi} = d\Phi/dt \tag{2. 29}$$

Where $\boldsymbol{\Phi}$ is the magnetic flux. In the simple case of a coil moving through a perpendicular magnetic field of constant strength, the maximum open circuit voltage across the coil is given by:

$$V_{open} = NBl\frac{dx_e}{dt} \tag{2. 30}$$

Where $\boldsymbol{N}$ is the number of turns in the coil, $\boldsymbol{B}$ is the strength of the magnetic field, $\boldsymbol{l}$ is the length of the coil, $\boldsymbol{x_e}$ is the distance the coil moves through the magnetic field.

There are a couple of significant strengths to electromagnetic implementation. First, no separate voltage source is needed to get the process started as in electrostatic conversion. Second, the system can be easily designed without the necessity of mechanical contact between any parts. It improves reliability and reduces mechanical damping. In theory, this type of converter could be designed to have very little mechanical damping.

According to [KHA 2010], the electromagnetic power generators can be classified into three categories: resonant, rotational, and hybrid devices, as shown in Figure 2. 24. Resonant generators operate in an oscillating mode. They usually utilize the relatively small displacements between a permanent magnet and a coil to harness power from environmental vibrations. In contrast, rotational generators operate in the same way as the operation of large-scale magnetic generators. They have been designed to operate using rotational power from small turbines or heat engines, which can provide continuous rotational motion under a steady driving torque. Lastly, hybrid devices convert linear motion into rotational motion using an imbalanced rotor. Based on different operating conditions, the power generated by rotation from these devices may be continuous, resonant, or chaotic.

The electromagnetic generators can generate high output current levels but the voltage is very low (typically < 1 V). Macroscale devices are readily fabricated using high performance bulk magnets and multi-turn coils. However, calibrating microscale systems is difficult due to the relatively poor properties of planar magnets, the

restrictions on the number of planar coil turns, and the too small vibration amplitudes. Both kinetic harvesting techniques have been shown to be capable of delivering power to the load from microwatts to milli watts.

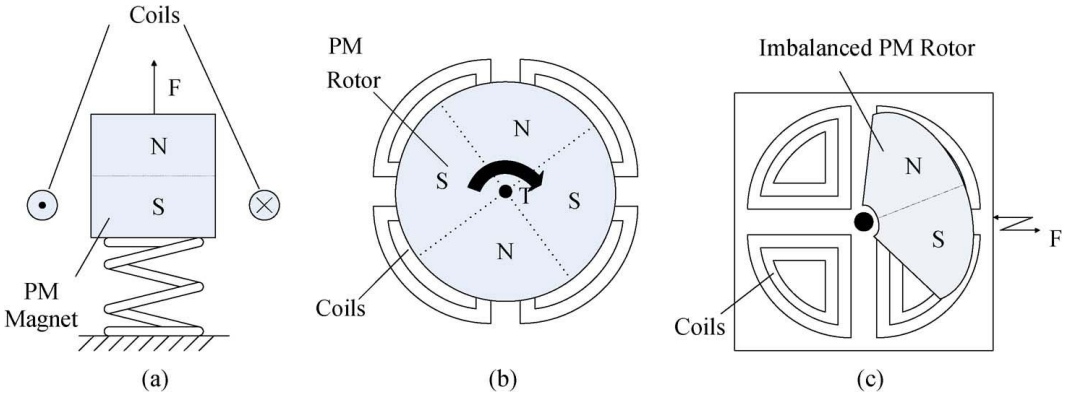

Figure 2. 24: Three different categories of Permanent Magnet (PM) power-generator topologies. (a) Resonant generator operating in oscillating mode under vibration force. (b) Rotational generator operating under steady torque. (c) Hybrid generator to convert linear motion into rotational motion. [KHA 2010]

2.4.2 Electrostatic energy harvesting

The electrostatic power generator consists of two conductors which move relative to one another. They are separated by a dielectric and create a capacitor. As the conductors move the energy stored in the capacitor changes, thus providing the mechanism for mechanical to electrical energy conversion. A simple rectangular parallel plate capacitor can be used to illustrate the principle of electrostatic energy conversion. The voltage across the capacitor is given by equation:

$$V_e = \frac{Q_e}{C_e} = \frac{Q_e t_e}{\varepsilon_e A_e} \tag{2. 31}$$

Where ε_e is the permittivity of the dielectric. If the charge Q_e on the capacitor is held constant, the voltage V_e can be increased by reducing the capacitance C_e, which can be accomplished either by increasing the thickness t_e or reducing the surface area A_e of the capacitor. If the voltage is held constant, the charge can be increased by reducing t_e, or increasing A_e. In either case, the energy stored on the capacitor increases.
According to [ROU 2003], the primary disadvantage of electrostatic power generator is that they require a separate voltage source to initiate the conversion process because the capacitor must be charged up to an initial voltage for the conversion process to start. Another disadvantage is that for many design configurations mechanical limit stops

must be included to ensure that the capacitor electrodes do not come into contact and short the circuit. The resulting mechanical contact could cause reliability problems as well as increase the amount of mechanical damping. Perhaps the most significant advantage of electrostatic converters is their potential for integration with microelectronics. Silicon micro machined electrostatic transducers are the backbone of MEMS technology. MEMS transducers use processes very similar to microelectronics. Therefore, because of the process compatibility, it is easier to integrate electrostatic converters based on MEMS technology than either electromagnetic or piezoelectric converters. Another advantage is that, unlike electromagnetic converters, appropriate voltages for microelectronics, on the order of two to several volts, can be directly generated.

According to [LEE 2009], there are three basic mechanisms of the electrostatic generator as shown in Figure 2. 25. All of them operate via a variable capacitance that can oscillate between a maximum and minimum value. However, what distinguishes the different mechanisms from each other is the manner in which this varying capacitance is achieved. The in-plane overlap converter varies its capacitance by changing the overlap area between electrode fingers, the in-plane gap closing converter varies its capacitance by changing the gap between electrode fingers and the out-of-plane gap closing converter varies its capacitance by changing the gap between two large electrode plates.

The capacitance of a prototype electrostatic generator [MIT 2004] varied from 15 to 127pF with maximum gap as 450μm. It generates a voltage of 250V from a pre-charge of 30V. Another prototype reported by [SHE 2010] is 3m×3m×0.5mm in dimension. With the excitation input of 10 μm amplitude at 105 Hz, the generator can provide an average output power of 92.4nW, or equivalent output density 21nWmm^{-3}.

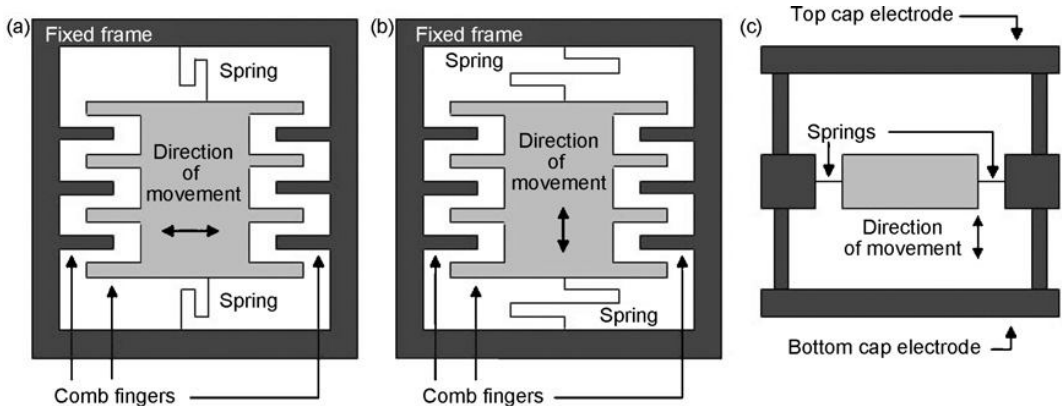

Figure 2. 25: The three different electrostatic mechanisms. The dark areas represent the fixed elements and the light areas, the movable elements. (a) In-plane overlap type. (b) In-plane gap-closing type. (c) Out-of-plane gap closing type. [LEE 2009]

2.5 Thermal energy storage with phase change material

Over the last 20 years, there has been a considerable variety of literature on the Phase Change Material (PCM). Zalba et al. [ZAL 2003] reviewed the history of thermal energy storage with a solid–liquid phase change, focusing on three aspects: materials, heat transfer and application. The main results on PCM show that it has many possible applications, such as (i) thermal energy storage [ISM 2002][ARK 2005], (ii) the air-conditioning in buildings [TYA 2007][ISM2 2002][AHM 2006], e.g. the "ice-storage" cooling of heat and electrical engines, (iv) the cooling of food, wine, dairy products, green-houses, (v) medical applications: transportation of blood, operating tables, hot-cold therapies, (vi) waste heat recovery [YAG 1995][ZHA 2009] (vii) off-peak power: heating water and cooling, heat pump systems, (viii) passive storage in bioclimatic building/architecture (HDPE, paraffin), thermal comfort in vehicles, textiles used in clothing and computer cooling.

The characteristics of PCM are similar to those of substances which melt and solidify at a high fusion temperature. The material can store and release large amounts of energy. Heat is absorbed or released when the material alternates between solid and liquid; PCMs are thus classified as latent heat storage (LHS) units. PCM latent heat storage is generally achieved through a solid-liquid phase change. Initially, the solid-liquid PCMs behave as sensible heat storage (SHS) materials: their temperature rises as they absorb heat. Unlike conventional SHS, however, when PCMs reach the temperature at which they change phase (their melting temperature) they absorb large amounts of heat at an almost constant temperature. The PCM continues to absorb heat with no significant rise in temperature until all the material has become liquid. When the ambient temperature around a liquid material falls, the PCM solidifies, releasing its stored latent heat. A large number of PCMs are available in the temperature range of -5 to 190°C [ZAL 2003][TYA 2007]. Within the human comfort range of 20 to 30°C, some PCMs are very effective [TYA 2007]. They store 5 to 14 times more heat per unit volume than conventional storage materials such as water, masonry, or rock. The most commonly used PCMs are salt hydrates, fatty acids, esters and various paraffins (such as octadecane). Recently, ionic liquids were investigated as PCMs. The temperature range offered by PCM technology provides new possibilities for building services and refrigeration engineers, regarding medium- and high-temperature energy storage applications. This thermo-energy is widely used for cooling and heating and for thermal energy storage applications.

As a typical application of PCM in the building Figure 2. 26 shows the comparison of the temperature variation indoor with a building using an ideal PCM and concrete. The PCM is placed at the outside face of the wall, reducing the thermal conductivity external for 10% of that with concrete. Besides, the heat capacity of the PCM is 100 $MJm^{-3}°C^{-1}$ while that of the concrete is $1.4MJm^{-3}°C^{-1}$. It concluded that with a sufficient volume of PCM, the indoor temperature can always maintain at the comfort range for human beings. This achievement is accomplished with the latent heat effect of the PCM.

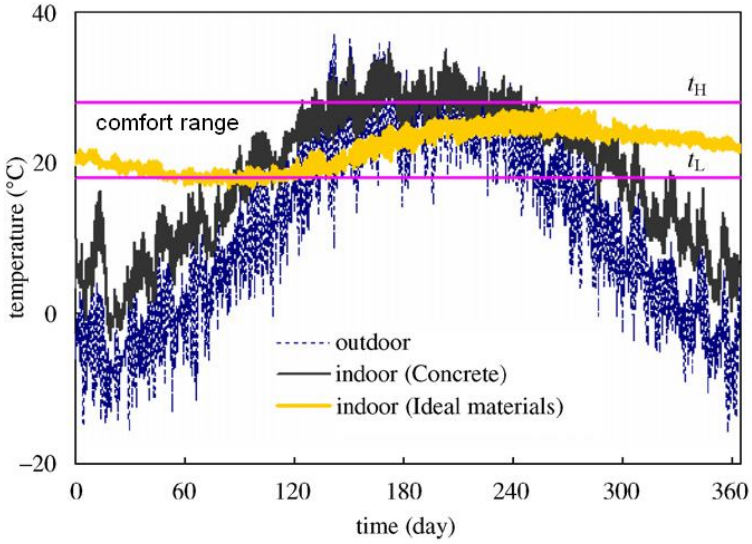

Figure 2. 26: Indoor temperature variation of a room applying concrete and ideal building PCM [ZHA 2007]

2.6 Sectional summary

In this section, several effects (including thermoelectric, pyroelectric, piezoelectric, electromagnetic and electrostatic) which can be utilized in energy harvesting are introduced. The fundamental of each effect is illustrated at first. Then a brief literature review which aims to provide a current state of art and the most recent progress is presented respectively. It is found that the development of energy harvesting technique with each effect is quite different. The research in thermoelectric energy harvesting is focusing on developing new material and seeking for potential energy source while that for pyroelectric energy harvesting is still focusing on the discussion of improving the energy conversion efficiency with optimized work cycle. The experimental prototype for pyroelectric energy harvesting is still rare at this time. The development in the piezoelectric energy harvesting is most flourishing and a lot of branch subjects are growing up, such as the active strategy with electrical interface, structure optimization, broadband technique and so on. The energy harvesting with electromagnetic and electrostatic effects are not as popular as the previous coupling effects in material. The physical mechanism limits the electromagnetic effect with low voltage generation while the electrostatic effect with micro structure application. It is noteworthy that the energy harvesting approach is not limited to these introduced above. The major advantage and disadvantage of the foregoing energy harvesting technologies are compared in the Table 2. 3:

Table 2. 3: Comparison of energy harvesting technologies

Type	Advantage	Disadvantage
Thermoelectric	No moving parts	Low material efficiency
Electromagnetic	Non-contact	Low voltage and bulky size
Pyroelectric	Potential high coupling (0.5)	Thermal loading challenge
Magnetostrictive	High coupling (>0.9)	Nonlinear effect
Piezoelectric	High power density	Depolarization and brittleness
Electrostatic	MEMS integration	Extra voltage source

In order to harvest ambient thermal energy, the thermoelectric effect and pyroelectric effect is proposed to be inspected. To harvest ambient wind energy, the piezoelectric effect is more favorable due to its large power density. Whatever is the energy harvesting effect, the inevitable challenge in an actual situation is to clarify the characteristics of the energy source and its suitable interface with the energy harvesting mechanism. Therefore, the next section tries to characterize the ambient energy source for thermoelectric, pyroelectric and piezoelectric effect. Besides, another group of literature review which focusing on harvesting ambient energy with these coupling effect will be presented. They are interested applications in buildings which are not limited by dimensions as those portable or wearable specimens.

3. Ambient energy harvesting

3.1 Characteristics of ambient energy source

The green power movement has spawned intense interest in the need for clean and renewable energy sources. This attention is usually focused on large scale power generation to supply homes and industry. However, the need for clean and renewable energy also finds a place with low power applications such as remote microprocessors or industrial sensors. Ambient light, heat and vibration sources can generate power for microcontroller or microprocessor circuits for wireless application.
There are numerous kinds of renewable energy around a building. They can be classified into two categories:

1. in environment outside: such as solar radiation, wind near ground, etc

2. inside the building: hot office machines, ventilation duct, etc

The renewable energy inside a building is adjacent to high electrical power which is not advantage. The energy outside is more interesting when utilized in a building. The main characteristics of these energies are their high variability and their low level of intensity [VUL 2009]. The focus in this section is to reveal the potential of these energies in application around buildings.

3.1.1 Analysis of typical case

Solar radiation, along with secondary solar-powered resources such as temperature difference in space, wind power near ground, variation of the ambient temperature accounts for most of the available renewable energy near a building. The temperature difference in space can be utilized by thermoelectric effect while the variation of ambient temperature can drive the pyroelectric material. The wind power is suitable for piezoelectric energy harvesting obviously.
In order to understand the characteristics of these ambient energy sources in both small and large time scale, a small weather station [BLA 1998] was used to record the ambient temperature, the intensity of solar radiation and the wind speed on the top of a building which is around 30m from the ground. The specimen is acquired at LOCIE Polytech Savoie, in Bourget du Lac, France. It is located at 45°38’44’’ north latitude on the earth. The raw data is updated at 10 minute intervals and the recording was maintained continuously for ten months (from 17th October 1997 to 10th August 1998). These three kinds of thermal load are shown in Figure 3. 1.

There are several basic characteristics which can be deduced from this specimen:

1. The intensity of solar radiation varied as a Gauss function each day, while the

temperature variation was similar to a triangular wave as shown in sub-graph (a). The maximum ambient temperature appeared 4 hours after the appearance of maximum radiation at midday. The annual variation of both the maximum value of the radiation and the average value of the temperature was also similar to a sinesoid wave as highlighted by gray lines in sub-graphs (c) and (d).

2. The average intensity of radiation during daytime was 250 Wm^{-2} when daytime is considered as being from 6:00 am to 6:00 pm each day. Radiation in the summer was 3 times higher than that during the winter. The average daily temperature variation is 10°C and the annual variation reaches 25°C.

3. The patterns of wind speed variation during a day or a year look like white noise, as illustrated subfigure (b) and (e). There is no specific function which is able to characterize them. The statistic analysis only show that the average wind speed through the year was 1.5 ms^{-1}.

4. The brief analysis to the raw data above provides the basic characteristics of the ambient thermal or mechanical load from a macro point view. However, the inherent properties of them are still unclear. It makes more sense to inspect these ambient loads from meteorology.

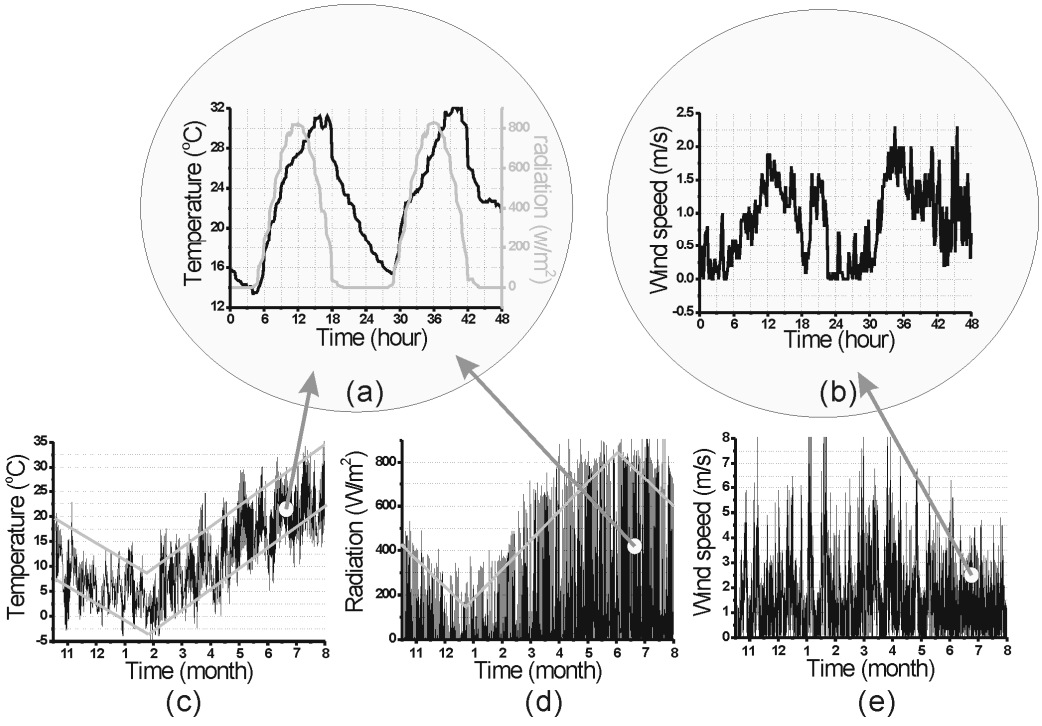

Figure 3. 1: Typical recorded ambient thermal loading

3.1.2 Modeling of solar thermal energy

In meteorology, an important parameter which is associated with the intensity of solar radiation named solar constant G_{sc}. It is a measure of flux density which describes the amount of incoming solar electromagnetic radiation per unit area that would be incident on a plane perpendicular to the rays, at a distance of one astronomical unit (roughly the mean distance from the Sun to the Earth). When solar irradiance is measured on the outer surface of Earth's atmosphere, the measurements can be adjusted using the inverse square law to infer the magnitude of solar irradiance at one astronomical unit and deduce the solar constant. The solar constant includes all types of solar radiation, not just the visible light. It is measured to be roughly 1367 Wm^{-2}[DUF 1991]. The solar constant does not remain constant over long periods of time, but over a year varies much less than the variation of direct solar irradiance at the top of the atmosphere arising from the ellipticity of the Earth's orbit.

At any given moment, the amount of solar radiation received at a location on the Earth's surface depends on the state of the atmosphere and the location's latitude. When the status of the daily weather (rainy, cloudy, sunny …) is neglected, the instantaneous extraterrestrial solar radiation P_{solar} on a horizontal surface can be expressed from the model illustrated by [YOR 2006] and [HE 2003]:

$$\begin{cases} P_{solar} = G_{sc} k(\cos\varphi\cos\delta\cos\omega_s + \sin\varphi\sin\delta) \\ k = 1 + 0.033\left[\cos\left(\dfrac{360n}{365}\right)\right] \\ \delta = 23.45\left[\sin\left(360\dfrac{284+n}{365}\right)\right] \\ \omega_s = 15*(n/24 - 12) \end{cases} \quad (3.\ 1)$$

Where φ is the latitude of the location, δ is the declination which causes an annual variation in location with nonzero latitude, ω_s is the sunset hour angle which comes from the combination of rotation and revolution of the earth, k is the eccentricity correction factor which is caused by the ellipticity of the Earth's orbit. n is the number of the day of the year starting from the first of January. The unit of all the angles is in degree.

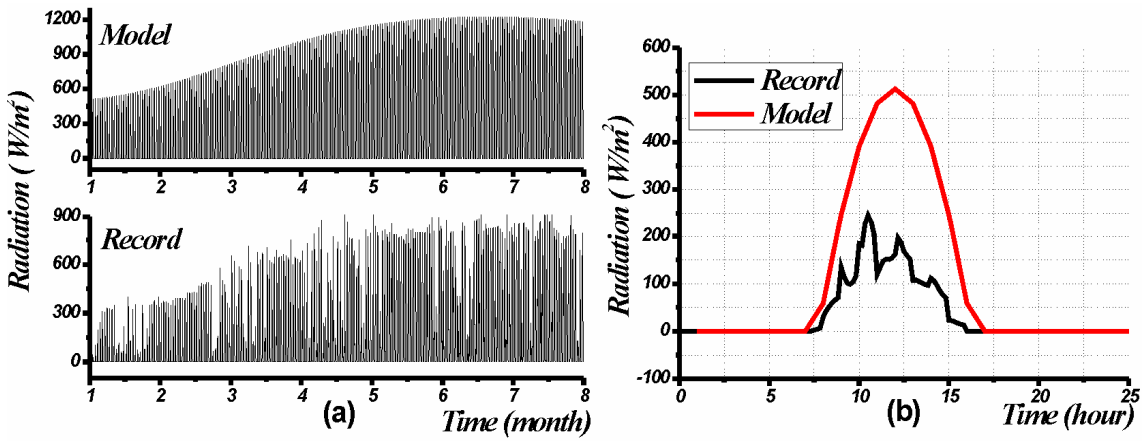

Figure 3. 2: Comparison of extraterrestrial solar radiation with modeling method and that recorded near the ground.

The extraterrestrial solar radiation at the same location (φ=45°38’44’’) as the foregoing recorded is generated by the model above. The calculated value is compared with the record as shown in Figure 3. 2. Subfigure (b) provides the comparison in a typical day (January 1st). The model predicts the trend of both the short time and long time variation of the solar radiation well according to Figure 3. 2. The recorded value is lower than the prediction because the radiation is absorbed and reflected by the atmosphere before it reaches the ground. It can be expected that with an improved model in meteorology, the ambient solar radiation at a given place can be estimated more precisely.

The mathematical model of extraterrestrial solar radiation with expression (3.1) provides with a global view on the near ground radiation available. It is helpful to the coming analysis which is in need of the ambient thermal loading, especially to those places with different latitude. The model of ambient temperature variation and wind flow in a given place is highly dependent on the landform, properties of ground surface, density of buildings or population and so on. They will not be expanded on since it will be far from the scope of this study.

3.2 Literature review

3.2.1 Direct Solar thermal energy harvesting

Thermoelectric power generation with solar energy begins at last century [TEL 1954]. The TEG with different material (Chromel P-constantan and ZnSb-type alloys in combination with a negative Bi-alloy) and different setup of radiation receiving method (flat-plate collector and solar energy concentrator) are analyzed. It concluded that an energy conversion efficiency of 3.35% is possible with 50-fold concentrated radiation and ZnSb-type thermoelectric material. The performance of the Chromel P-constantan material is 10 times lower which indicates the urgent need of excellent material. Later, the development of solar thermal energy harvesting technique with thermoelectric effect progresses in material, modeling, system design and applications.
Robert et al. [ROB 2005][ROB 2007] proposed to use perovskite structured material with improved Seebeck coefficient and decreased resistivity. It is indicated by [XIE2 2010] that the thermoelectric material with ZT=4 appears to have distinct advantages over magnetic induction technologies in solar thermal energy conversion.

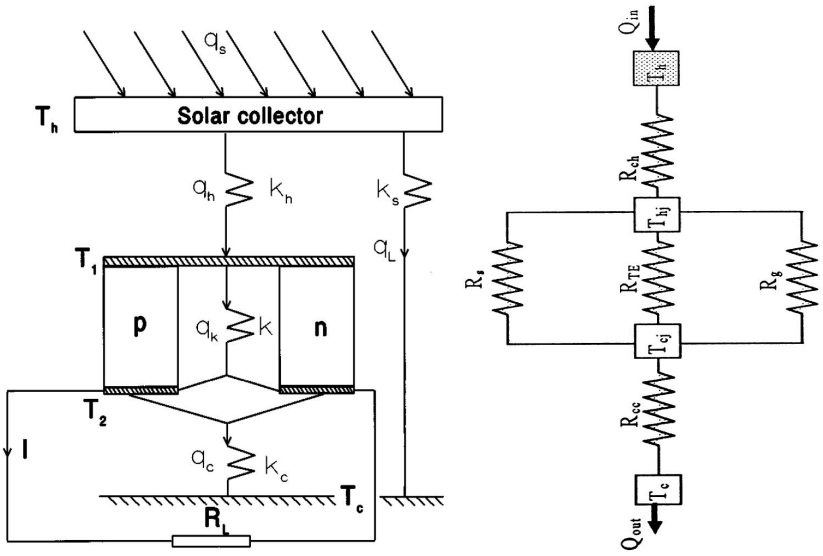

Figure 3. 3: Analytical model of solar TEG [CHE 1996][OME 1998]

Chen [CHE 1996] and Omer et al. [OME 1998] provided thermal model and system optimization to a solar TEG. However, both of their analyses are based on the steady performance (temperature boundary condition) of the TEG, as shown in Figure 3. 3. They are neither able to analyze the transient performance of the thermoelectric device when the applied thermal loading is changing nor able to analyze those cases with complicated thermal connections on the cold side of the thermoelectric device. In an actual situation, the variation of T_h and T_c need to be addressed. In our analysis, the

thermal boundary conditions comes from the intensity of ambient load instead of the achieved temperature difference on the TEG or total heat flux that goes into the TEG. The development of prototype solar energy harvesting system in typical applications can be categorized into two types. These ones with flat solar collector include [MAN 2004][MAN 2005][SHA 2007] [LER 2008] and more studies are interested about concentrating structure [OME 2000][KHA 2006][SOD 2007][AMA 2010][LI 2010][MGB 2010].

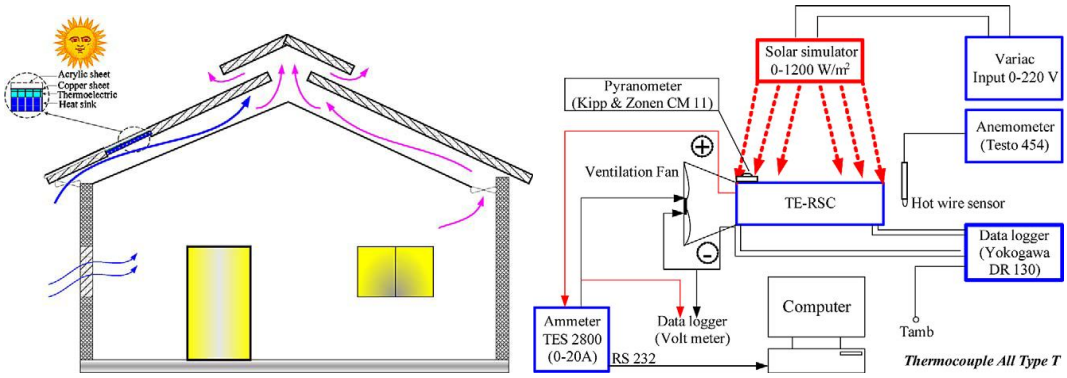

Figure 3. 4: Solar TEG as indoor ventilation [MAN 2004]

Maneewan et al. [MAN 2004] proposed to use thermoelectric roof solar collector to achieve roof heat gain reduction and indoor ventilation of spaces. The proposed system and experiment diagram are shown in Figure 3. 4. With 10 pieces of commercial thermoelectric cooling modules TEC1-12708 (0.0525m^2 surface area in total), their new roof design can generate about 1.2W under solar radiation intensity of about 800 Wm^{-2} at ambient temperature varying between 30 and 35°C. The corresponding air velocity generated by the ventilation fan was about 1.7 m/s. The energy conversion efficiency reaches 4.24% when the input radiation is 1000 Wm^{-2}. They extended their study [MAN 2005] and achieved higher energy conversion efficiency at 9% with the same thermoelectric material. The annual electrical energy saving was about 362kWh according to their analysis. Finally, economical calculations indicated that the payback period of their system is 4.36 years and the internal rate of return is 22.05%.

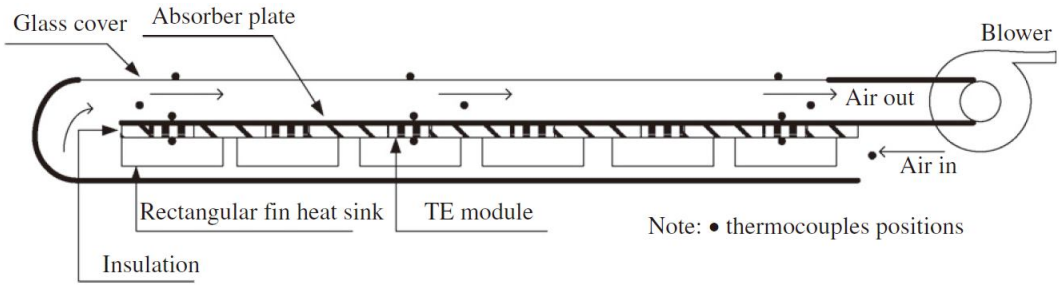

Figure 3. 5: Diagram of double-pass thermoelectric solar air collector [LER 2008]

Lertsatitthanakorn et al. [LER 2008] reported a double-pass thermoelectric solar air

collector which is shown in Figure 3. 5. They use an extra fan to provide airflow across the surface of the TEG which they believe that it will increase the temperature difference. Their prototype system achieved a power output of 2.13W and energy conversion efficiency of 6.17% with a temperature different of 22.8°C.

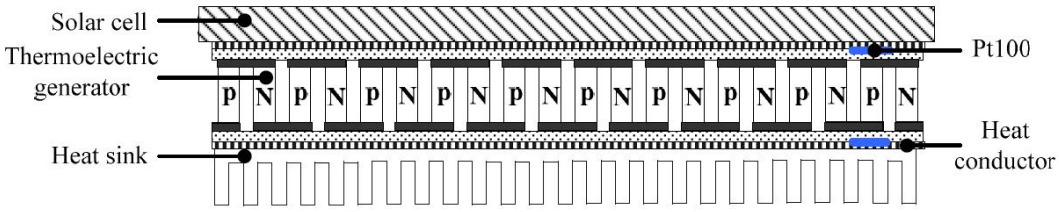

Figure 3. 6: PV and TEG hybrid system [SHA 2007]

Shang et al. [SHA 2007] introduced a micro hybrid system which combines the TEG with photovoltaic silicon solar cell, as shown in Figure 3. 6. It was found that when the surface area of the TEG was 150mm×60mm, it could generate 0.24V output voltage and 4.18mA short circuit at ambient temperature varying between 5~10°C at winter. It also could generate 1.3V output voltage and 16mA short circuit at ambient temperature varying between 30~36°C at summer.

In order to achieve much higher power generation with thermoelectric devices, the solar concentration technique is widely inspected.

Omer et al. [OME 2000] designed a special two stage solar concentrator for combined heat and thermoelectric power generation. The concentrator is comprised of a primary one axis parabolic trough concentrator and a second stage compound parabolic concentrator mounted at the focus of the primary. The thermoelectric device is attached to the absorber plate at the focus of the secondary. A cooling tube is fitted to the cold side of the thermoelectric device to extract the waste heat and maintain a high temperature difference across the device to improve conversion efficiency.

Khattab et al. [KHA 2006] inspected possibility of using a solar TEG (TEG) to drive a small thermoelectric cooler (TEC) is studied in the present work. The study includes the theory of both the TEG and the TEC, giving special consideration to determination of the number of TEG modules required to power the TEC to achieve the best performance of the TEG–TEC system all year round. Both mathematical model simulation and experimental test are included in their study. It concluded that 5 thermocouples of the TEG can drive one thermocouple of the TEC and 10 of the used TEG modules are required to power the used TEC at optimum performance most times of the year.

Sodano et al. [SOD 2007] recharges batteries using the solar concentration technique as shown in Figure 3. 7. The prototype system can generate a maximum power of 43mW when the hot side temperature reaches 200°C.

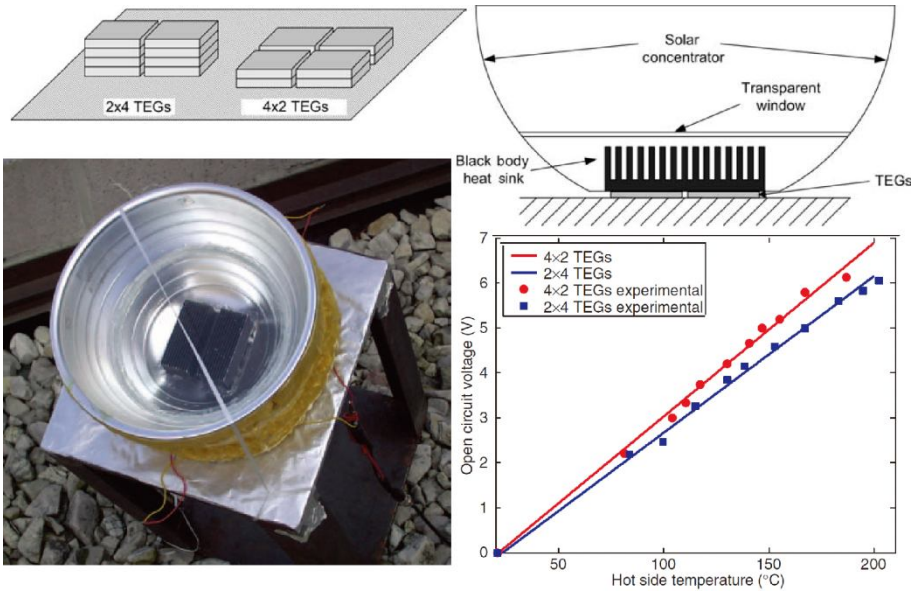

Figure 3. 7: TEG with solar concentrating [SOD 2007]

These prototype system in [MGB 2010][AMA 2010]and[LI 2010] are similar with [SOD 2007] except the cooling method on the cold face of the TEG as shown in Figure 3. 8. [MGB 2010] use airflow as the cooling method and an energy conversion efficiency of 3% is achieved experimentally with a Melcor thermoelectric module HT 6-12-40 and a cost estimated at about $35/Wp. [AMA 2010] use natural convection as the cooling method and a very high concentrating fold. It generated 1.8W with a commercial Bi_2Te_3 module with solar concentration of 66 fold and the efficiency reaches 3%. It also predicted that with novel thermoelectric material a conversion efficiency of 5.6% can be achieved with solar concentration of 120 fold.

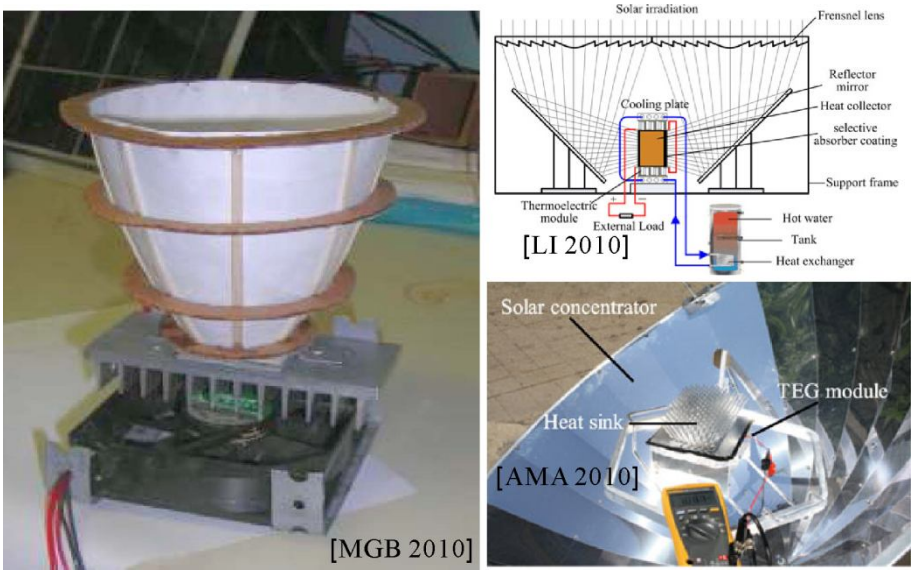

Figure 3. 8: TEG with different cooling methods

Li et al. [LI 2010] provide a relative comprehensive study on the TEG with different material (Bi_2Te_3, Skutterudite and LAST alloys), solar concentrating fold (11~337 times) and different intensity of heat dissipation on the cold side (40 ~ ∞ $Wm^{-2}°C^{-1}$). The summary of the performance of different case is shown in Table 3. 1.

Table 3. 1: Performance of the TEG based on the different thermoelectric materials, concentrating ratio (C_{gmax}) and convection coefficient (h_c) with different cooling methods [LI 2010]

Material	h (W/m^2 K)	C_{gmax}	P_{out} (W)	I(A)	η (%)	T_h (K)	T_c (K)	$T_h - T_c$ (K)
Bi_2Te_3	40	11	0.08	0.09	0.9	517.9	477.3	40.6
	100	22	0.35	0.21	2.1	524.8	441.9	82.9
	1000	51	2.40	0.59	6.2	524.3	329.5	194.8
	∞	60	3.38	0.72	9.8	525.6	298	227.6
Skutterudite	40	30	0.16	0.21	1.0	800.3	762.6	37.7
	100	65	0.85	0.48	2.4	802.7	715.7	87
	1000	242	13.69	2.03	9.9	799.3	444.6	354.7
	∞	337	26.11	2.88	13.5	800.5	298	502.5
LAST alloys	40	28	0.36	0.12	2.5	801.0	721.6	79.4
	100	55	1.52	0.27	5.0	795.8	639.8	156
	1000	150	11.28	0.87	13.3	801.3	385.8	415.5
	∞	189	17.54	1.12	16.3	800.7	298	502.7

3.2.2 Wind energy harvesting

The wind energy harvesting system with relatively small dimension can utilize piezoelectric effect and electromagnetic effect. According to the coupling structure between the wind and target movement, they can be categorized into four types: the direct cantilever, the micro windmill (indirect cantilever), the windbelt and the Helmholtz resonator.

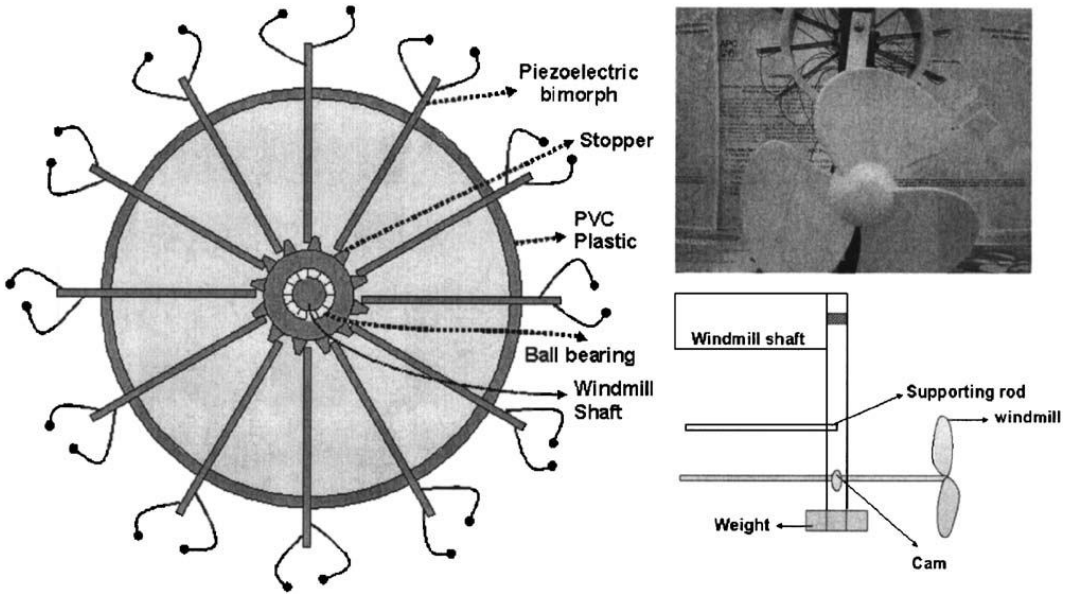

Figure 3. 9: Piezoelectric micro windmill [PRI2 2005]

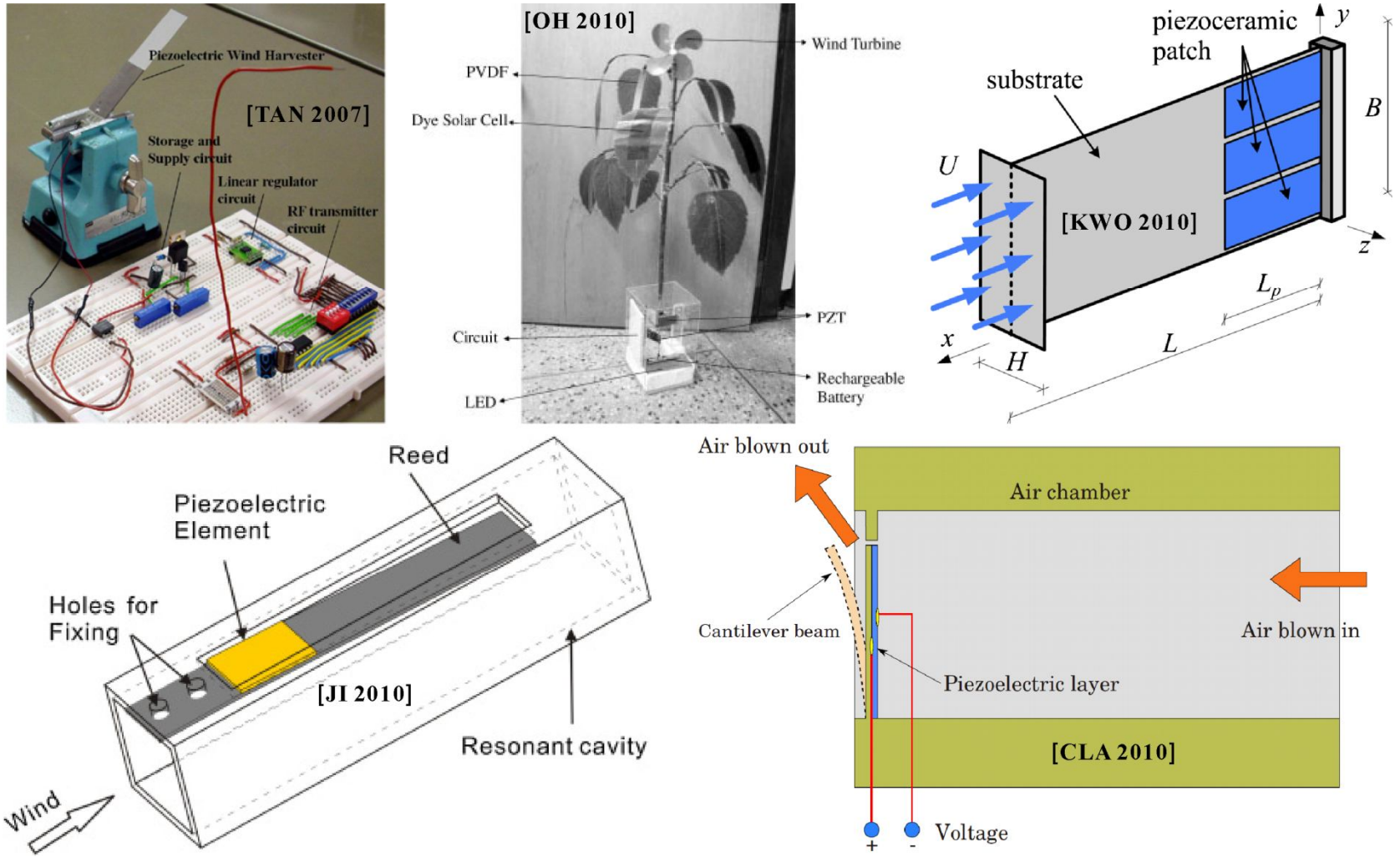

Figure 3. 10: Cantilever based piezoelectric energy harvesting prototype

The micro windmill structure proposed to harvest wind energy is introduced early by Priya et al. [PRI 2005], as shown in Figure 3. 9. Like common wind turbine, the wind power is changed into the kinetic energy of a rotational structure. The difference is that the turning movement is not converted by electromagnetic effect afterward. It is used to strike a cantilever and is converted by piezoelectric effect ultimately. A working prototype was fabricated utilizing 12 bimorphs ($60\times20\times0.5mm^3$) having a preload of 23.5 gm. Under a nominal torque level corresponding to normal wind flow and oscillating frequency of 6 Hz, a power of 10.2mW was successfully measured across a load of 4.6kΩ after rectification. A big drawback of this structure is the abrasion at the contact of the cantilever and rotational stopper as named in Figure 3. 9.

The direct coupling of wind and cantilever based PIEG is reported by [TAN 2007][OH 2010][KWO 2010][JI 2010][CLA 2010] which are shown in Figure 3. 10. The study in [TAN 2007] found the output power is very sensitive with the contact angle between the surface of the cantilever and the direction of incoming wind. The contact angle with three rotational degrees of freedom is inspected and it concluded that a zero contact angle which causes minimum contact surface at the initial place is favorable. The structure proposed by [OH 2010] is more suitable for low wind speed as it used PVDF material and fabricated a leaf structure. Kwon [KWO 2010] introduced a T-shaped cantilever. The working principle of the device is, according the author, based on aeroelastic flutter and utilizes a bimorph cantilever which hastens occurrence of flutter at a low fluid speed. Their prototype device ($100\times60\times30mm^3$) was tested in a wind tunnel. The device was found to provide power from a wind speed of $4ms^{-1}$ and a continuous peak electrical power output of 4mW. The proposal from [JI 2010] and [CLA 2010] are similar in structure. Instead of place the cantilever in an open field wind flow, they suggested to let the incoming wind pass through a cavity (or chamber) before it get in touch with cantilever. The dimensions of the wind inlet in [JI 2010] were approximately $30\times20mm^2$. The device was investigated with a wind speed ranging from 2.8 to 10 ms^{-1}. An output power of 0.5–4.5mW was obtained with a matching load of 0.46MΩ. The energy conversion efficiency of the device could reach up to 2.4%. The study from [CLA 2010] focused more on the principle of this structure. It proved that this self-excited oscillation is a nonlinear phenomenon that mimics the dynamics of the widely celebrated *Van der Pol* oscillator.

The windbelt structure consists of a tensioned belt (or airfoil) coupled to an electromagnetic transducer, and a power conditioning unit, as shown in Figure 3. 11(c) [HUM 2008]. When the wind passes through the belt, the aeroelastic flutter effect will induce a vibration in the airfoil according to [PIM 2010]. Flutter is a self-sustained oscillatory instability. For an airfoil that has both, flexural and torsional degrees of freedom, flutter occurs when there is a change in phase between the components. In the simplest case, there is one critical flutter speed, where the airfoil oscillates with steady amplitude. For wind speeds above the critical value, the airfoil flutters. When the wind speed is below the critical value, present oscillations will be dampened [FUN 2008]. Figure 3. 11(a) shows the flexural and torsional components of an airfoil supported at both ends. The power generation for a belt with dimension of 12×0.7cm is shown in subfigure (d). It can reach 5mW with an incoming wind at $7.5ms^{-1}$ and the minimum

wind speed available is $3ms^{-1}$ from the developer [HUM 2008].

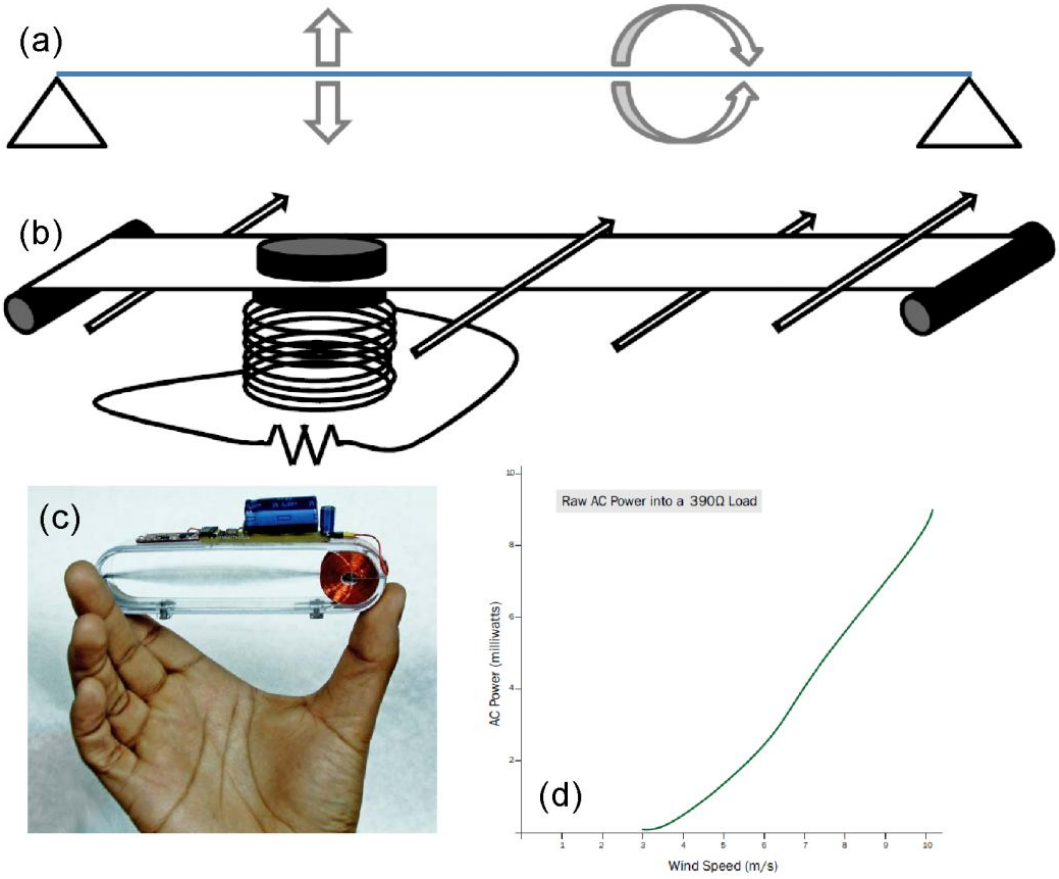

Figure 3. 11: Windbelt technique: (a) flexion and torsion of the belt (b) coupling diagram of wind flutter generator (c) prototype system (d) power generation [HUM 2008]

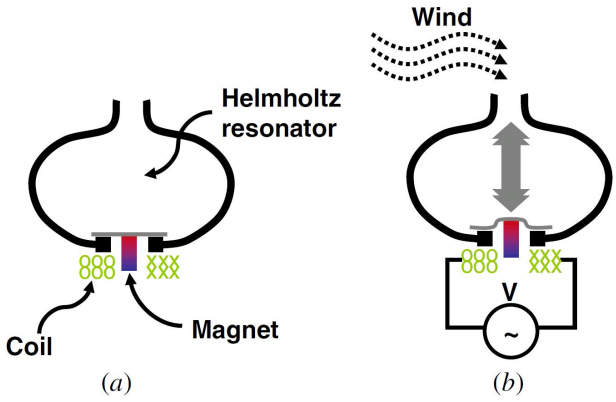

Figure 3. 12: Schematics showing the operation principle of the Helmholtz resonator based energy harvester: (a) at rest and (b) at resonance by external airflow. [KIM 2009]

Another kind of wind generator based on electromagnetic effect is report by [KIM

2009], as shown in Figure 3. 12. This energy harvesting device utilizes Helmholtz resonator as its wind energy pre-concentrator. A Helmholtz resonator is simply a gas-filled chamber with an open neck, in which a standard second-order (i.e. spring and mass) fluidic oscillation occurs. The air inside the neck acts as the mass and the air inside the chamber acts as the spring. In response to airflow across the opening, a single-frequency, large-amplitude acoustic wave develops. The prototype generator achieved a peak-to-peak output voltage of 4 mV at 1.4 kHz, from an input pressure of 0.2 kPa, which is equivalent to 5 ms^{-1} (10 mph) of wind velocity.

3.2.3 On harvesting other ambient energy

The potential energy source in environment is not limited to solar radiation and wind power. Lawrence [LAW 2002] suggested exploiting the natural temperature difference between the air and the soil to generate electrical energy with thermoelectric effect. It predicted that a power generation as much as 0.35mW is available. Maixner et al. [MAI 2009] give a more detailed study on the optimal location for the soil-end thermal reservoir of the TEG.

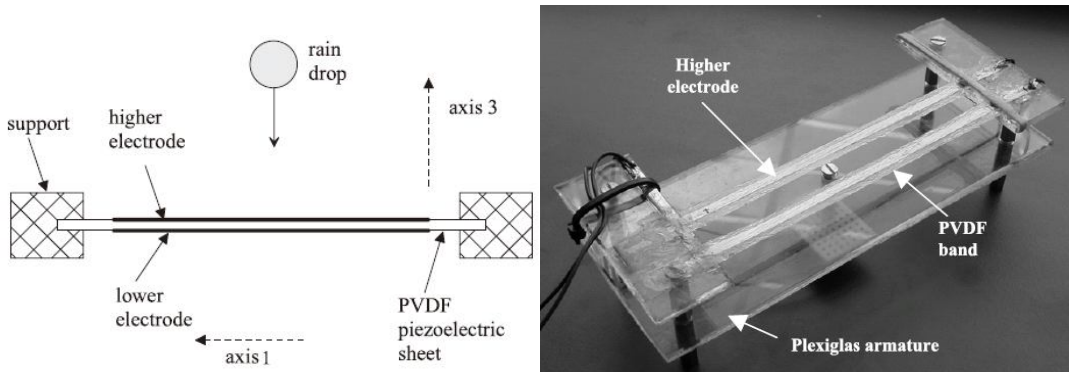

Figure 3. 13: Energy harvesting system with raindrop [GUI 2008]

An amazing work is introduced by [GUI 2008] which aims to harvesting raindrop energy with piezoelectric material, as shown in Figure 3. 13. The measurements conducted in various impact situations (different drop heights and drop sizes) show that the quantity of electrical energy that can be recovered using their structure is close to theoretical quantities [GUI2 2008], i.e. approximately 1 nJ of electrical energy and 1 μW of instantaneous power using raindrops. This is the worst case scenario, as simulations show that it would be possible to recover 25 μJ and 12 mW from a downpour drop.

3.3 Sectional summary

In this section, we give a brief description of the potential energy source around buildings. Special attention is devoted to those renewable energy sources in environment which can be utilized around buildings. The intensity of solar radiation, variation of ambient temperature and wind power are analyzed in long time scale. A basic model for the solar radiation is given, helping to understand the potential of thermal energy at different place annually. The characteristics of all the effective energy sources in environment and the potential of their corresponding power generation are analyzed by [VUL 2009] as shown in Table 3. 2.

Table 3. 2: Characteristics of various energy sources available [VUL 2009]

Source	Source power	Harvested power
Ambient light		
Indoor	0.1 mW/cm^2	10 μW/cm^2
Outdoor	100 mW/cm^2	10 mW/cm^2
Vibration/motion		
Human	0.5 m @ 1 Hz 1 m/s^2 @ 50 Hz	4 μW/cm^2
Industrial	1 m @ 5 Hz 10 m/s^2 @ 1 kHz	100 μW/cm^2
Thermal energy		
Human	20 mW/cm^2	30 μW/cm^2
Industrial	100 mW/cm^2	1–10 mW/cm^2
RF		
Cell phone	0.3 μW/cm^2	0.1 μW/cm^2

The current technique in harvesting solar thermal energy with thermoelectric effect and wind energy with piezoelectric or electromagnetic effect is reviewed. They provide important information on the possibilities of developing a real self-powered wireless sensor node around buildings. According to the scope of this study, we would like to give a more detailed analysis on the possibilities of utilizing thermoelectric, pyroelectric and piezoelectric effect to harvesting ambient thermal and mechanical energy. The focus of this study is to clarify the coupling process from the ambient loading to the output of the active material.

4. Solar energy harvesting through thermoelectric effect

4.1 Design of the thermoelectric energy harvesting system

4.1.1 Strategy for ambient thermal energy harvesting

The kernel problem for thermoelectric energy harvesting in environment is to find a suitable thermal structure which provides a promising temperature difference on the TEG (TEG) with ambient thermal load. Different from previous researches [CHE 1996] who provides with constant temperature as the thermal boundary condition to the TEG, it is heat flux or heat flow in our case. The common studies care about the steady thermal status of the TEG system. Therefore, they can use thermal resistance model to analyze the temperature difference available on the TEG. Suppose a TEG is placed in space and receiving constant heat flow αQ_{rad}, the thermal resistance model can be illustrated as Figure 4. 1.

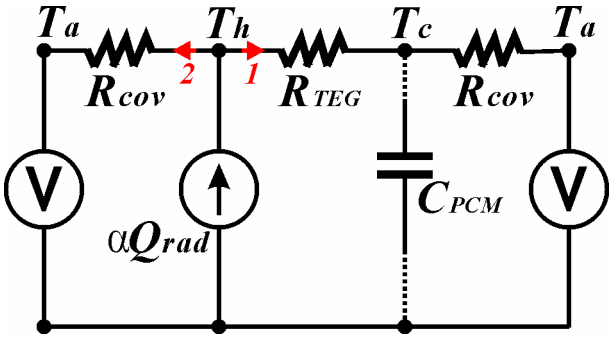

Figure 4. 1: Basic thermal model of TEG with input heat flow

R_{TEG} is the thermal resistance of the TEG, R_{cov} is the thermal resistance induced by convection, T_a is the ambient temperature. The thermal radiation from the TEG to the environment is neglected in this model for simplicity. There are two paths for the αQ_{rad} to release to the environment, as highlighted by the path 1 and path 2 in Figure 4. 1. The heat flow in path 1 passes through the TEG which is valid with energy harvesting. The heat flow in path 2 is lost directly to the environment. The shortcoming of this system is obvious that more than half of the αQ_{rad} is lost since the thermal resistance in path 1 is always larger than that in path 2. Besides, this system can only work when there is heat flow.

A new method is proposed to decrease the heat loss and keep the system to work continuously when the αQ_{rad} is stopped. Suppose a large thermal inertia component C_{PCM} is connected with the cold face of the TEG and maintains T_c at a constant value, as shown by dashed line in Figure 4. 1. Then the proportion of heat flow in two paths will change. The governing equation at this time is shown below:

$$\alpha Q_{rad} = \frac{T_h - T_a}{R_{cov}} + \frac{T_h - T_c}{R_{TEG}} \quad (4.\ 1)$$

T_c can be chosen similar to T_a. Then the proportion of heat flow in the tow paths depend on the proportion of thermal resistance of the TEG and the convection. Generally, R_{TEG} is much smaller than R_{cov}. Therefore, most of the input heat will pass through path 1 and can be utilized. Besides, if T_a decreases when the Q_{rad} is stopped, the heat flow in path 1 can be reversed and the TEG can go on with energy harvesting. According to the analysis above, a structure of solar thermal energy harvesting system is designed as shown in
Figure 4. 2 [AGB 2010].

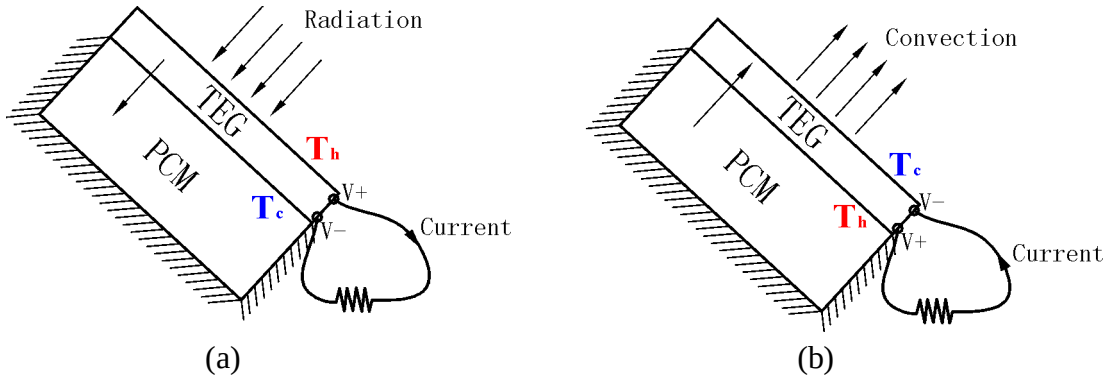

Figure 4. 2: Sketch map of the energy harvesting idea: (a) solar radiation on the TEG element during the day and (b) PCM work as the heat source at night.

A Phase Change Material (PCM) is used as the thermal inertia component. The PCM is a substance with a high heat of fusion which, melting and solidifying at a certain temperature, is capable of storing and releasing large amounts of energy. Heat is absorbed or released when the material changes from solid to liquid and vice versa; thus, PCMs are classified as latent heat storage units.
The PCM is placed at the back of the TEG where it is not irradiated by the sun. Then, the PCM is placed in an insulating material in order to apply no heat exchange with the external environment except through the contact face with the TEG. So, when the hot face of the TEG is loaded by solar radiation (Figure 4. 2(a)), the heat flow passes through the thickness of the TEG and is conducted to the PCM which, initially, is in a solid state. As the absorbed heat in the PCM increases, the temperature rises until it reaches its melting point. If we choose a PCM with sufficient latent heat, a suitable fusion temperature and sufficient volume, the temperature on the cold face of the TEG remains relatively stable over the whole day, as the PCM's temperature does not change enormously when it becomes liquid. We consider that the PCM changes completely into a liquid state after an entire day's heat. At night, the hot face of the TEG loses its high temperature thermal load and becomes the cold face (Figure 4.

2(b)). Meanwhile, the cold face of the TEG during the day, connected to the PCM, still maintains the temperature at around the melting point of the PCM. It can be higher than the temperature on the face that is connected to the external environment during the night. At this time, therefore, the PCM works as the heat source and the heat flows from PCM to TEG. Again, the TEG can harvest energy during this period. We could also choose appropriate PCM parameters to let it freeze completely during the night. We would expect this system to work non-stop, day and night. If we connect a resistor directly to the TEG, the output current could be reversed at the change between day and night.

4.1.2 Thermoelectric device

It is important to determine a right thermoelectric material and suitable structure of device when the objective is to harvest solar thermal energy. Thanks to the previous study [GOL 1980] which explained the rationale for using thermocouples made from Bi_2Te_3 alloys as solar thermal generators. This material is suitable for applications with relatively low temperatures (from 0°C to 100°C). This temperature range is suitable for an ordinary flat solar collector instead of a specially designed optical concentration system. It fits our need in this study.

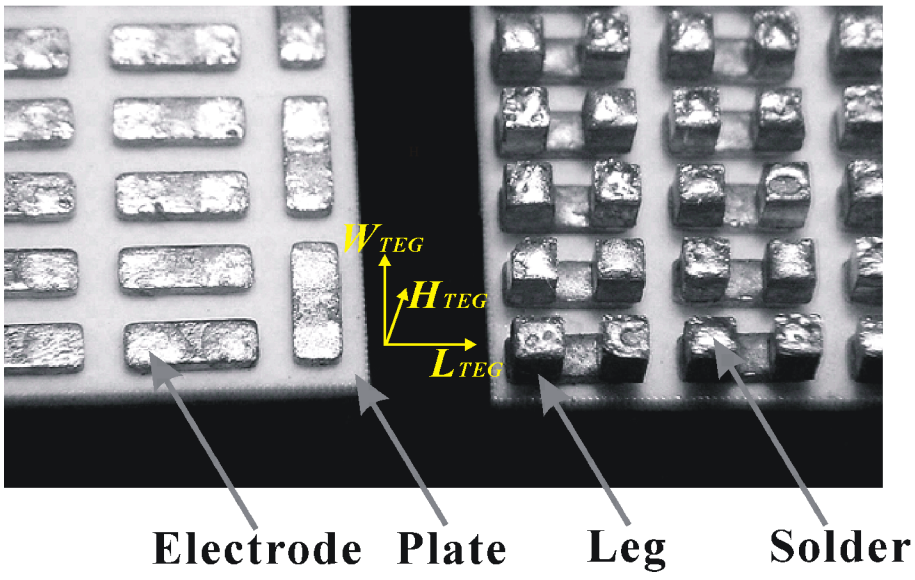

Figure 4. 3: The internal structure of the TEG (TEC-12708).

A commercial thermoelectric cooler (TEC-12708) using Bi_2Te_3 alloys is chosen as the TEG in the energy harvesting system. The internal structure of such a device is shown in Figure 4. 3. It has four basic parts. The ceramic plates have low electrical conductance but high thermal conductance. They work as matrix of the entire device and provide with rigidity of mechanical structure. The thermoelectric legs are planted on the plates as a square array (16×16) and are connected in series by electrodes. In this

way, the total output voltage is amplified. In order to maintain a good electrical and thermal contact between legs and electrodes, they are soldered together. The typical material properties and geometric dimensions of this device are listed in Table 4. 1

Table 4. 1: Properties of internal structure of typical thermoelectric device

Properties	***P**late* (Al_2O_3)	***E**lectrode* (Cu)	***S**older* (Sn)	***L**eg* (Bi_2Te_3)
K_{TEG_X} ($Wm^{-1}°C^{-1}$)	46	398	62	3
C_{TEG_X} ($JKg^{-1}°C^{-1}$)	753	385	234	16
ρ_{TEG_X} (kgm^{-3})	3960	8940	5765	7730
L_{TEG_X} (mm)	40	2.85	1.35	1.35
W_{TEG_X} (mm)	40	1.35	1.35	1.35
H_{TEG_X} (mm)	0.5+0.5	0.325+0.325	0.1+0.1	1.35

K_{TEG_X}, C_{TEG_X} and ρ_{TEG_X} denote the thermal conductivity, specific heat and density of sub-sections in the TEG respectively. The suffix X stands for each sub-section and it could be *P*, *E*, *S* and *L*. L_{TEG_X}, W_{TEG_X} and H_{TEG_X} denote the length, width and thickness of sub-sections in the TEG respectively.

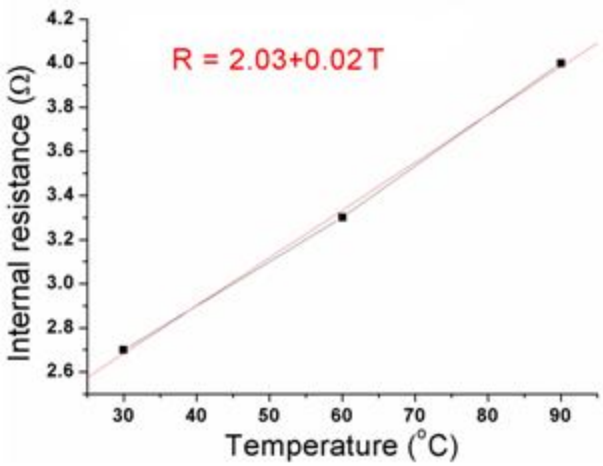

Figure 4. 4: Temperature dependence of internal resistance of the TEG

The performance of such a thermoelectric device is determined by its electrical resistance (r_{TEG}), thermal resistance (R_{TEG}) and Seebeck coefficient (α_s). In micro point of view, r_{TEG} is determined by four parts – the electrode, solder, leg and their contact condition. It is considered in this study that the first three parts are bonded tightly and their contact condition won't change during our study. Then r_{TEG} is mainly determined by the thermoelectric material which associates with temperature.

In order to give the electrical performance of such a device on macro point of view, r_{TEG} is measured by multimeter at different temperature provided by a thermostatic bath and the result is shown in Figure 4. 4. In the temperature range which is favorable in our research, r_{TEG} is almost direct proportional to the temperature and a

linear fit is used to achieve this relationship as highlight by red color in Figure 4. 4. It equals to 2.5Ω at room temperature 20℃. The deduced temperature dependent $\boldsymbol{r_{TEG}}$ will be used in the simulation part of this section.

$\boldsymbol{R_{TEG}}$ is calculated according to the internal structure of the TEG and their thermal connection. It is supposed that there is only thermal conduction exists in the thickness direction of the TEG. The thermal conduction in the direction parallel to the surface of the TEG is neglected since it is always considered to be irradiated with uniform solar radiation. Besides, the internal gaps among legs are occupied by air which is good at thermal insulation. Both thermal conduction and convection effect in that space are also neglected. Then the estimation of the $\boldsymbol{R_{TEG}}$ is realized according to the thermal resistance of each layer connected in series. The total thermal resistance is considered simply the sum of them:

$$R_{TEG} = \frac{2\times H_{TEG\_P}}{K_{TEG\_P}\times W_{TEG\_P}\times L_{TEG\_P}} + \frac{2\times H_{TEG\_E}}{K_{TEG\_E}\times W_{TEG\_E}\times L_{TEG\_E}\times 127} + \frac{2\times H_{TEG\_S}}{K_{TEG\_S}\times W_{TEG\_S}\times L_{TEG\_S}\times 254} + \frac{H_{TEG\_L}}{K_{TEG\_L}\times W_{TEG\_L}\times L_{TEG\_L}\times 254} \quad (4.\ 2)$$

The calculated $\boldsymbol{R_{TEG}}$ equals to 1 °CW^{-1}.

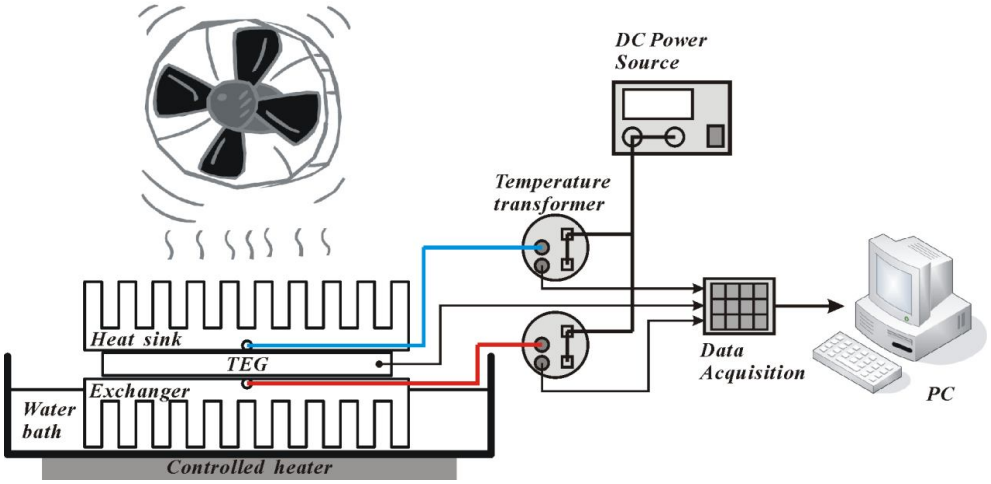

Figure 4. 5: Measurement system for Seebeck coefficient

The Seebeck coefficient of our prototype TEG is measured with a system shown in Figure 4. 5. The TEG is sandwiched between two heat exchangers by thermal grease. The exchanger on the lower face of the TEG can be warm up by a water bath which is heated by a controlled heater. The exchanger on the top face of the TEG is connected with a fan and they work as heat sink during the test. Two temperature sensors (PT100) are embedded separately into the heat exchanger, feeding back the temperature difference generated on the TEG. The temperature information from PT100 is converted by a temperature transformer (SBWZ). It can transform a temperature

variation from 0°C to 100°C into an output voltage from 2V to 4V. A data acquisition system (NI PCI-6024E with Labview8.0 software) is used to record both the temperature and the output voltages from the TEG. Since the input impedance of the data acquisition system is 100GΩ in parallel with 100pF. This is equivalent to an open circuit condition on to the TEG.

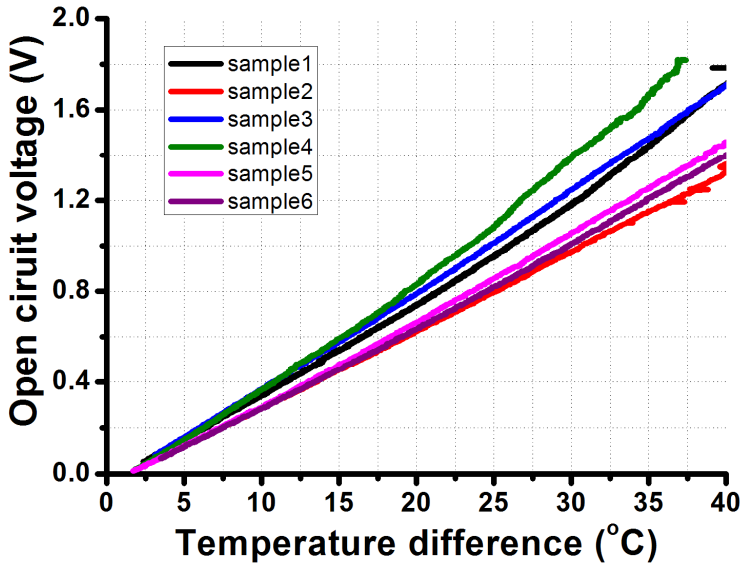

Figure 4. 6: Measured performance of TEC-12708

When the temperature of the water bath is set to 90°C, the temperature on the hot face of the TEG starts to increase. The fan is also turned on at this time, maintaining a relatively low temperature. The generated voltage as a function of applied temperature difference is illustrated in Figure 4. 6. It is noteworthy that the temperature dependence of the Seebeck coefficient is not considered in our test. A total of 6 pieces of TEGs of the same type are measured and it shows that the output voltage is linearly dependent on the input temperature difference when the maximum temperature difference is below 40°C. The temperature on the hot face of the TEG varied from 20°C to 85°C during the test. By extrapolation, it can be calculated that the equivalent Seebeck coefficient of TEC1-12708 module is 40mV°C^{-1}. The dimensionless figure of merit for the TEG with the interested temperature range is achieved:

$$\begin{cases} ZT_{avg} = \dfrac{R_{TEG}\alpha_s^2}{r_{TEG}} \times \dfrac{(T_h + T_c)}{2} = \dfrac{1 \times 0.04^2}{2.5} \times (273.16 + 50) = 0.21 \\ T_h = 273.16 + 100 \ , \ T_c = 273.16 + 0 \end{cases} \quad (4.\ 3)$$

4.1.3 Phase change material

There are two kind of PCMs inspected in this study. The candidate of organic PCM is a mix of a copolymer and a paraffin wax which comes from DuPont Company while the inorganic PCM is a salt hydrates provided by Rubitherm Technologies Company. Their basic characteristics are listed in Table 4. 2 and illustrated in Figure 4. 7:

Table 4. 2: Basic characteristics of PCM candidates

Characteristics	paraffin wax	salt hydrates
Density (Kgm^{-3})	856	1530~1710
Thermal conductivity ($Wm^{-1}°C^{-1}$)	0.14~0.18	0.54~1.1
Specific heat ($JKg^{-1}°C^{-1}$)	3000	1600
Melting point (°C)	21.7	26
Latent heat ($10^{6}Jm^{-3}$)	40	320

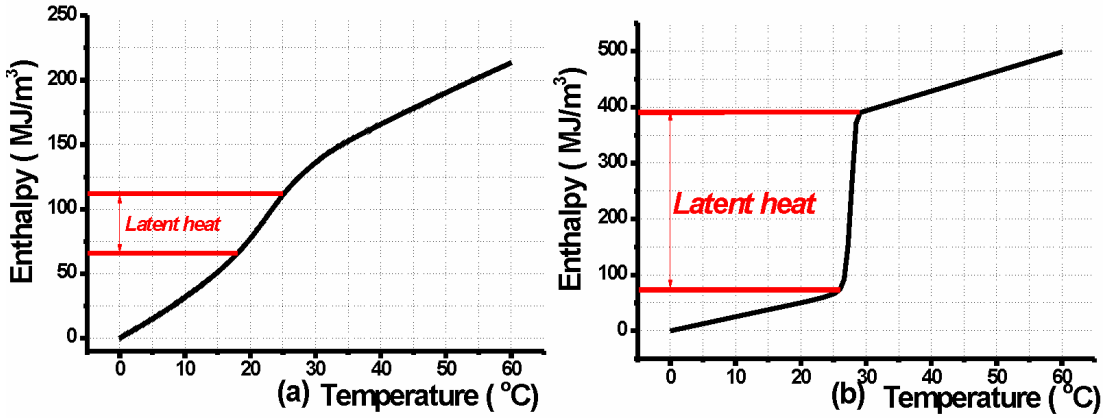

Figure 4. 7: Enthalpy of PCM as a function of temperature:
(a) paraffin wax (b) salt hydrates

4.2 Experimental study

4.2.1 Fabrication of the prototype TEG system

In order to prove the proposed idea of harvesting energy and show the possibility of such a system in typical wireless application, an experimental prototype work units, as shown in Figure 4. 8, are fabricated and analyzed in our study [ZHA2 2010]. The work unit is made of 1 piece of TEC-12708 and salt hydrate PCM. The fabrication processes is illustrated below:

1. The PCM is heated up until it changes into liquid and it is filled in a container.
2. A heat exchanger is inserted into the PCM and a small gap is left between them, avoiding leakage of the PCM when it is expanded with at high temperature. There are 35 fingers in total of the heat exchanger, as shown in Figure 4. 8(a), each measuring 3.3mm × 2.5mm × 45mm. The connecting part of this heat exchanger is 3 mm thick. A tiny temperature sensor head (Pt 100 from TC direct company) is embedded into the PCM during this process, monitoring internal temperature.
3. The thermoelectric module TEC-12708 is put on the heat exchanger with thermal grease and the irradiated surface is painted black, enhancing the heat absorption rate during the day.
4. Polystyrene insulating material was shaped to enclose the PCM container. To complete the PCM insulation, the air gap between the PCM container and the insulating material was filled with polystyrene foam, as shown in Figure 4. 8(b).

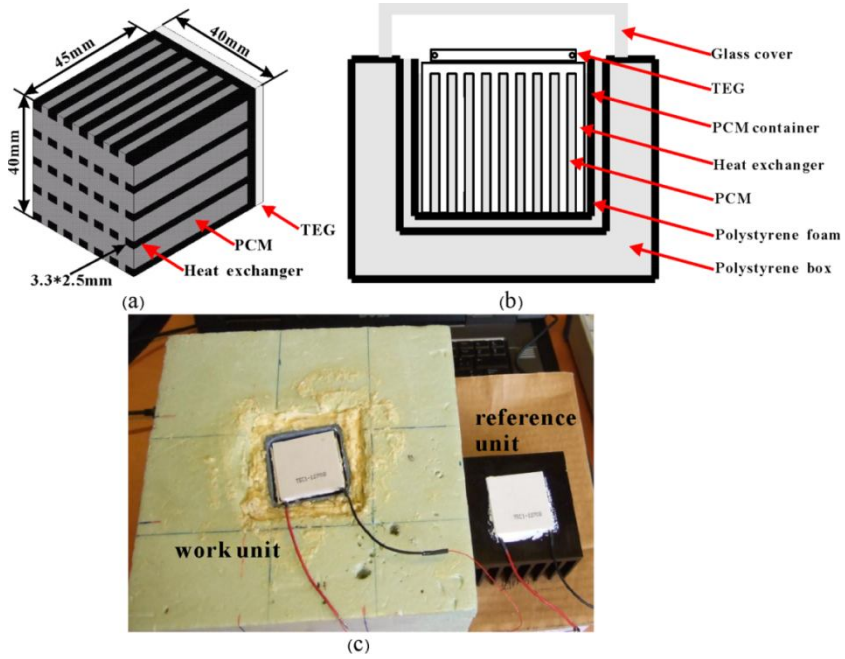

Figure 4. 8: Prototype work unit: (a) thermal connection between the TEG and the PCM (b) assembled sectional view (c) photo of work unit with reference unit

4.2.2 In lab test and results

To illustrate the feasibility of the proposed concept over a fixed period and also in laboratory conditions (independent of the high variability in actual solar radiation), we used the work unit with a self-developed system which simulates solar radiation with an electric spotlight, ambient temperature with a refrigerator and wind with a mini-fan, as shown in Figure 4. 9.

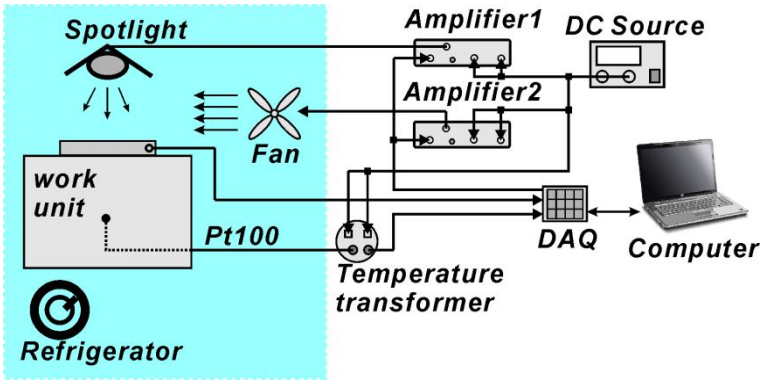

Figure 4. 9: Diagram of solar energy harvesting system in lab

We used an automatically-controlled spotlight (20W, 12V) in the laboratory; it can provide the TEG with a maximum radiation intensity of approximately 3000Wm^{-2}. A direct current (DC) power source and two pieces of MOSFET IRF740 form the power amplifier for the spotlight and the fan. A data acquisition system (NI USB-6259 BNC with Labview2009) was used to generate control signals for the spotlight and fan and record the generated voltage from the TEG at the same time. Real solar radiation is a complicated physical process that we approximated in two steps:

1. First we calibrate the equivalent intensity of radiation from the spotlight with a pyranometer (CM4 from Kipp & Zonen company). It shows in Figure 4. 10 that the equivalent intensity of radiation is a function of input power of spotlight in second order at a fixed distance between the objective and spotlight.

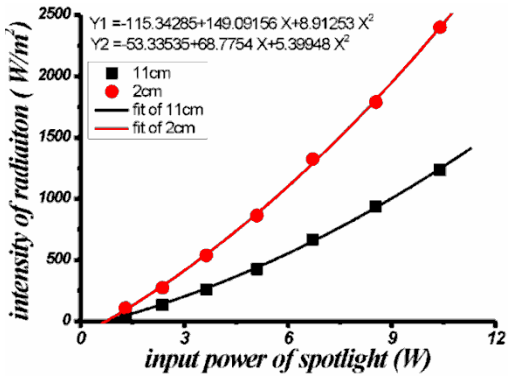

Figure 4. 10: Calibration results of radiation from the spotlight

2. Then we used a MOSFET switch to adjust the intensity of radiation and applied a pulse width modulation strategy to manage the device. The input power is proportional to the duty cycle of the square-wave control signal. The transformation from the duty cycle to the equivalent radiation on the TEG is square root. A duty cycle which varies as a square root of gauss function can generate the solar radiation required.

When the spotlight was in operation, it is place in front of the TEG at 2 cm. The frequency of the control signal was 50Hz and the refresh rate was 1MHz. The value of the gauss function was normalized at between 0 and 2700 Wm^{-2}. The maximum intensity of the simulated solar radiation can be adjusted manually with the voltage regulator on the DC power source. The fan was placed on the side of the TEG as shown in Figure 4. 9. The input power of 1.32W provided a wind speed of $5ms^{-1}$ on the surface of the TEG. It was switched controlled and driven by MOSFET also.

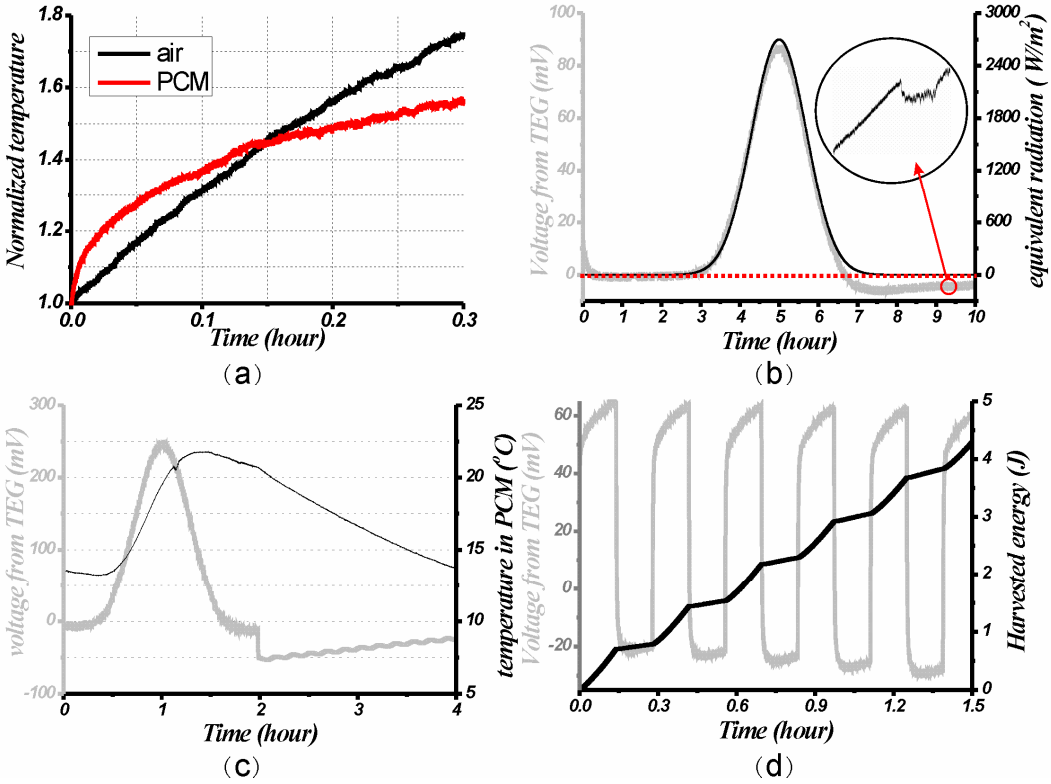

Figure 4. 11: Results of in lab test: (a) comparison of temperature stability (b) performance of the work unit with variable radiation (c) performance of the work unit with enhanced convection (d) maximum performance of the work unit in lab.

As a comparison, we prepared also a reference TEG which is one pieces of thermoelectric module TEC-12708 connected with a heat sink, as shown in Figure 4. 8(c). The experiment in lab is implemented in four groups:

1. The temperature stability on the shaded surface of the TEG plays an important part during the energy harvesting process. A more stable temperature will let more heat go through the TEG which is favorable as explained in Figure 4. 1. When a constant radiation is applied on the TEG, the heat exchanger on the shaded side is placed in the air at first. The temperature variation on the shaded surface of the TEG is recorded as shown with the black curve in Figure 4. 11(a). It kept on increasing over time. When the heat exchanger is placed in the PCM (hydrate salt), the temperature profile changed into the red curve in Figure 4. 11(a). It tended to a constant value. After 0.15 hour one can see that the relative temperature variation of the TEG with PCM is smaller. After 0.3 hour of heating, the temperature in the TEG without PCM is higher. These results show that the PCM improves temperature stability on the contact face between the TEG and the heat exchanger. This stability could be further increased by improving the design and fabrication of the heat exchanger as well as by choosing PCM with better latent heat characteristics.

2. In order to check the performance of the work unit with variable solar radiation, the spotlight provides with a representative radiation as shown by the black curve in Figure 4. 11(b). It is generated from gauss function and the total time for experiment is 10 hours. The fan is turned off and the work unit is taken out from the refrigerator in this test. It provides the work unit with natural convection at room temperature 20°C. The corresponding voltage generated from the TEG is shown in gray curve in Figure 4. 11(b). The PCM operated as a heat source after storing energy during the day and the voltage changed from a positive to a negative value after the radiation decreased to a relatively low value. The turning point was at 6.7 hours when the radiation still maintained a certain low value. It is obvious that the shape of the generated voltage is similar with the input radiation during the day. This properties is like those pyranometer made by thermopile. The latent heat began to release at 9.2 hours when the generated voltage became stable, as highlighted on the right side of Figure 4. 11(b). Besides, the total harvested energy by positive voltage is more than 100 times higher than that by negative voltage. It is reasonable since the natural convection is too weak and the ambient temperature is too high when the radiation fades away.

3. In order to check the influence of forced convection induced by wind and ambient temperature. Another artificial solar radiation is applied to the work unit within two hours. The major difference from the second test is that when the radiation is stopped, the fan is turned on. Besides, the ambient temperature is maintained by the refrigerator at 10°C. The recorded performance is shown in Figure 4. 11(c). The harvested energy by negative voltage is 10%. This proves that a strong wind induced forced convection and lower ambient temperature is favorable for our system during the night. The record of temperature variation in the PCM is also shown in Figure 4. 11(c) and it indicates that only sensible heat is utilized in this experiment. Therefore, the

generated negative voltage kept on decrease when the radiation is stopped which is different from the previous test.

4. In order to check the maximum performance of the work unit in lab, constant radiation and forced convection were applied as the thermal loads on the TEG. The two loads were applied alternately: when the radiation was on, the fan was off, and vice versa. The intensity of the input radiation is 1500Wm^{-2}. The wind speed is set as maximum available value 5ms^{-1}. A duty cycle of 1000 seconds was chosen for the energy harvesting process. The generated voltage and the harvested energy are shown in Figure 4. 11(d). The average power generation in this experiment was 0.8mW. The contribution from PCM as a heat source increased to 20% in each cycle. It should be noted that the mean value of voltage generation continued to decrease, indicating that the convection was still not strong enough and the temperature in the PCM keeps on increasing.

The experimental study in lab for work unit proves the feasibility of the proposed idea. It also shows the priority of our system compared with common TEG system with heat sink. Since the ambient thermal load is essential to the performance, we tested the TEG system outside.

4.2.3 Test outside and results

The work unit and the reference unit were placed outside and the record of generated voltages began at 11:16 on the 1st of November and ended 08:06 on the 2nd of November in Aix-les-Bains, France. There was sunshine for the first three hours, and a glass was used to cover the upper face of the work unit to reduce the convective effect of the wind. When the solar radiation ceased, the glass was taken off. The increased convection improves the performance of the work unit when PCM acts as the heat source. The referenced unit was exposed to environment during the whole test. The optimized 2.5Ω external resistor was connected to both of the two energy harvesting systems and the voltages obtained are shown in Figure 4. 12(a).

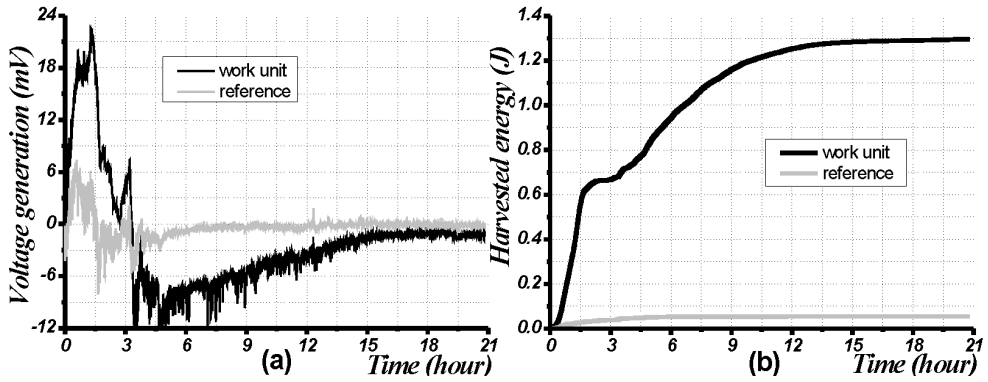

Figure 4. 12: Comparison of performance in actual situation between work unit and reference unit: (a) voltage generation (b) total harvested energy.

Analysis of this figure led to three comments:

1. Convection is also an important factor in the performance of TEG when the solar radiation works as heat source. The work unit with reduced forced convection presented better voltage generation during the day. Since the work unit is not optimized in this study, it is not expect a large divergence of voltage generation between the two energy harvesting systems during the day. However a large divergence exists in the measured performance. It could come from the different setup of convection condition in this test.

2. The energy harvesting period of the work unit is 4 times longer. The harvested energy is 1.3J over 21 hours, which represents an average power of 17μW, as shown in Figure 4. 12(b). Energy harvested at night by the PCM work unit forms half of the total energy. The absolute power generation in this real situation (in late autumn) is small compared to the maximum value achieved in the laboratory. This is in accordance with the ambient thermal load since the radiation in late autumn is weak in local place.

3. Voltage generation was very sensitive to both solar radiation and wind speed (Figure 4. 12(a)). The significant reduction of positive voltage in work unit which started at hour 1.5 was due to the cloud which reduced the radiation, and the tiny vibration of negative voltages was due to variations in wind speed. Variations in voltage generation can be used by smart control strategies in some processes.

The experimental study in outside situation give us a brief idea of the real working process of TEG with PCM system. Although it proves that the proposed work unit is a better solution than common TEG structure when harvesting ambient thermal energy, the total measured performance is still poor which is depressing. However, there are many reasons for the poor performance outside at this time:

1. The commercial thermoelectric module we use is low in dimensionless figure of merit which is 0.2.

2. The fabrication is not perfect and the latent heat provided with the PCM is not sufficient.

3. The solar radiation is low during the autumn in local place.

There is still chance to prove that our proposed idea of harvesting solar thermal energy is promising with carefully design and better choice of material. Instead of waiting to construct again such a work unit with TEG of high ZT ($0.7< ZT <1.1$) which is commercially unavailable to us, we propose to use modeling method to analyze the possible performance of the proposed TEG system.

4.3 Modeling of the prototype system

4.3.1 Electrical analogy method

The temperature difference ($\Delta T=T_h-T_c$) on the TEG determines the instantaneous output power and the transient variation of ΔT gives the total harvested energy. The kernel problem for harvesting energy with such a system is to obtain ΔT as a function of time when applied with ambient thermal load. It can be realized by two steps. The first step is to give an appropriate thermal description of the TEG since its internal structure is complicated compared with the PCM and there is coupling effect which needs to be considered. The second step is to develop an entire thermal model which predicts ΔT with arbitrary thermal load.

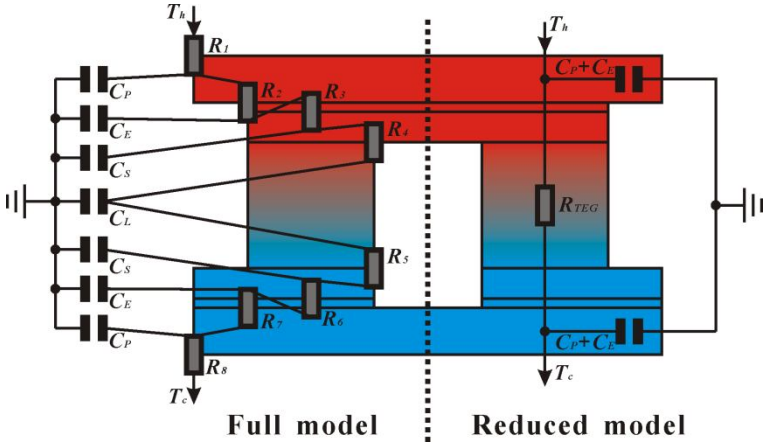

Figure 4. 13: Corresponding relationship between internal sections of the TEG and their electric model. Characters in subscript indicate the corresponding internal sections as shown in Table 4. 1 and the value of each parameter are calculated in appendix A.

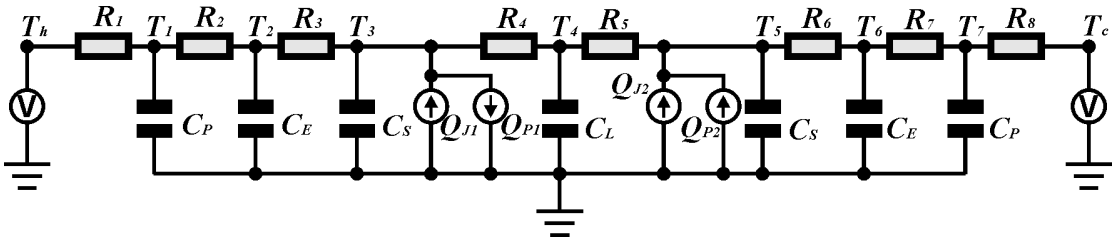

Figure 4. 14: Full electric model of the TEG

In view of the arrangement of internal sections, it is possible to consider the heat transfer in the TEG as a problem with one dimension. Each internal section is represented by a thermal resistance and a thermal capacitance as shown in Figure 4.

13 (left side). The complete equivalent electric model of the TEG is shown in Figure 4. 14. It is reference from [FRA 2010]. The temperature and heat correspond to the voltage and current in the electric model. The Peltier effect is taken into account by heat absorption $\boldsymbol{Q_{P1}}$ from the hot side and heat release $\boldsymbol{Q_{P2}}$ to the cold side of the legs. The generated Joule heat $\boldsymbol{Q_J}$ in total is associated with the external load. It is divided into two parts equally ($\boldsymbol{Q_{J1}} = \boldsymbol{Q_{J2}} = \boldsymbol{Q_J}/2$) and released to both sides of the legs.
According to the energy conservation (or Kirchhoff's current law) the governing equation system below describes the thermal response of the TEG.

$$\begin{cases} (T_1) & \dfrac{T_h - T_1}{R_1} = C_P \dfrac{dT_1}{dt} + \dfrac{T_1 - T_2}{R_2} \\ (T_2) & \dfrac{T_1 - T_2}{R_2} = C_E \dfrac{dT_2}{dt} + \dfrac{T_2 - T_3}{R_3} \\ (T_3) & \dfrac{T_2 - T_3}{R_3} + Q_{J1} = C_S \dfrac{dT_3}{dt} + \dfrac{T_3 - T_4}{R_4} + Q_{P1} \\ (T_4) & \dfrac{T_3 - T_4}{R_4} = C_L \dfrac{dT_4}{dt} + \dfrac{T_4 - T_5}{R_5} \\ (T_5) & \dfrac{T_4 - T_5}{R_5} + Q_{J2} + Q_{P2} = C_S \dfrac{dT_5}{dt} + \dfrac{T_5 - T_6}{R_6} \\ (T_6) & \dfrac{T_5 - T_6}{R_6} = C_E \dfrac{dT_6}{dt} + \dfrac{T_6 - T_7}{R_7} \\ (T_7) & \dfrac{T_6 - T_7}{R_7} = C_P \dfrac{dT_7}{dt} + \dfrac{T_7 - T_c}{R_8} \end{cases} \tag{4. 4}$$

In this equation system, $\boldsymbol{T_1}$~$\boldsymbol{T_7}$ represent the average temperature in each internal section, $\boldsymbol{r_{ext}}$ is an external resistor. $\boldsymbol{R_{TEG\_L}}$ and $\boldsymbol{R_{TEG\_S}}$ are the thermal resistance of leg and solder layer of the TEG. The coupling effect is described by the expressions below:

$$\begin{cases} Q_{J1} = Q_{J2} = 0.5\left[\dfrac{\alpha_s \times (T_3 - T_5) \times R_{TEG\_L}}{\left(R_{TEG\_L} + R_{TEG\_S}\right) \times (r_{TEG} + r_{ext})}\right]^2 \times r_{TEG} \\ Q_{P1} = \dfrac{\alpha_s^2 \times (T_3 - T_5) \times R_{TEG\_L} \times T_3}{\left(R_{TEG\_L} + R_{TEG\_S}\right) \times (r_{TEG} + r_{ext})} \\ Q_{P2} = \dfrac{\alpha_s^2 \times (T_3 - T_5) \times R_{TEG\_L} \times T_5}{\left(R_{TEG\_L} + R_{TEG\_S}\right) \times (r_{TEG} + r_{ext})} \end{cases} \tag{4. 5}$$

The full model of the TEG is mathematically complex and we suggest using a reduced model, as shown on the right side of Figure 4. 14, to understand the internal thermal structure of the TEG. In the reduced model, there are only one thermal resistance and

two thermal capacitances. It is more effective in computation when evaluate the transient performance for a long time. The thermal resistance is calculated in (4.2), while the major thermal capacitance comes from the ceramic plate and the electrodes.
The thermal boundary condition in the general model, as shown in Figure 4. 14, is temperature. It is different from the problem we want to analyze. The TEG is receiving solar radiation during the day and there is PCM connected with the TEG by heat exchanger. A lumped parameter model as shown in Figure 4. 15 is proposed to analyze the performance:

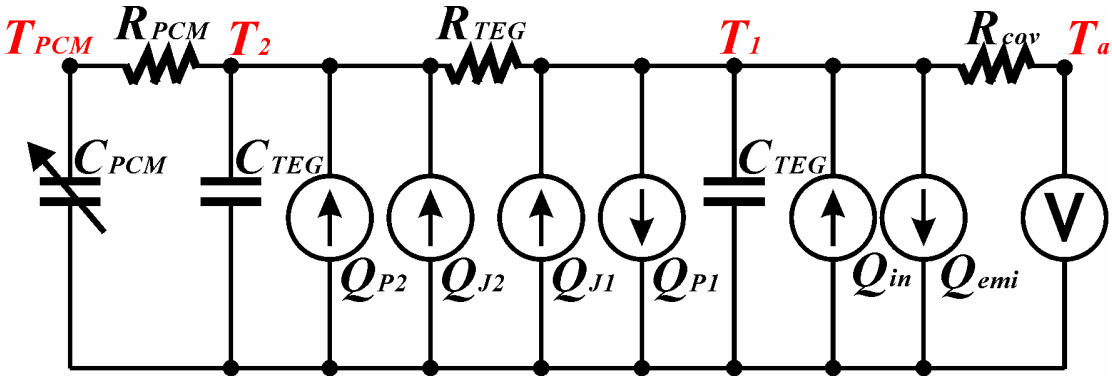

Figure 4. 15: Proposed lumped parameter model of TEG with PCM in environment

T_1, T_2 and T_{PCM} are the temperature on the two sides of the TEG and that in the PCM respectively. R_{PCM} is a fixed thermal resistance which represents the heat exchanger. $C_{TEG}=C_P+C_E$ is the thermal capacitance of the TEG on one side of its surface and C_{PCM} is a variable thermal capacitance which represents the PCM. The capacitance varies with temperature T_{PCM}. Q_{in} and Q_{emi} are the heat flow absorbed on the irradiated surface of the TEG and heat radiation from the surface of the TEG to the environment respectively. The governing equation system for this model is shown in (4.6). The three thermal equations are deduced from energy conservation on the irradiated and shaded side of the TEG and that in the phase change material. Q_{rad} is the intensity of solar radiation and it is considered that a fixed proportion of radiation is absorbed by the TEG as described by heat absorption rate α which is determined by the gray scale of the surface material of TEG. Likewise the emissivity ε determines the intensity of heat radiation loss. σ is the Stefan–Boltzmann constant (σ = 5.67e^{-8} Wm^{-2}K^{-4}). A_{TEG} is the surface area of the TEG. In order to estimate the intensity of convective heat exchange R_{cov}, the natural and forced convection coefficient h_c is calculated by different empirical criteria, as illustrated in Appendix B. The numerical simulation of this model will be addressed in detail in section 4.3.2.
It is noteworthy that the thermal equations in (4.6) are first order ordinary differential equations. They can be solved numerically. There are two points to note regarding the solution. First, the ground voltage in the electric model should correspond to the initial temperature in the environment. Second, each internal section also needs an initial temperature for calculation. It is equal to the initial ambient temperature with no special considerations.

$$
\begin{aligned}
&\text{Thermal} \quad \begin{cases} Q_{in} + Q_{J1} = C_{TEG}\dfrac{dT_1}{dt} + \dfrac{T_1 - T_a}{R_{cov}} + \dfrac{T_1 - T_2}{R_{TEG}} + Q_{emi} + Q_{P1} \\ \dfrac{T_1 - T_2}{R_{TEG}} + Q_{J2} + Q_{P2} = C_{TEG}\dfrac{dT_2}{dt} + \dfrac{T_2 - T_{PCM}}{R_{PCM}} \\ \dfrac{T_2 - T_{PCM}}{R_{PCM}} = C_{PCM}\dfrac{dT_{PCM}}{dt} \end{cases} \\
&\text{Coupling} \quad \begin{cases} Q_{J1} = Q_{J2} = \dfrac{1}{2} r_{ext}\left(\dfrac{\alpha_s (T_1 - T_2)}{(r_{ext} + r_{TEG})}\right)^2 \\ Q_{P1} = \alpha_s \dfrac{\alpha_s (T_1 - T_2)}{(r_{ext} + r_{TEG})} T_1 \\ Q_{P2} = \alpha_s \dfrac{\alpha_s (T_1 - T_2)}{(r_{ext} + r_{TEG})} T_2 \end{cases} \\
&\text{Loading} \quad \begin{cases} Q_{in} = \alpha A_{TEG} Q_{rad} \\ Q_{emi} = \varepsilon \sigma A_{TEG} (T_1^4 - T_a^4) \\ R_{cov} = 1 / \left(h_c A_{TEG}\right) \end{cases}
\end{aligned}
\tag{4. 6}
$$

4.3.2 Finite element method

The simplified electrical analogy model introduced above provides a method to evaluate the output performance of the TEG system. It is suitable for long time prediction especially since each component in the system is represented by highly concentrated thermal structure which reduced the complexity of computation. It also brings a question that is the precision of the evaluated performance. A potential challenge for electrical analogy model also lies in that a heat exchanger is always necessary between the TEG and the PCM since the proposed PCM candidates are not good at thermal conduction. The special geometry of the heat exchanger let the electrical analogy model in vain. Therefore Finite Element Method (FEM) is also proposed to give the transient performance of the system, improving the precision of the estimation and solving the thermal conduction problem with special geometries in the system. ANSYS software is used to realize the finite element modeling and analysis. The major problem addressed in the FEM modeling of a proposed system is that of transient analysis which applied to materials and properties depends on time and temperature. Six basic assumptions were made during the analysis in the FEM model:

1. The P type and N type thermoelectric legs of the TEG have the same material properties. Their Seebeck coefficient, electrical resistivity and thermal conductivity of are all associated with temperature.

2. The TEG is considered as an isotropic thermal bulk and its internal sub-structure is neglected. This treatment is special but reasonable since the internal structure of the TEG is periodical and the repeated sub-structure are large in quantity (16×16 square array). It is not necessary to let ANSYS give an independent estimation of each thermoelectric leg since all of them are identical with each other.
3. The PCM is always considered as a solid material in the numerical models. The internal heat is only transferred by conduction. The PCM is suitable for such treatment, since an ordinary ambient thermal load cannot produce a sufficiently high internal temperature or a temperature difference capable of providing strong convection in the liquid PCM.
4. The PCM and the heat exchanger have no heat exchange with the external environment except for the contact face of the TEG. To ensure this case in actual situation, insulating material was placed around the side and bottom surfaces of the work unit.
5. The TEG is loaded with equivalent heat on the contact face with environment. All the three kinds of ambient thermal load including - the intensity of solar radiation, ambient temperature and wind speed which induces forced convection will influence the heat exchange on this face. The thermal radiation from the TEG to the environment is neglected.
6. The heat absorption rate on the irradiated surface of the TEG is constant.

In a typical modeling process, the dimensions of the work unit are input to ANSYS according to the actual situation, and the temperature dependent material properties are defined as table information. It should be careful about the determination of the electrical resistivity $\boldsymbol{\rho_{TEG\_e}}$ of the TEG since it is modeled as a uniform bulk structure. It can be calculated below where $\boldsymbol{t_{TEG}}$ is the total thickness of the TEG.

$$\rho_{TEG\_e} = r_{TEG}\frac{A_{TEG}}{t_{TEG}} = r_{TEG}\frac{L_{TEG\_P}\times W_{TEG\_P}}{(2H_{TEG\_P}+2H_{TEG\_E}+2H_{TEG\_S}+H_{TEG\_L})} \qquad (4.\ 7)$$

There are two elements which are used in the FEM model. Both the PCM and the heat exchanger can be meshed with solid90 element while the TEG section should be meshed with solid226. The element solid90 has 20 nodes with temperature as the single degree of freedom at each node. It is applicable to a 3D, steady-state or transient thermal analysis. The element solid226 also possesses 20 nodes but with up to five degrees of freedom per node. The field key of this element is activated as 110, enabling a thermal-electric analysis. It guarantees that both temperature and voltage are chosen as degrees of freedom while the corresponding force labels are heat flow and electric current. When the TEG is meshed, there are many nodes on the two surfaces. The voltages of all the nodes located at the same surface are coupled. Then it is simple to connect an external resistive load to just one node on each surface of the TEG.

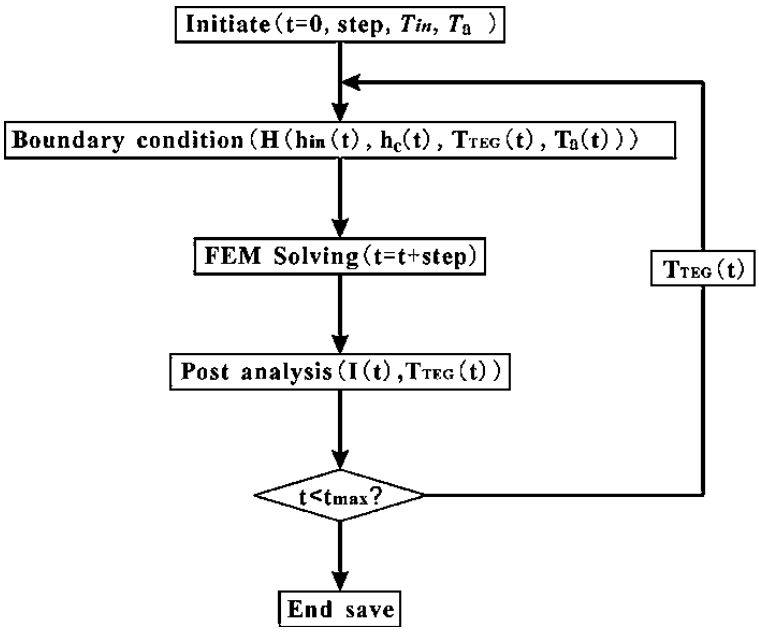

Figure 4. 16: Diagram for the calculation process implemented in the FEM model

For transient analysis with variable thermal load, a loop program as shown in Figure 4. 16 is developed and implemented. The state variables at each calculation step are updated in the program. The developed finite elements model is intended to give the voltage generated by the TEG module when it undergoes time varied thermal load. It begins with initialization of internal uniform temperature T_{in} and determination of time step which can refer to the updating rate of recorded ambient thermal load. Then the equivalent heat flux H applied on the TEG in this step is calculated according to the ambient thermal load h_{in}, h_c, T_a and the last calculated temperature on the irradiated surface of the TEG T_{TEG}. The combination of the ambient loading as an equivalent heat flux is expressed as:

$$H = h_{in} - h_c \times (T_{TEG} - T_a) \tag{4. 8}$$

Where h_{in} is the input heat flux from hot reservoir. The model is then solved by FEM with a short time and the generated current in the resistive load I is achieved by post analysis.

In order to achieve convergence during the computation, it is suggested to mesh the geometric model with hexahedral element and adjust the convergence value for the nonlinear analysis manually. It was found that the calculation is converged when both the heat and current flow in the simulation is set to 10^{-3}.

4.3.3 Simulation and results

As an example, our prototype work unit is analyzed by the FEM model at first for two days and by the electrical analogy model after for half a year. The geometries of the prototype system with its FEM model are shown in Figure 4. 17.

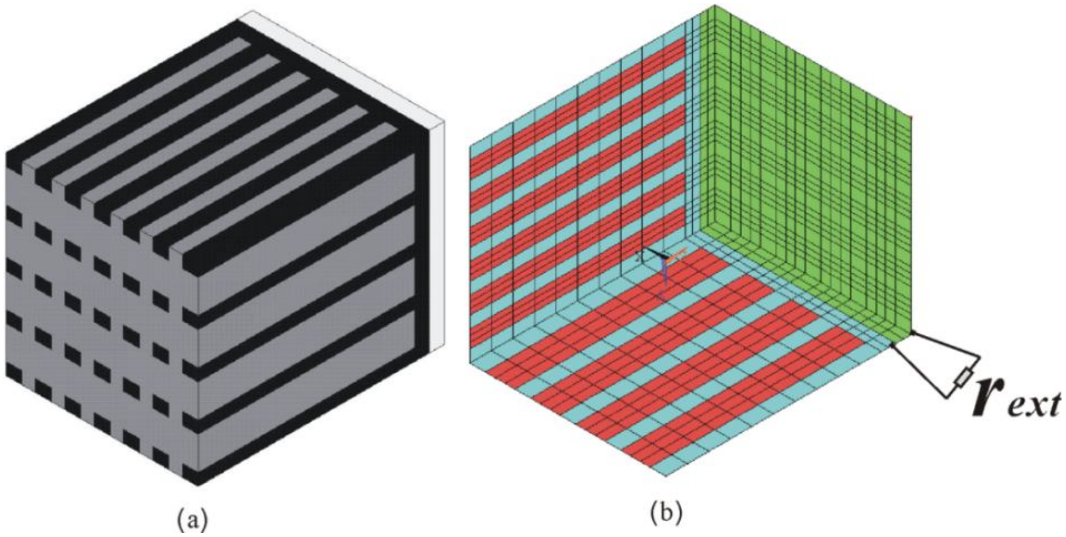

Figure 4. 17: Prototype work unit: (a) geometry (b) meshed model.

The meshed FEM model is shown in Figure 4. 17(b). There are a total of 5950 elements in the meshed model. A constant 2.5Ω external resistor r_{ext}, which equals to the internal resistor r_{TEG} at room temperature 20°C, is connected to the two faces of the TEG as shown in Figure 4. 17. It is an optimized choice of impedance matching which can achieve maximum output energy at this temperature. According to constitutive equations of thermoelectricity, the current generation is determined below:

$$I = \frac{\alpha_s(T) \times (T_h - T_c)}{r_{ext} + r_{TEG}(T)} = \frac{\alpha_s(T) \times \Delta T}{r_{ext} + r_{TEG}(T)} \qquad (4.\ 9)$$

It clarifies the variation in output performance which is brought by the temperature dependent material properties $\alpha_s(T)$ and $r_{TEG}(T)$. The total temperature difference across the thickness direction of the TEG ΔT is proportional to the current generation and it represents the Seebeck effect.

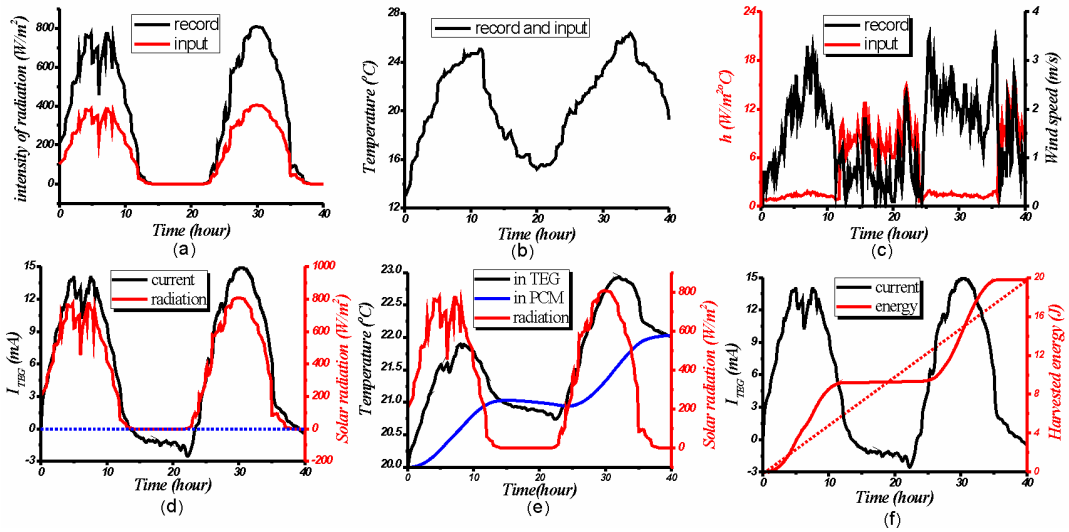

Figure 4. 18: Typical thermal load for FEM model and the predicted performance: (a) intensity of solar radiation and input heat flux (b) ambient temperature (c) wind speed and input convection coefficient (d) generated current in the resistive load (e) temperature variation in the PCM (f) Total Harvested energy as a function of time

Typical records for intensity of solar radiation, daily temperature variation and wind speed (from 6:00 am on 09/07/1998 to 10:00 pm on 11/07/1998), as provided by LOCIE Polytech Savoie, are shown in Figure 4. 18(a)-(c) with a black curve. The updating rate of record is 10 minutes. It is assumed that 50% of the radiation is used by the TEG (α=0.5) which is equal to the input heat flux as indicated by the red curve in Figure 4. 18(a). Besides, it is obvious that we need weak convection on the TEG during the day and strong convection at night. We assumed that some extra technique could reduce the strength of the forced convection by 10 times during the day (from 6:00 am to 6:00 pm each day) in which case the total calculated convection coefficient is achieved as shown by the red curve in Figure 4. 18(c). The daily ambient temperature variation (in spring and autumn) is described, generally and approximately, by the formula below (unit of time: second):

$$T_a(t) = 20 + 10 \times Sin(\frac{2\pi}{60 \times 60 \times 24} t) \quad ^\circ\mathrm{C} \qquad (4.\ 10)$$

The temperature fluctuates between 10°C and 30°C. The melting point of the selected PCM is in accordance with the average temperature, enabling the maximum utilization of latent heat. We can estimate the volume of PCM $\boldsymbol{V_{PCM}}$ that is sufficient for heat storage in daytime from Fourier's law:

$$V_{PCM} = \frac{K_{TEG} \times A_{TEG} \times dT \times \Delta t}{t_{TEG} \times \Delta E} = \frac{0.5 \times (40 \times 40) \times 10 \times (3600 \times 12)}{3.2 \times 10^{-3} \times (40 \times 10^{6})} = 2.7e^{-3} \qquad (4.\ 11)$$

where K_{TEG} is the equivalent thermal conductivity in the thickness direction of the TEG module. dT represents the average temperature difference on the TEG in daytime and we use the half-amplitude of input temperature load to substitute this value, so the calculated volume should be larger than the necessary volume. Δt represents the time of half a day and ΔE represents the latent heat per unit volume of the paraffin wax as mentioned in Table 4. 2. The volume of the PCM in our prototype work unit is $7.2e^{-5}$ m^3 which is 37 times smaller than the calculated necessary volume. The duration of an actual ambient thermal load in FEM simulation could thus be reduced by 30 times in order to compensate for this mismatch.

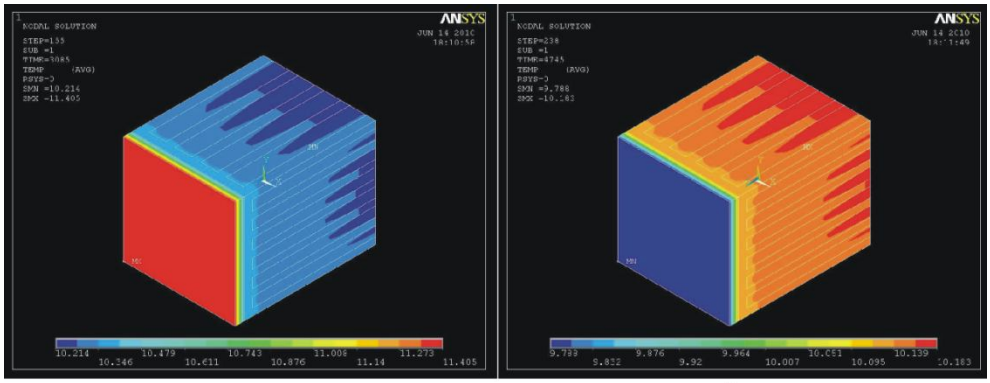

Figure 4. 19: Typical temperature distribution in work unit: (a) day time (b) night time

When all the preparation is completed, a uniform initial temperature is set to 20°C which indicates that the PCM is in good status. The simulation starts and the continuous ambient load of 40 hours is decreased to 5000 seconds in the program. Some important performance characteristics are predicted by the FEM modeling method as below:

1. The generated electric current in the external resistor is shown by black curve in Figure 4. 18(d). The daily current (from 0 to 12 hours) is positive and the night current (from 12 to 24 hours) is negative. It proves the idea of continuous energy harvesting as illustrated in Figure 4. 2
2. It is found that the current generated during the day is similar to the intensity of input solar radiation as shown in Figure 4. 18(d). This indicates a potential simple linear relationship between them. The night part contains a partial negative peak value which is in agreement with the maximum local convection coefficient. It proves that the conditions are favorable for energy harvesting at night.
3. A typical temperature distribution in the work unit is shown in Figure 4. 19. It proves that the heat exchanger can help the PCM to keep the major temperature difference on the TEG. The temperature in the PCM is quit uniform.
4. The temperature variation in the middle part of the TEG and the PCM are shown by black and blue curve in Figure 4. 18(e) respectively. The trend of increasing temperature in the PCM reveals an accumulation of heat internally. It indicates that insufficient heat is released from the PCM to the environment at night.

Further techniques, such as putting a heat sink on the surface of the TEG to enhance the forced convection, are needed to optimize system performance.

5. The maximum current passes through the external resistor reaches 15 mA during the day and the total harvested energy ***E(t)*** as a function of time is shown by red curve in Figure 4. 18(f). It is achieved simply by the formula below:

$$E(t) = \int_0^t I(t)^2 \times r_{ext} dt \tag{4. 12}$$

The total harvested energy during 40 hours reaches 19.1J which equals to an average output power around 133μW, as indicated by the slope of the red dashed line in Figure 4. 18(f). This power is generated from a maximum intensity of solar radiation of 800Wm-2 and a minimum ambient temperature of 13°C. It can be improved by the heat absorption rate α.

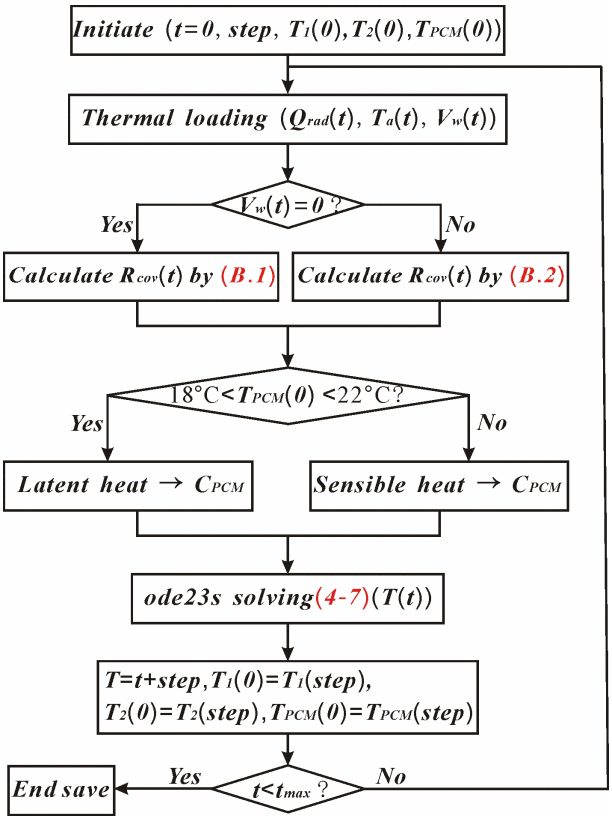

Figure 4. 20: Diagram for the calculation process implemented in the electrical analogy model

The evaluation of the proposed energy harvesting work unit by FEM model gives us a basic idea of the performance in short time. However, the computation is time consuming. The time for calculation of such two days performance of the work unit in

an ordinary computer takes more than two days. It is inconvenient to use this method to predict a long time performance or to analyze the internal parametric influence of each section in the work unit to the total output, such as the thermal resistance of the heat exchanger, melting point of the PCM, latent heat and sensible heat of the PCM and so on. Therefore the electric analogy model introduced in Figure 4. 15 was used to analyze the work unit. A numerical procedure in Matlab software was developed as and it goes following the strategy shown in Figure 4. 20.

It begins with initialization of all representative temperatures in the work unit. The time step for each computation can still refer to the updating rate of the ambient thermal load. The pattern of heat convection is then determined by wind speed and the convection coefficient is calculated according to appendix B. The thermal capacitance of PCM is also updated according to the current temperature in the PCM. The ordinary differential equation solver is then used to give an estimation of temperature variation in a short time.

The first simulation by the electrical analogy model is implemented with better thermoelectric devices and large time scale. Materials such as Bi_2Te_3 and Bi_2Se_3 comprise some of the best performing room temperature thermoelectric with a temperature-independent ZT between 0.8 and 1.0. It is 5 times of our prototype TEG. Therefore the thermal resistance of the TEG $\boldsymbol{R_{TEG}}$ is improved by 4 times in this simulation. Applied with a typical record of ambient thermal load shown in Figure 3. 1 from February 1st to August 1st, a temperature variation in the PCM and temperature difference on the TEG is achieved as illustrated in Figure 4. 21. The other parameters used in the second simulation are the same with the first simulation.

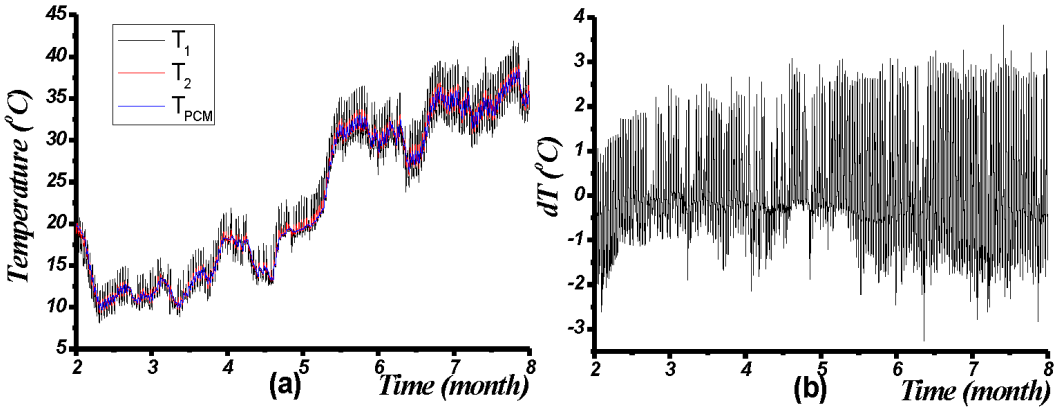

Figure 4. 21: Typical performance of the work unit in half a year: (a) temperature variation (b) temperature difference on the TEG

It is shown in Figure 4. 21 (a) that the temperature in the PCM changes following the trend of the ambient temperature in Figure 3. 1 in large time scale. However, there is no direct relationship between $\boldsymbol{T_{PCM}}$ and $\boldsymbol{\Delta T}$. The temperature difference is mainly dependent on the intensity of the solar radiation and the thermal resistance of the TEG. The total harvested energy in half a year with matched impedance is 3300J which

equals an average power of 0.2mW. The power density of this energy harvesting system is 0.34mW/cm^3 or 132mW/m^2. Keep in mind that the TEG in this system is with $\boldsymbol{ZT}$=1 and the heat absorption rate $\boldsymbol{\alpha}$=0.5.

In order to analyze the internal parametric influence of each section in the work unit to the total output performance, a representative 2 years solar radiation is generated based on expression (3.1). Different thermal resistance of heat exchanger and the melting point of the PCM are checked with the developed electrical analogy method. The output performance is described as average power density which is normalized. The results are shown in Figure 4. 22.

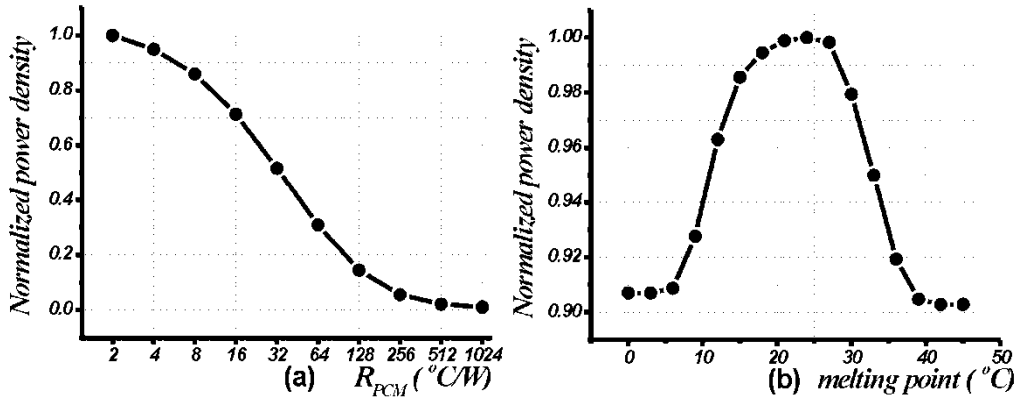

Figure 4. 22: Parametric influence predicted with electrical analogy method: (a) thermal resistance of the heat exchanger (b) melting point of the PCM

The updating rate of thermal load is 1 hour and the time of computation for 2 years simulation is less than 5 minutes. According to the numerical analysis, both the thermal resistance $\boldsymbol{R_{PCM}}$ and the melting point of the PCM can influence the performance of the energy harvester. The influence from $\boldsymbol{R_{PCM}}$ is essential as indicated in Figure 4. 22(a). When $\boldsymbol{R_{PCM}}$ is 10 times larger compared with current value 2 °CW^{-1}, the performance can lose by 50%. It indicates that the optimization design for heat exchanger between the TEG and the PCM is important in this energy harvesting system.

On the influence from the melting point of the PCM, there is an optimized value as revealed in Figure 4. 22(b). This is reasonable since the temperature in the PCM varies in long time scale actually. In order to utilize the latent heat instead of sensible heat in the PCM as much as possible, the melting point should be close to the annual average value of $\boldsymbol{T_{PCM}}$. When the melting point is less than 3°C or higher than 42°C the total performance changes stable since only the sensible heat of the PCM is utilized. The variation of the normalized power density in Figure 4. 22(b) is small in absolute value since the latent heat and sensible heat of the PCM used in the simulation is not very different.

4.4 Sectional summary

In this section, we introduced a new method to harvested ambient solar energy with TEG. Phase change material is proposed to work as a companion whom serves as the heat sink to the TEG and maintains a relatively stable temperature when the solar radiation provides thermal energy. This system is expected to keep on working during the night when PCM serves as the heat source and convection as the heat sink. The work cycle of such a system is one day when the generated voltage will pass through both positive and negative value.

Experimental prototype system is fabricated to prove the feasibility of our idea both in lab and outside. The test in lab shows that the generated voltage from the TEG is proportional to the intensity of solar radiation when there is no wind and the ambient temperature is stable. This characteristic is similar with pyranometer which indicate potential sensor application. The forced convection induced by natural wind and ambient temperature are both essential with the performance of the system especially during the night. It is also found that not only the latent heat but also the sensible heat in the PCM can be utilized by the TEG. The idea of continuous thermal energy harvesting is proved both in lab and outside. The major divergence lies in the typical power generation (0.8 mW in lab which is 47 times higher than that outside).

Besides, both finite element method and electrical analogy model are established to evaluate the system performance. The FEM is precise to estimate both the temperature variation and the generated current when the TEG is connected with external resistance. The electrical model as is highly concentrated with thermal substitutions of each internal section is able to analyze the influence of each internal parameters and give a prediction of long time performance with the proposed system. With better thermoelectric module and typical local ambient thermal loading in half a year, the predicted power generation is 0.2mW (or 340μWcm^{-3} or 132mWm^{-2}). It is promising for such kind of energy harvesting system in near future with carefully design.

5. Solar energy harvesting through pyroelectric effect

5.1 Design of the pyroelectric energy harvesting system

Different from TEG who needs to find a promising temperature difference in space, the PYEG is looking for a temperature difference in time – temperature variation more accurately since it is not reasonable to expect that the temperature in the PYEG increases or decreases to an infinite large value. Therefore, the great challenge for pyroelectric energy harvesting in environment lies in seeking for promising temperature variation or an alternating thermal loading in actual situation. Our proposal is that the solar radiation works with wind fluctuation in environment. It could be a potential solution of temperature variation, as illustrated in Figure 5. 1. The PYEG received solar radiation and its temperature keeps on increase until thermal balance reaches when the absorbed heat on the PYEG equals to the heat loss to the environment by radiation and convection. There are many balanced thermal status in PYEG according to the intensity of convection heat exchange. If there is no wind passes through the PYEG, as shown in subfigure (a), it follows the rule of natural convection which is relatively weak. The temperature on the PYEG can reach a relative high value in this case. When the wind comes, as shown in subfigure (b), the governing law of convection heat exchanges is different. The strong forced convection takes out heat from the PYEG very quickly and its temperature becomes relative low at this moment. Therefore, a wind fluctuation is able to yield a temperature variation in the PYEG only if there is solar radiation. With a right regulated circuit, the temperature variation can be further transformed to electrical power useful.

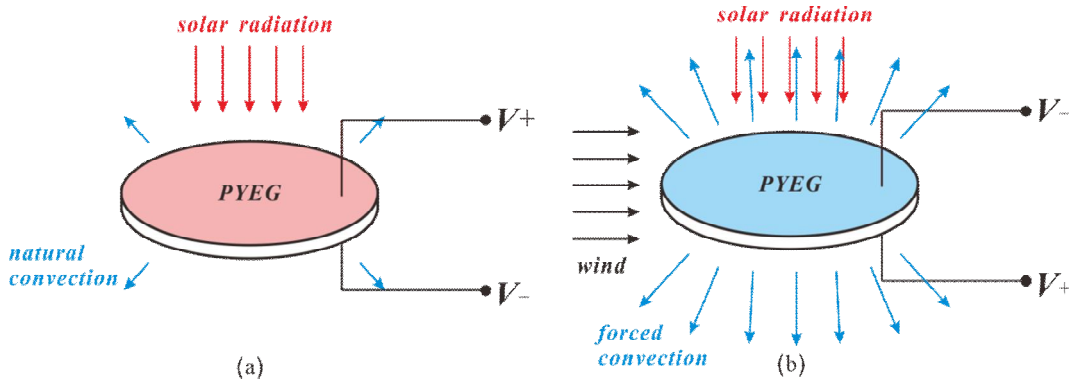

Figure 5. 1: Principle of solar energy harvesting with PYEG and wind: (a) temperature increases with weak natural convection (b) temperature decreases with strong forced convection

In order to inspect the feasibility of this idea, a common buzzer (KPSG100, Kingstate Electronics Corporation) is chosen as the PYEG. The PYEG is a disk structure with

radius of 12mm and thickness of 0.14mm. The pyroelectric material is PZT and its basic properties are listed in Table 5. 1. Since it is designed as a piezoelectric actuator, the pyroelectric property of this material is not optimized and unavailable from the manufacturer. We have to measure the pyroelectric coefficient of this element before further researches.

Table 5. 1: Basic properties of prototype PYEG

Properties	**Symbol**	**Value**
Thickness (mm)	t_{PYEG}	0.14
Area (mm^2)	A_{PYEG}	452
Electrical capacitance (nF)	c_{PYEG}	65
Electrical resistance (GΩ)	r_{PYEG}	80
Heat capacity ($JKg^{-1}°C^{-1}$)	C_{PYEG}	300
Thermal conductivity ($Wm^{-1}°C^{-1}$)	K_{PYEG}	1.1
Density (Kgm^{-3})	ρ_{PYEG}	7800

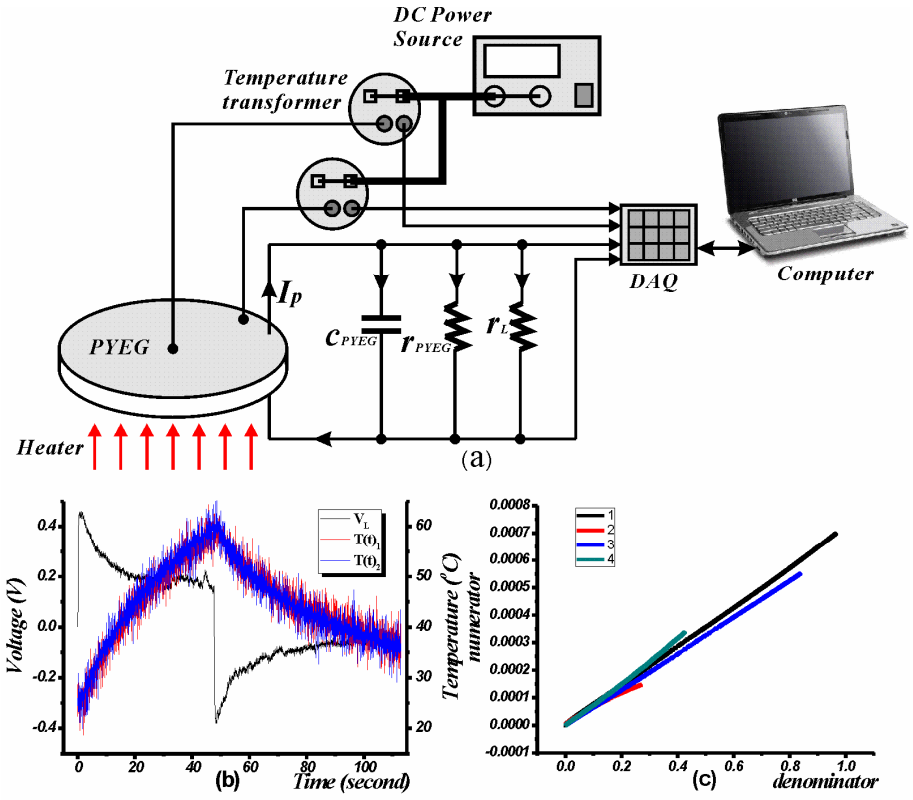

Figure 5. 2: (a) measurement system of pyroelectric coefficient (b) temperature variation and voltage generation of PYEG (c) manipulated data for calculation of ***p***

A measurement system as shown in Figure 5. 2(a) is adopted to test the pyroelectric coefficient. The PYEG is placed on the output glass cover of a spotlight. When heated uniformly the temperature variation in the material is recorded. Meanwhile, the PYEG is connected with an external resistor (r_L=1MΩ) and the generated voltage V_L is recorded at the same time. Since r_{PYEG} is much larger than r_L, the relation between pyroelectric current I_P and V_L can be illustrated below:

$$I_P = c_{PYEG}\frac{dV_L(t)}{dt} + \frac{V_L(t)}{r_L} \tag{5. 1}$$

The PYEG is heated for the first 50 seconds during the test and is cooled down for another 50 seconds after. The temperature increased from 25°C to around 60°C at first and decreased to 35°C at the end. The recorded voltage V_L and temperature from both the center $T(t)_1$ and a typical part on the edge $T(t)_2$ of the PYEG are shown in Figure 5. 2(b). The sampling rate of these records is 100Hz. Since there is highly noise in the records of the temperature, it is not able to deduce p directly from (5.1). It is suggested to use numerical integration to solve this problem. The calculation of p is based on the data manipulation below (the temperature dependence of p is neglected in our study):

$$p = \frac{\int_0^t [c_{PYEG}(V_L(t) - V_L(0)) + \frac{1}{r_L}\int_0^t V_L(t)dt]dt}{A_{PYEG}\int_0^t (T(t) - T(0))dt} \tag{5. 2}$$

Several tests are implemented and the pyroelectric coefficient p is represented by the slope of each curve in the Figure 5. 2(c). The measured average pyroelectric coefficient between 25°C and 65°C is 688μCm^{-2}°C^{-1} with this way of data manipulation which is in the right range of the PZT material.

5.2 Experimental study

5.2.1 In lab test and results

As prepared for all the necessary properties of PYEG, the proposed idea is verified by an experimental procedure developed in lab at first. A sketch map of the experiment system in top view is shown in Figure 5. 3. The PYEG is glued to the tip of a polymethyl methacrylate base which is good at thermal insulation. The generated pyro current is regulated by a bridge circuit made of 1N4148 diodes and charges a 2.2μF WIMA film capacitor. The spotlight (20W, 12VDC) is placed in the front of PYEG with distance of 11 cm. Its equivalent intensity of radiation at this distance is calibrated with input voltage in advance. The front face of PYEG is paint black while a tiny flat film PT100 temperature sensor is placed on the back face by thermal grease. An centrifugal fan (G3G160-AC70-01) is placed on the side of PYEG, generating wind fluctuation. A differential pressure transducer (Setra Systems Model 264) is placed on the other side, recording the generated wind by transformation from dynamic pressure. A data acquisition system (NI DAQcard-6024E with Labview 2009) is used to record all the generated voltages with the information of harvested energy, temperature and wind fluctuation. The input impedance for the DAQ system is 100 GΩ in parallel with 100 pF. The acquisition device is also used to control the fan, providing a given pattern of wind fluctuation.

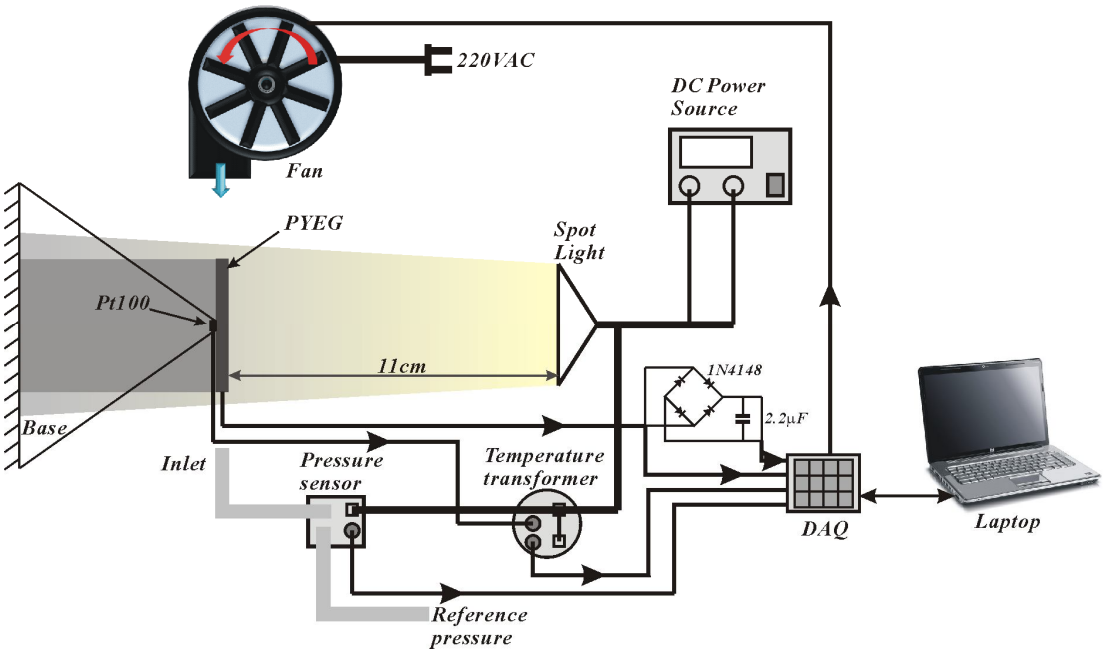

Figure 5. 3: Diagram of experiment system of solar PYEG in lab

As a typical thermal loading, the intensity of radiation was fixed at 1000 Wm^{-2} and

the wind speed at 2 ms^{-1}. The wind was applied to the PYEG for each 100 seconds and lasting for 30 seconds each time. The recorded wind fluctuation is shown in Figure 5. 4(a) and the measured performance are shown in Figure 5. 4(b)-(c). The temperature variation in PYEG reaches 16 °C. Although the maximum and minimum temperature has not been reached during each work cycle, it is still evident that the temperature decreases quicker than it increases. It shows that the forced convection induced by wind can cool down the PYEG easily. On the electrical response, the voltage on the PYEG alternates from positive to negative while that on capacitor increases step by step, following the trend of PYEG when diodes are open. The voltage on the capacitor reaches 10V at time 415 seconds. It provides a total harvested energy of 0.11 mJ and an average power of 4.2μWcm^{-3}. This performance is comparable with a previous study [CUA 2010] which uses hot and cold wind as the thermal loading.

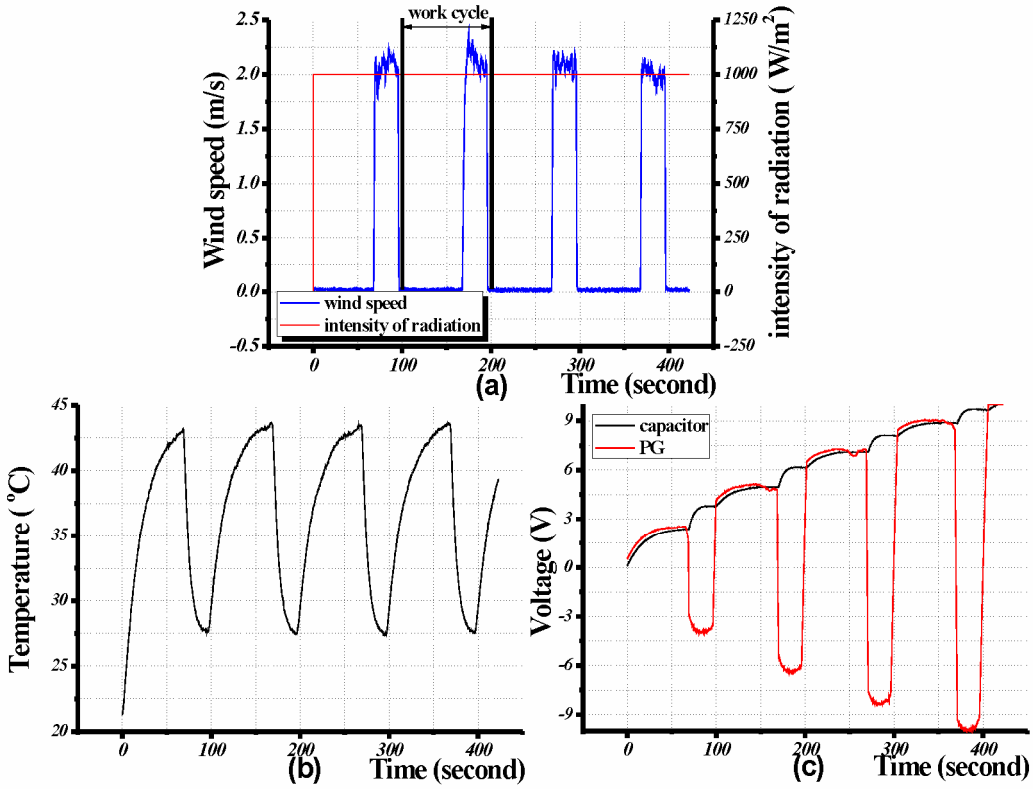

Figure 5. 4: Experiment results of PYEG in lab: (a) thermal loading (b) temperature variation in the PYEG (c) voltage on the PYEG and energy storage capacitor

5.2.2 Test outside and results

The experimental study in lab shed light on the idea of utilizing wind fluctuation when harvesting solar thermal energy. It can be recognized that the PYEG is very sensitive with wind fluctuation which is proposed to be used as anemometer [HSI 1995]. However, the test in lab doesn't tell the potential of temperature variation in PYEG in natural condition which is essential in pyroelectric energy harvesting. Therefore, experimental study is implemented outside. The analysis is realized in two steps. A thin copper plate is used to test the temperature variation available in environment during the day at first. Then a continuous energy harvesting process is realized by connecting the PYEG with a constant resistance.

The copper plate is with dimension 880mm×200mm×0.2mm. It is glue on a polystyrene insulating base. In order to increase the heat absorption rate, the irradiated surface of the plate was covered with special films made by Clipsol, France Several temperature sensors are placed on the back surface of the plate. The experiment is done at 16th April 2010 in CSTB Grenoble. The sampling rate of the record is 3.3Hz and there are three samples in total during that day. They began in the morning, midday and afternoon respectively and each record lasts for 40 minutes. The results are shown in Figure 5. 5.

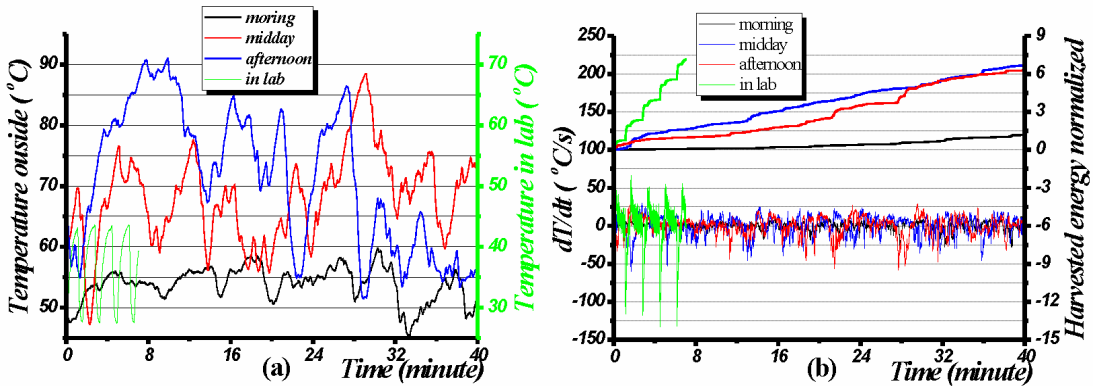

Figure 5. 5: Comparison of temperature variation in lab and outside: (a) pattern of variation (b) temperature difference with time and harvested energy normalized

Analysis of this figure led to four comments:

1. The amplitude of temperature variation is different all over the day as shown in Figure 5. 5(a). It is larger during the midday and afternoon than in the morning. This performance should depend on the intensity of solar radiation.
2. The amplitude of temperature variation can be more than one times larger than that achieved in lab where we applied the PYEG with almost the maximum thermal radiation available in local place. This divergence should come from two parts. The thermal insulation installation on the backside of the plate increases the

maximum available temperature. Besides, the special covering layer could also help.

3. There is hardly any short time during the day with stable temperature. The cycle of temperature variation with visible amplitude is comparable with the test in lab which is 0.01Hz. There are abounding component of wind fluctuation within this period.
4. The temperature difference with time and harvested energy normalized are shown in Figure 5. 5(b). It reveals that the temperature difference achieved in lab is still larger than that outside. These curves represent harvested energy normalized $\boldsymbol{E_{Normal}}$ are generated below:

$$E_{Normal} = \int \left(\frac{dT(t)}{dt} \right)^2 dt \Big/ \max \left(\int \left(\frac{dT(t)}{dt} \right)^2 dt \right) \tag{5. 3}$$

The average power yield in lab is 6 times higher than the outside situation according to the slope of these curves on the upside of Figure 5. 5(b).

The foregoing experimental study outside provides a brief description of temperature variation available which is helpful in estimation of power generation from the PYEG in environment. The next step is to inspect a typical energy harvesting process of PYEG outside. Instead of using the prototype system in lab, we propose to use the system in Figure 5. 2(a) in this test since it is easier to understand the generated pyroelectric current without the voltage regulation.

Figure 5. 6: PYEG prototype for outside test

The prototype PYEG is suspended on a tree with a thread, as shown in Figure 5. 6. The painted face points to the direction of incoming sunlight originally. We believe that this setup utilizes not only the forced convection, but also a rotational movement of the irradiated surface induced by wind which can enhance the cooling process of the PYEG further. The temperature sensors are taken off, leaving only a slim electrical wire. There are two tests implemented in this step. The first test is conducted in October 28th from 11:00 to 17:00. The PYEG is connected with the 1MΩ external resistor and the sampling rate of this test is 1Hz. The second test began at 6:00 and ended at 18:00 in May 26th. The PYEG is in open circuit status and the sampling rate is 10Hz. The recorded performances are shown in Figure 5. 7. (a) and (b) come from the first test while (c) and (d) describe the second test.

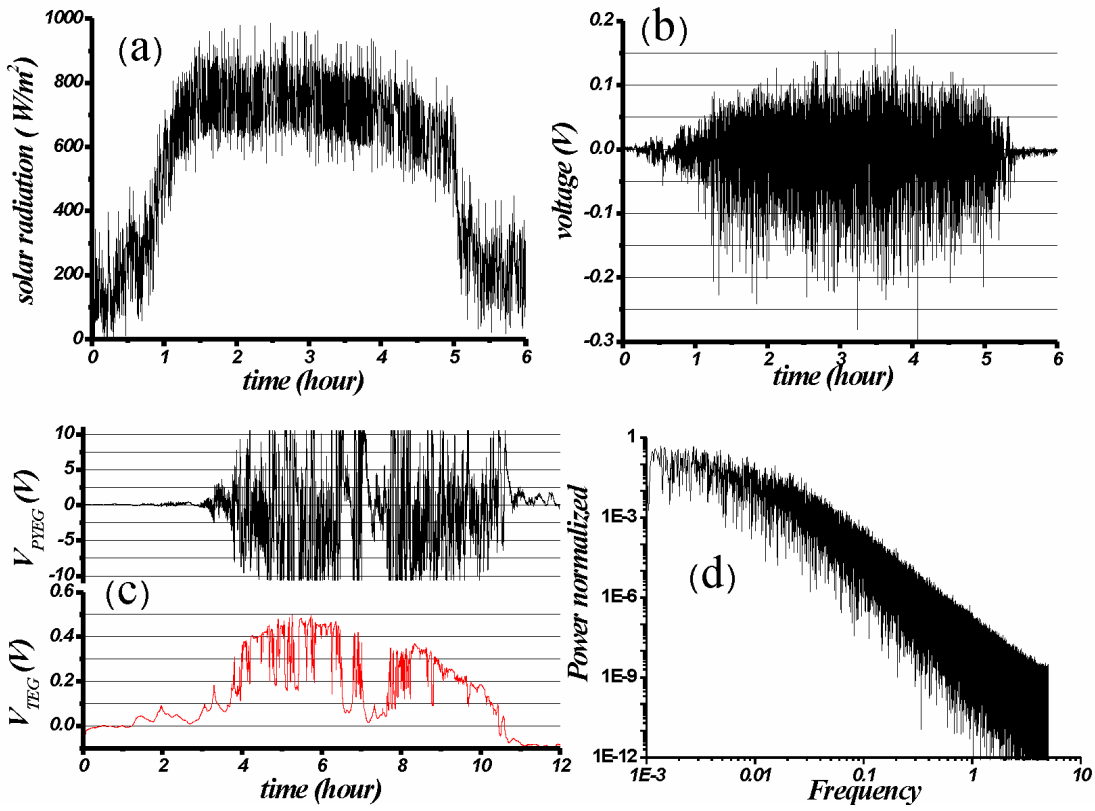

Figure 5. 7: Experiment results of PYEG outside: (a) recorded solar radiation (b) voltage generation on the external resistor (c) voltage generation in open circuit status (d) power spectrum of the voltage generation in open circuit status

Analysis of Figure 5. 7 led to another four comments:

1. The average power generated in the first test is 1.8nW while that achieved in lab is 265nW. The giant difference comes from the different type of external load.

2. Positive voltage is yield when the temperature of PYEG is increasing. It is obvious that the generated negative voltage, as shown in subfigure (b), is larger than the positive voltage in average value. The cooling of PYEG with natural wind is effective.

3. The output voltage of PYEG without external load is shown in the upside of subfigure (c). It is proportional to the temperature variation in the PYEG. The lower side shows the generated voltage of a TEG which is near to the PYEG, providing a reference of solar radiation. The voltage from the TEG reveals that the intensity of solar radiation varies with time. It could come from the shadow induced by cloud. This effect is also favorable in harvesting solar thermal energy with PYEG.

4. Fast Fourier Analysis (FFT) is applied on the recorded voltage of PYEG in subfigure(c) and the power spectrum is achieved in subfigure (d). It is found to be in agreement with the Von Karman's form [KAR 1948] of spectrum equation which is widely used in the modeling of natural wind. This is helpful for the analysis of the system performance with modeling method in future.

The previous experimental study proves the feasibility of the proposed concept of PYEG driven by solar radiation and wind. However, the energy harvesting process in environment is complicated especially with the unpredictable thermal loading. A numerical method is developed below in order to estimate the performance of a PYEG with ambient thermal loading.

5.3 Modeling of the prototype system

5.3.1 Equivalent electrical model

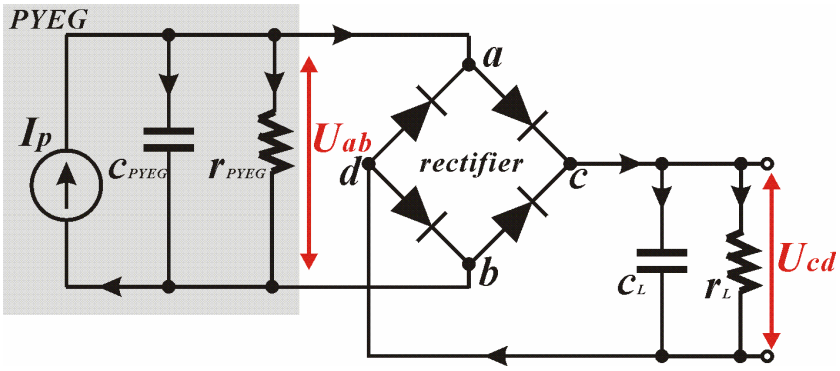

Figure 5. 8: Electrical model of the PYEG charging a capacitor

The PYEG is usually considered as a source of current in parallel with its equivalent capacitance c_{PYEG} and resistance r_{PYEG}, as shown in Figure 5. 8. The intensity of current I_p is determined by equation (5.1). U_{ab} is the generated voltage on the PYEG. U_{cd} corresponds to the voltage on the energy storage capacitor c_L. It contains a resistance r_L. The governing equations for the electric model are:

$$\begin{cases} I_p(t) = c_{PYEG}\dfrac{dU_{ab}(t)}{dt} + \dfrac{U_{ab}(t)}{r_{PYEG}} & (|U_{ab}| < |U_{cd}| + 2V_d) \\ c_L\dfrac{dU_{cd}(t)}{dt} = \dfrac{U_{cd}(t)}{r_L} \end{cases} \tag{5. 4}$$

$$\begin{cases} I_p(t) = c_{PYEG}\dfrac{dU_{ab}(t)}{dt} + \dfrac{U_{ab}(t)}{r_{PYEG}} + c_L\dfrac{dU_{cd}(t)}{dt} + \dfrac{U_{cd}(t)}{r_L} \\ |U_{ab}| = |U_{cd}| + 2V_d \qquad (|U_{ab}| \geq |U_{cd}| + 2V_d) \end{cases} \tag{5. 5}$$

It is supposed that the bridge rectifier has two distinct statuses. When the bridge is off, the PYEG is considered electrically insulated from energy storage capacitor. The inherent leakage in the diodes is neglected here. When the bridge is on, the diodes are represented by their forward voltage V_d.

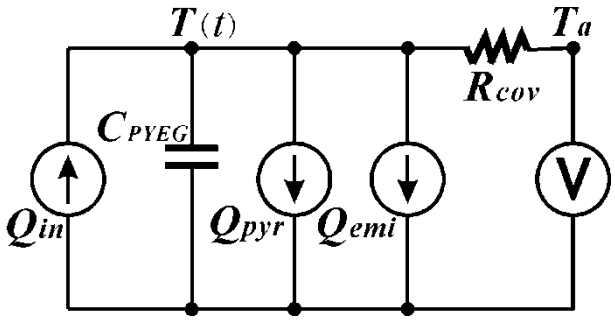

Figure 5. 9: Electrical model of the PYEG charging a capacitor

Apart from the electrical model of the PYEG, the transient thermal response is essential to the energy harvesting process. A lumped parameter thermal model, as shown in Figure 5. 9, is adopted to estimate the transient thermal response of the PYEG. The rationality of this thermal model is further addressed in Appendix C by calculation of the Biot number. The modeling method of input thermal loading is similar with that introduced in Figure 4. 15 which is used to analyze TEG. Q_{in}, Q_{emi}, R_{cov} and T_a are mentioned before. Q_{pyo} stands for the part of energy converted to electricity useful by the pyroelectric effect. C_{PYEG} is the thermal capacitance of the PYEG. The governing equations for the thermal model are:

$$\begin{aligned}
&\text{Thermal:}\quad Q_{in} = C_{PYEG}\frac{dT(t)}{dt} + \frac{T(t)-T_a}{R_{cov}} + Q_{emi} + Q_{pyr} \\
&\text{Coupling:}\quad Q_{pyr} = U_{ab} I_p \\
&\text{Loading:}\quad \begin{cases} Q_{in} = \sigma A_{PYEG} Q_{rad} \\ Q_{emi} = \varepsilon A_{PYEG}\sigma\left(T(t)^4 - T_a{}^4\right) \\ R_{cov} = 1/\left(2h_c A_{PYEG}\right) \end{cases}
\end{aligned} \tag{5. 6}$$

5.3.2 Numerical simulation

With the combined electric and thermal model of the PYEG, its performance can be evaluated by a numerical procedure as shown in Figure 5. 10. It begins with the selection of initial temperature $T(0)$, and initial voltages $U_{ab}(0)$ and $U_{cd}(0)$. The time step depends on the accuracy of the calculation. $T(0)$ is normally set to initial ambient temperature $T_a(0)$. $U_{ab}(0)$ and $U_{cd}(0)$ are set to zero with no special indications. The first time step is selected at 0.1 second. Solar radiation Q_{rad}, ambient temperature T_a and wind speed V_w are prepared in advance, as functions of time. They are inserted to the simulation at once and in totality, and serve as a local database. The mode of convective heat exchange is thereafter determined by V_w. The calculation of the

convection coefficient takes account of the calculated temperature on the PYEG in most recent step. The energy harvesting process begins with the computation of transient temperature variation $T(t)$ by the ordinary differential equation solver. The generated pyroelectricity I_p is achieved as an average value which is deduced from the difference between the initial and latest values of temperature in this step. The electrical procedure follows the thermal response. The status of the bridge rectifier is determined first and it is decided whether to maintain the newly produced charges on the PYEG or to deliver them to the energy storage capacitor.

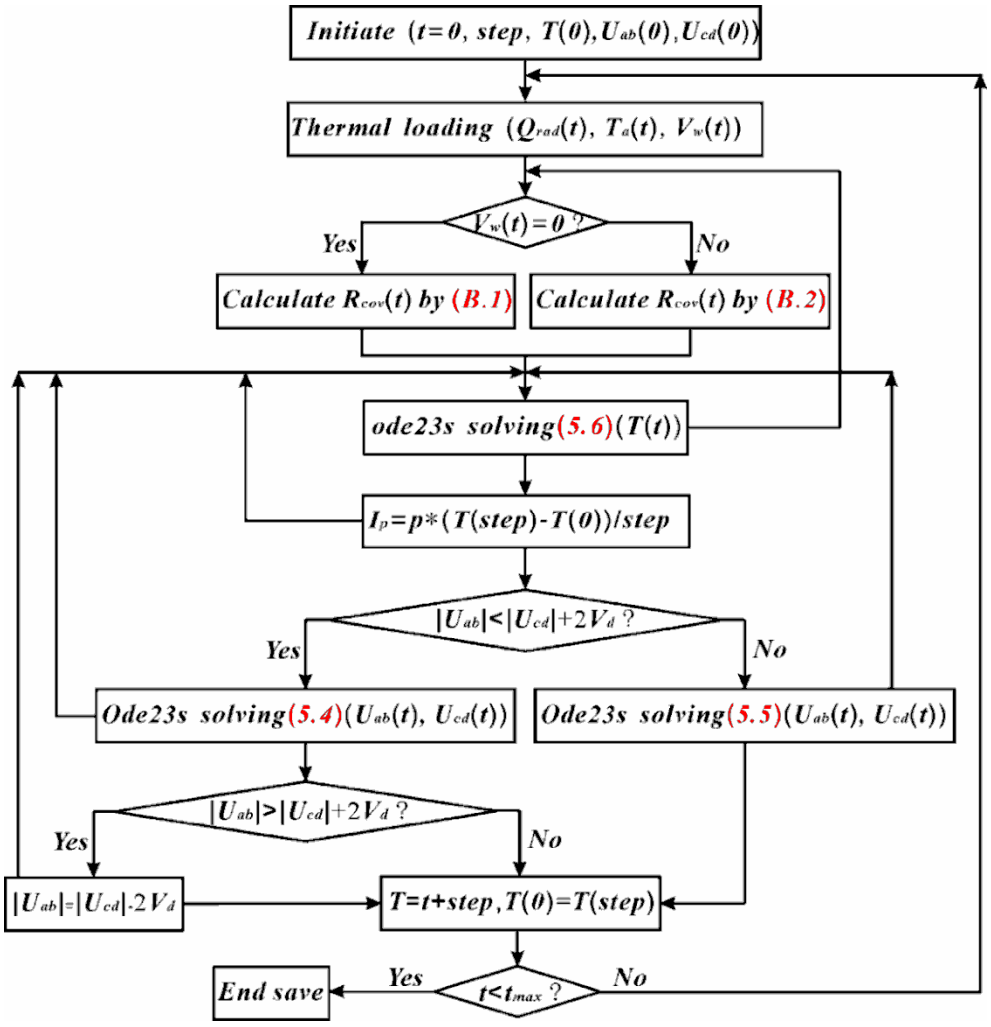

Figure 5. 10: Diagram of the simulation for the pyroelectric energy harvesting

An extra consideration is the charge process of the PYEG when the bridge is off. For such a computation step, the bridge is able to be open during the process of calculation. In order to retain the continuity of $U_{ab}(t)$ which accords with the actual situation, $U_{ab}(t)$ is given the value of $U_{cd}(t)$ when the bridge is opened. Generally, c_{PYEG} is much smaller than c_L. The lost energy caused by this special treatment can be neglected. At the end of each step, $T(t)$, $U_{ab}(t)$ and $U_{cd}(t)$ are updated by the last calculated value from each ordinary differential equation solver.

5.3.3 Results of the simulation

In order to check the reliability of the proposed model of PYEG and numerical procedure, a thermal loading similar to that applied in the experiment test in lab (Figure 5. 4(a)) is used in the primary simulation. The wind speed is 3.5 ms^{-1} and the intensity of solar radiation is 500 Wm^{-2}. Other parameters used in the simulation are listed in Table 5. 2. The calculated performance is compared with the experiment in Figure 5. 11.

Table 5. 2: Parameters used in simulations

Parameters	Symbol	Value
Heat absorption rate	α	0.5
Emissivity	ε	0.5
Load capacitance (µF)	c_L	2.2
Leakage resistance (GΩ)	r_L	0.4
Forward voltage (V)	V_d	0.62

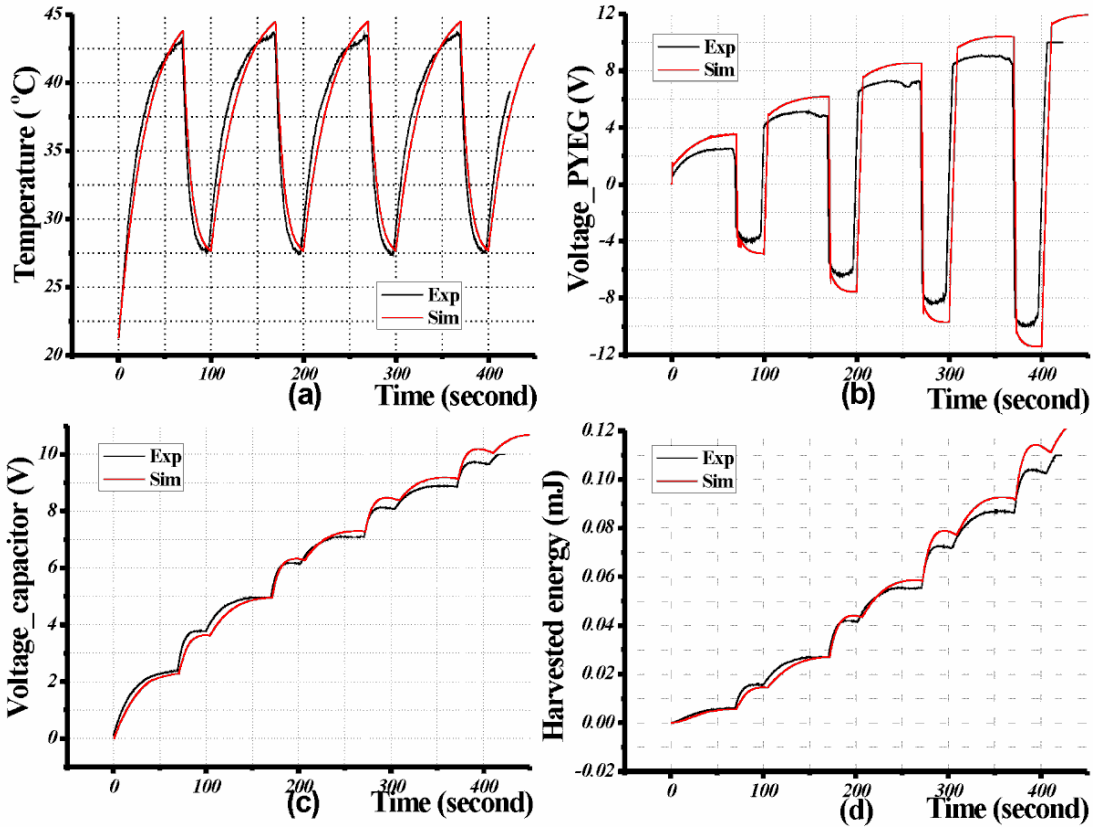

Figure 5. 11: Simulated results of PYEG compared with experiment: (a) ***T(t)*** (b) U_{ab} (c) U_{cd} (d) energy harvested and stored in c_L

The simulation can accurately predict both the thermal response and the electrical performance. The pattern of temperature variation in the simulation mimics the experiment as shown in Figure 5. 11 (a). Both the natural and forced convection empirical formulae used in this model are suitable. The divergence lies in the intensity of applied radiation and wind which contains a measurement error in the experiment. The simulated voltages in Figure 5. 11 (b) and (c) show the same trend relative to the experiment in each work cycle. The discrepancy may result from the simplification of the characteristics of the bridge circuit in the model. In short, the proposed model and numerical procedure provides a useful method of estimating the performance of such an energy harvesting process.

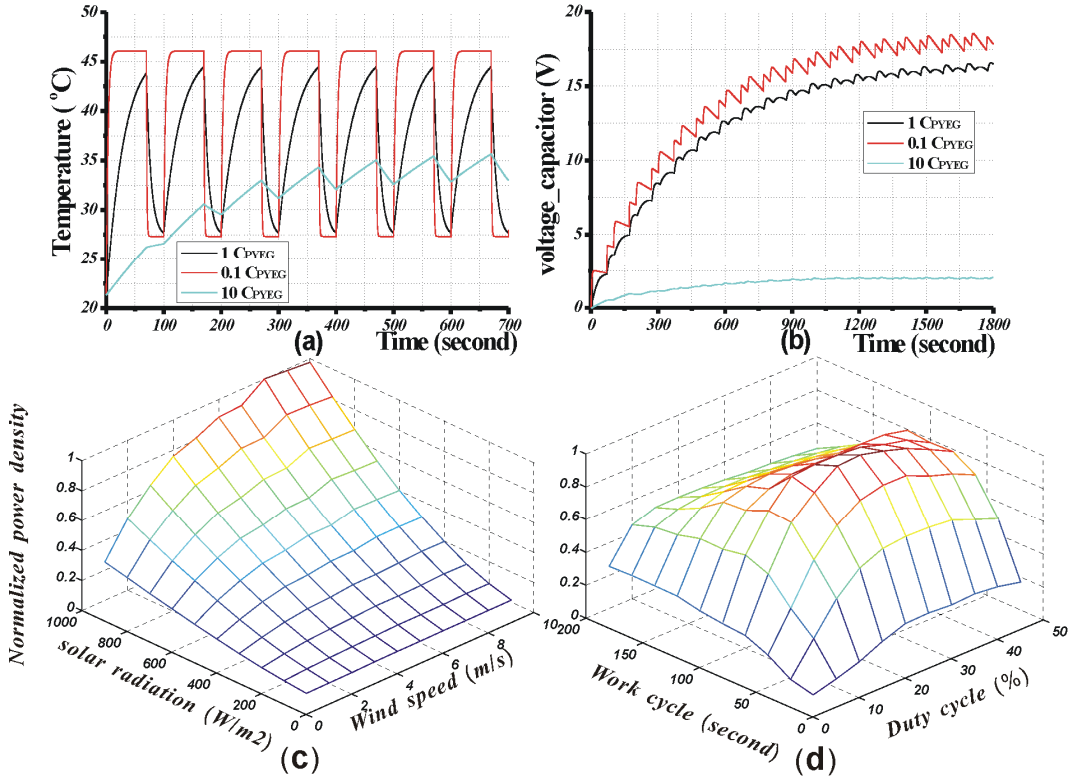

Figure 5. 12: Parametric influence analyzed by numerical model: (a) temperature variation with different C_{PYEG} (b) U_{cd} with different C_{PYEG} (c) normalized power density as a function of intensity of solar radiation and wind speed (b) normalized power density as a function of work cycle and duty cycle of wind

There are three other simulations performed in the numerical study, illustrating the characteristics of a PYEG driven by solar radiation and wind fluctuation:

1. The first simulation gives information on the influence of the thermal capacitance C_{PYEG} on the energy harvesting process. With the same thermal loading in the primary simulation applied but with a different C_{PYEG} used, a new simulation is implemented; the results are shown in Figure 5. 12(a)(b). When C_{PYEG} is 10 times smaller, the temperature changes very quickly. Thermal equilibrium can be

reached for both maximum and minimum temperatures in each work cycle. It proves that a low thermal capacitance can provide a high power density. Although the amplitude of temperature variation does not change greatly at this time, it is advantageous to work with more rapid changes in the wind. When $\boldsymbol{C_{PYEG}}$ is 10 times larger, the performance is very poor as shown in Figure 5. 12 (b); the reason is revealed in Figure 5. 12 (a). The large thermal inertial effect decreases the temperature variation.

2. The second simulation is conducted with different intensity of radiation and wind speed. The work cycle and duty cycle of wind fluctuation are still the same as the primary simulation. The time step is 1 second and the total time for simulation is 2000 seconds, when $\boldsymbol{U_{cd}}$ reaches 90% of its ultimate value. The calculated average power density at the end time is shown in Figure 5. 12 (c). The calculated power density is normalized, as the absolute value is not optimized. It shows that the power density is quadratic function of solar radiation. Actually, $\boldsymbol{U_{cd}}$ is almost linear with solar radiation. This characteristics makes it easy to evaluate the performance of the generator when the solar radiation changes with time. Besides, the influence of wind speed on power density can be divided into two parts. When the radiation is low, the wind speed gives no significant change of power density. When the radiation is strong and the wind speed is low, a tiny increase of wind speed gives a remarkable improvement in power density. It indicates that even a small wind speed can drive such a PYEG very satisfactorily.
3. The dependence of power density on the work cycle and duty cycle of wind is studied in the third simulation. The work cycle varies from 20 to 200 seconds while the duty cycle varies from 5 to 50%. The other thermal loading is the same as the primary simulation and it also stops at 2000 seconds. The numerical solution is given in Figure 5. 12 (d). The normalized average power density increases until the work cycle reaches 80 seconds and then decreases. When the work cycle is too short, the temperature variation in the PYEG is limited. It yields a similar weak voltage which is not able to efficiently charge the energy storage capacitor. When the work cycle is too long, the leakage in the energy storage capacitor becomes dominant, also leading to poor performance. Considering the influence of the duty cycle, it presents also a peak value at 30%. A good characteristic revealed in this subfigure is that a wind passing even for a short period can cool down the PYEG effectively.

In short, there is a favorable pattern of wind fluctuation for a given PYEG structure. The idea of changing the temperature in the PYEG by wind is promising.

5.4 Sectional summary

In this section, we proposed a new concept of harvesting ambient solar energy with a pyroelectric generator. The ambient wind fluctuation is found to be a potential motivation of temperature variation in the active material. The basic concept of how pyroelectric material works with solar radiation and wind fluctuation is explained in detail.

The proposed concept is first proved by specially designed laboratory experiment. The measured temperature variation, with solar radiation at 1000 Wm^{-2} and natural wind speed at 2ms^{-1}, is as much as 16°C. The corresponding average power density with PZT as the pyroelectric material is 4.2 μWcm^{-3} with a capacitive external load. The feasibility of this concept in natural condition is inspected by two steps. The temperature variation available with improved thermal properties of prototype system is measured at first. It indicates that a typical generated power outside is in the same order of magnitude as that achieved in lab. Further experiment is implemented outside in order to check a real energy harvesting process. It is found that the PYEG is not suitable with resistive external load. The generated power is much lower than that with capacitive external load. Besides, the wind is proved to be effective to cool down the PYEG at work.

The detailed analysis of the proposed concept is realized by numerical simulation. Both the lumped parameter thermal model and electric model are considered in an energy harvesting process aiming at driving low-power electronics. A numerical procedure is developed to predict the performance. It provides with good prediction to both the thermal and electrical performance of the PYEG as compared with experiment test in lab. The relationship between the thermal capacity of PYEG, intensity of solar radiation, patterns of wind fluctuation and the generated power of PYEG is also inspected with the developed numerical procedure. Both the modeling and experimental study support the concept of harvesting solar thermal energy with pyroelectric effect in environment.

6. Wind (or airfow) energy harvesting through piezoelectric effect

6.1 Design of the piezoelectric energy harvesting system

It is a great challenge to harvest kinetic energy of the airflow around buildings with piezoelectric effect since the energy conversion efficiency is low which is due to the inherent mismatch between their power densities. Generally, the wind power density near ground can reaches only 1.75Wcm^{-2} with wind speed at 30 ms^{-1} which is already seldom on land. The power density $\boldsymbol{p_{wind}}$ of wind can be expressed as:

$$p_{wind} = \frac{1}{2}\rho_{air} v_{wind}^3 \tag{6. 1}$$

Where $\boldsymbol{\rho_{air}}$ is the density of the air, $\boldsymbol{v_{wind}}$ is the velocity of the wind. The piezoelectric material can reach 135Wcm^{-3} according to [SHA 2010]. The power density of the piezoelectric material can be more than ten times higher than that of the wind. An important influence factor in the energy harvesting system is the mechanical coupling structure which needs to concentrate the dispersed kinetic energy of wind. The design and analysis of this coupling structure will be the focus in this study.

The common windmill which utilizes electromagnetic effect to get electricity is able to get a maximum energy conversion efficiency of 59% theoretically. The advantage of this power generator lies in that the power density of electromagnetic field can be chosen freely in large range. Besides the wind mill turns continuously therefore the wind can always provide effective power. This is not the case for PIEG who needs an alternating force as actuation. Three important problems for harvesting wind energy with PIEG become clear.

1. To find a leverage structure which transfers the small force with large displacement into large force with tiny displacement, improving the power density.
2. To let the leverage structure change the wind which is originally blows in one direction into an alternating force which is applied on its self.
3. To provide a mathematical or numerical model of the fluid structure interaction problem. To be straightforward, the force loading on the structure with a given input wind speed need to be clarified.

A cantilever as the most popular coupling structure between various energy source and piezoelectric material is adopted in this study. It solves the first problem for a PIEG. The major work on this study focuses on the two problems afterward. In order to change the wind blow into an alternating wind pressure, it is proposed that the cantilever is place at the outlet of a cavity in order to realize a flow-induced self-excited oscillation, as shown in Figure 6. 1.

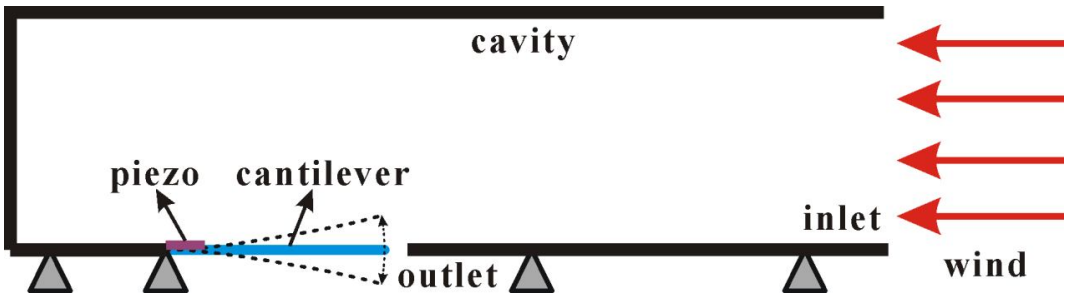

Figure 6. 1: Proposed structure of wind energy harvesting

This figure shows the proposal on the side view. It is similar with the pronouncing unit in a harmonica. The wind comes in the cavity from one side and leaves the cavity from a small aperture where it meets with the cantilever. It is easy to understand the generation of alternating wind pressure on the cantilever in this structure. When there is no wind, the cantilever maintains at its initial place where it covers the maximum part of the outlet of cantilever and leaves the minimum space of the aperture. When the wind arrives at the inlet of the cavity, the total pressure in the cavity is increased. The pressure on the upper surface of the cantilever is higher than that on the lower surface therefore the cantilever will move downward. The cantilever obtains energy from the wind during this process. Meanwhile, the total pressure in the cavity decrease since the deformation of cantilever increase the space of aperture. When the dynamic force (pressure difference between upper and lower surfaces product surface area of the cantilever) applied on the cantilever reaches the mechanical restoring force of the cantilever, the speed of cantilever begins to decrease until it stops with the maximum downward deformation. The total pressure in the cavity is still slightly higher than that outside at this time. Then the cantilever will move upward until it almost goes back to the initial place. This process is repeated and the amplitude of cantilever keeps on increasing to a maximum value which is determined by the wind speed. The periodic variation of the dynamic force is generated by the cantilever itself which guarantees a resonance ultimately.

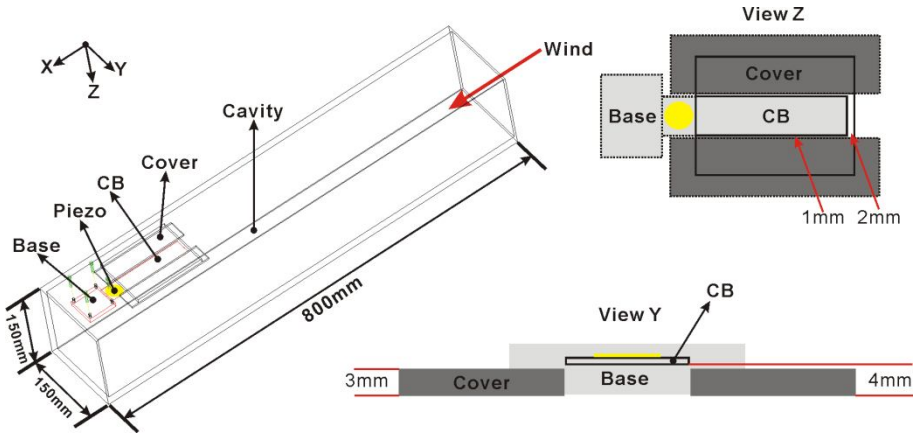

Figure 6. 2: Prototype piezoelectric energy harvesting system

This structure of wind energy harvesting has been introduced by [JI 2010] and [CLA 2010] most recently. Both of these two studies talk about the generated power as a function of incoming wind speed. Our study is a further inspection of this idea, aiming at giving a more detailed description between the input wind pressure and the vibration of the cantilever. Besides, the performance of harvested energy is described with energy that regulated by bridge circuit and stored in a capacitor. A prototype system, as shown in Figure 6. 2, is fabricated in order to check this idea.

The cavity is made of polystyrene material which is transparent. The inlet is with dimension of 150mm×150mm while the outlet is 125mm×100mm. The outlet is far from and perpendicular to the inlet. The end of the cavity which is far from the inlet is sealed. The cantilever is made of steel and its dimension is 150mm×30mm×0.5mm. It is held tightly by an aluminum base which is fixed well on the side of cavity with screws. A piezoelectric element is glued with the cantilever at the supporting end by epoxy adhesive DP460 (3M). The piezo patch is the same as the PYEG used in Section 5. The assembled cantilever has a resonant frequency of 18.5Hz. It is suitable with a wind speed between 1.5 ms^{-1} and 3.5 ms^{-1} which is abundant in natural condition. A much too large wind speed is able to generate a violent vibration of the cantilever in the prototype system. However it is harmful with the piezoelectric element. The shape and dimension of the aperture is very sensitive with the performance of the system. It is formed with two covers adjacent to the cantilever. The configuration of the aperture is highlighted on the right side of Figure 6. 2.

6.2 Experimental study

6.2.1 In lab test and results

The performance of the wind energy harvesting system is measured in lab. An axial fan (W4S200-DA02-02, 40W, 1630rpm) is used to generate a constant wind load. It can provide a maximum wind speed of 4.7ms^{-1}. The differential pressure transducer (Setra Systems Model 264) is used to monitor the total pressure in the cavity. The sampling point is placed adjacent to the free tip of the cantilever, feeding back the variation of pressure. The reference pressure is 1 atm. With different input wind speed which is calibrated with an anemometer (testo 405-V1) in advance, the generated voltage from the piezo element and pressure are recorded by data acquisition system (NI DAQcard6024e with Labview2009) and shown in Figure 6. 3 (a).

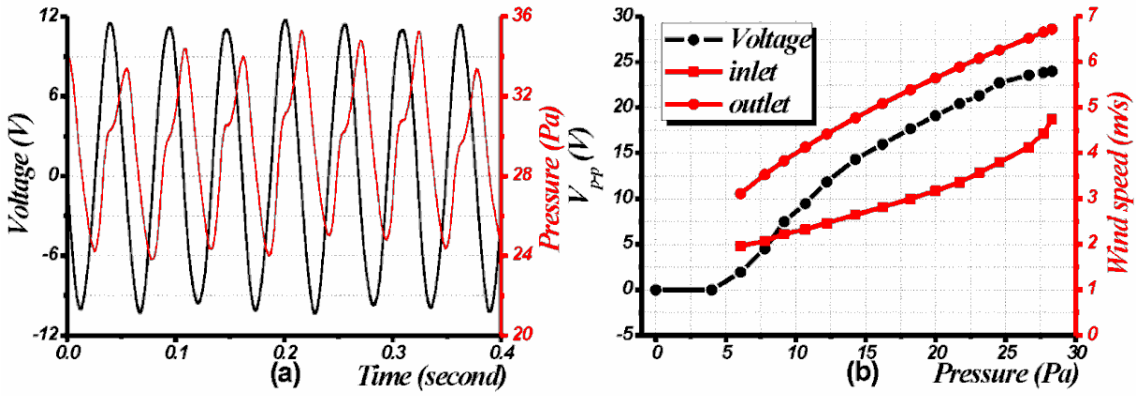

Figure 6. 3: Performance of wind energy harvesting system: (a) voltage generation and pressure variation (b) peak to peak voltage and wind speed at inlet and outlet

When the input wind speed is maintained at 4.5ms^{-1}, a resonance of the cantilever is achieved. The cantilever vibrated at its first bending resonance. The generated $\boldsymbol{V_{p\text{-}p}}$ is 24V as shown in Figure 6. 3 (a). The amplitude on the free tip of the cantilever reaches 15mm in this case. The period of total pressure around the tip of the cantilever is the same with the resonance of the cantilever. It proves the self-excited vibration. Since the phase between the pressure and deformation of the cantilever are not the same (or reverse), it guarantees a continuous vibration.

The peak to peak voltage as a function of total pressure in the cavity and the corresponding wind speed is shown in Figure 6. 3 (b). Analysis of this figure leads to three comments:

1. There is a minimum pressure which is able to activate the vibration of the cantilever. It is 5 Pa in this study. It corresponds to an input wind speed of 2 ms^{-1}. It depends on the shape and dimension of the cavity and aperture.

2. When the cantilever is able to vibrate, the relationship between the total pressure internal and the amplitude of the vibration is nonlinear. The amplitude of the vibration can be deduced from the voltage generation of the piezo element since it is in open circuit status when measured. The V_{p-p} increases more quickly at the beginning when the total pressure is enhanced. This performance is favorable for harvesting ambient wind energy. A low wind speed is able to generate an efficient vibration of the cantilever.

3. The wind speed at the outlet of the cavity is transformed by the recorded total pressure according to the Bernoulli's equation. It is much higher than that at the inlet. When the input wind speed is maintained at 4.5ms^{-1}, the wind speed at the outlet reaches 7ms^{-1} in the prototype system. In other words, the wind pressure applied on the cantilever is improved with the structure of cavity. It realizes the enhancement of the power density of the wind.

In order to estimate the power generation of the prototype system, an external resistor is connected with the piezo element. The matched resistance is measured in advance. When the cantilever is excited by a constant wind speed, a stable wave form is generated from the piezo element. Different external resistor is connected in order to check the maximum power generation. The measured performance is shown in Figure 6. 4. The matched impedance which causes the maximum power is measured as 90KΩ.

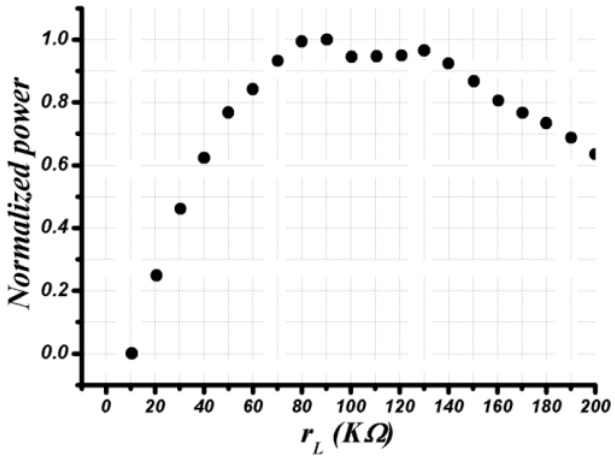

Figure 6. 4: Power generation with different external resistor

Suppose an external resistor of 90KΩ is connected with the PIEG, the generated power and efficiency of the prototype system is shown in Figure 6. 5.

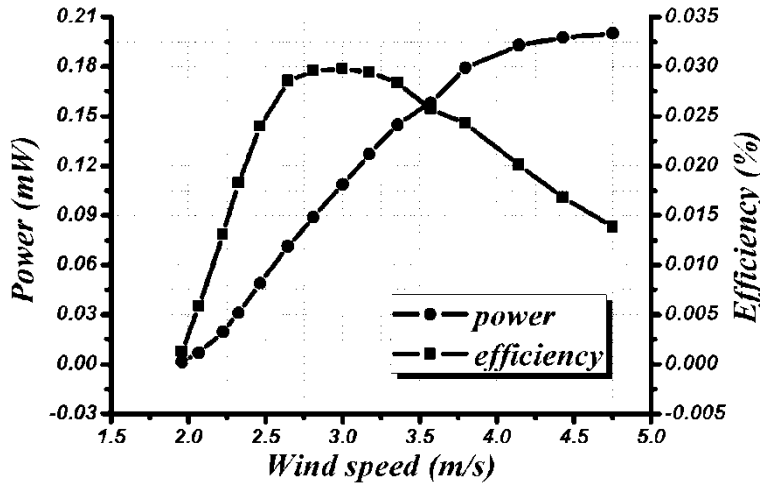

Figure 6. 5: Power generation and efficiency of the prototype PIEG

The output power with the prototype system keeps on increasing when the input wind speed is increased. The maximum power is 0.2mW when the input wind speed is 4.7 ms^{-1}.The energy conversion efficiency of this system η_E which is based on experiment is defined as:

$$\eta_E = \frac{P_{PIEG}}{P_{wind}} = \frac{\left(\int_0^{n_0 T_0} \left(V_L^2(t)/r_L\right)dt\right)/n_0 T_0}{p_{wind} A_{wind}} \qquad (6.\ 2)$$

Where A_{wind} is the sectional area of the inlet. P_{wind} is the input wind power at the inlet of the cavity. P_{PIEG} is the generated electrical power in the PIEG. The energy conversion efficiency increases at first when the input wind speed is increased then it decreases. The maximum energy conversion efficiency which is 0.03% occurs at 3ms^{-1}.

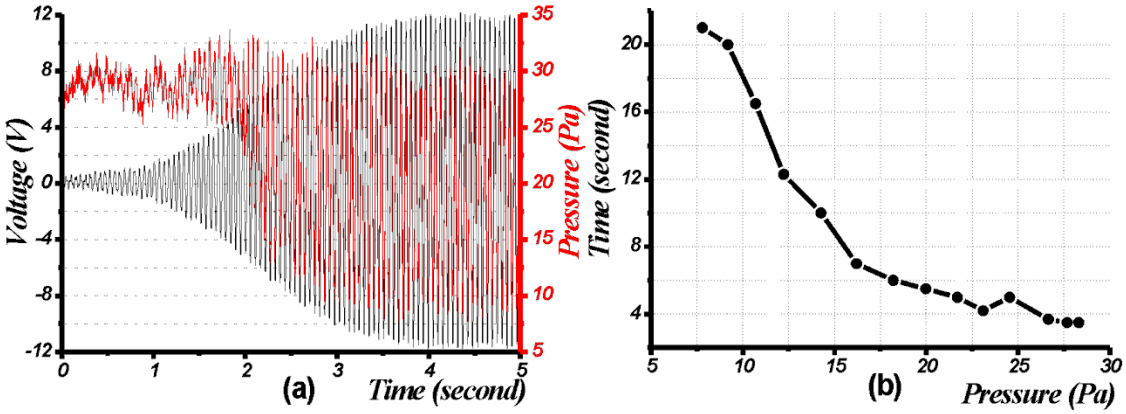

Figure 6. 6: typical process of oscillation starting of the cantilever

Apart from the steady performance of the prototype energy harvesting system, the

transient response of the cantilever is also important in harvesting energy with natural condition since the incoming wind is always changing. The initialization of the vibration in the cantilever is inspected in this study. The cantilever is held stable manually at first and a constant input wind speed of 4.5ms^{-1} is generated. When the cantilever is released, it begins to vibrate. The generated voltage and variation of pressure at the free tip of the cantilever are shown in Figure 6. 6(a). It takes 3.5 second for the cantilever to reach the steady status of the vibration.

With different input wind speed, the time of initialization of the vibration of the cantilever is measured and shown in Figure 6. 6(b). The input wind speed is transformed with the average internal pressure of the cavity. It could be deduced that the minimum time is 2 second and there is no maximum time. That means there is cut off wind speed which is not able to activate a stable vibration of the cantilever.

6.2.2 Test outside and resutls

In order to validate the proposed piezoelectric energy harvesting system in natural condition, the experimental test is implemented outside.

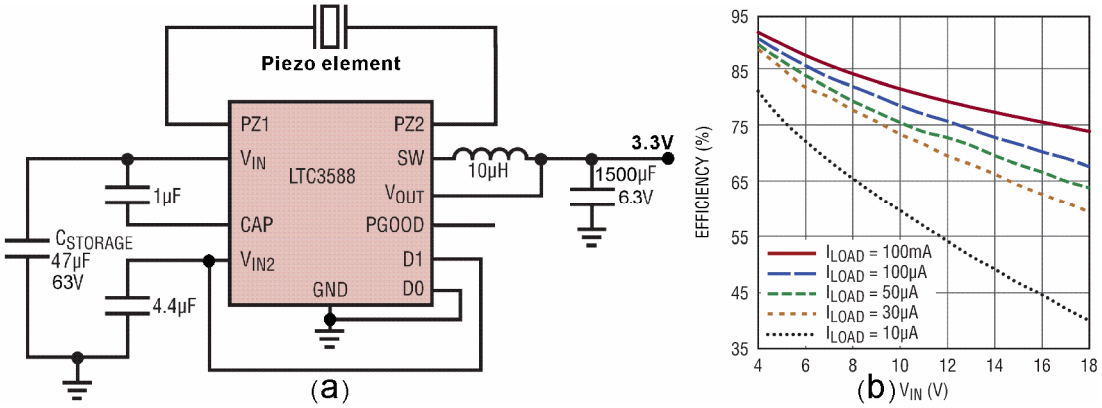

Figure 6. 7: (a) power management circuit of piezoelectric energy harvesting (b) energy conversion efficiency of LTC3588 with regulated voltage at 3.3V

Instead of using a resistive load to estimate the harvested energy, a commercial power management device (LTC3588 Linear Technology Corporation) is used to transfer the alternating voltage and store the energy in a capacitor. The energy harvesting circuit is shown in Figure 6. 7(a). The output of the piezo element is converted by a bridge circuit at first and then regulated at 3.3V which is suitable with majority of current low power electronic devices. The energy conversion efficiency of this device is shown in Figure 6. 7(b) according to peripheral equipment of this device.

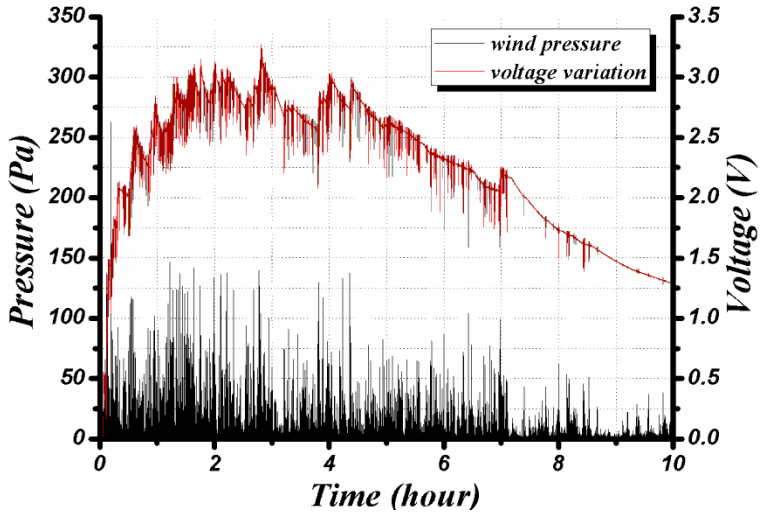

Figure 6. 8: typical energy harvesting process outside

The test outside is done in a windy day (26th October at Aix-Les-Bain, France). The generated wind pressure in the cavity and the variation of the regulated voltage is shown in Figure 6. 8. It is found that there is abundant wind energy with much higher speed than that provide in lab. The generated voltage on the 1500µF capacitor reaches 3V in two hours which corresponds to an average power generation of 1µW and power density of 16µWcm^{-3}.

6.3 Modeling of a self-exctied energy harvester

6.3.1 Fluid structure interaction analysis with dynamic pressure

A) Preview of the dynamic pressure on the cantilever

The previous experimental study provides the basic characteristics of an energy harvesting system based on a cavity structure and a cantilever. There are three energy conversion processes included in Figure 6. 1. They are not at the same degree of interest in the current researches of energy harvesting. The structure coupling from the beam to the piezo element and the limitations from their material properties are widely studied. The energy harvesting strategies with improved electrical interface (such as SSHI) are also popular. However, we focused on the energy transfer from the input wind to the vibration status of the cantilever.

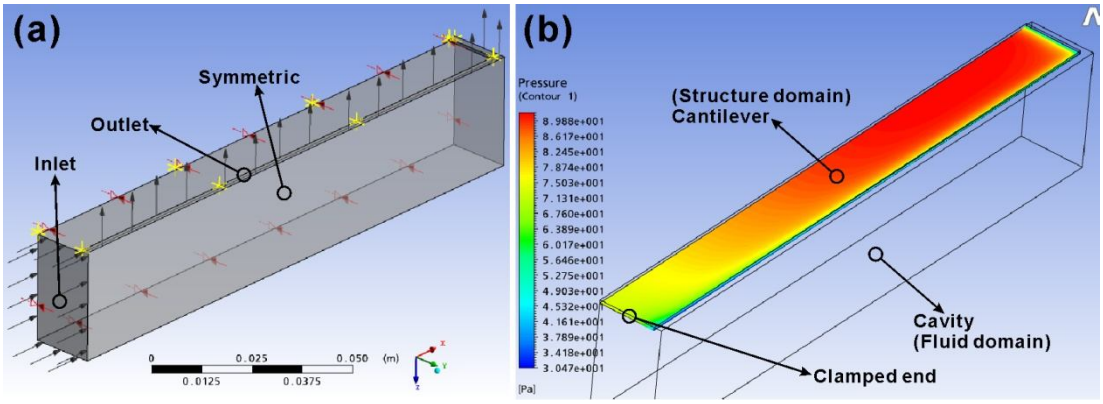

Figure 6. 9: Simulation of FSI (a) fluid domain model (b) pressure distribution

In order to achieve the force loading on the cantilever generated from the input wind, a numerical model with FEM software (ANSYS Workbench) is setup to estimate the dynamic pressure ***p(t)***. It is taken as a transient fluid structure interaction simulation. There are two domains for such an analysis. The cantilever occupied the structure domain while the fluid domain is built with the shape of the cavity.

As a case study, a fluid domain model, as shown in Figure 6. 9(a), is established. The fluid model is 152×17×30mm in dimension while the size of the cantilever is 150×15×0.8mm. The fluid material is air in 25°C and that of the cantilever is structural steel. The input wind speed is considered as a total pressure of 100Pa applied on the inlet where the cantilever is clamped. The airflow leaves the cavity from the outlet which includes the aperture on both one side and the free tip of the cantilever. A symmetric boundary condition is applied on one surface of the fluid domain, taking account the structure symmetry of the aperture.

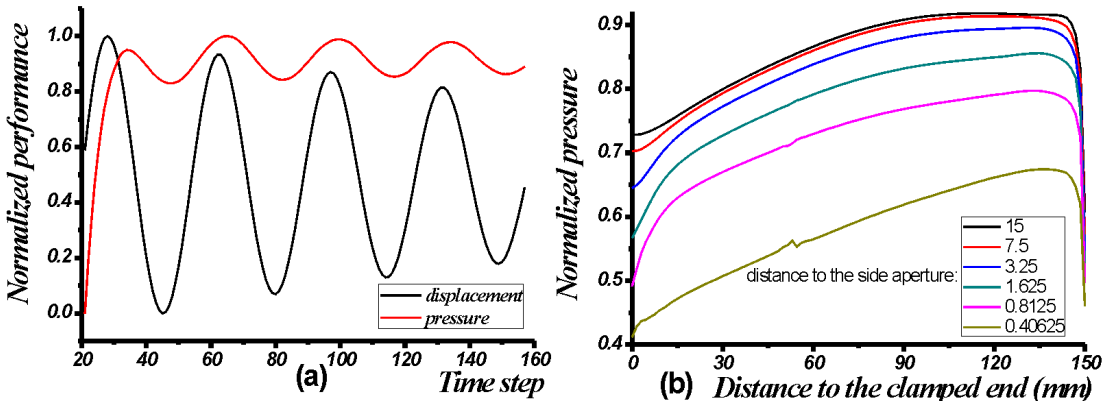

Figure 6. 10: Dynamic pressure (a) time dependent (b) space dependent

When the major conditions for simulation are prepared, the last step is to provide an initial status of the two domains. The velocity of the fluid domain is set to zero while the structure domain is also without movement. The simulation begins with fluid domain calculation. The displacement and pressure change at the free tip of the cantilever is monitored as shown in Figure 6. 10(a). When the vibration of the cantilever is generated, the pressure distribution on the interaction surface between the fluid and structure domain is achieved, as shown in Figure 6. 10(b). A contour plot of the pressure at a typical time is shown in Figure 6. 9(b). It is found that the pressure adjacent to the free tip is higher compared with the clamped end and those parts near the aperture is lower generally.

B) Theoretical model of the dynamic pressure

According to the simulation, the dynamic pressure on the cantilever ***p(t)*** vary with the location on the cantilever. Since the fluid pressure is always associated with the fluid speed, we propose to estimate the pressure with three basic assumptions below:
(1) The fluid velocity adjacent to the interaction surface of the cantilever has two components. It is the normal component ***V(t, x, y)*** which yields the effective dynamic pressure. According to the previous simulation, if the width of the cantilever is large, the pressure distribution is almost uniform except those parts near the aperture which is lower in the value. We suggest to neglect the dynamic pressure from those part near the aperture and the normal component of velocity ***V(t, x, y)*** becomes ***V(t, x)***.
(2) The ***V(t, x)*** depends on both the time and the space. It is supposed that the time function $V_1(t)$ and space function $V_2(x)$ are independent with each other. Then ***V(t, x)*** is expressed:

$$V(t,x) = V_1(t) * V_2(x) \tag{6. 3}$$

where ***x*** is the distance from a local point to the clamped end of the cantilever.
(3) The space function is supposed to have the form:

$$V_2(x) = V_2(0) k_t \ln(x / x_0) \tag{6. 4}$$

Where $V_2(0)$ is the reference speed near the clamped end, x_0 is the "roughness length", k_t is a factor related to the shape of the cavity. The assumption of space function is based on the Eurocode 1 which is recommended to assess the wind speed on windmill towers. The trend of this function is in accordance with the simulated result in Figure 6. 10(b) at a given time.

With the three basic assumptions above, the local active force $f(t, x)$ on the cantilever is expressed:

$$f(t,x) = \frac{1}{2} \rho_{air} C_D W dx V_1^2(t) V_2^2(x) \tag{6. 5}$$

where W is the width of the cantilever. C_D is the drag coefficient which depends on the nature and shape of the cantilever in the fluid. Its value depends also on the Reynolds number which associated the flow speed. Then the total active force on the cantilever $F(t)$ can be expressed as:

$$\begin{cases} F(t) = \int_0^L f(x,t) = F_0 V_1^2(t) \\ F_0 = \frac{1}{2} \rho_{air} C_D W V_2^2(0) k_t^2 \int_0^L (\ln(x / x_0)^2 dx \end{cases} \tag{6. 6}$$

According to the characteristics of the self-excited vibration, the fundamental frequency of the dynamic pressure is the same with the vibration, the time function of the dynamic pressure can be expressed as:

$$V_1^2(t) = \sin(\omega t) + (F_{sta} / F_0) \tag{6. 7}$$

Where ω is pulsation vibration of the cantilever. F_{sta} is the steady static force yield on the cantilever when the vibration is ceased. It could be estimated by the FEM analysis with high structure damping factor.

According to the proposed model above, the complicated fluid structure interaction problem is simplified to the estimation of three basic coefficients (C_D, k_t and $V_2(0)$).

C) Linear vibration model of a cantilever with forced vibration

When the basic coefficients are achieved, the next problem is to model the forced

vibration of a cantilever. For an Euler-Bernoulli beam, the Euler-Lagrange equation is:

$$\frac{\partial}{\partial x^2}\left(EI \frac{\partial^2 v}{\partial x^2} \right) + \rho_b S_0 \frac{\partial^2 v}{\partial t^2} = f(t,x) \qquad (6.\ 8)$$

Where ***EI***, ***ρ_b*** and ***S_0*** are the flexural rigidity, density and sectional area of the beam respectively. The solution of this equation, which is a first order approximation of a beam vibration, is obtained by decomposing the displacement field as follow:

$$v(x,t) = \sum_{i=0}^{\infty} q_i(t) V_i(x) \qquad (6.\ 9)$$

Where ***v(x,t)*** is the displacement of each point in the cantilever. By introducing this expression into the differential equation of equilibrium and by multiplying each member by ***V_i*** and finally integrating along the beam, one obtains using the orthonormal properties of the modes:

$$\ddot{q}_i(t) + \omega_i^2 q_i(t) = Q_i(t) = \int_0^L V_i f(t,x)\, dx \qquad i = 1 \ldots \infty \qquad (6.\ 10)$$

The term ***$Q_i(t)$*** is called projection of the imposed force on the mode i. The problem of solving the forced vibrations is reduced to solving a scalar system with one independent degree of freedom. In our case, this vibration solution describes the beam movement once it starts operating.
To take into account the effects of first vibration, we present in the following section the initiation of vibration by adopting the *Van der Pol* model, which is an extension of the presented first order approximation model.

D) Nonlinear model of the vibration - on *Van der Pol* oscillator

In physics, the phenomenon study is generally looks by focusing on the most important elements. This often leads to linearize the characteristic phenomena of the analyzed system (there is proportionality between cause and effect). Therefore, the nonlinear effects are often considered as disturbed terms and are neglected. However they lead sometimes to remarkable effect. We propose to analyze the non-linear effects of the vibration of cantilever through the equation of *Van der Pol* oscillator.
Based on the previous first order approximation analysis, one can show easily that to start the beam vibration it is necessary to introduce in the differential equation (6.10) a first order term $\dot{x}$ with a negative coefficient. Then to limit the amplitudes of the

vibrations the sign of this coefficient must changes, then the system evolves to a limit circle. This idea is the basic analysis of *Van der Pol* equation, which can be writing as follow:

$$\ddot{x} + a\left[\left(\frac{x}{b}\right)^2 - 1\right]\dot{x} + \omega^2 x = 0 \qquad (6.\ 11)$$

When analyzing this equation we can see that for small amplitudes (***x*** << ***b***) the ratio (***x/b***) is negligible compared to unity and the differential equation could be reduced to a differential equation corresponding to the birth (start) of vibrations whose amplitude grows exponentially due to the coefficient of first order equal to ***-b***. When the amplitude of these vibrations becomes large the ratio (***x/b***) becomes greater than unity and the coefficient of the first order term $\dot{x}$ changes the sign. Consequently, the amplitude of vibration decreases exponentially and the system evolves between two states close limits that describe the amplitude and shape of the vibration. One can already intuitively understands that the term ***b*** will control the value of vibration amplitude while the term ***a*** will affect more or less sinusoidal behavior of the beam. The solution of *Van der Pol* equation was done by Matlab software.

6.3.2 Lumped parameter model with SSHI technique

It is supposed that the incoming wind flow will drive the cantilever to work at its first resonant mode with both mechanical and electrical damping. The amplitude of the vibration will reach a constant value when the input wind speed is stable. In order to estimate the relationship between the incoming wind speed ***v*** and voltage generation ***V*** in the piezoelectric element, the governing equation for a single-mode dynamic equilibrium of the cantilever as established in expression 2.18 is used:

$$\begin{cases} \ddot{u}(t) + \dfrac{C}{M}\dot{u}(t) + \dfrac{(K_{PE} + K_S)}{M}u(t) = \dfrac{F(t)}{M} - \dfrac{\alpha_0 V(t)}{M} \\ \dfrac{F}{M} = \dfrac{1.5WL_0\, p(t)}{M} \end{cases} \qquad (6.\ 12)$$

Where ***u(t)*** is the displacement at the tip of the cantilever, ***M*** is the equivalent mass of the cantilever, $\boldsymbol{\alpha_0}$ is an electromechanical coupling term, ***p(t)*** is the air pressure exerted on the up surface of the cantilever relative to the ambient pressure. $\boldsymbol{L_0}$ is the length of the cantilever respectively. The form of the equivalent force on the cantilever is based on the precondition that the cantilever can be recognized as a *Bernoulli-Euler Beam* and it vibrate at the first resonant mode.

According to [CLA 2010] and [TAR 2000], the pressure ***p(t)*** in the cavity can be determined with steady *Euler-Bernoulli* equation when it is associated with the volumetric air flow rate through the aperture, ***U(t)***, as:

$$\begin{cases} p(t) = \dfrac{\rho_{air} U(t)^2}{2C_c^2 f(u)^2} \\ f(u) = W\sqrt{u^2 + b^2} + 2L\sqrt{a(u)^2 + b^2} \approx (W + 0.8L)u \end{cases} \quad (6.\ 13)$$

Where C_c=0.61 is the flow contraction coefficient for flow through a sharp edged slit. ***f(u)*** is the total exit area of the aperture. ***b*** is the size of the aperture when the cantilever is stopped. ***a(u)≈0.4u*** is the average width along the sides of the cantilever. ***U(t)*** is the volume flow through the cantilever opening. Finally, using the continuity equation, the variation of ***p(t)*** can be expressed as:

$$\frac{dp}{dt} = \frac{\rho_{air} v_s^2}{V_c}\left(U_0 - U(t) - 0.4WL\frac{du}{dt}\right) \quad (6.\ 14)$$

Where v_s is the speed of sound, V_c is the volume of the cavity, U_0 is a constant input volumetric flow rate which is associated with the input wind speed.
According to the SSHI technique introduced in section 2.3.3, the generated voltage ***V*** can be regulated at a constant value V_{cc} when the input force ***F(t)*** is stable. The V_{cc} is only determined by the amplitude of the input force $F(t)_{max}$ expressed as:

$$V_{cc} = \frac{2\alpha_0 RF(t)_{\max}}{\left(C\left(C_0R(1-e^{\frac{-\pi}{2Q_I}})\omega + \pi\right) + \frac{4R\alpha_0^2}{\pi}\frac{(RC_0(1-e^{\frac{-\pi}{Q_I}})\omega + 2\pi)}{(RC_0(1-e^{\frac{-\pi}{2Q_I}})\omega + \pi)}\right)} \quad (6.\ 15)$$

It is noteworthy that the electromechanical coupling term α is different from the definition in expression 2.19, as illustrated in Figure 2. 18. It depends on many experimental parameters including the shapes, dimensions and materials of the piezo element and the metal beam. It is also influenced by the bonding conditions between them. We suggest to use FEM software (such as ANSYS) to achieve α for a typical experimental prototype. By solving equations (6.4)~(6.7) and (6.12)~(6.15) numerically, the power generation in the self-excited energy harvester with SSHI technique can be determined.

6.4 Sectional summary

In this section, we proposed to use the structure of a cavity and a cantilever to harvest ambient wind or airflow power with piezoelectric generator. This structure is able to change a constant fluid flow into an alternating mechanical loading on a piezo element via the self-excited vibration. The mechanism of the self-excited vibration is illustrated and it is found to have similar characteristics with a *Van der Pol* oscillator.

An experimental prototype is fabricated and measured. With the given cavity, it is found that there is limitation for the minimum wind speed which can activate the vibration. A constant input wind speed corresponds to stable amplitude of vibration. The prototype energy harvester with internal electrical impedance of 90KΩ at 18.5Hz can work with minimum wind speed at $2ms^{-1}$. The average power generation is 0.2mW when the input wind speed is 4.7 ms^{-1} and the maximum energy conversion efficiency which is estimated as 0.03% occurs at wind speed of $3ms^{-1}$. Apart from the steady performance, the transient response of the system is studied. It is deduced that the cantilever could reach the steady vibration in 2 second from completely stable status with input wind speed as high as $5ms^{-1}$. The test outside which was implemented in a windy day found that the prototype system can charge a 1500μF capacitor with common AC-DC circuit from 0 to 3V in 2 hours which corresponds to an average power generation of 1μW and power density of $16\mu Wcm^{-3}$.

In the modeling part, we are trying to give a new method of taking account the complicated nonlinear fluid structure interaction problem in the energy harvesting system which is based on decomposing the time and space function in the expression of the dynamic active force loading. It is only an assumption which is not proved due to the lack of time in this PhD study. What we want to emphasize is the energy transfer process from the fluid flow to the vibration structure which we believe should be the dominant factor in the coming study of piezoelectric energy harvesting. The classic method which is based on lumped parameter model to solve the fluid structure interaction problem is also introduced in this study. It is able to be combined with the governing equations in SSHI technique and achieve a higher performance of a PIEG.

7. Typical application of thermoelectric generator in building

7.1 Architecture of the application

The previous studies on thermoelectric, pyroelectric and piezoelectric effect utilized in harvesting ambient thermal and wind energy provide us with their potentials as energy source in wireless application. It is found that the prototype system based on thermoelectric effect can provide more power with the same volume of both active material and prototype system compared with the other two effects. It motivates us to give a further study on a typical wireless application of the proposed TEG system in section 4. The study hereinafter is to show the feasibility of using such micro energy harvested to improve macro power generation by photovoltaic (PV) panel.

It is well known that the weakness of photovoltaic power is that the power generation decreases when the panels become hot. The loss is often remarkable when the solar radiation is high. A simple method to solve this problem is to use water cooling system to decrease the temperature on the PV panel. Therefore, we proposed to use the TEG-PCM system to drive a temperature sensor and send out control signal of the cooling system. The general scheme of the prototype wireless application system is shown in Figure 7. 1.

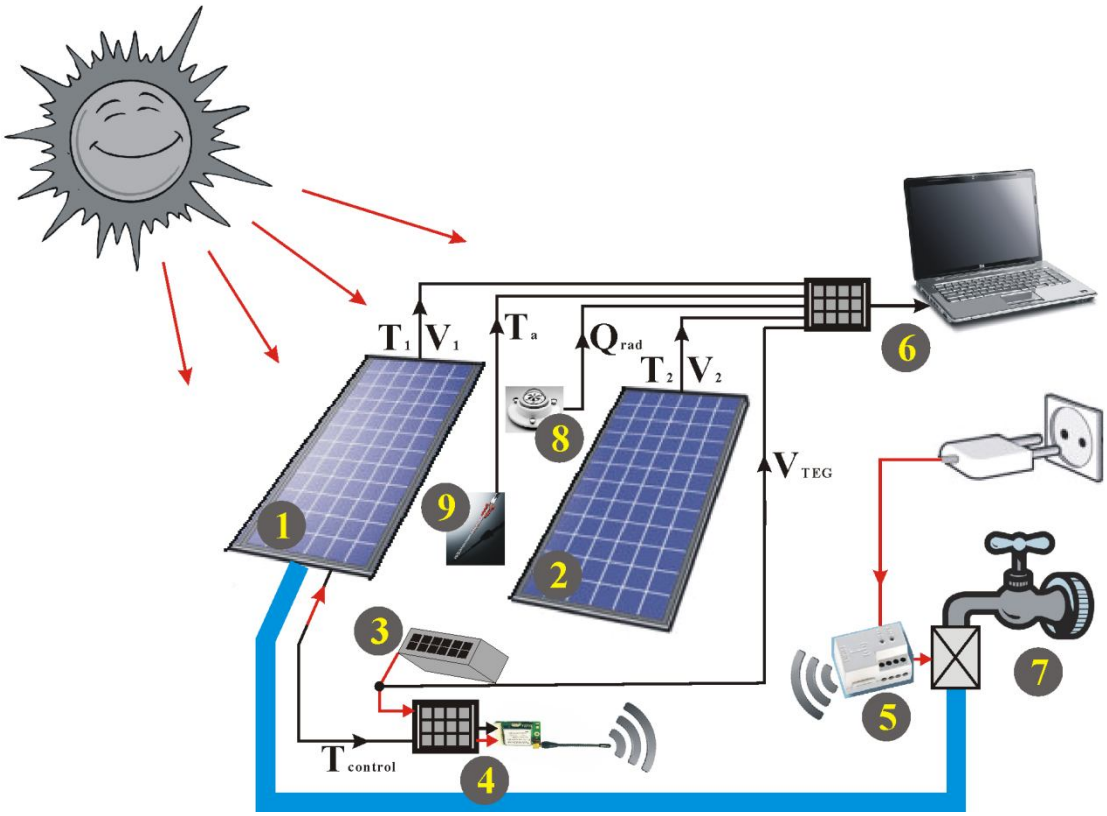

Figure 7. 1: Scheme of the prototype wireless application system

There are in total eight components in this system:

1. A PV panel with water cooling system and temperature sensor on the back side, which aims to prove the improvement of macro power generation.
2. Another same PV panel (TE2000 Tenesol) with normal configuration which works as reference.
3. Thermoelectric energy harvesting work unit.
4. A self-powered wireless temperature sensing system.
5. An electronic switch integrated with wireless receiver.
6. A data acquisition system records all the information during the experiment.
7. A water pipe with controllable tap which aims to cool the PV panel.
8. A pyranometer which records ambient solar radiation.
9. A temperature sensor which records ambient temperature.

Red lines in Figure 7. 1 stands for power supply while black lines represent transfer of information. The arrows indicate the direction of power flow or information flow. It is noteworthy that our current prototype wireless application system is not autonomous completely. The suitable wireless transmitter and receiver are not available for us during the experiment. Instead, the function of wireless transmitting and receiving are realized by a wireless door bell and manual control. It will be addressed in detail later. The performance of the entire system is described in three parts separately and their interface is power generation. The first part is the energy harvesting work unit. The second one is the self-powered wireless temperature sensing system and the last part is the PV panel with water cooling system. It is considered that the temperature sensing system can be activated when the output voltage of the work unit is more than 20mV. The water cooling system can be activated only if the voltage in the energy storage device of sensing system reaches 3V.

7.2 Experimental study

7.2.1 Performance of an improved TEG

As the key component in the application, it is expected that the developed work unit is able to activate the sensor most of the time. The prototype work unit in section 4 is insufficient to drive a typical sensor as shown in Figure 4. 12(a). Therefore, another similar TEG system is fabricated as shown in Figure 7. 2. It is made up of 12 pieces of TEC-12708 module. They are connected in series electrically. The PCM used in this new system is paraffin wax instead of salt hydrate. The thermoelectric module and PCM are connected with three pieces of heat sink (63730 AAVID THERMALLOY).

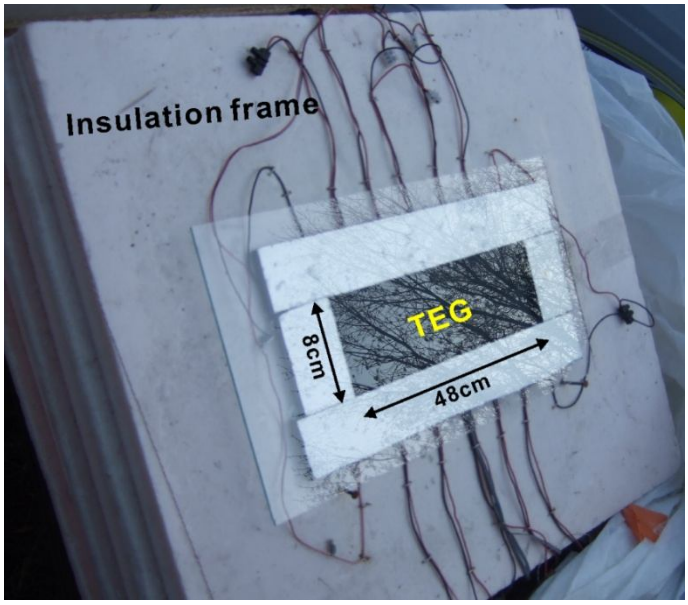

Figure 7. 2: Photo of a newly fabricated TEG system

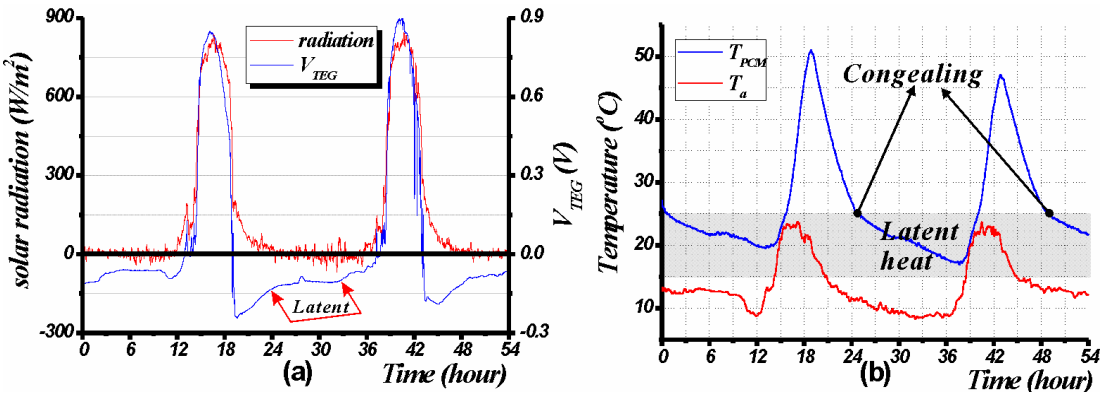

Figure 7. 3: Performance of the new TEG system outside

The performance of the newly fabricated TEG is measured simultaneously on continuous two sunny days of autumn (started at 20:05 4th November 2010) in Aix-les-Bains, France. The total internal resistance of the new TEG is 40Ω. An external resistor of 40Ω is connected respectively. The generated voltage on the external resistor is shown in Figure 7. 3(a), referenced with recorded solar radiation. The temperature variation in the PCM of the TEG system is shown in Figure 7. 3(b), referenced with ambient temperature. Analysis of this figure leads to seven comments:

1. The generated voltage during the day reaches 0.9V for intensity of solar radiation of 900Wm^{-2}. Although the voltage generated during the night is still lower than that achieved during the day, their absolute value is larger than 0.02V most of the time (more than 90%) which guarantees the activation of the sensor continuously.
2. There is obvious phase change process as indicated in Figure 7. 3(b). The decrease of ambient temperature is smooth from 21h to 27h, however there is a turning point in the temperature variation of PCM at time 25h. This point comes out again at time 49h with the same temperature at 25°C. According to the melting point of wax provided in Table 4. 2, it is believed that this is the congealing point of the PCM
3. When the PCM releases the latent heat, the generated voltage becomes stable as highlighted in Figure 7. 3(a). However, the latent heat in the newly fabricated system is still not enough. Its sensible heat is utilized during the experiment. It can be expected that with more PCM or latent heat capacity, the TEG will work better.
4. The harvested energy in total is 463 J over 54 hours, which represents an average power of 2.38 mW. The daily maximum power reaches 20 mW which corresponds to an energy conversion efficiency of 0.12%. This performance is already able to drive most of the current ultra-low power electronics.
5. Variations in voltage generation during the day can be used for sensing radiation. It can be utilized in some smart systems.
6. The temperature curve shows clearly the inertial effects of PCM in generating a temperature difference on the TEG. Indeed there is a shift of peak ambient temperature and peak internal temperature of the PCM. The shifts of temperatures between ambient and internal temperature PCM is favorable to maintain a gradient of temperature on TEG. It can be note that, in the absence of sun, the temperature inside the PCM remains high. This confirms the idea of heat storage in the PCM for the generation of micro-energy during night
7. Energy harvested at night forms 10% of the total energy. The absolute power generation in this real situation is achieved in autumn. It can be expected that the performance is better in the summer and lower in the winter.

In short, our newly fabricated TEG system is able to provide with maximum power density of 3.33$mWcm^{-3}$. The average power density varied with day in the year and the intraday weather. A typical sunny day can reach 0.4 $mWcm^{-3}$.

7.2.2 Configuration and performance of the self-powered system

The output voltage of the TEG system varies from 0 to maximum 1 V (with maximum solar radiation at 1000Wm^{-2}) which is not suitable to drive most of the common commercial low power electronic devices directly. A DC-DC converter is a possible solution to this problem. A self-powered temperature sensing system with step-up converter is proposed in our study, regulating the voltage at 3.3V which meets the voltage supply of the electronics. The configuration is shown in Figure 7. 4.

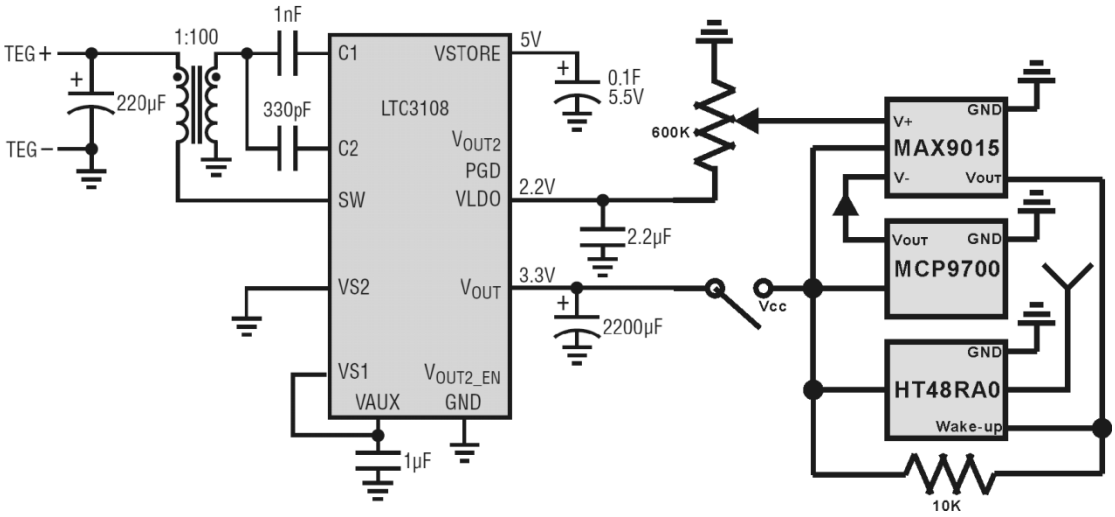

Figure 7. 4: Architecture of the self-powered temperature sensing system

There are six basic components in this system: transformer, step-up converter, temperature sensor, comparator, micro-controller and wireless transmitter. The ultralow voltage step-up converter (LTC3108 Linear Technology Corporation) begins to work when the input voltage is larger than 20mV. In order to let the system works with output voltage from the TEG as low as possible, a coupled inductor (LPR6235-752SML Coilcraft Inc.) with ratio of 1:100 is chosen as the transformer. The main output of the converter is set to 3.3V and a 2200 µF capacitor is connected to store the energy temporarily. It is sufficient to drive the temperature sensor, comparator, micro-controller and wireless transmitter at the same time. The output for the battery of the converter is connected to a 0.1 F capacitor, storing extra energy from the TEG when the primary capacitor is fully charged. A low-power linear active thermistor (MCP9700 Microchip Technology Inc.) is used to sensing the temperature on the PV panel. It is placed on the back side of the panel and it can transfer the temperature into analog output voltage. In order to limit our test to the demonstration of the efficient use of harvested micro-energy, without developing a specific wireless transmitter and electric switch with receiver, we have chose a commercial wireless doorbell which contains an integrated transmitting micro-controller (HT48RA0-2 Holtek Semiconductor Inc.) working at 433 MHz. In the present study, the smart action of electric switch with

wireless receiver is done manually when the bell rings. The wireless doorbell (D403 Friedland Company) is powered by the step-up converter directly, which keeps our system as a semi autonomous system. The micro-controller is put on standby most of the time when there is no command sent to the transmitter. It can be waken-up by a grounded triggering from the voltage comparator (MAX9015A Maxim Integrated Products, Inc.) and the doorbell will ring. The Inverting input of comparator is connected to the output of the temperature sensor while the port of noninverting input gets a given reference temperature from potentiometer driven by the low dropout linear regulator in the step-up converter.

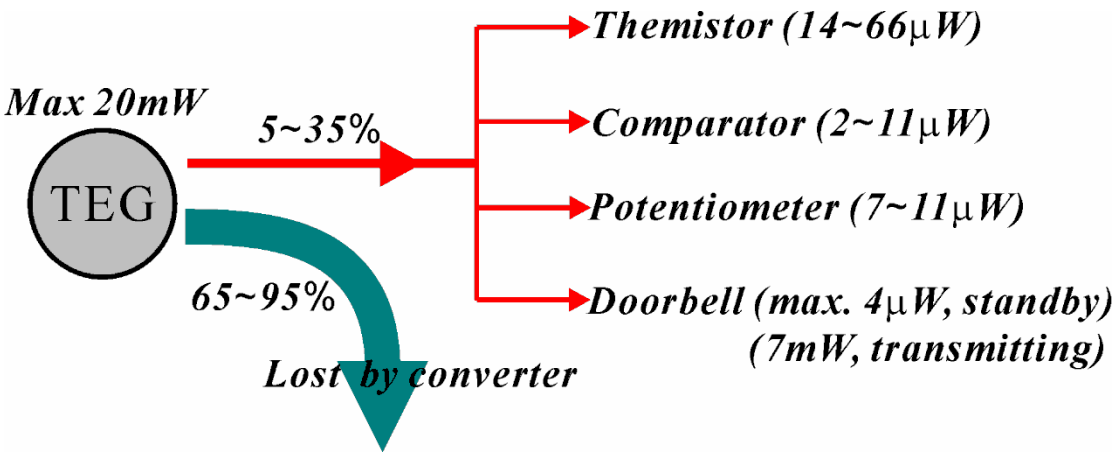

Figure 7. 5: Energy flow and consumption in the self-powered system

The characteristic of the self-powered system depends on the energy conversion efficiency of the DC-DC and the power consumption in the electronic devices. Figure 7. 5 shows the diagram of energy flow in the system. The TEG system can provide with maximum power of 25 mW. When the TEG is connected with the step-up converter, the output DC signal is changed into switched AC signal at first and amplified by the transformer after. Some part of the energy is lost in this process which depends on both the ratio of transformer and the input voltage to the converter. The maximum energy conversion efficiency can reach 35% in our case and the maximum possible efficiency for the converter is 60%. It is found that the step-up converter consumes the largest part of the harvested energy. The second largest power consumer is the doorbell when it is active. The temperature monitoring and the strategy of ring control is much less power consumption since it is not very smart. The control strategy can be improved when uses better controller, such as MSP430 mixed signal controller from Texas Instruments. The power consumption of that MCU is 1mW when it is active.

As a typical case study, the prototype work unit in section 4 is used to drive the self-powered system. It is irradiated by a constant radiation with maximum recorded value outside and it generates 150 mV in open circuit status. It is used to drive the step-up converter and the charge process is shown in Figure 7. 6. The voltage variation in the two capacitors (V_{out} is connected with 2200 μF while V_{store} with 0.1 F)

were recorded. It is found that the generated voltage decreases to 100 mV when the TEG is connected with the converter. It indicates that the external load is smaller than the internal resistance of the TEG. The ratio of the transformer is too large. It can be calculated that a ratio of 14 can realize the impedance matching. The calculated input power to the converter is 2 mW.

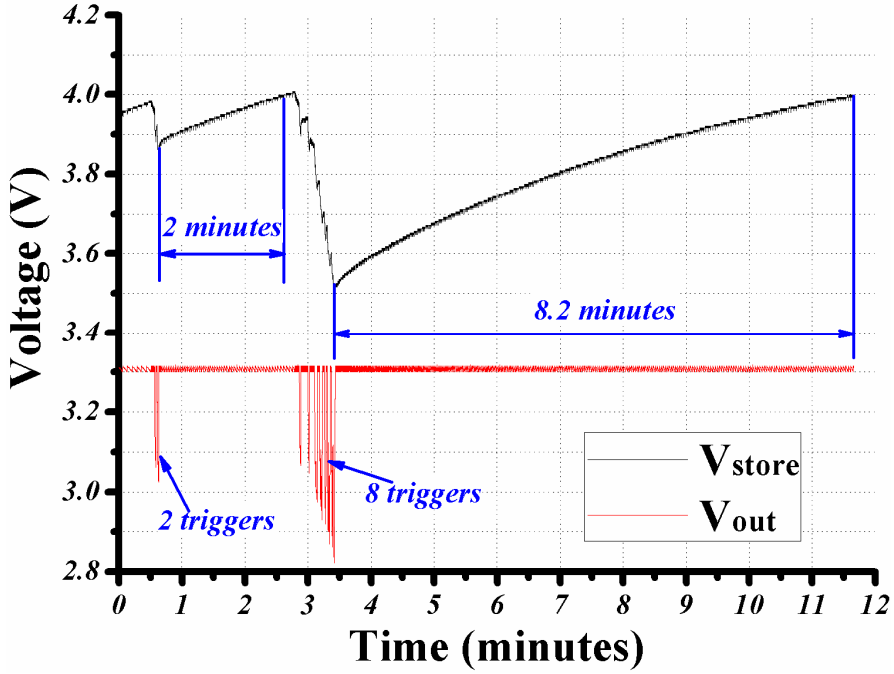

Figure 7. 6: Transmitting process of the temperature sensing system

When V_{out} is fully charged and V_{store} is charged to 4V, two groups of doorbell command were sent out by heating of temperature sensor manually. The recorded pattern of voltage variation shows that V_{out} is used to drive the electronic consumers directly while V_{store} will sense the change of V_{out} and recharge it quickly. The decrease of the V_{store} is in accordance with the power consumption of doorbell while the increase corresponds to the majority part of harvested energy from the TEG. The measured harvested power after converter is between 0.39 and 0.47 mW. The calculated energy conversion efficiency is 19.5~23.5% which is in accordance with the characteristics provided by the manufacturer. It can be expected that a transformer with suitable ratio will increase the energy conversion efficiency of converter and supply the electronic consumers more efficiently.

In short, the step-up converter is a potential solution in the self-powered temperature sensing system when the generated power from the TEG is insufficient to drive the electronic devices directly. With one pieces of TEC-12708 module and without matched impedance, the temperature sensor can send out at least one signal in every two minute. It can be expected that with the newly fabricated TEG system and a smaller ratio of transformer, the door bell can ring in less than 10 seconds during a sunny midday which is able to control the water cooling system continuously.

7.2.3 Configuration and performance of the PV with water cooling

The cooling of the PV panel is realized by water evaporation instead of water cycling system. At the backside of the panel, a water pipe system (WaterSmart drip line) was glued as the first layer. The drip line is controlled with a tap timer in order to create automatic drip system that is designed to work at low pressure and without a pump. A superabsorbent cloth is glued after the first layer of water pipe system. Then another layer of drip line is put on the first layer of cloth which is then covered again with another layer of superabsorbent cloth. It has two layers of both drip line and superabsorbent cloth. The assembled PV system is shown in Figure 7. 7.

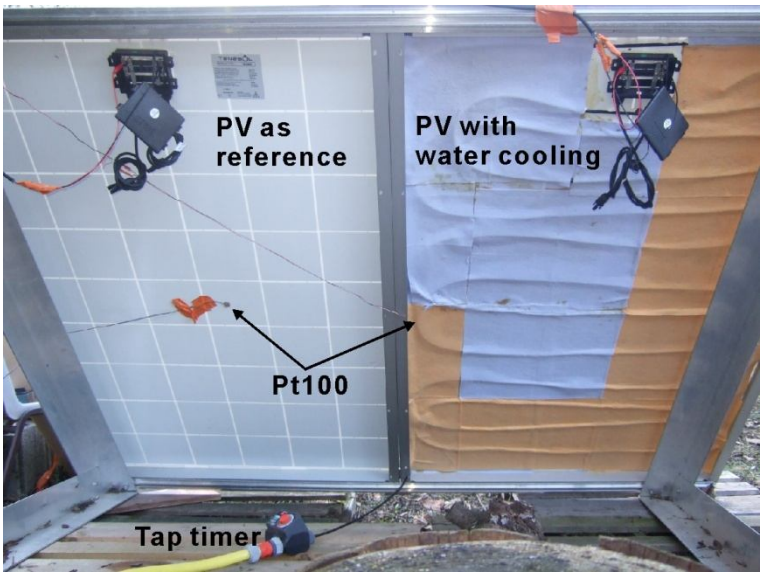

Figure 7. 7: PV panels with and without water cooling

In our test, without a wireless electric switch, the water supply is controlled manually but initialized with door bell. This function can be realized automatically by an universal switching receiver RCM 250 from Enocean Company. When opening the water drip line, the superabsorbent cloth is immerged quickly with the diffuse of water. Once the water supply is cut off, the refresh of the PV panel is done through drying process of the superabsorbent cloth. The water in the cloth evaporates by the heat absorbed from the PV panel.

In order to show clearly that the proposed TEG system and self-powered temperature system can help to improve the performance of the PV panel, we present in this paper the results when the water cooling system is turned on manually during each ten minutes in a sunny midday when the temperature on the PV panel is pretty high. It is supposed that the initialization of the water cooling system comes from the ring of door bell when the monitored temperature is higher than 47°C.

The tests were implemented as the same time and same place as shown in Figure 7. 3. It is obvious that the two consecutive days are quite the same in solar radiation and

ambient temperature. Besides, these two days are windless and convection effect is considered as natural convection. The records of the performance during these two days begin at 7:00 and last for 10 hours. The ambient temperature changes from 10 °C to 26 °C at midday and falls back to 10 °C during the night. It can be noted that the ambient thermal loading for the PV panels is low during this test. The maximum temperature on the PV panel reaches only 65 °C. However this test is still interesting for us since it illustrates our point of view by showing the small improvement. The improvement could be essential during the summer when the thermal loading is relatively strong. The two PV panels work without any special treatment during the first day. The cooling system is activated in the second day. Figure 7. 8(a)(b) present the voltage generation from the PV panels and the temperature variation on the back side of them. The results of the two PV panels are also compared with dimensionless value. Figure 7. 8(c)(d) present the ratio of measured data. These graphs show clearly that:

1. The variation in their temperature ratios is less than 15% while that of their voltage generation is less than 3%. The temperature of the PV panels with the cooling system is a little higher when the water is not supplied because the cloth on the rear side reduces convection.
2. When the cooling system is active at 39.7h, as shown in Figure 7. 8(d), significant improvements in voltage generation are achieved. The variation of their temperature ratios is more than 50%, while that of their voltage generation is 10%. It is thus seen that temperature monitoring by our self-powered wireless sensor can improve the output of PV panels by controlling a water-cooling system.

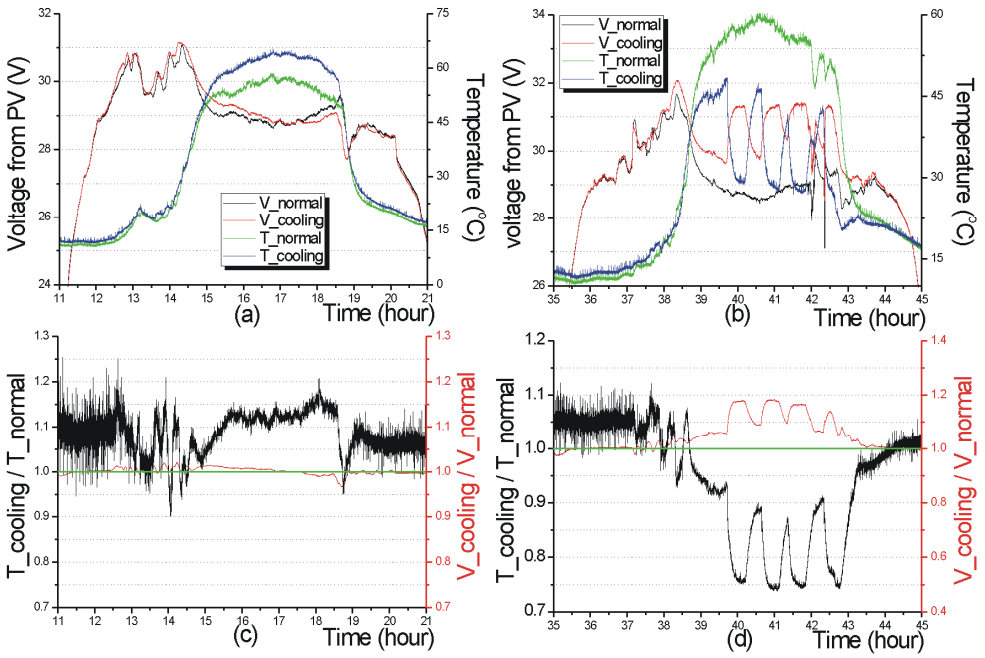

Figure 7. 8: Experimental results of the PVs with and without cooling: (a) and (c) are performance during the first day; (b) and (d) are performance during the second day.

7.3 Sectional summary

In this section, a framework of independent wireless temperature sensor node aims at improving the performance of a PV panel is introduced. It is considered as a typical application of harvested energy in buildings. The feasibility of the proposed wireless application is proved step by step. The solar thermal micro generator based on thermoelectric device and phase change material is inspected with its output voltage and power outside at first. It is found that the generated power from the improved work unit is 2.38mW in a typical sunny day in the autumn. It is sufficient to drive both a temperature sensor and wireless transmitter not continuously but intermittently. Since the generated voltage is not able to drive the electronic consumers directly, a step-up converter is adopted in the proposed power management circuit. The step-up converter also solves the problem of storage of electric energy as the output of TEG keeps on changing. It works like a filter of the varied daily solar thermal energy. The shortcoming of the step-up converter is that a major part (40%~95%) of the harvested energy can be lost during the voltage regulation. However, with our prototype power management circuit, it can respond to the target temperature in less than 10 seconds when the input solar radiation is around $900Wm^{-2}$.

The results of the semi autonomous temperature monitoring show that with a simple cooling system and without any other energy than the harvested micro-energy, one can increase the performance of a PV panel (10% profit with thermal loading in autumn).
This section shorts the distance between a scientific research and an engineering problem. It highlights the research of energy harvesting in substance and encourage us to devote more effort on this topic.

8. General conclusion and perspective

General conclusion

The harvesting of solar thermal energy with thermoelectric (or pyroelectric) effect and the harvesting of wind (or airflow) power with piezoelectric effect are studied in this thesis. The aim is to use the harvested micro energy to drive those ultra-low power electronics in buildings.

In the problem of solar thermal energy harvesting with thermoelectric effect, the energy conversion process includes three steps – optical conversion, thermal transformation and thermoelectric coupling. The focus in this study is the optimization of the thermal design. Therefore, we propose to use the thermal inertia effect on the cold face of the TEG which can be realized via phase change material or other method that provides with large heat capacitance. It aims to increases the temperature difference on the TEG by maintain a relatively low average temperature in the active material during the day. It aims also to enhance the heat flow going through the active material and reduces the thermal energy which is released by convection. Another advantage of the thermal inertia effect is that it can let the TEG work continuously all over the night. Currently, with flat solar thermal collector and material figure of merit at $6.4\times10^{-4}°C^{-1}$ the achieved maximum power with ambient solar radiation at $894Wm^{-2}$ is $1Wm^{-2}$ which corresponds to an energy conversion efficiency of 0.1%. It is measured with matched resistor. The major shortcomings in an energy harvesting system with thermoelectric effect is the volume power density when taking account the assistant cooling structure such as the PCM proposed by us, the heat sink in an ordinary design and so on. When the total volume of the system is not so important such as those portable or wearable applications, the potential ability of power generation with solar radiation and thermoelectric device is great. This situation meets nicely the condition in applications with buildings or any other fixed place. The ambient solar radiation is abundant and more and more predictable with the development of meteorology. It is a reliable energy source and is helpful to analyze the variation of the performance of the TEG. The rapid progress of the thermoelectric material with high figure of merit and the simple method of efficiency improvement through solar concentration technique make the TEG promising in the low power applications in buildings.

In the problem of harvesting solar thermal energy with pyroelectric effect, our major contribution lies in the proposal and analysis of utilizing the inherent characteristics of the ambient wind speed which is always changing with time. It is recognized from the literature review that the energy conversion efficiency of a PYEG could be higher than a TEG since the coupling process is electrically controllable. The major obstacle which is seeking for a feasible alternating temperature source blocks the progress the PYEG. Therefore, we aim to solve this problem with ambient wind speed fluctuation when

there is solar radiation. The combination of radiation as the hot reservoir and strong forced convection as the cold reservoir provides temperature variation in the active material. The prototype PYEG without concentration of solar radiation and with pyroelectric coefficient of $688\mu Cm^{-2}°C^{-1}$ between 25°C and 65°C can provide an average power of $0.6mWm^{-2}$ when measured with energy storage from AC-DC transformation. The temperature variation with our proposal reaches 16°C with wind speed alternating between 0 and $2ms^{-1}$ and intensity of radiation at $1000Wm^{-2}$. It is proved available in ambient situation with experiment. The actual energy conversion efficiency of the PYEG is very low compared with the TEG however our work is very different from most of the experimental prototypes in literatures which generate arbitrary temperature variation in the PYEG without caring about the feasibility of the input loading. The major advantage of the proposed PYEG is the extraordinary simple 2D structure which is different from the newly developed TEG that needs to occupy a relatively large 3D space. It could be especially suitable when there is aesthetic demand in the typical application around buildings. The improvement of the performance of a PYEG could be realized by circuit conditioning with Ericsson cycle (e.g. SSHI technique). With breakthrough in material which contains giant pyroelectric and electrocaloric effect, the proposed PYEG can also be favorable in applications in buildings.

In the problem of wind (or airflow) power harvesting with piezoelectric effect, we focuses on a newly proposed cavity structure which enhance the alternating interaction between the fluid flow and the mechanical structure. This structure is interested in our study since the reported energy conversion efficiency [JI 2010] without improvement of SSHI technique has already reaches 1% with wind speed at $3ms^{-1}$. However, the performance of our prototype is very different. The average power generation is $8.9mWm^{-2}$ when the input wind speed is 4.7 ms^{-1} and the maximum energy conversion efficiency which is estimated as 0.03% occurs at wind speed of $3ms^{-1}$ in our case. The huge difference in the energy conversion efficiency of these two experimental prototypes could come from the different setup of the cavity, aperture and cantilever. It makes us to highlight the importance of the fluid structure interaction problem in such a PIEG. The major advantage of such a PIEG is the potential high energy conversion efficiency especially when it is combined with SSHI technique. The ultimate structure could be compact according to the previous study [JI 2010] which could favorable in some special applications in buildings.

Perspective

Further work on the ambient energy harvesting based on coupling effect in material could progress in these directions below:

1. For the case of the proposed TEG:

   (a) The analysis on the thermal energy balance between the PCM and the environment according to the local solar radiation, ambient temperature and wind speed is necessary in order to further optimize the long time performance of the system according to our developed electrical analogy model.

   (b) When the coupling from the thermal energy to the electrical energy is much higher (the energy conversion efficiency is more than 1%) with improved material or input thermal loading, the proposed electrical analogy model is not precise. A more precise simplified model needs to be setup to analyze the thermal and electrical response together.

   (c) The output voltage of the TEG is alternating between the day and night, a low power electronic switch is necessary in an ultimate total autonomous application.

2. For the case of the proposed PYEG:

   (a) The SSHI technique can be utilized in the PYEG with the self-sensing ability of the PYEG. Since the pyroelectric material is sensitive with temperature variation, it can be expected that the voltage inverter is controlled by the PYEG itself. According to [GUY 2009], the performance increase of 2.5 times is possible.

   (b) There is a similar problem of the proposed modeling method in the PYEG as that in the TEG when the thermal electrical coupling becomes strong. A more precise model is needed when analyzing a strong coupling process.

3. For the case of the proposed PIEG:

   (a) The SSHI technique can be utilized in the PIEG. The performance increase of 9 times is possible according to [GUY 2005].

   (b) The mechanism of the fluid structure interaction process needs to be inspected in detail. Currently, the lumped parameter model has already provided the relationship between the input volumetric flow rate and the output

performance. However, the problem is completely different when harvesting the natural wind (or airflow) which is low impedance source. It is still not clear with the relationship between the incoming wind speed and the actual volumetric flow rate in the cavity. According to our comprehension, it becomes a problem of form drag analysis in fluid dynamics.

(c) On the compact design of a PIEG, a newly developed piezoelectric torsional transducer [PAN 2008] is proposed to be inspected. It is able to transform torque instead of force into electricity.

In a building, it is expected that more and more self-powered wireless sensors with low energy consuming are integrated making people's life more comfortable and convenient. Based on the results of the TEG device, one can easily expect many other applications different from the one presented as example with PV-panels in this thesis. The harvested energy could be used to charge the battery for emergency light, which is active for short time. It may be used to drive a smart weather monitor, sensing the ambient temperature, rainfall, wind, solar radiation…, which decides the status (open or close) of the windows in a house, utilizing the maximum illumination, fresh air and avoiding moisture at the same time……

Figure 8. 1: Location of energy harvesting technology

The energy harvesting technology is promising in the near future since people's life are more and more dependent on the information in the digital world. The Figure 8. 1 reminds us that it is not only high power (more than one watt) that can make our life convenient and comfortable but also low power that is helpful in our daily life. One important fact is that there isn't still limitation for the minimum power consumption with transfer of information.

List of Publication

International Journal

PhD topic on energy harvesting in France (2009 - 2011)

[AGB 2010] A. Agbossou, Q. Zhang, G. Sebald, D. Guyomar, Solar micro-energy harvesting based on thermoelectric and latent heat effects. Part I: Theoretical analysis, Sens. Actuators A: Phys. 163 (2010) 277-283

[ZHA 2010] Q. Zhang, A. Agbossou, Zhihua Feng, Mathieu Cosnier, Solar micro-energy harvesting based on thermoelectric and latent heat effects. Part II: Experimental analysis, Sens. Actuators A: Phys. 163 (2010) 284-290.

[ZHA 2011] Q. Zhang, A. Agbossou, Z.H. Feng, M. Cosnier, Solar micro-energy harvesting with pyroelectric effect and wind flow, Sensors and Actuators A: Physical (DOI: 10.1016/j.sna.2011.04.045) Accepted

PhD topic on piezoelectric motor in China (2008 - 2011)

[ZHA 2011] Q. Zhang, C.L. Pan, Y.T. Ma, F.R. Kong, Z.H. Feng, Piezoelectric rotary motor based on active bulk torsional element with grooved helical electrodes, IEEE/ASME Trans. Mechatron. 10.1109/TMECH.2010.2099129

[HAN 2009] W.X. Han, Q. Zhang, Y.T. Ma, C.L. Pan, Z.H. Feng, An impact rotary motor based on a fiber torsional piezoelectric actuator, Rev. Sci. Instrum. 80 (2009) 014701.

[MA 2009] Y.T. Ma, C.L. Pan, Q. Zhang, F.R. Kong, and Z.H. Feng, Two-phase piezoelectric motor using a multiple-tube structure actuator, Japanese Journal of Applied Physics 48 (9) (2009) 096501.

[PAN 2008] C.L. Pan, Y.T. Ma, Y.B. Liu, Q. Zhang, and Z.H. Feng, Torsional displacement of piezoelectric fiber actuators with helical electrodes, Sensors and Actuators A: Physical 148 (1) (2008) 250-258.

[MA 2009] Y.T. Ma, F.R. Kong, C.L. Pan, Q. Zhang, and Z.H. Feng, Miniature tubular centrifugal piezoelectric pump utilizing wobbling motion, Sensors and Actuators A: Physical 157 (2) (2010) 322-327.

International conference

[ZHA 2011] Q. Zhang, A. Agbossou, Z.H. Feng, A. Grillet, Phase change material and the thermoelectric effect for solar energy harvesting and storage, Proceedings of the ASME/JSME 2011 8th Thermal Engineering Joint Conference, March 13-17, 2011, Honolulu, Hawaii, USA

References

[AGB 2010] A. Agbossou, Q. Zhang, G. Sebald, D. Guyomar, Solar micro-energy harvesting based on thermoelectric and latent heat effects. Part I: Theoretical analysis, Sens. Actuators A: Phys. 163 (2010) 277-283

[AHM 2006] M. Ahmad, A. Bontemps, H. Sallee, D. Quenard, Thermal testing and numerical simulation of a prototype cell using light wallboards coupling vacuum isolation panels and phase change material, Energy Build. 38 (6) (2006) 673–681.

[AMA 2010] R. Amatya, R.J. Ram, Solar thermoelectric generator for micropower applications, J. Electron. Mater. 39 (2010) 1735-1740.

[ANT 2007] S.R. Antonal, H.A. Sodano, A review of power harvesting using piezoelectric materials (2003–2006), Smart Mater. Struct. 16 (2007) R1-R21.

[ARK 2005] C. Arkar, S. Medved, Influence of accuracy of thermal property data of a phase change material on the result of a numerical model of a packed bed latent heat storage with spheres, Thermochim. Acta 438 (2005) 192–201.

[BIR 1986] E. Birks, L. Shebanov, A. Sternberg, Electrocaloric effect in PLZT ceramics, Ferroelectrics, 69 (1986) 125-129.

[BUC 1999] R.C. Buchanan J. Huang, Pyroelectric and sensor properties of ferroelectric thin films for energy conversion, J. Eur. Ceram. Soc. 19 (1999) 1467-1471.

[BUD 2004] M. Budinger, J.F. Rouchon, B. Nogarede, Analytical modeling for the design of a piezoelectric rotating-mode motor, IEEE/ASME Trans. Mechatron. 9 (2004) 1-9.

[BLA 1998] Eric BLANC, Etude du comportement thermique de bâtiments tertiaires chauffés au gaz naturel, Thèse en Génie Civil et Sciences de l'Habitat - Université de Savoie, 27 novembre 1998.

[CAR 2010] J.P. Carmoa, L.M. Goncalvesa, R.F. Wolffenbuttelb, J.H. Correiaa, A planar thermoelectric power generator for integration in wearable microsystems, Sens. Actuators, A 161 (2010) 199-204.

[CAR2 2010] E.J. Carlson, K. Strunz, B. P. Otis, A 20 mV input boost converter with efficient digital control for thermoelectric energy harvesting, IEEE J. Solid-State Circuits 45 (2010) 741-750.

[CHA 2010] D. Champier, J.P. Bedecarrats, M. Rivaletto, F. Strub, Thermoelectric power generation from biomass cook stoves, Energy 35 (2010) 935-942.

[CHE 1996] J.C. Chen, Thermodynamic analysis of a solar-driven thermoelectric generator, J. Appl. Phys. 79 (1996) 2717-2721.

[CHI 1984] M. Chirtoc, R.M. Candea, V. Mercea, Operation theory of pyroelectric detectors.1. a new physical model and the resulting operation modes, Ferroelectrics 56 (1984) 283-291.

[CHU 2003] D.L. Churchill, M.J. Hamel, C.P. Townsend, S.W. Arms, Strain energy harvesting for wireless sensor networks, Proc. SPIE 5055 (2003) 319-327.

[CLA 2010] D. St. Clair, A. Bibo, V. R. Sennakesavababu, M. F. Daqaq, G. Li, A scalable concept for micropower generation using flow-induced self-excited oscillations, Appl. Phys. Lett. 96 (2010) 144103.

[COO 2008] K.A. Cook-Chennault, N. Thambi and A.M. Sastry, Powering MEMS portable devices—a review of non-regenerative and regenerative power supply systems with special emphasis on piezoelectric energy harvesting systems, Smart Mater. Struct. 17 (2008) 043001 (33pp).

[CUA 2010] A. Cuadrasa, M. Gasullaa, V. Ferrari, Thermal energy harvesting through pyroelectricity, Sens. Actuators, A 158 (2010) 132-139.

[DEN 2009] Y.G. Deng, J. Liu, Recent advances in direct solar thermal power generation, J. Renewable Sustainable Energy 1 (2009) 052701.

[DUF 1991] J.A. Duffie, W.A. Beckman, Solar engineering of thermal processes. 3nd ed. New York: Wiley; 2006.

[FAN 2010] J. Fang, H. Frederich, L. Pilon, Harvesting nanoscale thermal radiation using pyroelectric materials, J. Heat Transfer 132 (2010) 092701.

[FAT 1966] E. Fatuzzo, H. Kiess, R. Nitsche, Theoretical efficiency of pyroelectric power converters, J. Appl. Phys. 37(1966) 510-516.

[FRA 2010] G. Fraisse, M. Lazard, C. Goupil, J.Y. Serrat, Study of a thermoelement's behavior through a modeling based on electrical analogy, Int. J. Heat Mass Transfer 53 (2010) 3503-3512.

[FUN 2008] Y.C. Fung, An introduction to the Theory of Aeroelasticity, N.Y.: Dover Publications, 2008.

[GHA 2008] N. Ghafouri, H. Kim, M.Z. Atashbar, and K. Najafi, A micro thermoelectric energy scavenger for a hybrid insect, IEEE SENSORS 2008 Conference (2008) 1249-1252.

[GOL 1980] H. J. Goldsmid, J.E. Giutronich, M.M. Kaila, Solar thermoelectric generation using bismuth telluride alloys, Sol. Energy 24 (1980) 435-440.

[GOL 2008] F. Goldschmidtboeing, P. Woias, Characterization of different beam shapes for piezoelectric energy harvesting, J. Micromech. Microeng. 18 (2008) 104013 (7pp).

[GOU 2009] C. Goupil, Thermodynamics of the thermoelectric potential, J. Appl. Phys. 106 (2009) 104907.

[GOU 2010] X.L. Gou, H. Xiao, S.W. Yang, Modeling, experimental study and optimization on low-temperature waste heat thermoelectric generator system, Appl. Energy 87 (2010) 3131-3136.

[GUI 2008] R. Guigon, J.J. Chaillout, T. Jager, G.Despesse, Harvesting raindrop energy: experimental study, Smart Mater. Struct. 17 (2008) 015039 (6pp).

[GUI2 2008] R. Guigon, J.J. Chaillout, T. Jager, G. Despesse, Harvesting raindrop energy: theory, Smart Mater. Struct. 17 (2008) 015038 (8pp).

[GUY 2005] D. Guyomar, A. Badel, E. Lefeuvre, C. Richard, Toward energy harvesting using active materials and conversion improvement by nonlinear processing, IEEE Trans. Ultrason. Ferroelectr. Freq. Control 52 (2005) 584-595.

[GUY 2008] D. Guyomar, S. Pruvost, G. Sebald, Energy harvesting aased on FE-FE transition in ferroelectric single crystals, IEEE Trans. Ultrason. Ferroelectr. Freq. Control 55 (2008) 279-285.

[GUY 2009] D. Guyomar, G. Sebald, E. Lefeuvre, A. Khodayari, Toward heat energy harvesting using pyroelectric material, J. Intell. Mater. Syst. Struct. 20 (2009) 265-271.

[GYS 2005] B. Gyselinckx, C. Van Hoof, J. Ryckaert, R.F.Yazicioglu, P. Fiorini, V. Leonov, Human++: Autonomous wireless sensors for body area networks, Custom Integrated Circuits Conference, 2005, Proceedings of the IEEE 2005 (2005) 13-19.

[HE 2003] H.L. He, G.G. Yu, D. Niu, Method of global solar radiation calculation on complex territories, Resources Science, 25 (2003) 78-85.

[HOA 2009] D.C. Hoang, Y.K. Tan, H.B. Chng, S.K. Panda, Thermal energy harvesting from human warmth for wireless body area network in medical healthcare system, International Conference on Power Electronics and Drive Systems, 2009. PEDS 2009.(2009) 1277-1282.

[HSI 1995] H.Y. Hsieh, H.H. Bau, J.N. Zemel, Pyroelectric anemometry: theory of operation, Sens. Actuators, A 49 (1995) 125-132.

[HSI 2010] Y.Y. Hsiao, W.C. Chang, S.L. Chen, A mathematic model of thermoelectric module with applications on waste heat recovery from automobile engine, Energy 35 (2010) 1447-1454.

[HSU 2010] C.T. Hsu, D.J. Yao, K.J. Ye, B. Yu, Renewable energy of waste heat recovery system for automobiles, J. Renewable Sustainable Energy 2 (2010) 013105.

[HUD 2008] N.S. Hudaka, G.G. Amatucci, Small-scale energy harvesting through thermoelectric, vibration, and radiofrequency power conversion, J. Appl. Phys. 103 (2008) 101301.

[HUM 2008] http://www.humdingerwind.com/pdf/microBelt_brief.pdf

[IEEE 1987] IEEE Standard on Piezoelectricity. 1988. The Institute of Electrical and Electronic Engineers, Inc.

[INC 2007] Frank P. Incropera et al., Fundamentals of Heat and Mass Transfer, 6th edition, J. Wiley & Sons: New York, 2007.

[ISM 2002] K.A.R. Ismail, J.R. Henrıquez, Numerical and experimental study of spherical capsules packed bed latent heat storage system, Appl. Therm. Eng. 22 (2002) 1705–1716.

[ISM2 2002] K.A.R. Ismail, J.R. Henrıquez, Parametric study on composite and PCM glass systems, Energy Convers. Manage. 43 (2002) 973–993.

[JEF 2003] G. Jeffrey Snyder, T. Ursell, Thermoelectric efficiency and compatibility, Phys. Rev. Lett. 91 (2003)

[JI 2010] J. Ji, F.R. Kong, L.G. He, Q.C. Guan, and Z.H. Feng, Piezoelectric

wind-energy-harvesting device with reed and resonant cavity, Jpn. J. Appl. Phys. 49 (2010) 050204 (3 pages).

[JIA 2011] L.Q. Jiang, D.Q. Zhao, C.M. Guo, X.H. Wang, Experimental study of a plat-flame micro combustor burning DME for thermoelectric power generation, Energy Convers. Manage. 52 (2011) 596-602.

[KAR 1948] T. Von Karman, Progress in the statistical theory of turbulence, Proc Natl Acad Sci USA 34(1948) 530-539.

[KHA 2006] N.M. Khattab , E.T. El Shenawy, Optimal operation of thermoelectric cooler driven by solar thermoelectric generator, Energy Convers. Manage. 47 (2006) 407-426.

[KHA 2010] A. Khaligh, P. Zeng, C. Zheng, Kinetic energy harvesting using piezoelectric and electromagnetic technologies—state of the art, IEEE Trans. Ind. Electron. 57 (2010) 850-860.

[KHO 2009] A. Khodayari, S. Pruvost, G. Sebald, D. Guyomar, S. Mohammadi, Nonlinear pyroelectric energy harvesting from relaxor single crystals, IEEE Trans. Ultrason. Ferroelectr. Freq. Control 56 (2009) 693-699.

[KIM 2008] R.Y. Kim, J.S. Lai, A seamless mode transfer maximum power point tracking controller for thermoelectric generator applications, IEEE Trans. Power Electron. 23 (2008) 2310-2318.

[KIM 2009] S.H. Kim, C.H. Ji, P. Galle, etc. An electromagnetic energy scavenger from direct airflow, J. Micromech. Microeng. 19 (2009) 094010 (8pp).

[KOU 2007] L. Kouchachvili, M. Ikura, Pyroelectric conversion—Effects of P(VDF – TrFE) preconditioning on power conversion, J. Electrostat. 65 (2007) 182-188.

[KWO 2010] S.D. Kwona, A T-shaped piezoelectric cantilever for fluid energy harvesting, Appl. Phys. Lett. 97 (2010) 164102.

[LAW 2002] E.E. Lawrence, A study of heat sink performance in air and soil for use in a thermoelectric energy harvesting device, 21st International Conference on Thermoelectronics (2002) 446-449.

[LAY 2009] A. Lay-Ekuakille, G. Vendramin, A. Trotta, G. Mazzotta, Thermoelectric generator design based on power from body heat for biomedical autonomous devices, MeMeA 2009-International Workshop on Medical Measurements and Applications (2009) 1-4.

[LEE 2004] C.S. Lee, J. Joo, S. Han, S.K. Koh, Multifunctional transducer using poly (vinylidene fluoride) active layer and highlyconducting poly (3,4 - ethylenedioxythiophene) electrode: actuator and generator, Appl. Phys. Lett. 85 (2004) 1841-1843.

[LEE 2005] C.S. Lee, J. Joo, S. Han, J.H. Lee, S.K. Koh, Poly (vinylidene fluoride) transducers with highly conducting poly (3, 4-ethylenedioxythiophene) electrodes, Synth. Met. 152 (2005) 49-52.

[LEE 2009] C. Lee, Y.M.Lim, B. Yang, ect. Theoretical comparison of the energy harvesting capability among various electrostatic mechanisms from structure aspect, Sensors and Actuators A 156 (2009) 208-216.

[LEF 2005] E. Lefeuvre, A. Badel, C. Richard, D. Guyomar, Piezoelectric energy

harvesting device optimization by synchronous electric charge extraction, J. Intell. Mater. Syst. Struct. 16 (2005) 965-876.

[LEO 2007] V. Leonov, R.J.M. Vullers , Thermoelectric generators on living beings, Proc. 5th Euro. Conf. Thermoelectrics, Odessa, Ukraine, Sep. 10-12, 2007 (these proceedings).

[LEO2 2007] V. Leonov, T. Torfs, P. Fiorini, C. Van Hoof, Thermoelectric converters of human warmth for self-powered wireless sensor nodes, IEEE Sensors J. 7 (2007) 650-657.

[LER 2008] C. Lertsatitthanakorn, N. Khasee, S. Atthajariyakul, etc. Performance analysis of a double-pass thermoelectric solar air collector, Sol. Energy Mater. Sol. Cells 92 (2008) 1105-1109.

[LI 2010] P. Li, L.L. Cai, P.C. Zhai, X.F. Tang, Q.J. Zhang, M. Niino, Design of a concentration solar thermoelectric generator, J. Electron. Mater. 39 (2010) 1522-1530.

[LIU 1978] S.T. Liu, D. Long, Pyroelectric detectors and materials, Proc. IEEE 66 (1978) 14-26.

[LIU 2004] S.B. Liu, Y.Q. Li, Research on the electrocaloric effect of PMN/PT solid solution for ferroelectrics MEMS microcooler, Mater. Sci. Eng., B 113 (2004) 46-49.

[LIU 2007] W.Q. Liu, Z.H. Feng, J. He, R.B. Liu, Maximum mechanical energy harvesting strategy for a piezoelement, Smart Mater. Struct. 16 (2007) 2130-2136.

[LOS 2010] M. Lossec, B. Multon, H. Ben Ahmed, C. Goupil, Thermoelectric generator placed on the human body: system modeling and energy conversion improvements, Eur. Phys. J. Appl. Phys. 52 (2010) 11103

[MAI 2009] M.R. Maixner, J.W. Stevens, Assessment of near-surface ground temperature profiles for optimal placement of a thermoelectric device, Energy Convers. Manage. 50 (2009) 2361-2365.

[MAN 2004] S. Maneewan, J. Khedari, B. Zeghmati, J. Hirunlabh, J. Eakburanawat, Investigation on generated power of thermoelectric roof solar collector, Renewable Energy 29 (2004) 743-752.

[MAN 2005] S. Maneewan, J. Hirunlabh, J. Khedari, B. Zeghmati, S. Teekasap, Heat gain reduction by means of thermoelectric roof solar collector, Sol. Energy 78 (2005) 495-503.

[MAT 2007] L. Mateu, C. Codrea, N. Lucas, M. Pollak, P. Spies, Human body energy harvesting thermogenerator for sensing applications, 2007 International Conference on Sensor Technologies and Applications (2007) 366-372.

[MGB 2010] C. A. Mgbemene, etc. Electricity generation from a compound parabolic concentrator coupled to a thermoelectric module, J. Sol. Energy Eng. 132 (2010) 031015.

[MIS 2006] A.S. Mischenko, Q. Zhang , R.W. Whatmore, etc. Giant electrocaloric effect in the thin film relaxor ferroelectric 0.9 PbMg1/3Nb2/3O3-0.1 PbTiO3 near room temperature, Appl. Phys. Lett. 89 (2006) 242912.

[MIS2 2006] A.S. Mischenko, Q. Zhang, J.F. Scott, R.W. Whatmore, N.D. Mathur, Giant Electrocaloric Effect in Thin-Film PbZr0.95Ti0.05O3, Science 311 (2006) 1270-1271.

[MIT 2004] P.D. Mitcheson, P. Miao, B.H. Stark, E.M. Yeatman, A.S. Holmes, T.C. Green,MEMS electrostatic micropower generator for low frequency operation, Sens. Actuators, A 115 (2004) 523–529.

[MOR 2010] A.N. Morozovska, E.A. Eliseev, G.S. Svechnikov, and S.V. Kalinin, Pyroelectric response of ferroelectric nanowires: Size effect and electric energy harvesting, J. Appl. Phys. 108 (2010) 042009.

[MUN 1991] W.V. Münch, V. Thiemann, Pyroelector array with PVDF on silicon integrated circuit, Sens. Actuators, A 25 (1991) 167-172.

[NAV 2010] A. Navid, D. Vanderpool, A. Bah, L. Pilon, Towards optimization of a pyroelectric energy converter for harvesting waste heat, Int. J. Heat Mass Transfer 53 (2010) 4060-4070.

[NAV2 2010] A. Navid, C.S. Lynch, L. Pilon, Purified and porous poly(vinylidene fluoride - trifluoroethylene) thin films for pyroelectric infrared sensing and energy harvesting, Smart Mater. Struct. 19 (2010) 055006 (13pp).

[NEE 2000] D.A. Neeper, Thermal dynamics of wallboard with latent heat storage, Sol. Energy 68 (2000) 393-403.

[NI 2009] X,X. Ni, G. C. Liang, J.S. Wang, B.W. Li, Disorder enhances thermoelectric figure of merit in armchair graphane nanoribbons, Appl. Phys. Lett. 95 (2009) 192114.

[NIU 2009] X. Niu, J.L. Yu, S.Z. Wang, Experimental study on low-temperature waste heat thermoelectric generator, J. Power Sources 188 (2009) 621-626.

[NUW 2005] R.Y. Nuwayhid, A. Shihadeh, N. Ghaddar, Development and testing of a domestic woodstove thermoelectric generator with natural convection cooling, Energy Convers. Manage. 46 (2005) 1631-1643.

[OH 2010] S.J. Oh, H.J. Han, S.B. Han, J.Y. Lee, W. G. Chun, Development of a tree-shaped wind power system using piezoelectric materials, Int. J. Energy Res. 34 (2010) 431-437.

[OLS 1982] R.B. Olsen, Ferroelectric conversion of heat to electrical energy- a demonstration, J. Energy 6 (1982) 91-95.

[OME 1998] S.A. Omer, D.G. Infield, Design optimization of thermoelectric devices for solar power generation, Sol. Energy Mater. Sol. Cells 53 (1998) 67-82.

[OME 2000] S.A. Omer, D.G. Infield, Design and thermal analysis of a two stage solar concentrator for combined heat and thermoelectric power generation, Energy Convers. Manage. 41 (2000) 737-756.

[PAL 2008] J.A. Palyvos, A survey of wind convection coefficient correlations for building envelope energy systems' modeling, Appl. Therm. Eng. 28 (2008) 801-808.

[PAN 2008] C.L. Pan, Z.H. Feng, Y.T. Ma, Y.B. Liu, Small torsional piezoelectric fiber actuators with helical electrodes, Appl. Phys. Lett. 92 (2008)

012923.

[PEN 2008] J. Penders, B. Gyselinckx, R. Vullers, ect. Human++: from technology to emerging health monitoring concepts, The 5th International Summer School and Symposium on Medical Devices and Biosensors. ISSS-MDBS 2008. (2008) 94-98.

[PEN 2009] J. Penders, J.van de Molengraft, L. Brown, etc. Potential and challenges of Body Area Networks for personal health, 31st Annual International Conference of the IEEE EMBS (2009) 6569-6572.

[PIM 2010] D. Pimentel, P. Musilek, A. Knight, J. Heckenbergerova, Characterization of a wind flutter generator, 9th International Conference on Environment and Electrical Engineering (EEEIC) (2010) 81-84.

[PRI 2005] S. Priya, C.T. Chen, D. Fye, J. Zahnd, Piezoelectric windmill: a novel solution to remote sensing, Jpn. J. Appl. Phys. 44 (2005) L104-L107.

[PRI2 2005] S. Priya, Modeling of electric energy harvesting using piezoelectric windmill, Appl. Phys. Lett. 87 (2005) 184101.

[QIU 2008] K. Qiu, A.C.S. Hayden, Development of a thermoelectric self-powered residential heating system, J. Power Sources 180 (2008) 884-889.

[RIC 2000] C. Richard, D. Guyomar, D. Audigier, H. Bassaler, Enhanced semi passive damping using continuous switching of a piezoelectric device on an inductor, Proceedings of SPIE 3989 (2000) 288-299.

[RIC 2004] C.D. Richards, M.J. Anderson, D.F. Bahr, R.F. Richards, Efficiency of energy conversion for devices containing a piezoelectric component, J. Micromech. Microeng. 14 (2004) 717-721

[RIF 2003] S.B. Riffat, X.L. Ma, Thermoelectrics: a review of present and potential applications,Appl. Therm. Eng. 23 (2003) 913-935.

[ROB 2005] R. Robert, S. Romer, A. Reller, A. Weidenkaff, Nanostructured complex cobalt oxides as potential materials for solar thermoelectric power generators, Adv. Eng. Mater. 7 (2005) 303-308.

[ROB 2007] R. Robert, L. Bocher, B. Sipos, M. Dobeli, A. Weidenkaff, Ni-doped cobaltates as potential materials for high temperature solar thermoelectric converters, Prog. Solid State Chem. 35 (2007) 447-455.

[ROU 2003] S.J. Roundy, Energy scavenging for wireless sensors nodes with focus on vibration to electricity conversion, Phd thesis in the University of California, Berkeley

[ROU 2005] S. Roundy, ect. Improving power output for vibration-based energy scavengers, IEEE Pervasive Comput. 4 (2005) 28-36.

[ROW 2006] D.M. Rowe, Thermoelectric waste heat recovery as a renewable energy source, International Journal of Innovations in Energy Systems and Power, 1 (2006) 13-23.

[SCH 2008] A.D. Schlichting, S.R. Anton, D.J. Inman, Motorcycle waste heat energy harvesting, Proc. SPIE 6930 (2008) 69300B.

[SEB 2006] G. Sebald, L. Seveyrat, D. Guyomar, L. Lebrun, B. Guiffard, S. Pruvost, Electrocaloric and pyroelectric properties of

$0.75Pb(Mg_{1/3}Nb_{2/3})O_3$-$0.25PbTiO_3$ single crystals, J. Appl. Phys. 100 (2006) 124112.

[SEB 2008] G. Sebald, E. Lefeuvre, D. Guyomar, Pyroelectric energy conversion: optimization principles, IEEE Trans. Ultrason. Ferroelectr. Freq. Control 55 (2008) 538-551.

[SEB2 2008] G. Sebald, S. Pruvost, D. Guyomar, Energy harvesting based on Ericsson pyroelectric cycles in a relaxor ferroelectric ceramic, Smart Mater. Struct. 17 (2008) 015012 (6pp).

[SHA 2007] Y.H. Shang, Y.H. Li, H.Y. Yu, H.G. Sun, B. Su, Experimental investigation on thermoelectric generator of micro hybrid power source, Proc. SPIE 6724 (2007) 672412.

[SHA 2010] W.W. Shao, Z.H. Feng, J.W. Xu, C.L. Pan and Y.B. Liu, Radiator heightens power density of piezoelectric transformers, Electron. Lett. 46 (2010) 1662-1663.

[SHE 1992] L. Shebanovs, K. Borman, On lead-scnadium tantalate solid solutions with high electrocaloric effects, Ferroelectrics 127 (1992) 143-148.

[SHE 2010] G.-J. Sheu, S.-M. Yang, T. Lee, Development of a low frequency electrostatic comb-drive energy harvester compatible to SoC design by cmos process, Sensors and Actuators: A Physical (2010), doi:10.1016/j.sna.2010.07.013.

[SNY 2003] G.J. Snyder, T.S. Ursell, Thermoelectric efficiency and compatibility, Phys. Rev. Lett. 91 (2003) 148301

[SNY 2008] G.J. Snyder, E.S. Toberer, Complex thermoelectric materials, Nat. Mater. 7 (2008) 105-114.

[SOD 2004] H.A. Sodano, J. Lloyd, D.J. Inman, An experimental comparison between several active composite actuators for power generation, Proc. SPIE 5390 (2004) 370–378.

[SOD 2007] H.A. Sodano, G.E. Simmers, R. Dereux, D.J. Inman, Recharging batteries using energy harvested from thermal gradients, J. Intell. Mater. Syst. Struct. 18 (2007) 3-10.

[STA 2006] I. Stark, Thermal energy harvesting with thermo life, Proceedings of the International Workshop on Wearable and Implantable Body Sensor Networks (BSN'06) (2006) 19-22.

[SUD 2005] E. Sudhakar Reddy, J.G. Noudem, S. Hebert, C. Goupil, Frabrication and properties of four-leg oxide thermoelectric modules, J. Phys. D: Appl. Phys. 38 (2005) 3751–3755

[TA 1938] Y. Ta, Effects of radiations on pyroelectric crystals, C.R. Hebd. Seances Acad. Sci. 207 (1938) 1042-1044.

[TAN 2007] Y.K. Tan, S.K. Panda, A novel piezoelectric based wind energy harvester for low-power autonomous wind speed sensor, The 33rd Annual Conference of the IEEE Industrial Electronics Society (IECON) (2007) 2175-2180.

[TAR 2000] A.Z. Tarnopolsky, N.H. Fletcher, J.C.S. Lai, Oscillating reed valves – an experimental study, J. Acoust. Soc. Am. 108 (2000) 400-406

[TEL 1954] M. Telkes, Solar thermoelectric generators, J. Appl. Phys. 25 (1954) 765-777.

[TOR 2006] T. Torfs, V. Leonov, C.V. Hoof, B. Gyselinckx, Body-heat powered autonomous pulse oximeter, IEEE Sensors (2006) 427-430.

[TOR 2008] T. Torfs, V. Leonov, R.F.Yazicioglu, etc. Wearable autonomous wireless electro-encephalography system fully powered by human body heat, IEEE Sensors 2008 Conference (2008) 1269-1272.

[TUT 1981] B.A. Tuttle, D.A. Payne, The effects of microstructure on the electrocaloric properties of Pb(Zr,Sn,Ti)O3 ceramics, Ferroelectrics 37 (1981) 603-606.

[VAN 1974] A. van der Ziel, Solar power generation with the pyroelectric effect, J. Appl. Phys. 45 (1974) 4128-4128.

[VAN 2008] D. Vanderpool, J.H. Yoon, L.Pilon, Simulations of a prototypical device using pyroelectric materials for harvesting waste heat, Int. J. Heat Mass Transfer 51 (2008) 5052-5062.

[VUL 2009] R.J.M. Vullers, R. van Schaijk, I. Doms, C. Van Hoof, R. Mertens, Micropower energy harvesting, Solid-State Electron. 53 (2009) 684-693.

[WAN 1999] Q.M. Wang, L.E. Cross, Constitutive equations of symmetrical triple layer piezoelectric benders, IEEE Trans. Ultrason. Ferroelectr. Freq. Control 46 (1999) 1343-1351.

[WAN 2009] Z.Y. Wang, V. Leonov, P. Fiorini, C.V. Hoof, Realization of a wearable miniaturized thermoelectric generator for human body applications, Sens. Actuators, A 156 (2009) 95-102.

[WEB 1999] J. Webster, Piezoelectricity Wiley Encyclopedia of Electrical and Electronics Engineering

[WEB 2006] J. Weber, K. Potje-Kamloth, F. Haase, P. Detemple, F. Volklein, T. Doll, Coin-size coiled-up polymer foil thermoelectric power generator for wearable electronics, Sens. Actuators, A 132 (2006) 325-330.

[WHA 1978] R.W. Whatmore, Pyroelectric devices and materials, Rep. Prog. Phys. 49 (1986) 1335-1386

[WHA 2008] S.A. Whalen, C.A. Apblett, T. L. Aselage, Improving power density and efficiency of miniature radioisotopic thermoelectric generators, J. Power Sources 180 (2008) 657-663.

[XIE 2010] J. Xie, X.P. Mane, C.W. Green, K.M. Mossi, K.K. Leang, Performance of thin piezoelectric materials for pyroelectric energy harvesting, J. Intell. Mater. Syst. Struct. 21 (2010) 243-249.

[XIE2 2010] M. Xie, D.M. Gruen, Potential impact of ZT = 4 thermoelectric materials on solar thermal energy conversion technologies, J. Phys. Chem. B 114 (2010) 14339-14342.

[XU 2010] J.W. Xu, W.W. Shao, F.R. Kong, Z.H. Feng, Right-angle piezoelectric cantilever with improved energy harvesting efficiency, Appl. Phys. Lett. 96 (2010) 152904.

[YAD 2008] A. Yadav, K.P. Pipe, M. Shtein, Fiber-based flexible thermoelectric

power generator, J. Power Sources 175 (2008) 909-913.

[YAG 1995] J. Yagi, T. Akiyama, Storage of thermal energy for effective use of waste heat from industries, J. Mater. Process. Technol. 48 (1995) 793–804.

[YAM 2008] O. Yamashita, Effect of linear temperature dependence of thermoelectric properties on energy conversion efficiency, Energy Convers. Manage. 49 (2008) 3163-3169.

[YAN 2007] Y. Yang, X.J. Wei, J. Liu, Suitability of a thermoelectric power generator for implantable medical electronic devices, J. Phys. D: Appl. Phys. 40 (2007) 5790-5800.

[YOR 2006] M. Yorukoglu, A.N. Celik, A critical review on the estimation of daily global solar radiation from sunshine duration, Energy Convers. Manage. 47 (2006) 2441-2450.

[YU 2007] J.L. Yu , H. Zhao, A numerical model for thermoelectric generator with the parallel-plate heat exchanger, J. Power Sources 172 (2007) 428-434.

[YU 2009] C. Yu , K.T. Chau, Thermoelectric automotive waste heat energy recovery using maximum power point tracking, Energy Convers. Manage. 50 (2009) 1506-1512.

[ZAL 2004] B. Zalba, J.M. Marina, L.F. Cabeza, H. Mehling, Free-cooling of buildings with phase change materials, nt. J. Refrig. 27 (2004) 839-849.

[ZHA 2007] Y.P. Zhang, G.B. Zhou, K.P. Lin, Q.L. Zhang, H.F. Di, Application of latent heat thermal energy storage in buildings: State-of-the-art and outlook, Build. Environ. 42 (2007) 2197-2209.

[ZHA 2009] L. Zhang, T. Akiyama, How to recuperate industrial waste heat beyond time and space, Int. J. Energy 6 (2) (2009) 214–227.

[ZHA 2010] J. Zhao, W.Q. Liu, Y.B. Liu, Z.H. Feng, Research on uniform—strain piezoelectric energy harvesting mechanism, Piezoelectrics and Acoustooptics 32 (2010) 406-409.

[ZHA2 2010] Q. Zhang, A. Agbossou, Zhihua Feng, Mathieu Cosnier, Solar micro-energy harvesting based on thermoelectric and latent heat effects. Part II: Experimental analysis, Sens. Actuators A: Phys. 163 (2010) 284-290.

[ZHU 2010] D.B. Zhu, M.J. Tudor, S.P Beeby, Strategies for increasing the operating frequency range of vibration energy harvesters: a review, Meas. Sci. Technol. 21 (2010) 022001 (29pp).

List of figures

List of tables

Appendix A

Calculation of parameters in the electrical model of the TEG:

$$R_1 = R_8 = \frac{1}{2}\frac{H_{TEG\_P}}{K_{TEG\_P}L_{TEG\_P}W_{TEG\_P}} = \frac{1}{2}\frac{0.5e^{-3}}{46\times 0.04\times 0.04} = 3.4e^{-3} \quad ^\circ\text{C/W}$$

$$R_2 = R_7 = \frac{1}{2}\left(\frac{H_{TEG\_P}}{K_{TEG\_P}L_{TEG\_P}W_{TEG\_P}} + \frac{H_{TEG\_E}}{127K_{TEG\_E}L_{TEG\_E}W_{TEG\_E}}\right) = 4.2e^{-3} \quad ^\circ\text{C/W}$$

$$R_3 = R_6 = \frac{1}{2}\left(\frac{H_{TEG\_E}}{127K_{TEG\_E}L_{TEG\_E}W_{TEG\_E}} + \frac{H_{TEG\_S}}{254K_{TEG\_S}L_{TEG\_S}W_{TEG\_S}}\right) = 2.6e^{-3} \quad ^\circ\text{C/W}$$

$$R_4 = R_5 = \frac{1}{2}\left(\frac{H_{TEG\_S}}{254K_{TEG\_S}L_{TEG\_S}W_{TEG\_S}} + \frac{H_{TEG\_L}}{254K_{TEG\_L}L_{TEG\_L}W_{TEG\_L}}\right) = 0.49 \quad ^\circ\text{C/W}$$

$$C_P = C_{TEG\_P}\rho_{TEG\_P}L_{TEG\_P}W_{TEG\_P}H_{TEG\_P}$$
$$= 753\times 3960\times 0.04\times 0.04\times 0.5e^{-3} = 2.39 \quad \text{J/}^\circ\text{C}$$

$$C_E = 127C_{TEG\_E}\rho_{TEG\_E}L_{TEG\_E}W_{TEG\_E}H_{TEG\_E} = 0.55 \quad \text{J/}^\circ\text{C}$$

$$C_S = 254C_{TEG\_S}\rho_{TEG\_S}L_{TEG\_S}W_{TEG\_S}H_{TEG\_S} = 0.062 \quad \text{J/}^\circ\text{C}$$

$$C_L = 254C_{TEG\_P}\rho_{TEG\_P}L_{TEG\_P}W_{TEG\_P}H_{TEG\_P} = 0.077 \quad \text{J/}^\circ\text{C}$$

Appendix B

When there is no wind, the estimation of natural convection coefficient $\boldsymbol{h_c}$ depends on the calculation of Rayleigh number (***Ra***) and Nusselt number (***Nu***) [INC 2007]:

$$Ra = Gr * Pr = \frac{G\beta\left(T(t) - T_a\right)L_c^3}{\nu^2} * \frac{\nu}{\alpha_d} \tag{B.1-1}$$

$$Nu = \frac{h_c L}{K_f} = 0.68 + \frac{0.67 \times Ra^{1/4}}{[1 + (0.492/Pr)^{9/16}]^{4/9}} \quad Ra \le 10^9 \tag{B.1-2}$$

Where $\boldsymbol{G}$ = 9.81 ms^{-2} is the gravitational constant, $\boldsymbol{\beta}$ = 1/298 K^{-1} is volumetric thermal expansion coefficient of air at film temperature $\boldsymbol{T_f}$ ($\boldsymbol{T_f}$ =($\boldsymbol{T(t)}$+$\boldsymbol{T_a}$)/2, $\boldsymbol{\nu}$ = 1.59e^{-5} m^2s^{-1} is kinematic viscosity of air at $\boldsymbol{T_f}$, $\boldsymbol{\alpha_d}$ = 2.24e^{-5} m^2s^{-1} is thermal diffusivity of air at $\boldsymbol{T_f}$. $\boldsymbol{L_c}$ is the characteristic length of the objective. It can be the length of the TEG or diameter of the PYEG. $\boldsymbol{K_f}$ = 0.0263 $Wm^{-1}K^{-1}$ is the thermal conductivity of air at $\boldsymbol{T_f}$.

When there is wind, the estimation of forced convection coefficient $\boldsymbol{h_c}$ is illustrated by Nusselt–Jürges correlation [PAL 2008]:

$$h_c = 5.678\left\{a + b\left[\left(\frac{294.26}{273.16 + T_a}\right)V_w \Big/ 0.3048\right]^n\right\}$$
$$V_w < 4.88 \text{ m/s: } a = 0.99, b = 0.21, n = 1$$
$$4.88 \le V_w \le 30.48 \text{ m/s: } a = 0, b = 0.5, n = 0.78 \tag{B.2}$$

Where $\boldsymbol{V_w}$ is the wind speed. a, b and n are empirical constants.

Appendix C

In order to provide high power density, the PYEG is always made as a flat and thin structure. It is possible to use a lumped parameter model to predict the thermal response of the PYEG. The criterion is the calculation of the Biot number given below (the PYEG is supposed to work with a maximum wind speed of 30 ms^{-1} and a minimum ambient temperature of -50°C) [INC 2007]:

$$h_c = \frac{5.678}{2}\left[\left(\frac{294.26}{273.16+T_{min}}\right)V_{max}\Big/0.3048\right]^{0.78} \qquad (\mathrm{Wm^{-2}K^{-1}})$$

$$L_{Bi} = \frac{\pi r^2 d}{(2\pi r^2 + 2\pi r d)} = \frac{1}{2}\frac{rd}{(r+d)} \qquad (m)$$

$$B_i = \frac{hL_{Bi}}{K_{PYEG}} \approx 0.008 << 0.1 \text{ , } V_{max} = 30 \text{ , } T_{min} = -50 \text{ , } K = 1.1$$

Where $\boldsymbol{L_{Bi}}$ is the characteristic length of PYEG which approximates half of the thickness. ***r*** and d are the radius and thickness of PYEG. The calculated Biot number is much less than 0.1 with extreme thermal boundary conditions. It guarantees the use of a lumped parameter model to analyze the transient thermal response of the PYEG.